AFRL-RZ-WP-TR-2009-2088

PROPULSION AND POWER RAPID RESPONSE R&D SUPPORT

Delivery Order 0047: Fundamental Science Investigations for Propulsion and Power Systems

Donald B. Hanson

Universal Technology Corporation

JANUARY 2009
Final Report

Approved for public release; distribution unlimited.

See additional restrictions described on inside pages

STINFO COPY

AIR FORCE RESEARCH LABORATORY
PROPULSION DIRECTORATE
WRIGHT-PATTERSON AIR FORCE BASE, OH 45433-7251
AIR FORCE MATERIEL COMMAND
UNITED STATES AIR FORCE

NOTICE AND SIGNATURE PAGE

Using Government drawings, specifications, or other data included in this document for any purpose other than Government procurement does not in any way obligate the U.S. Government. The fact that the Government formulated or supplied the drawings, specifications, or other data does not license the holder or any other person or corporation; or convey any rights or permission to manufacture, use, or sell any patented invention that may relate to them.

This report was cleared for public release by the USAF 88th Air Base Wing Public Affairs Office and is available to the general public, including foreign nationals. Copies may be obtained from the Defense Technical Information Center (DTIC) (http://www.dtic.mil).

AFRL-RZ-WP-TR-2009-2088 HAS BEEN REVIEWED AND IS APPROVED FOR PUBLICATION IN ACCORDANCE WITH ASSIGNED DISTRIBUTION STATEMENT.

*//Signature//	//Signature//
JOHN HORNER	CURTIS M. REEVES
Assistant to the Chief Scientist	Chief, Plans & Programs Branch

This report is published in the interest of scientific and technical information exchange and its publication does not constitute the Government's approval or disapproval of its ideas or findings.

*Disseminated copies will show "//Signature//" stamped or typed above the signature blocks.

REPORT DOCUMENTATION PAGE

Form Approved
OMB No. 0704-0188

The public reporting burden for this collection of information is estimated to average 1 hour per response, including the time for reviewing instructions, searching existing data sources, searching existing data sources, gathering and maintaining the data needed, and completing and reviewing the collection of information. Send comments regarding this burden estimate or any other aspect of this collection of information, including suggestions for reducing this burden, to Department of Defense, Washington Headquarters Services, Directorate for Information Operations and Reports (0704-0188), 1215 Jefferson Davis Highway, Suite 1204, Arlington, VA 22202-4302. Respondents should be aware that notwithstanding any other provision of law, no person shall be subject to any penalty for failing to comply with a collection of information if it does not display a currently valid OMB control number. **PLEASE DO NOT RETURN YOUR FORM TO THE ABOVE ADDRESS**.

1. REPORT DATE *(DD-MM-YY)*	2. REPORT TYPE	3. DATES COVERED *(From - To)*
January 2009	Final	06 March 2007 – 01 January 2009

4. TITLE AND SUBTITLE
PROPULSION AND POWER RAPID RESPONSE R&D SUPPORT
Delivery Order 0047: Fundamental Science Investigations for Propulsion and Power Systems

5a. CONTRACT NUMBER
F33615-02-D-2299-0047

5b. GRANT NUMBER

5c. PROGRAM ELEMENT NUMBER
62203F

6. AUTHOR(S)
Donald B. Hanson

5d. PROJECT NUMBER
06WP

5e. TASK NUMBER
UT

5f. WORK UNIT NUMBER
06WPUT47

7. PERFORMING ORGANIZATION NAME(S) AND ADDRESS(ES)
Universal Technology Corporation
1270 N. Fairfield Road
Dayton, OH 45432-2600

8. PERFORMING ORGANIZATION REPORT NUMBER

9. SPONSORING/MONITORING AGENCY NAME(S) AND ADDRESS(ES)
Air Force Research Laboratory
Propulsion Directorate
Wright-Patterson Air Force Base, OH 45433-7251
Air Force Materiel Command
United States Air Force

10. SPONSORING/MONITORING AGENCY ACRONYM(S)
AFRL/RZOP

11. SPONSORING/MONITORING AGENCY REPORT NUMBER(S)
AFRL-RZ-WP-TR-2009-2088

12. DISTRIBUTION/AVAILABILITY STATEMENT
Approved for public release; distribution unlimited.

13. SUPPLEMENTARY NOTES
PAO Case Number: 88ABW 2009-1163, 23 Mar 2009. Report contains color.

14. ABSTRACT
Research was conducted for the Propulsion Directorate's research and development efforts in core technology areas for turbine engines, hypersonics, and aerospace power. Experimental and theoretical research was conducted in the technical disciplines of fuels and combustion; mechanical subsystems and life management; aerodynamics; aerospace power systems including applied and high temperature superconductivity, physics of electrical discharges, applied atomic and molecular spectroscopy, thermophysics and high temperature dielectric materials, thermal nanofluids for heat transfer enhancement, optical controlled power electronics and sensors for harsh environments, logistic fuel capable, power dense fuel cells, superconducting and other materials research for power applications; high temperature superconductor (HTS) devices for high power applications; and hypersonics including high speed propulsion, advanced diagnostics for high speed flows, injection and flameholding in supersonic flows, and modeling and diagnostics of plasma/combustion environments.

15. SUBJECT TERMS

16. SECURITY CLASSIFICATION OF:			17. LIMITATION OF ABSTRACT:	18. NUMBER OF PAGES	19a. NAME OF RESPONSIBLE PERSON (Monitor)
a. REPORT	b. ABSTRACT	c. THIS PAGE			
Unclassified	Unclassified	Unclassified	SAR	240	John E. Horner 19b. TELEPHONE NUMBER *(Include Area Code)* N/A

Standard Form 298 (Rev. 8-98)
Prescribed by ANSI Std. Z39-18

TABLE OF CONTENTS

Section **Page**

1.0 SUMMARY 1

2.0 INTRODUCTION 6

3.0 DISCUSSION 7

APPENDIX A
Pinning Properties of YBCO Thin Films Doped With BZO, Y203, and BSnO 13

APPENDIX B
Ball Bearing Raceway Fatigue Spall Propagation 42

APPENDIX C
Experimental Research Involving the Use of Pulsed Voltage to Modify Flame Speed and Flame Instability 53

APPENDIX D
An Energy-Based Fatigue Life Estimation Method for Common Gas Turbine Engine Materials 69

APPENDIX E
Physics of Electric Discharge 81

APPENDIX F
Modeling Spall Growth in Ball Bearing Raceways 82

APPENDIX G
Double-Pulsed Digital Holographic Diagnostics for Aerated Liquid Jets in Crossflow 92

APPENDIX H
Flow Loop Experiments Using PAO/CNT Nanofluids 115

APPENDIX I
Thermal Management High Heat Flux 136

APPENDIX J
Neural-Fuzzy Modeling in Model-Based Fault Detection, Isolation and Control Adaptation and Reconfiguration in Turbine Engines 171

APPENDIX K
Optimization of Supersonic Inlet Based on Multi-Objective Optimization Approach Using Genetic Algorithm 214

1.0 SUMMARY

This Task Order was initiated to provide technical support to AFRL/RZTS from 30 March2007 through 27 November 2008 to conduct research for the Propulsion Directorate's Research and Development efforts in the core technology areas for turbine engines, hypersonics, and aerospace power. The Statement of Work requirements were as follows:

2.0 REQUIREMENTS

2.1 Fuels and Combustion

2.1.1 Model Development and Validation Experiments for Aircraft Fuel: The contractor shall conduct experimental and theoretical research on the influence of dissolved oxygen content, turbulence, thermal loads, pressure, catalytic reactions, or heat-exchanger geometry on the thermal degradation of hydrocarbons found in jet fuels.

2.1.2 Combustion and Spray Studies and Diagnostic Development: The contractor shall conduct research to address the physics and chemistry of processes in gas turbine combustors and pulsed-detonation engines through the study of isolated and interacting droplets, sprays, jet premixed and diffusion flames, swirling flames, and bluff-body stabilized flames.

2.1.3 Computational Modeling for Advanced Concepts in Gas Turbine Engine Combustion: The contractor shall design, analyze and optimize efficient combustion systems for turbomachinery applications using Computational Fluid Dynamic (CFD) techniques applying improvements in numerical algorithms, geometric modeling, numerical discretization, grid generation, physical parameter modeling, and adaptability in the supercomputing environment (including parallel architecture).

2.2 Mechanical Subsystems and Life Management

2.2.1 Advanced Turbine Engine Lubrication: The contractor shall develop novel mechanical and magnetic systems to minimize the weight and complexity of the traditional lubrication system. Finite element methods may be used to model heat dissipation, stress fields, and shaft dynamics. The contractor shall conduct research in high-temperature lubrication addressing thermal-oxidative degradation; and tribological, toxicological, and environmental properties of candidate lubricants.

2.2.2 Gas Turbine Control Systems and Engine Health Management Research: The contractor shall conduct research in the study of control system performance including investigation of control systems behavior with specific propulsion platforms, the effects of component changes on propulsion system performance, and characterization of mission-related turbine operating parameters. In addition, the contractor shall evolve characterization and prediction of component degradation and control system modifications for the purpose of identifying and managing engine health issues. The contractor shall exploit research areas to include real-time, physics-based simulation of engine and control system operation; development of improved sensors, actuators, and engine control algorithms; simulation-based hardware testing; model-based control; diagnostic, prognostic, and engine health management techniques; and integration of the propulsion systems with other air vehicle subsystems.

2.2.3 Structural Dynamics of Turbo machine Components: The contractor shall conduct research to assess life capability and vibrational characteristics of turbine engine components. The contractor shall quantify the capability of components under cyclic loading to reduce or even

alleviate the need for costly repairs and diminish the possibility of failure. The contractor shall investigate mistuning in higher order modes of bladed disks, interaction of closely spaced modes, evaluation of inherent and added damping in airfoil systems, and integration of experimental results into prediction codes. The contractor shall improve bench experimentation by developing simulated engine operating conditions (rotational forces, contact mechanics, component interactions), the development of innovative test techniques for component characterization, and the validation of advanced instrumentation techniques.

2.3 Aerodynamics

2.3.1 Aero and Thermodynamics of Rotating Machinery: The contractor shall develop techniques to accurately predict heat transfer of cooled and uncooled components in the hot section of turbine engines. The contractor shall accurately predict the nonsteady, aero thermal forcing functions and blade loadings to calculate thermal or structural fatigue lifetimes. The contractor shall characterize aerodynamic thermal and structural effects using two- and three-dimensional computational schemes, and experimental techniques capable of spatial and temporal resolution comparable to that achievable computationally.

2.3.2 Fluid Mechanics of Turbo machinery: The contractor shall conduct research in the fundamental knowledge of complex flows within transonic compressors that is essential to achieving maximum performance. The contractor shall use techniques of analytical and experimental methods to establish strategies for control of complex flows to enhance performance improvements in turbo machinery. In addition, the contractor shall account for the presence of unsteady effects inherent in turbo machinery flows, identify the relative importance of length and time scales of unsteady flow phenomena, establish the influence of unsteady flows on blade forced response, and provide for future improvements in turbo machinery technology based on the recognition of unsteady phenomena.

2.4 Aerospace Power Systems

2.4.1 Micro-System Technologies in Advanced Aerospace Vehicle Power Systems: The contractor shall conduct research and development activities to demonstrate the potential use of innovative micro-systems integral to aerospace vehicle prime power and secondary power systems. These innovative micro-systems may incorporate such approaches as micro sensing for diagnostic surveillance, micro-fluidics for thermal control, or microscale control of macroscale processes. Micro-systems will be required to be robust and operate in harsh environments such as elevated temperature, vibration, and acceleration.

2.4.2 Lithium-Ion Conducting Channel: The contractor shall simulate the electric field gradient in rechargeable lithium polymer batteries using computational chemistry and applying it to the lithium ion conducting channel molecular system in order to correlate molecular structure with ionic conductivity. In addition, the contractor shall investigate the electrolyte/electrode interface through computational chemistry.

2.4.3 Applied and High-Temperature Superconductivity: The contractor shall study new high-temperature superconductors, such as the copper oxide Perovskites using extensive in-house magnetic property characterization equipment, including a variable temperature transport current apparatus, a vibrating sample magnetometer, and an AC susceptometer. The contractor shall manufacture and evaluate superconducting materials for a wide range of applied devices. The contractor shall devise and test novel conductor configurations to minimize transient magnetic

field losses. The contractor must have an understanding of losses that result from transient magnetic fields for short-conductor samples and small models of high-power devices, such as pulsed-energy storage magnets, generator magnets, and rotating electrical generators. Transient heat transfer, normal zone propagation, and quench protection analyses are also important.

2.4.4 Physics of Electric Discharges: The contractor shall conduct theoretical studies and experiments of low-pressure, electrically excited gas discharges in a number of configurations that involve direct current, radio frequency, and microwave excitation. This research includes excitation processes, energy transfer processes under nonequilibrium conditions, and electron transport.

2.4.5 Applied Atomic and Molecular Spectroscopy: The contractor shall develop and apply spectroscopic methods for quantitative measurements in nonequilibrium plasmas and high-temperature reacting flows. The contractor shall investigate well-defined low to medium pressure discharges using CW and pulsed direct current, low frequency to radio frequency, and microwave excitations for their application to flow control in hypersonics, plasma enhanced etching, surface modifications, and dielectric breakdown. The contractor shall conduct experimental and theoretical studies to characterize homogeneous and heterogenous processes in plasmas including plasma-surface interactions, plasma assisted ignition, and the creation and influence of self-ordered nanoparticles in plasmas. The contractor shall investigate the flux scaling properties of atmospheric pressure or near atmospheric pressure short pulse duration, high reduced electric field dielectric barrier discharges for both vacuum ultraviolet/ultraviolet light source and low-cost surface coating applications.

2.4.6 Thermophysics and High-Temperature Dielectric Materials: The contractor shall examine basic and applied heat-transfer and thermodynamic phenomena both analytically and experimentally of active electronic devices with emphasis on their adaptation to airborne secondary power-systems, spacecraft prime power, and electronic component thermal management. The contractor shall develop superior high-temperature, high-power capacitors using novel/innovative dielectric materials and electrode methods. The contractor shall place emphasis on understanding the dielectric microstructure and its effect on such macroscopic properties as dielectric constant, voltage breakdown strength, and dissipation factor. The contractor shall conduct molecular modeling of amenable and promising dielectric materials using numerical analysis to more fully understand these micro/macro relationships.

2.4.7 Thermal Nanofluids for Heat Transfer Enhancement: The contractor shall develop novel research ideas for exploration, characterization and technology maturation strategies pertaining to all aspects of nanofluids including formulation, functionalization and molecular dynamics modeling and simulation of the new fluid suspensions. The nanofluid must be useful in -50 to +200 deg C and capable of functioning in single and two phase modes. Pilot scale production and synthesis of nanofluids for use in proof-of- the-concept test rigs containing microchannel, liquid-liquid, liquid-air heat exchangers, heat pipes, and spray cooling loops may be required.

2.4.8 Optical Controlled Power Electronics and Sensors for Harsh Environments: The contractor shall investigate the areas of micro-systems sensor and power electronic device development with an emphasis on developing schemes for optical control and interrogation. Significant interest exists in developing sensors and optical interrogation technologies that are capable of providing accurate, repeatable, high-resolution response to small changes in pressure, temperature, electrical current, voltage, and fluid flow. The contractor shall perform fundamental

and advanced research in the areas of optical carrier generation and carrier transport under high electric field and high level injection conditions in wide bandgap semiconductors being considered for optically activated high power switching functions. The contractor shall develop optical signal processing schemes and devices, including micro-scale gratings, mirrors, and filters enabling high-speed adaptive feedback control of a system or subsystem.

2.4.9 Logistic Fuel Capable, Power Dense Fuel Cells: The contractor shall explore materials and technologies for significantly improving the performance of fuel cell technology. The contractor shall examine materials and application processes that reduce barriers to achieving high performance utilization of military logistic fuels and examination of electrochemical factors which influence high performance. The contractor shall investigate different approaches to include discrete fuel reformation, indirect fuel reformation, and direct oxidation fuel cells. The contractor shall apply basic electrochemical analysis in order to elucidate electrochemical factors that influence power dense, high performance operation. Of primary interest are methods for decreasing interfacial impedances through exploration of novel electrode structuring.

2.4.10 Superconducting and Other Materials Research for Power Applications: The contractor shall explore the fundamental understanding of superconductors with their associated development necessary to realize high-temperature superconductors (HTS) applications in power systems such as generators, motors, and transformers. The contractor shall develop coated conductors, carbon nanotubes, nonsuperconducting magnetic materials, and pinning enhancements. Emphasis for carbon nanotubes is research necessary to achieve long lengths for electrical wiring. Magnetic materials research is to develop improved permanent magnets, such as high saturation and nanoparticle composite materials. The contractor shall develop methods to minimize AC losses associated with hysteretic, eddy current, coupling, ferromagnetic, and self-field transport.

2.5 High Temperature Superconductor (HTS) devices for high power applications.

2.5.1 The contractor shall experimentally analyze three-dimensional quench simulation and protection in HTS devices. The contractor shall provide technical research in the development of a quench analysis code capable of addressing quench performance and protection of HTS coils. Specifically, this effort will encompass:

Task 1: The contractor shall evaluate alternatives to proceed with model development and determine what platform is best suited for a 3D model of HTS devices. In particular, the contractor shall assess alternatives for Finite Element Method (FEM) codes that may be employed. The contractor shall evaluate the following platforms as a minimum: Ansoft/Maxwell, Flux3D, Ansys, Vector Fields/Opera, and CERN's modified SABER. The contractor shall establish the requirements and criteria to be used in the selection. The contractor shall determine, in consultation with Air Force personnel, which one represents the best option to proceed with quench model development or if in-house simulation tools need to be developed.

Task 2: The contractor shall characterize electrical, thermal, and mechanical properties of HTS conductors and other coil materials, including insulation and dielectrics as well as their interactions due to their different properties (thermal expansion, etc.) through collaboration with appropriate academia technical experts, interaction with conductor manufacturers, and/or literature search.

Task 3: The contractor shall develop a combined thermal/electrodynamic 3D model of a quenching HTS tape including all pertinent material property models. The contractor shall validate simulations using experimental data. This task will include collaboration with appropriate academia and industry technical experts.

2.6 Hypersonics

2.6.1 High-Speed Propulsion: The contractor shall conduct research on ramjet/scramjet and mixed-cycle propulsion components applicable to supersonic and hypersonic flight regimes; this includes fluid-dynamic studies of inlet, combustor, and nozzle components. The contractor shall pursue development of efficient computational methods, turbulent models, and kinetic schemes for reacting, high-speed flows. The contractor shall integrate experimental and theoretical methods to address challenges in mixing of multistream flows and/or two-phase flows; nonintrusive, multidimensional diagnostic instrumentation for applications to realistic combustor flow environments; and time-averaged and time-dependent computational-fluid-dynamics codes for flow and combustion simulations in complex geometries.

2.6.2 Advanced Diagnostics for High-Speed Flows: The contractor shall develop laser diagnostic tools to further the understanding of high-speed combustion processes in order to improve combustor performance. These diagnostics include planar laser-induced fluorescence, particle-image velocimetry, Rayleigh and Raman scattering, coherent anti-stokes Raman scattering, pulsed holography, and diode-laser absorption. The contractor shall develop emerging imaging techniques such as filtered Rayleigh scattering, planar Doppler velocimetry, combined planar laser-induced fluorescence and particle-image velocimetry, and other techniques—particularly those capable of high framing rates—enabling the study of high-speed combustion.

2.6.3 Injection and Flameholding in Supersonic Flows: The contractor shall conduct research on the understanding of flame holding in supersonic flows. The contractor shall design and investigate more robust flame stabilization techniques for hydrocarbon-fueled scramjets.

2.6.4 Modeling and Diagnostics of Plasma/Combustion Environments: The contractor shall apply modern chemical physics addressing the chemical issues associated with supersonic combustion. The development of next generation aerospace vehicles requires a precise understanding of fluid dynamics with detailed chemistry. The contractor shall develop a detailed understanding of the plasma-chemistry-flow field coupling. Key research areas include (1) the identification of fundamental kinetic parameters and their measurement using advanced laser based diagnostic methods, and (2) the development of reduced mechanisms and supplemental thermodynamics data for computational fluid dynamics modeling applications. The contractor shall investigate large hydrocarbon mechanism development and validation to provide a detailed understanding of the key processes involved. An important part of the research is the reduction of these mechanisms for use in CFD models describing the extremely complicated and computationally demanding supersonic combustors proposed for hypersonic vehicles. The contractor shall experimentally verify the computational results by providing species-specific information through the use of laser diagnostics experiments. Particular emphasis shall be placed on sensitive diode laser absorption measurements, which are capable of being packaged as flight weight diagnostic systems.

2.0 INTRODUCTION

Under Prime Contract F33615-02-D-2299, Task Order 0047 was initiated to provide technical support to AFRL/RZ to conduct research for the Propulsion Directorate's Research and Development efforts from 30 March 2007 through 27 December 2008.

3.0 DISCUSSION

The overall objective of this task was to conduct research for the Propulsion Directorate's research and development efforts in core technology areas for turbine engines, hypersonics, and aerospace power. Experimental and theoretical research was conducted in the technical disciplines of fuels and combustion; mechanical subsystems and life management; aerodynamics; aerospace power systems including applied and high temperature superconductivity, physics of electrical discharges, applied atomic and molecular spectroscopy, thermophysics and high temperature dielectric materials, thermal nanofluids for heat transfer enhancement, optical controlled power electronics and sensors for harsh environments, logistic fuel capable, power dense fuel cells, superconducting and other materials research for power applications; high temperature superconductor (HTS) devices for high power applications; and hypersonics including high speed propulsion, advanced diagnostics for high speed flows, injection and flameholding in supersonic flows, and modeling and diagnostics of plasma/combustion environments.

The effort was accomplished by subcontracts with various individuals and institutions.

Subcontracted Efforts

0047-02-C1

Nanoscale Flex Pinning Enhancements in PLD YBCO Conductors

From 4 Jun 07 – 26 Aug 07, technical support was provided to AFRL/RZPG in support of research efforts involving nanoscale flex pinning enhancements in PLD YBCO conductors.

This Task is complete and a Final Report was submitted to AFRL/RZPG for review and comment. (See Appendix A)

0047-02-C2

Ball Bearing Raceway Fatigue Spall Propagation

From 27 Aug 07 – 18 Nov 07, technical support was provided to AFRL/RZTM with research efforts involving ball bearing raceway fatigue spall propagation.

This Task is complete and a Final Report was submitted to AFRL/RZTM for review and comment. (See Appendix B)

0047-02-C3

Experimental Research Involving the Use of Pulsed Voltage to Modify Flame Speed and Flame Instability

From 25 Jun 07 – 21 Aug 07, technical support was provided to AFRL/PRPE with experimental research involving the use of pulsed voltage to modify flame speed and flame instability in order to gain a better understanding of flame holding in supersonic flows.

This Task is complete and a Final Report was submitted to AFRL/RZPE for review and comment. (See Appendix C)

0047-02-C4

Structural Dynamics of Turbomachine Components

From 4 Jun 07 – 26 Aug 07, technical support was provided to AFRL/ RZTS with the research efforts involving the structural dynamics of turbomachine components.

This Task is complete and a Final Report was submitted to AFRL/RZTS for review and comment. (See Appendix D)

0047-02-C5

Physics of Electric Discharge

From 8 May 07 – 31 Jul 07, technical support was provided to AFRL/ RZPE with theoretical studies and experiments of low-pressure, electrically excited gas discharges in a number of configurations that involve direct current, radio frequency, and microwave excitation. This research included excitation processes, energy transfer processes under non-equilibrium conditions, and electron transport.

This Task is complete and a Final Report was submitted to AFRL/RZPE for review and comment. (See Appendix E)

0047-02-C6

Ball Bearing Raceway Fatigue Spall Propagation

From 8 May 07 – 14 Aug 07, technical support was provided to AFRL/ RZTM with research efforts involving ball bearing raceway fatigue spall propagation.

This Task is complete and a Final Report was submitted to AFRL/RZTM for review and comment. (See Appendix F)

0047-02-C7

Ball Bearing Raceway Fatigue Spall Propagation

From 7 May 07 – 3 Aug 07, technical support was provided to AFRL/RZTM with research efforts involving ball bearing raceway fatigue spall propagation.

This Task is complete and a Final Report was submitted to AFRL/RZTM for review and comment. (See Appendix F)

0047-02-C8

Holographic Diagnosis of Fuel Injection

From 1 Jun 07 – 26 Aug 07, technical support was provided to AFRL/RZAS with research efforts associated with advanced diagnostics for high-speed flows, specifically the holographic diagnosis of fuel injection. Digital holographic microscopy was used to probe the near-field of aerated-liquid just injected in supersonic cross flow and to provide benchmark data for drops sizes and velocities in the near-injector area. Measurements and analysis were undertaken in order to gain a better understanding of the secondary breakup of aerated jets in supersonic cross flow.

This Task is complete and a Final Report was submitted to AFRL/RZAS for review and comment. (See Appendix G)

0047-02-C9

Combustion Modeling

From 4 Jun 07 – 30 Jul 07, technical support was provided to AFRL/RZTC by studying in detail both the combustion-turbulence models and the numerical procedures in AEROFLO/ Combustion, gaining a better understanding of the inputs to and the outputs from the code, and performing analysis for a problem that was relevant to some of the efforts at AFRL/RZTC.

0047-02-C10

Investigation Into the Use of Nanofluids as a Viable Heat Transfer Fluid

From 21 May 07 – 13 Aug 07, technical support was provided to AFRL/RZPS by conducting an investigation into the use of nanofluids as a viable heat transfer fluid.

This Task is complete and a Final Report was forwarded to AFRL/RZPS for review and comment. (See Appendix H)

0047-03-C1

Thermal Management for High Heat Flux Components Using Spray Cooling and Surface Enhancement Techniques

From 1 Sep 07 – 28 Dec 08, technical support was provided to AFRL/ RZ with the development of thermal management innovative methodologies to protect devices that generate high heat flux. This effort involved the completion of Phase I of a two-phased effort and entailed completion of the following five tasks—

Task 1: Scaling analysis to identify characteristic time and length scales

- Elicit system requirements
- Identify the thermal physical processes and the partial differential equations which describe the physics
- Identify the control physics to obtain the characteristics parameters (timescales, length scales, velocity and temperature scales)
- Normalize the partial differential equations to extract the non-dimensional numbers which describe the process.

Task 2: Development of numerical models for flow in the manifold

- Acquire the solid CAD model of the manifold and clean CAD prior to volume meshing
- Identify surfaces in contact with the fluid or vapor
- Build a fluid model using these surface or Boolean mathematics
- Choose mesh type (tetrahedral, polyhedral or hexahedral) after identifying boundary layers surfaces which need special attention
- Identify symmetry and inlet and outlet conditions
- Write advanced scripting for parametric studies

- Define the multi domain interfaces and the interpolation schemes
- Determine the maximum conditions and if exceeds laminar hydrodynamic range then choose the best-fit turbulence model
- Determine the optimal grid size for resolved and convergent data
- Write scripts to process the data and compare with experimental observations.

Task 3: Build a subscale ammonia spray cooling system for testing and demonstration purposes

Task 4: Acquire baseline data

- Generate baseline data against in which all cases will be compared. The baseline data will be obtained from subscale ammonia spray cooling system using a 1cm x 2cm heater with smooth surface.

Task 5: Improve spray cooling performance by surface enhancements using micro/macro structures

Optimum micro structured surface

Particle blasted surface

- Define three size range (fine, medium, coarse) for abrasive particles that will be used to particle blast heater surfaces
- Prepare heater samples using fine, medium, coarse particles at proper blasting conditions

Spray coated surface

- Define three size range (fine, medium, coarse) for Al particles that will be used to spray coat heater surfaces
- Prepare heater samples using fine, medium, coarse Al particles
- Measure roughness of heater samples using optical profiler
- Take SEM images of heater samples
- Test heater samples on subscale system
- Compare spray cooling performance of particle blasted and spray coated heater samples and determine the optimum micro structured surface
- Find effect of surface condition on heat transfer coefficient and CHF
- Explain heat transfer mechanism based on experimental results

Optimum macro structured surface

- Evaluate different fabrication techniques (e.g., CNC machining, EDM…) to make millimeter size macro structures on heater surfaces
- Prepare heater samples with straight fin, cubic pin fin, groove and pyramid geometries all having same structure height

- Test heater samples on subscale system
- Compare spray cooling performance of heater samples and determine the best geometry
- Prepare heater samples with best geometry and vary the structure height
- Test heater samples on subscale system
- Compare spray cooling performance of heater samples and determine the optimum macro structured surface
- Find effect of surface condition on heat transfer coefficient and CHF
- Explain heat transfer mechanism based on experimental results

This Task is complete and a Final Report was forwarded to AFRL/RZ for review and comment. (See Appendix I)

0047-03-C2

Neuro-Fuzzy Probabilistic Systems For Fault Diagnosis of Turbine Engines

From 1 Sep 07 – 27 Nov 08, technical support was provided to AFRL/RZ in conducting basic and applied research related to fault detection, isolation, accommodation, and reconfiguration of turbine engine adaptive control and health management leading to intelligent turbine engines with damage-tolerant control, health and life management system. This multi-year/multi-phase effort accomplised the following objectives—

- Conduct research, and develop algorithms for, sensor data processing and feature extraction suitable for turbine engine fault and operation abnormality detection.
- Investigate and develop sensor fusion algorithms of multimodality sensors used in turbine engine control and health management system.
- Develop software and tools for fault detection and isolation in turbine engine based on features extracted by processing and fusion of sensor data (diagnosis).
- Develop software and algorithms for predicting remaining useful life (URL) of faulty components detected in turbine engine (prognosis).
- Develop software for reasoning and intelligent decision-making system for reconfiguration and adaptation of control loops in turbine engine.
- Develop software for system adaptation and performance optimization of turbine engine health-management system.

The following portion of the overall effort involved completion of the first year of a three-year effort and served as a preparatory year during which the specific problem at hand and the scope of the research was clearly established by accomplishing the following tasks—

- Obtain turbine engine model from the propulsion Directorate at AFRL, run simulation tests under normal operating conditions, and develop solid understanding of different aspects of the engine health-management challenges to be addressed in the research.

- Identify specific section of the engine most appropriate to work on and software requirements based on recommendations from the technical monitor of the research.
- Compile a list of anomalies, classes of faults including potential sensor failures and redundancy, and generate simulation measurements and data associate with each identified fault and receive approval of its validity from AFRL.
- Perform advanced data preprocess on the simulation measurements and data collected above including noise filtering and fault feature extractions.

This Task is complete and a Final Report was forwarded to AFRL/RZ for review and comment. (See Appendix J)

0047-03-C3

Optimization of a Supersonic Inlet Based on a Multi-Objective Optimization Approach Using Genetic Algorithm

From 1 Oct 07 – 30 Sep 08, technical support was provided to AFRL/RZ with a research effort to simulate supersonic inlets for ramjet/scramjet engines. The main objective of this effort was to perform optimization of a supersonic inlet through a range of Mach numbers ranging from 3 to 10. In order to accomplish this main objective, the following tasks were performed—

Task 1

1a. Acquire base model

1b. Finalize design variables and objectives.

Task 2

Upgrade cluster capability

Task 3

Conduct a baseline run/validation

Task 4

Perform CFD simulations for response surface

Task 5

Develop global Pareto optimal front/surface

This Task is complete and a Final Report was submitted to AFRL/RZ for review and comment. (See Appendix K)

PINNING PROPERTIES OF YBCO THIN FILMS DOPEDWITH BZO, Y2O3, and BSnO

FINAL REPORT

M.D. Sumption

Dec 30, 2007

1. Introduction/Abstract

YBCO samples with B-zirconate, Y_2O_3, and Ba-Sn-O pinning centers dopants were measured for their magnetic properties. For the sake of completeness, data taken here is compared to previous measurements. In general, J_cs, pinning energies, α, and B^* are under study. The J_c curves are parameterized for J_{sv}, B^*, and α, and compared to previous results, including control samples.

Multilayer $(BZO_n/123_{15nm})_{19}$ and $(123_{1-x}BZO_x)$ films were deposited by pulsed laser deposition (PLD. The substrates substrates used were $LaAlO_3$ (LAO) 100 oriented single crystals, with epi-polish. An automated target rotation and pulse-triggering system was used to control the deposition sequences. The 'pseudo-layer' thickness in the multilayer films was calculated assuming smooth continuous film coverage, although the insulating layer in most cases consisted of discontinuous and discrete nanoparticles. Deposition rates for Y123 and $(Y123_{1-x}BZO_x)$ were 13-15 nm/min and for BZO was 30-35 nm/min. Conditions were similar for Y2O3 dopants, again layered composites were formed.

The B-Sn-O doped samples were made with a 30 deg BSO sector on a YBCO target. However, the BSN-A and BSN-B (PV119 and PV104, respectively) were fabricated with AFRL-made YBCO targets and BSO sectors. On the other hand, PV231-B was fabricated with a commercial YBCO powder and a more recent AFRL-made BSO target which incorporated a better control of the fabrication process. The size of the nanoparticles for BSN-A and BSN-B were approximately 10 nm while the density was about $3.5x10^{11}/cm^2$ in both cases. Particulars for PV231 are now being determined. TEM studies on the BSO samples show nanocolumns extending through the thickness of the sample, where the nanoparticles/nanocolumns are thought to be self-assembled BSO structures.

2.0 Measurement Methods and Samples

2.1 Measurement Methods

Two different magnetometers have been used to measure the magnetic response of YBCO samples. The first vibrating sample magnetometer was a 1.7 T PAR EG&G VSM with a water cooled electromagnet used in conjunction with a He-flow varitemp. Two different measurements were made. The first was fixed ramp *M-H* loops used to extract a magnetic J_c.

Measurements were performed in a face-on orientation at lower fields from 4.2 K to 77 K. A series of loops with increasing amplitude were measured at each temperature. Using these loops magnetic J_c curves could be extracted, and it was possible to parameterize these curves with a field below which magnetization-derived J_c is flat, B^*, a low field (maximal) J_c value at lowest fields, $J_{c,max}$, and the exponent for J_c decay with field, α. The second type of measurement was ramp rate dependent *M-H* loops, from which pinning potentials will be extracted.

The second magnetometer was a 14 T PPMS. The measurements with this machine, just now beginning, allowed magnetic J_cs to be extracted up to much higher fields (14 T), and also allowed B_{irr} values to be identified at higher temperatures.

2.2. Samples

Sample specifications are listed in Table 2.2.1, in preparation for magnetic J_c comparisons. Included also are magnetization values at 4.2 K and 77 K. The nanoparticles in the BSN samples seemed to have formed self-assembled nano-rod structures. Not all parameters have been extracted from the data yet, the partial results are given in this interim report.

Table 2.2.1. Sample Specifications I.

Sample ID	Tracer ID	Type	Particle nominal diameter, nm	Number Density particle, 10^{11} cm^{-3}	Nano Distr	*t*, μm	*2nd phase Vol%*
BSN-A	PV119D	$BaSnO_3$	10	3.5	SA NR	0.33	
BSN-B	PV104C	$BaSnO_3$	10	3.5	SA NR	0.33	
BZO-A	TJ1130A	BZO (.02 BaZrO)	?	?	?	0.271	?
BSN-C	PV231-B	$BaSnO_3$	?		??		
Cont-D	TJ912A	Control	--	LAO	0	0.265	0
			123/nano t, nm	Substrate			
BZO-B	TJ1622 C	BZO/L	7.45/0.496	LAO	34 layers	0.278	6.24
BZO-C	TJ1625C	BZO/L	4.92/0.491	LAO	52 layers	0.282	9.07
BZO-D	TJ1619C	BZO/L	4.73/0.689	LAO	54 layers	0.282	12.7
BZO-E	TJ1616C	BZO/L	10	LAO	35 layers	0.305?	
CONT-H	TJ1601C	Cont	none	LAO	none	0.308	0
CONT-I	TJ1595C	Cont	none	LAO	none	0.301	0
Y2O3-A	TJ1554A	Y_2O_3	3.81/0.497	LAO	80 layers	0.345	4.10
Y2O3-B	TJ1533A	Y_2O_3	8.50/0.414	LAO	26 layers	0.232	4.65
Y2O3-C	TJ1551A	Y_2O_3	9.79/0.414	LAO	26 layers	0.265	4.10

Table 2.2.1. Sample Specifications II.

Sample ID	Tracer ID	Δm, emu, 4.2K, 0T	Δm, emu, 77K, 0T	J_c factor (emu to MA/cm^2)	Vol., 10^{-6} cm^3	t, μm	$\langle w \rangle$, mm
BSN-A	PV119D	0.448	0.019	26.3	3.45	0.317	3.30
BSN-B	PV104C	0.281	0.098	30.6	2.97	0.273	3.30
BZO-A	J1130A	0.637	0.0358	37.6	2.51[b]	0.271	3.18
BSN-C	PV231-B				?	?	?
Cont-D	TJ912A	0.984	0.0430	41.5	2.26[b]	0.265	3.20
BZO-B	TJ1622C	1.9825	0.036	33.6	2.81	0.278[a]	3.18
BZO-C	TJ1625C	2.05	0.017	32.8	2.87	0.282	3.19
BZO-D	TJ1619C	1.55	0.164	32.8	2.87	0.282	3.19
BZO-E	TJ1616C	1.268	0.028	?	?	?	??
CONT-H	TJ1601C	1.955	0.0635	29.8	3.15	0.308	3.20
CONT-I	TJ1595C	1.72	0.0644	29.6	3.14	0.301	3.23
Y2O3-A	TJ1554A	0.496	0.0284	26.8	3.51	0.345	3.19
Y2O3-B	TJ1533A	1.66	0.0426	39.9	2.36	0.232	3.19
Y2O3-C	TJ1551A	1.58	0.056	34.8	2.70	0.265	3.19

[a] error is 4%
[b] Post etch volumes

3.0 Low Field Pinning Results

Figures 3.1-3.4 give the magnetic J_c vs B for samples BSN-A, BSN-B, BZO-A, and CONT-D. Table 3.1 lists a summary of the results at 77 K and 4.2 K for intercomparison. Typically three regimes are seen, a low field regime, below B^*, where the field dependence is small, which we can denote the self-field regime, J_{sf}, a middle regime where $J_c = J_{c0}B^{-\alpha}$, and a high field regime. Values for J_{sv}, α, and B^* at 77 K and 4.2 K are given in Table 3.1 where available.

Table 3.1. 77 K and 4.2 K values for J_{sv}, B^*, and α

Sample ID	Tracer ID	J_{sf} 4 K	J_{sv}, MA/cm^2 (77 K)	B^*, mT (4 K)	B^*, mT (77 K)	α (4 K)	α (77 K)
BSN-A	PV119D	11.8	0.50			VS	0.50
BSN-B	PV104C	8.60	0.50			VS	0.30
BZO-A	J1130A	24.0	1.34	130	0	0.14	0.341
Cont-D	TJ912A	40.8	1.79	60	0	0.334	0.327
BZO-B	TJ1622C	66.6	1.30	144	?	0.21	0.19
BZO-C	TJ1625C	67.3	0.57	210	?	0.19	0.12
BZO-D	TJ1619C	42.7	0.54	54.6	?	0.19	0.37
BZO-E	TJ1616C	?	?	?	?	?	
CONT-H	TJ1601C	58.3	1.89	125	?	0.36	0.37
CONT-I	TJ1595C	55.5	1.92	120	?	0.36	0.34
Y2O3-A	TJ1554A	13.3	0.76	157	?	0.33	0.59
Y2O3-B	TJ1533A	46.5	1.7	294	?	0.33	0.36
Y2O3-C	TJ1551A	54.9	1.94	95	?	0.35	0.33

Table 3.1 gives J_{sv}, B^* , and α for all samples at 4 K and 77 K. Generally, we see $\alpha = 0.5$ for control samples and a better (lower) α for various kinds of pinning. Figures 3.1-3.4 are fully normalized results from previous data.

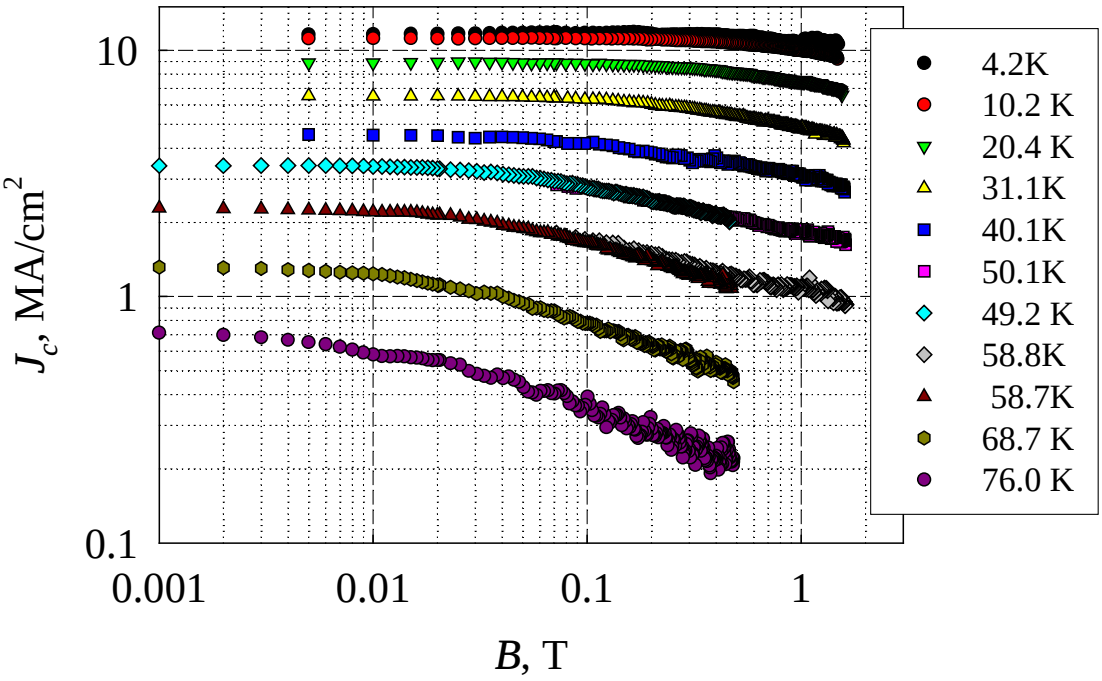

Figure 3.1. J_c vs. B for BSN-A (PVD119D) at various T.

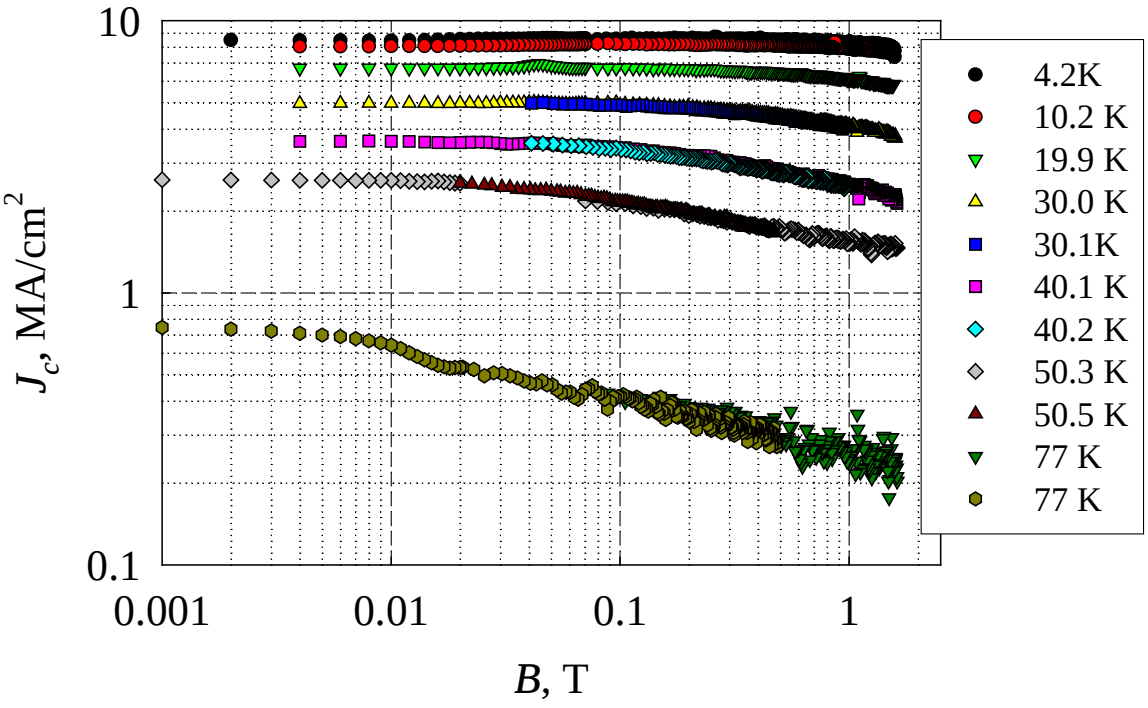

Figure 3.2. J_c vs. B for BSN-B (PVD104C) at various T.

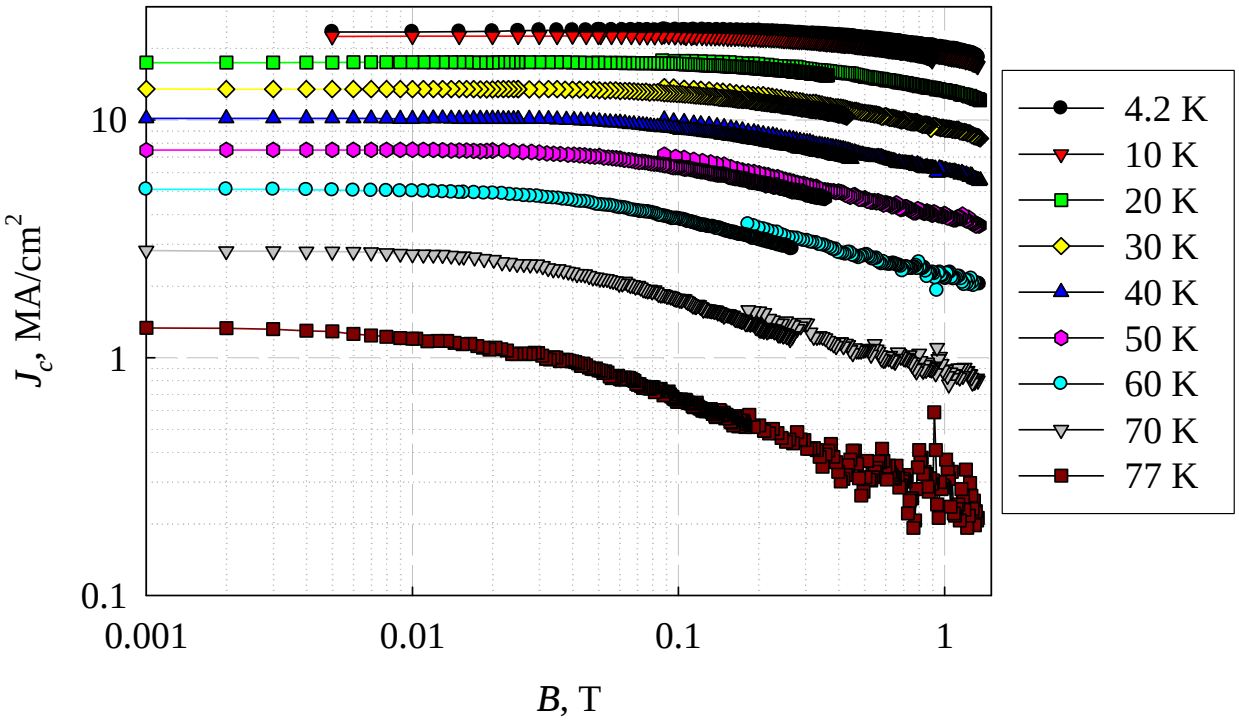

Figure 3.3. J_c vs. B for BZO-A (TJ1130A) at various T.

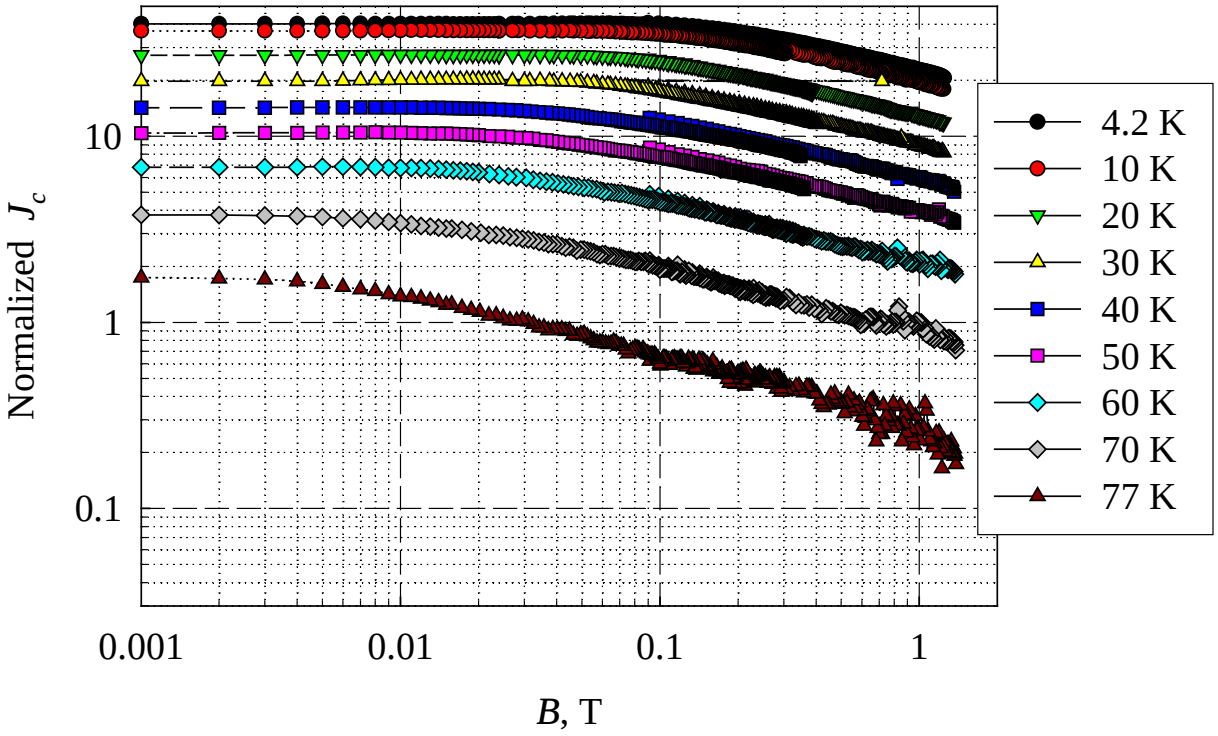

Figure 3.4. J_c vs B for CONT-D (TJ912A) at various T.

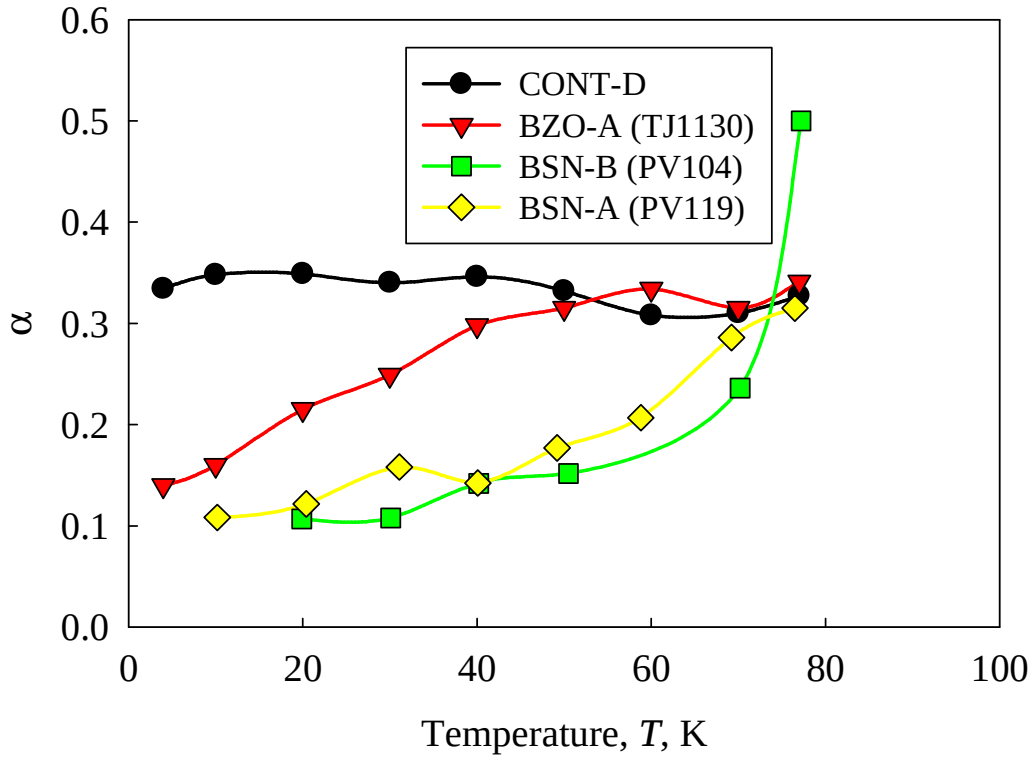

Figure 3.5. α for various samples as a function of T.

4.0. Magnetization Decay

Magnetization decay was characterized using the ramp rate dependence of the *M-H* measurements of several samples. *M-H* loops were measured for samples using ramp rates ranging from 1 mT/s to 70 mT/s. The results for TJ1130 A are shown in Figure 4.1-4.9 for temperatures from 4.2 K to 77 K, with fields up to 1.7 T. During period 2, standard expressions will be used to convert from this ramp rate dependence to an apparent pinning energy, *U*. We then can use the collective creep-vortex glass interpolation expression to describe the results, where

$$U(J) = \frac{U_0}{\mu}\left[\left(\frac{(J_c)}{J}\right)^{\mu} - 1\right] \tag{2.4.1}$$

where μ is the glassy exponent. It is also possible to fold in the field dependence by adding a mupliplicative term $B^{v.}$ The pinning strength can then be properly compared to control samples, as well as the glassy exponent, which will help define the dimensionality of the pinning.

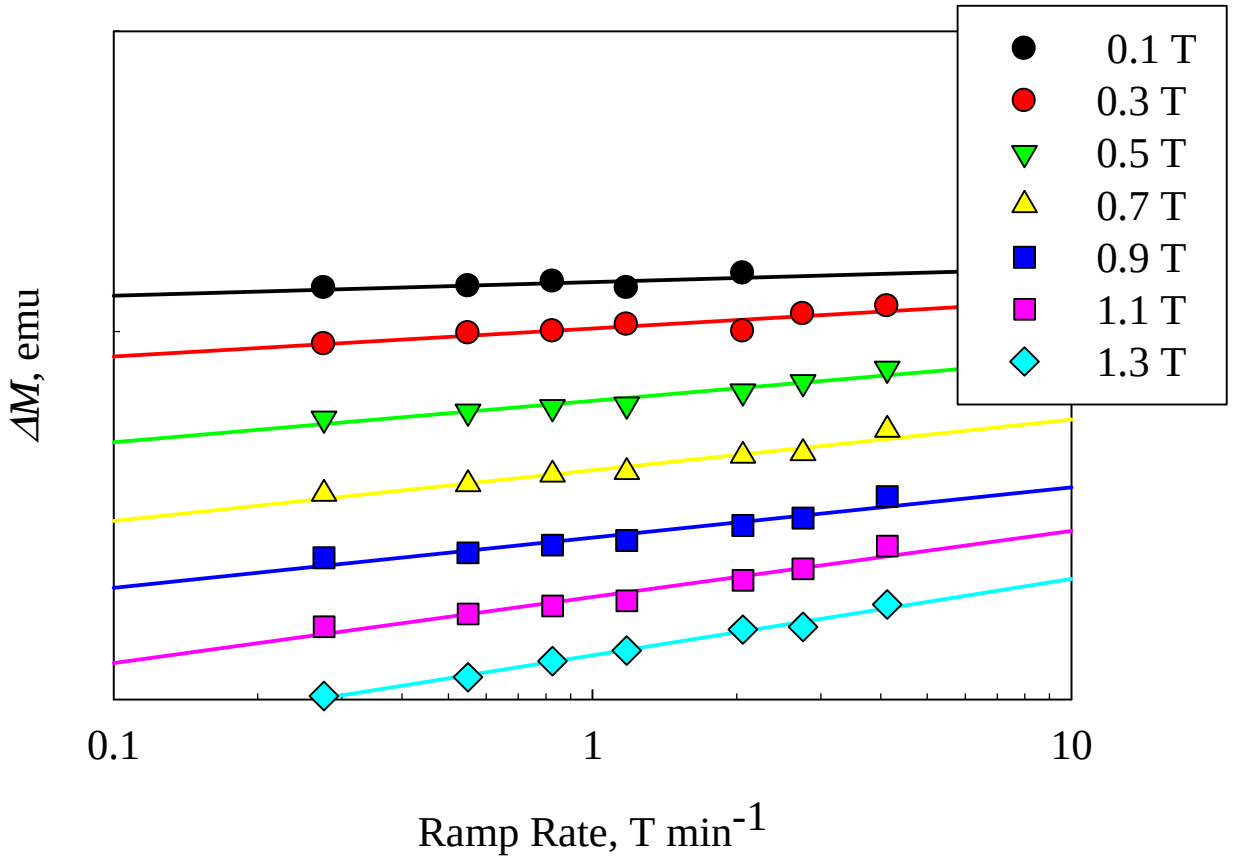

Figure 4.1. Ramp Rate dependence of magnetization at 4.2 K.

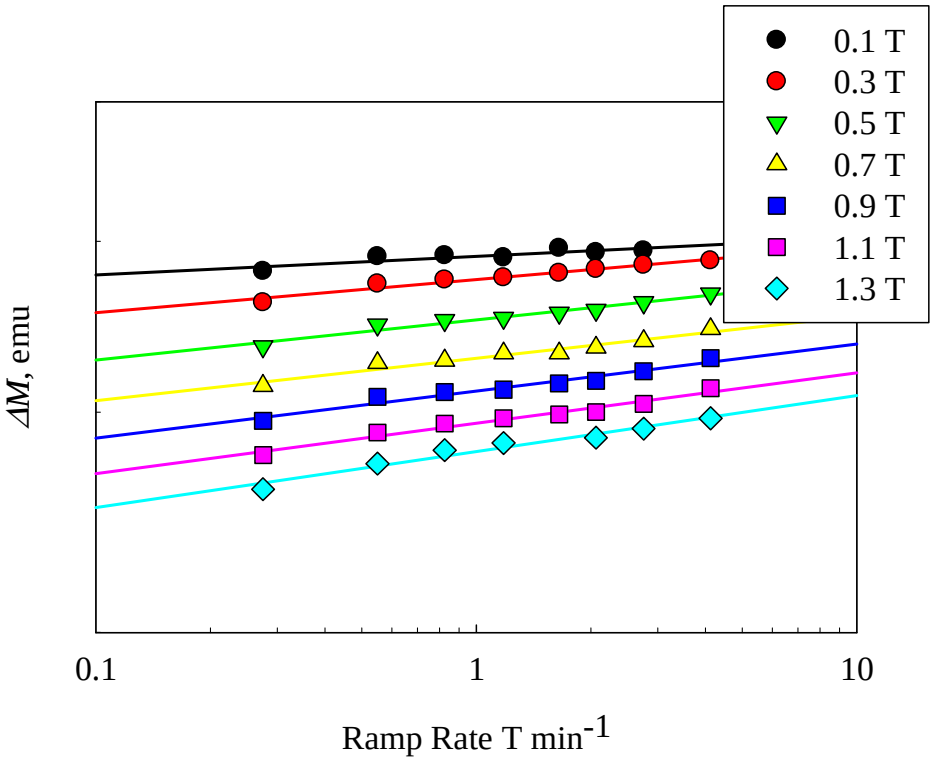

Figure 4.2. Ramp Rate dependence of magnetization at 10 K

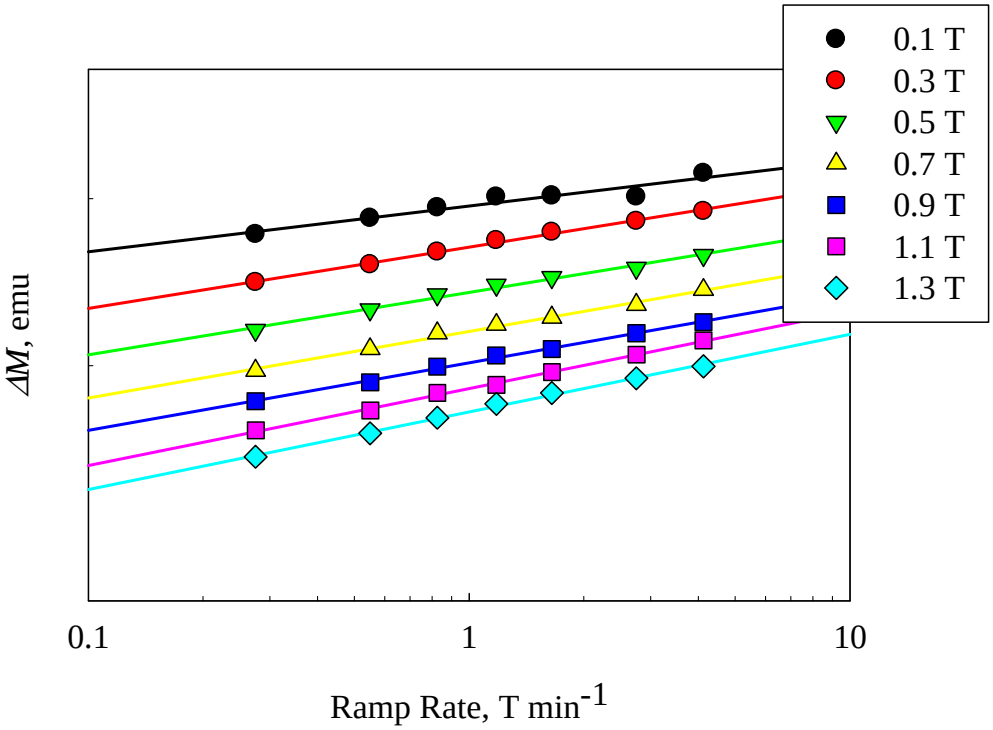

Figure 4.3. Ramp Rate dependence of magnetization at 20 K

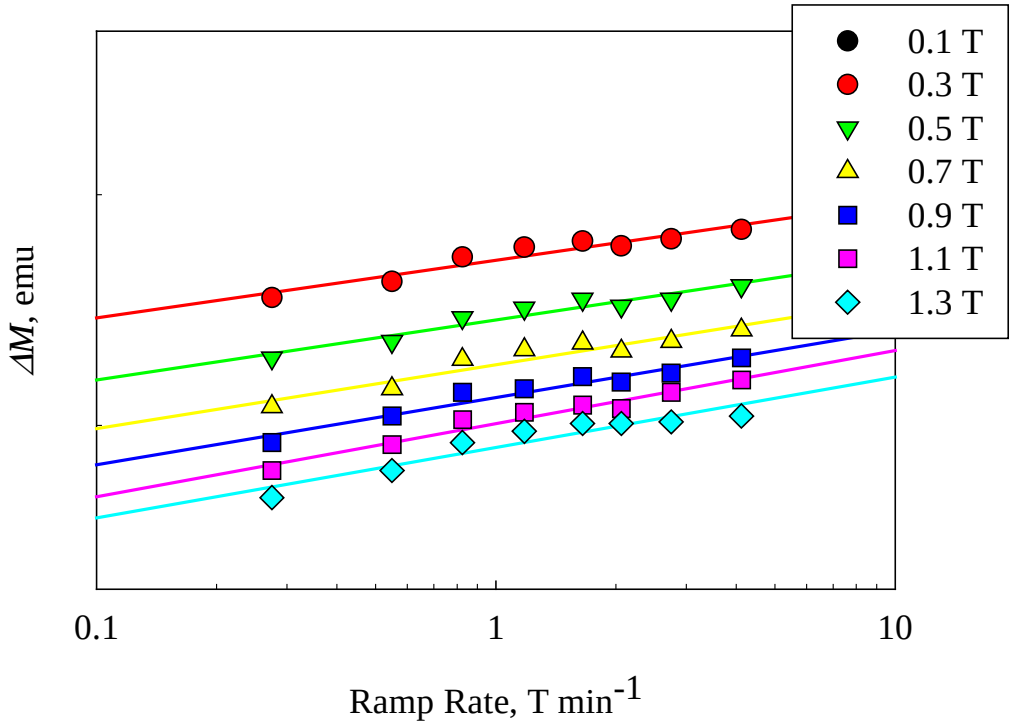

Figure 4.4. Ramp Rate dependence of magnetization at 30 K

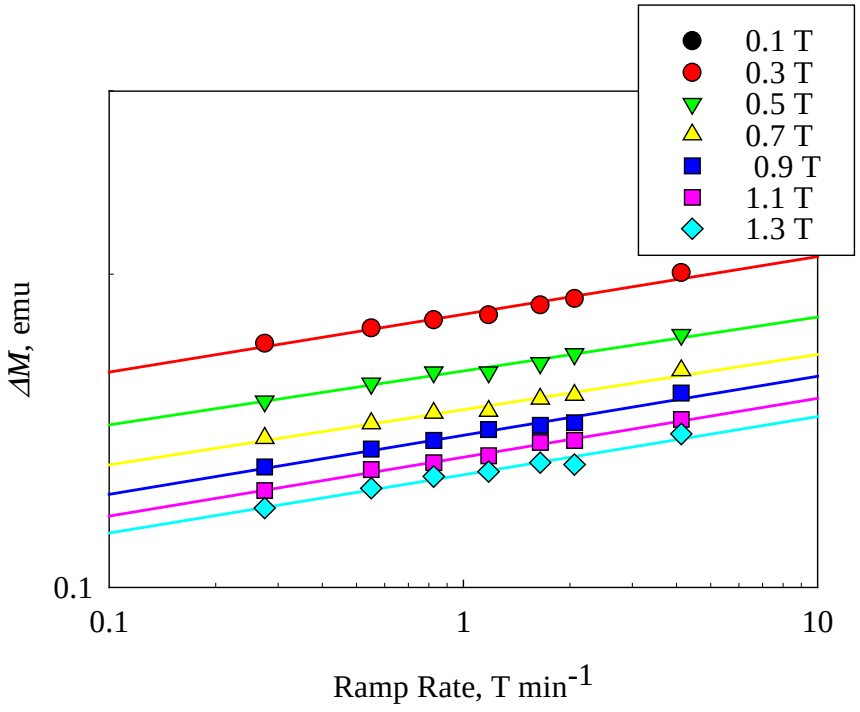

Figure 4.5. Ramp Rate dependence of magnetization at 40 K

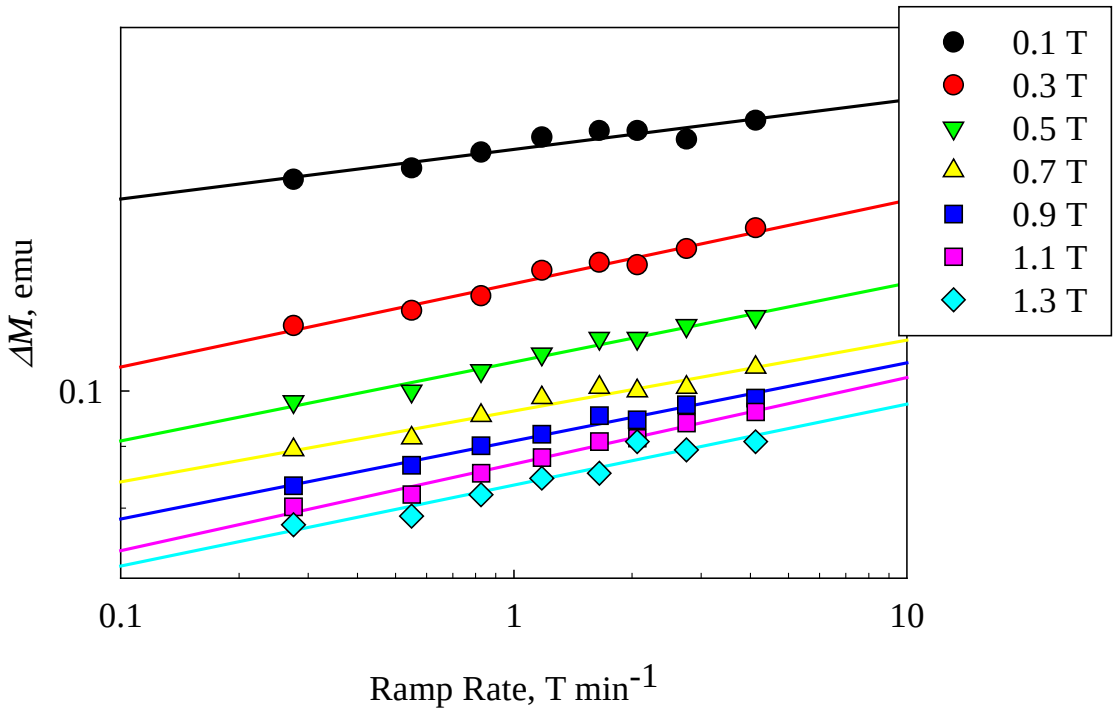

Figure 4.6. Ramp Rate dependence of magnetization at 50 K

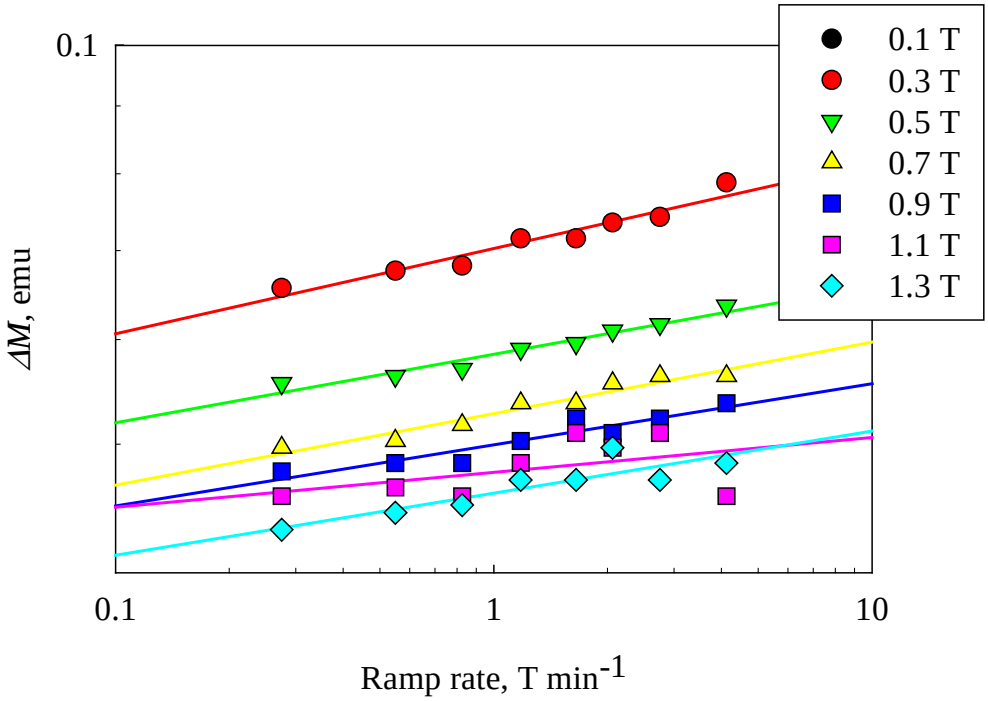

Figure 4.7. Ramp Rate dependence of magnetization at 60 K

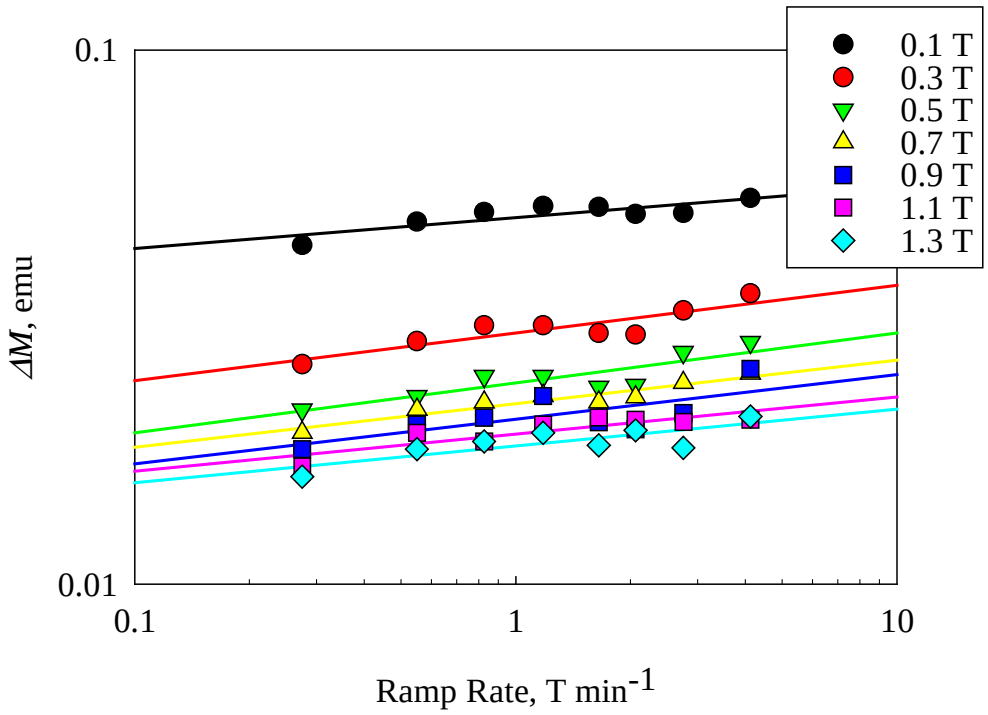

Figure 4.8. Ramp Rate dependence of magnetization at 70 K

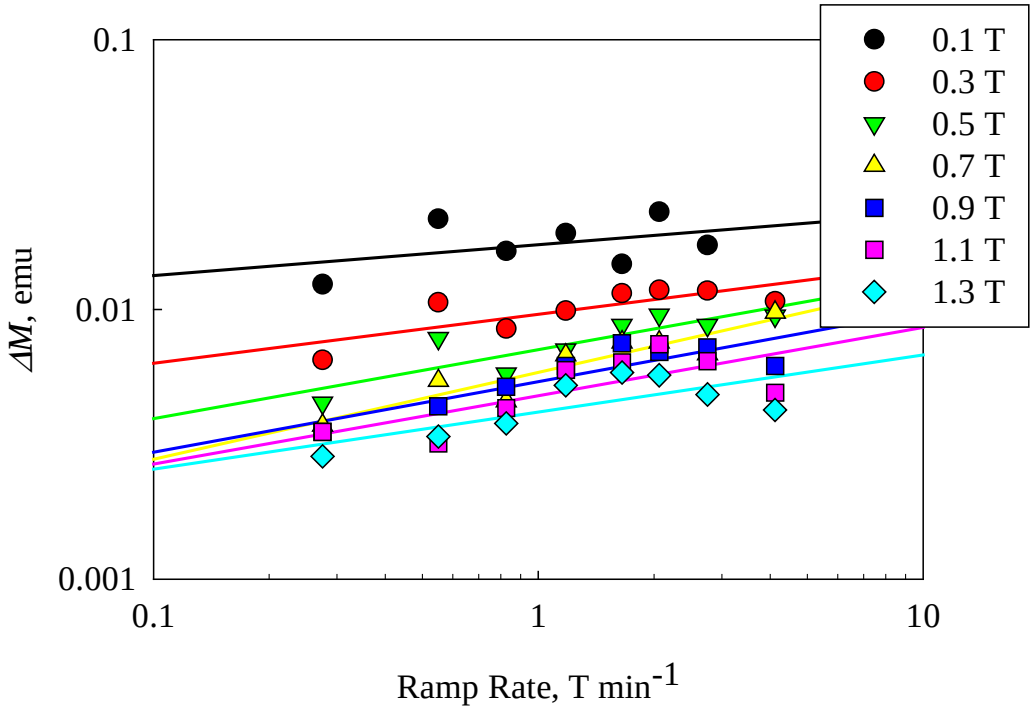

Figure 4.9. Ramp Rate dependence of magnetization at 77 K

5.0 High Field Magnetization Results

Various samples from Tables I and II were measured at higher field up to 14 T in a PPMS. These nine samples (set II) contained BZO layer pinned samples, Y_2O_3 layer pinned samples, and control samples. The *M-H* loops for all samples of the second set are shown in Figures 5.1-5.9. The data has been transferred into magnetic J_c vs B as well, and is displayed in Figures 5.10-5.18. The α, B^*, J_{sv}, and F_p curves are then extracted below. The results are compared and analyzed in sections below.

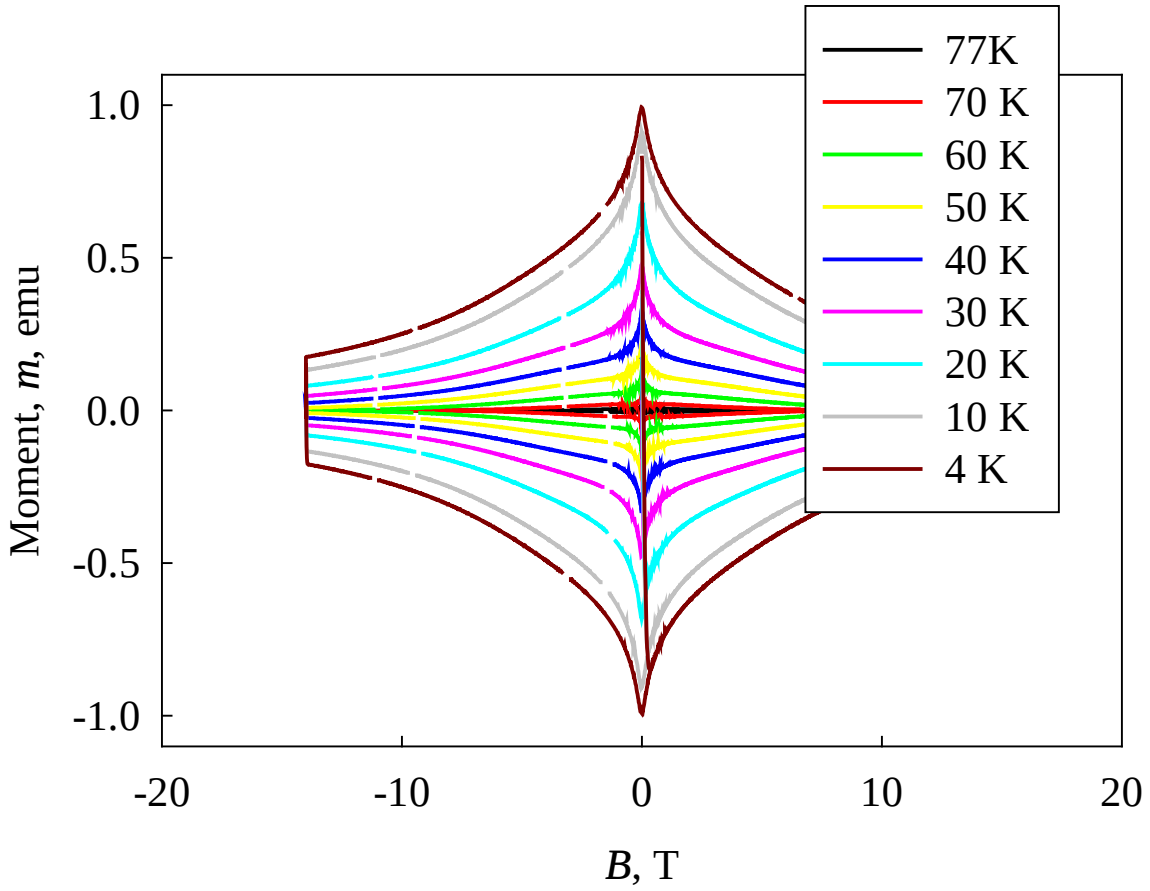

Figure 5.1 *M-H* loops for TJ1622C at various temperatures.

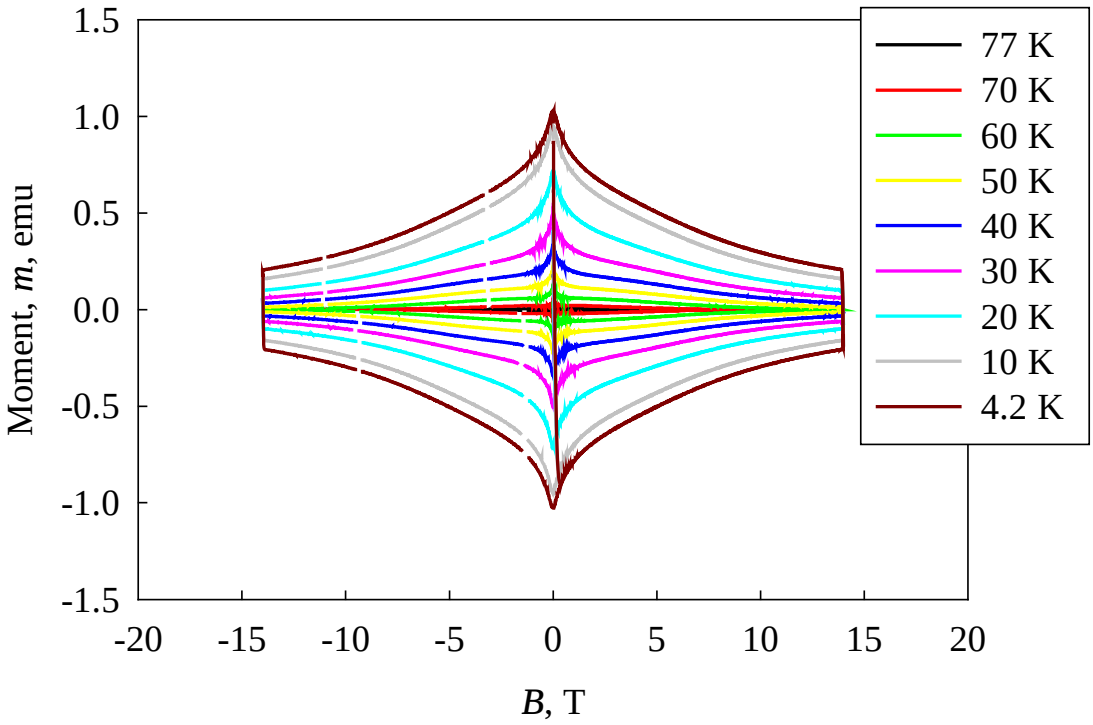

Figure 5.2. *M-H* loops for TJ1625C at various temperatures.

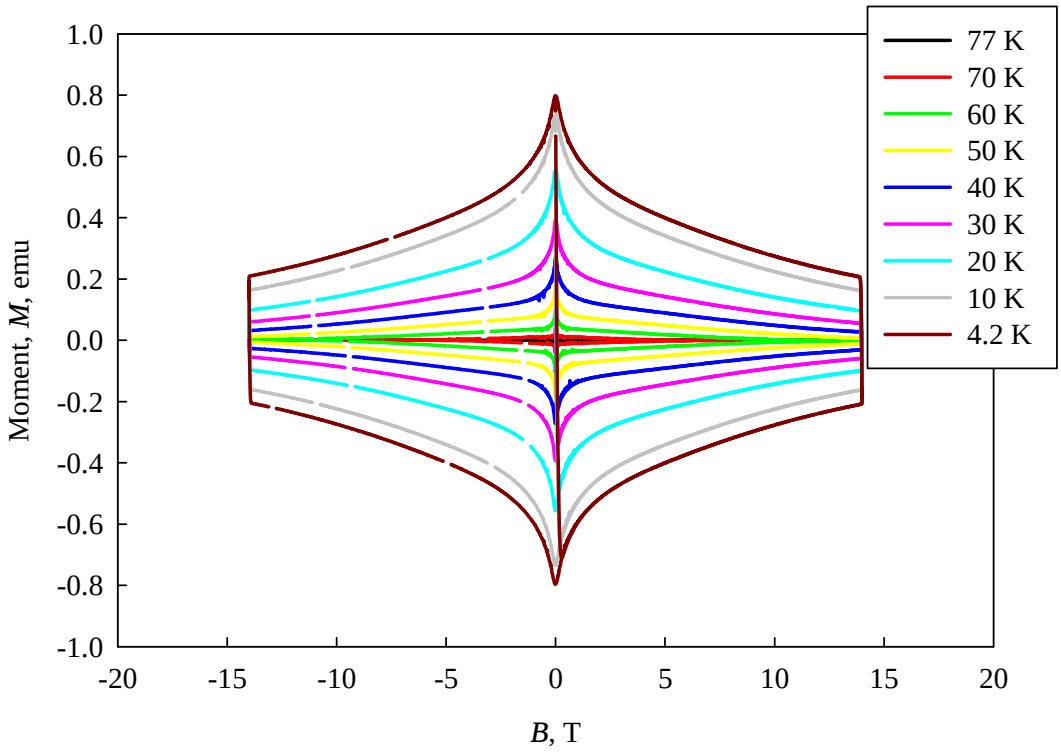

Figure 5.3. *M-H* loops for TJ1619C at various temperatures.

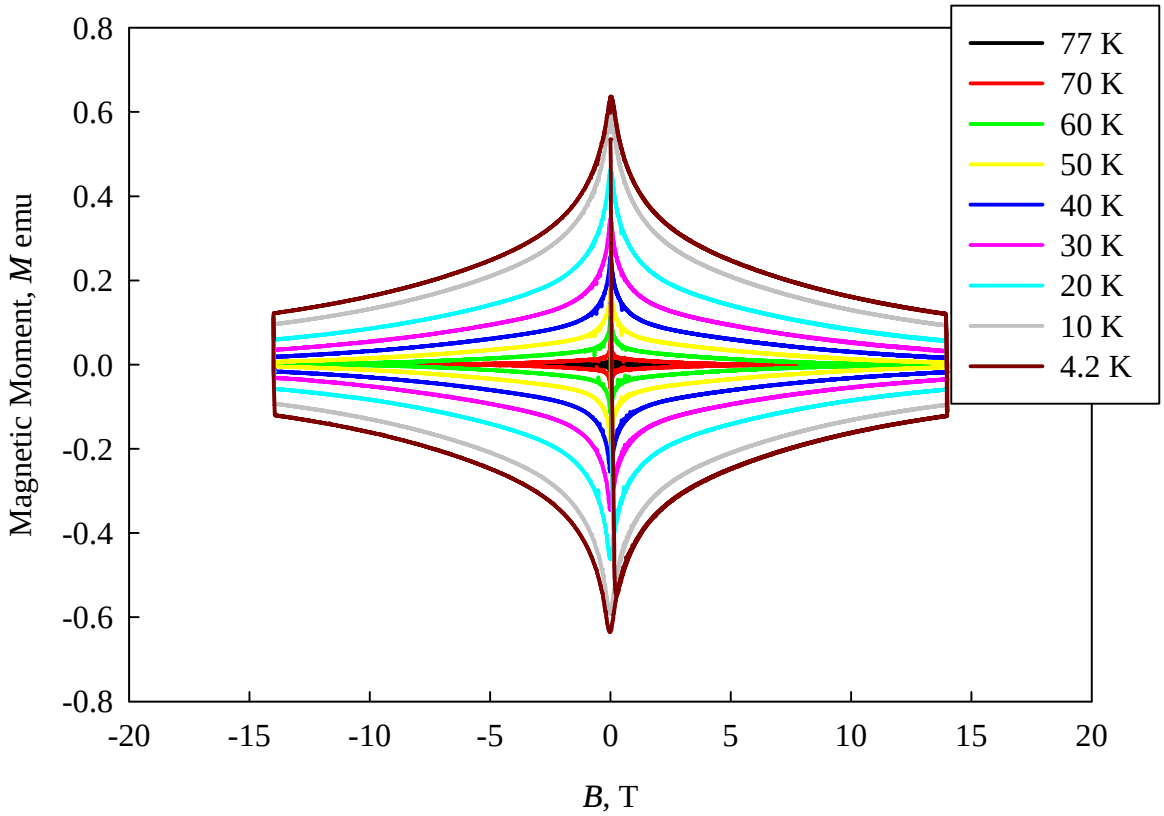

Figure 5.4. *M-H* loops for TJ1616C at various temperatures

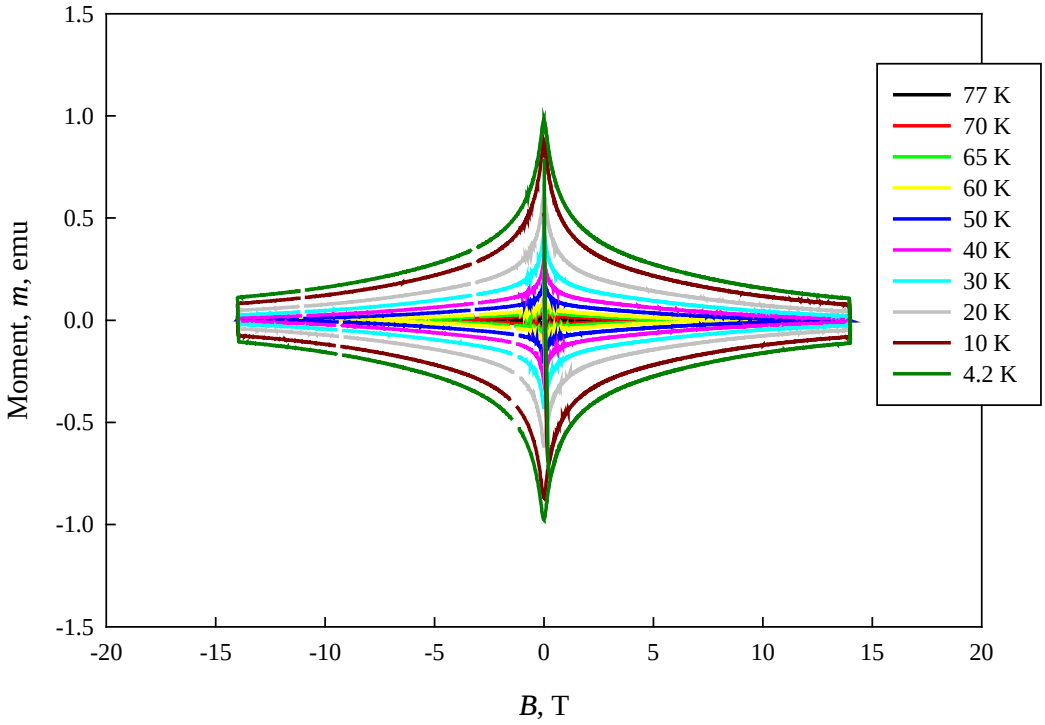

Figure 5.5. *M-H* loops for TJ1601C at various temperatures

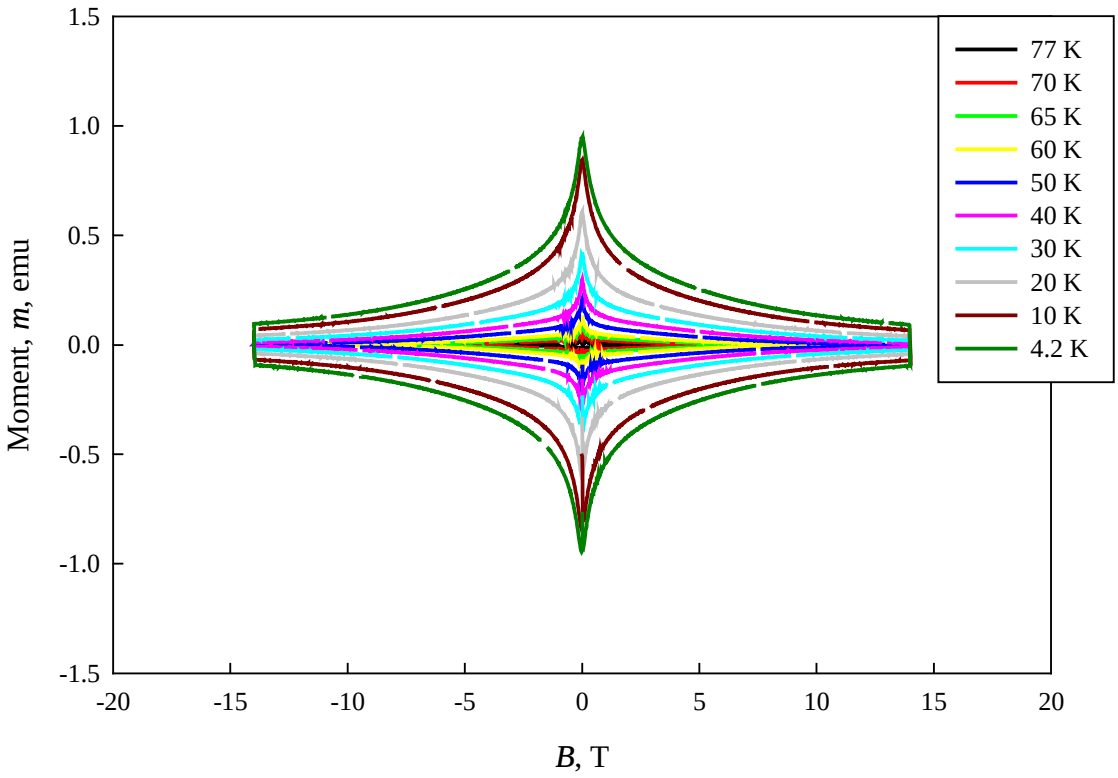

Figure 5.6. *M-H* loops for TJ1595C at various temperatures

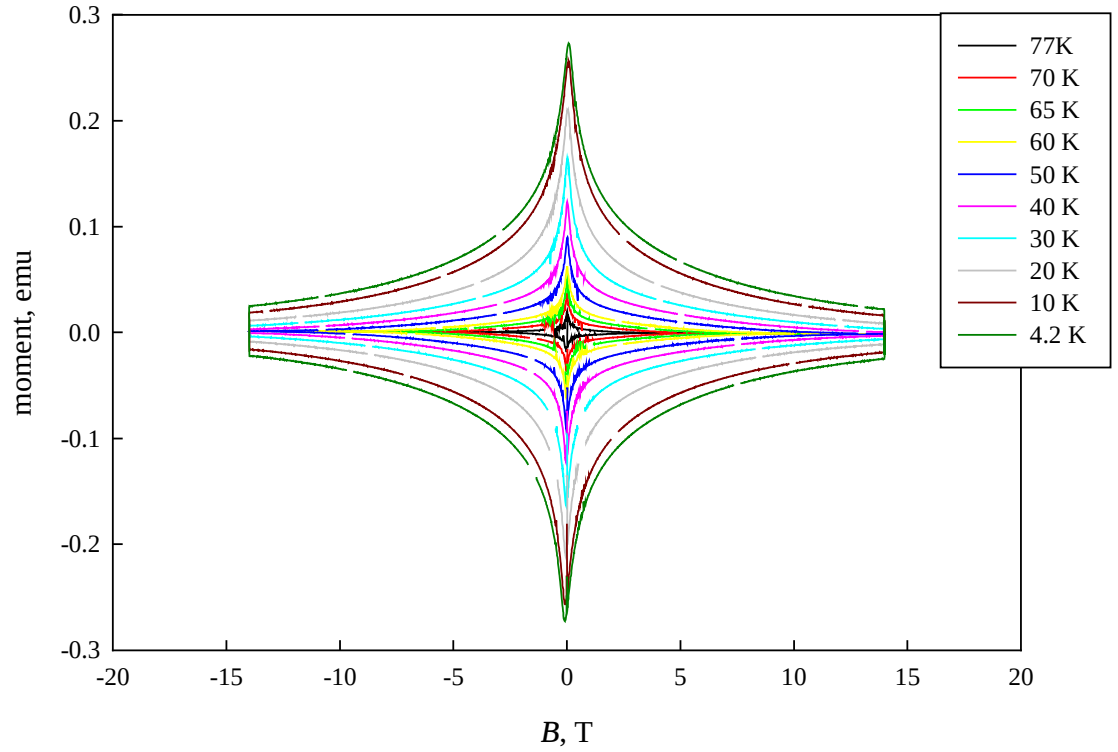

Figure 5.7. *M-H* loops for TJ1554A at various temperatures

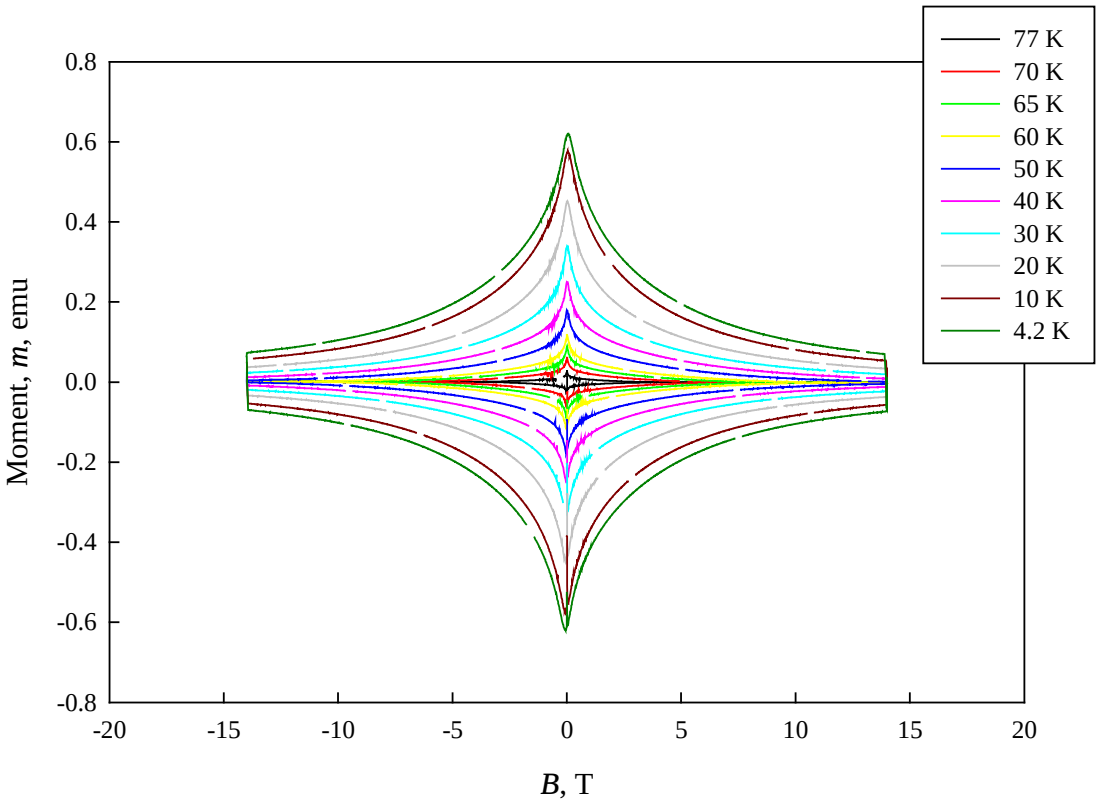

Figure 5.8. *M-H* loops for TJ1533A at various temperatures.

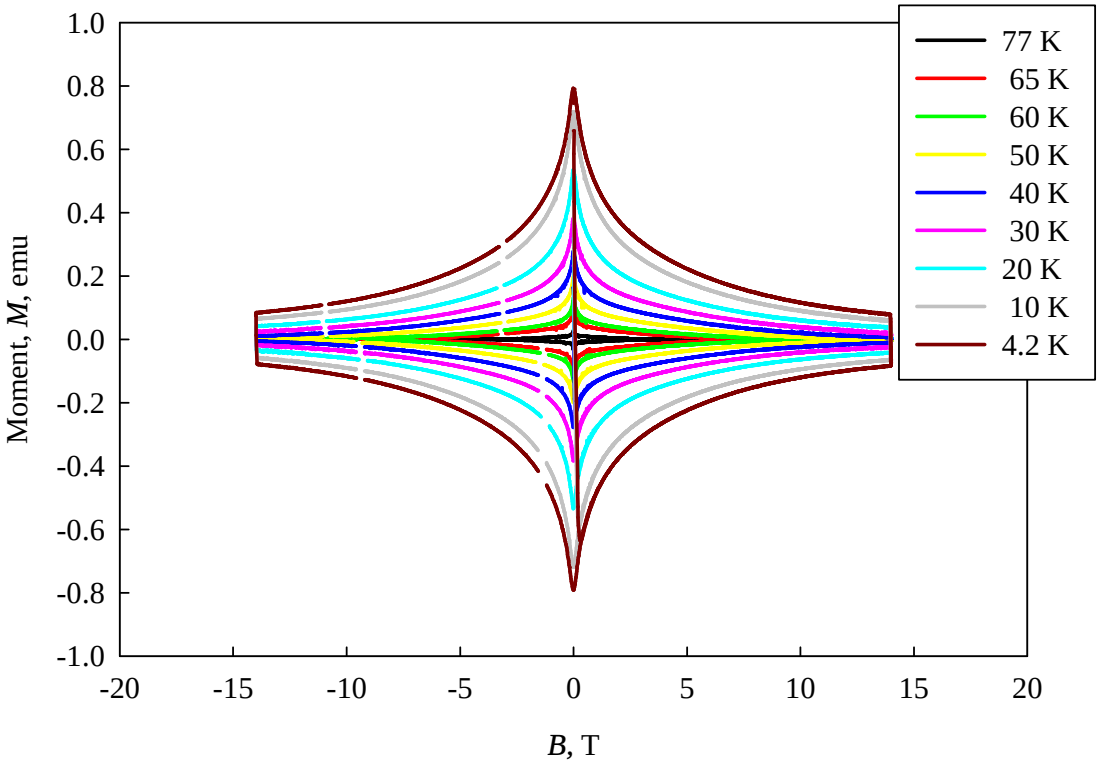

Figure 5.9. *M-H* loops for TJ1551A at various temperatures.

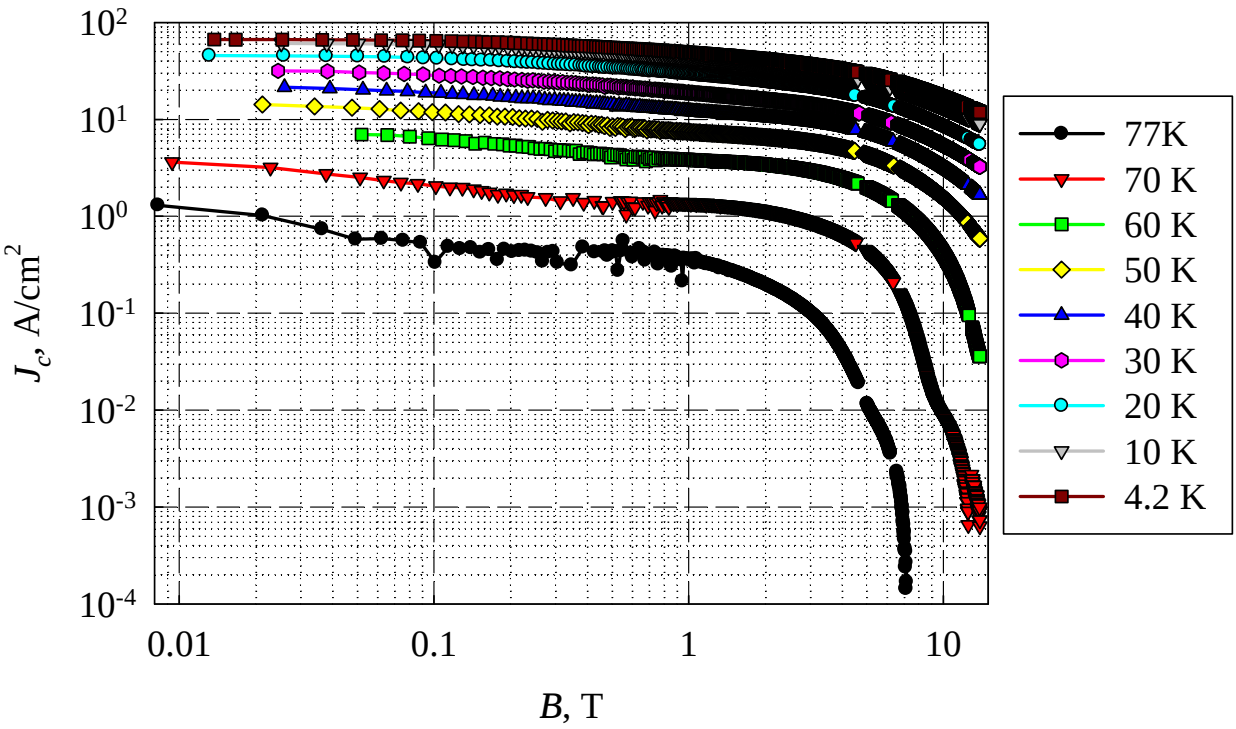

Figure 5.10. J_c vs B for TJ1622C at various temperatures.

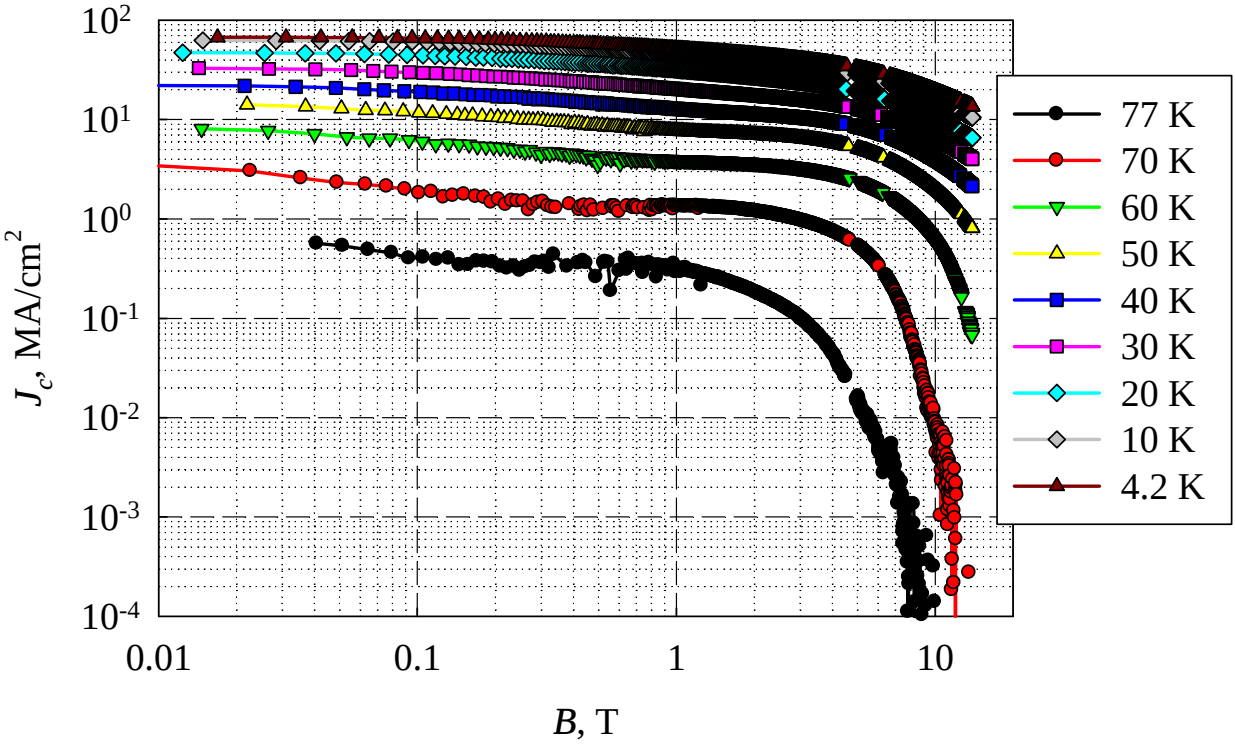

Figure 5.11. J_c vs B for TJ1625C at various temperatures.

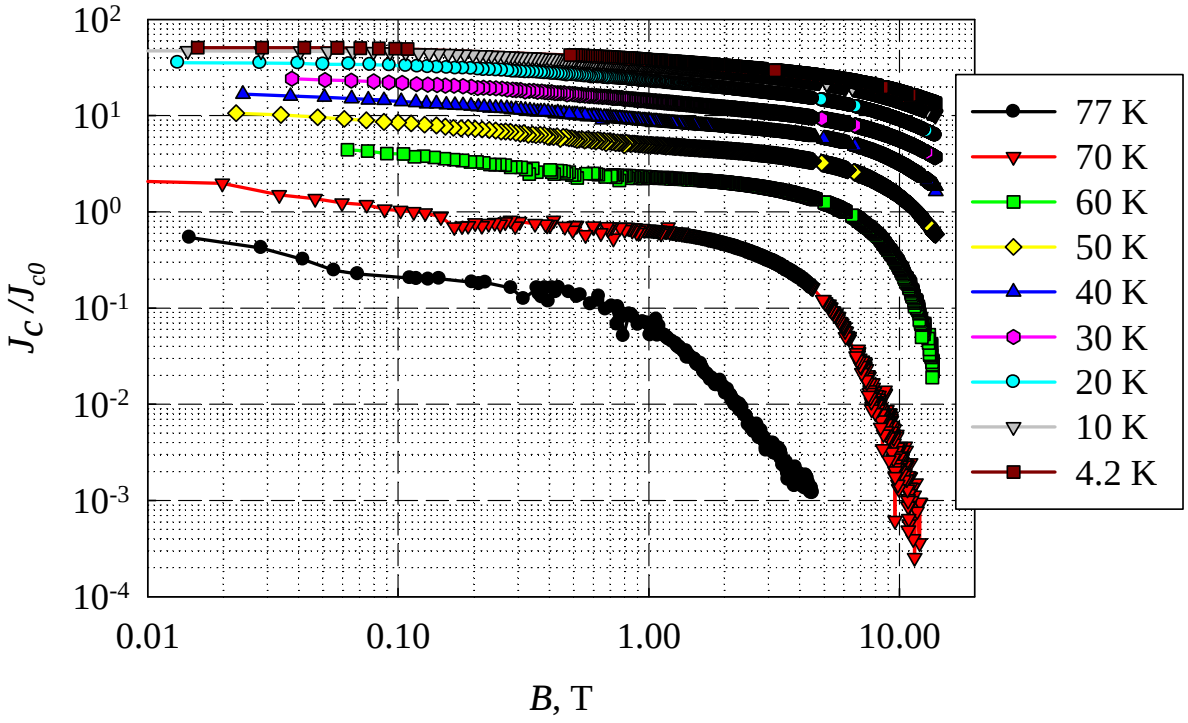

Figure 5.12. J_c vs B for TJ1619C at various temperatures.

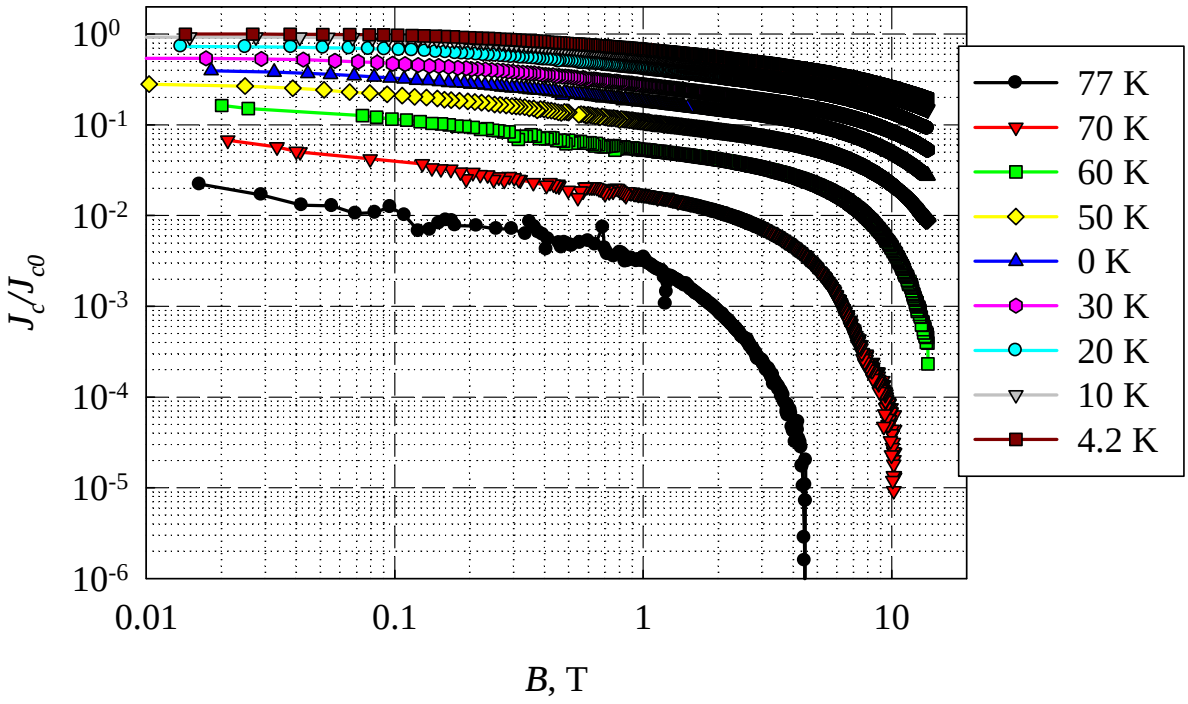

Figure 5.13. Normalized J_c vs B for TJ1616C at various temperatures.

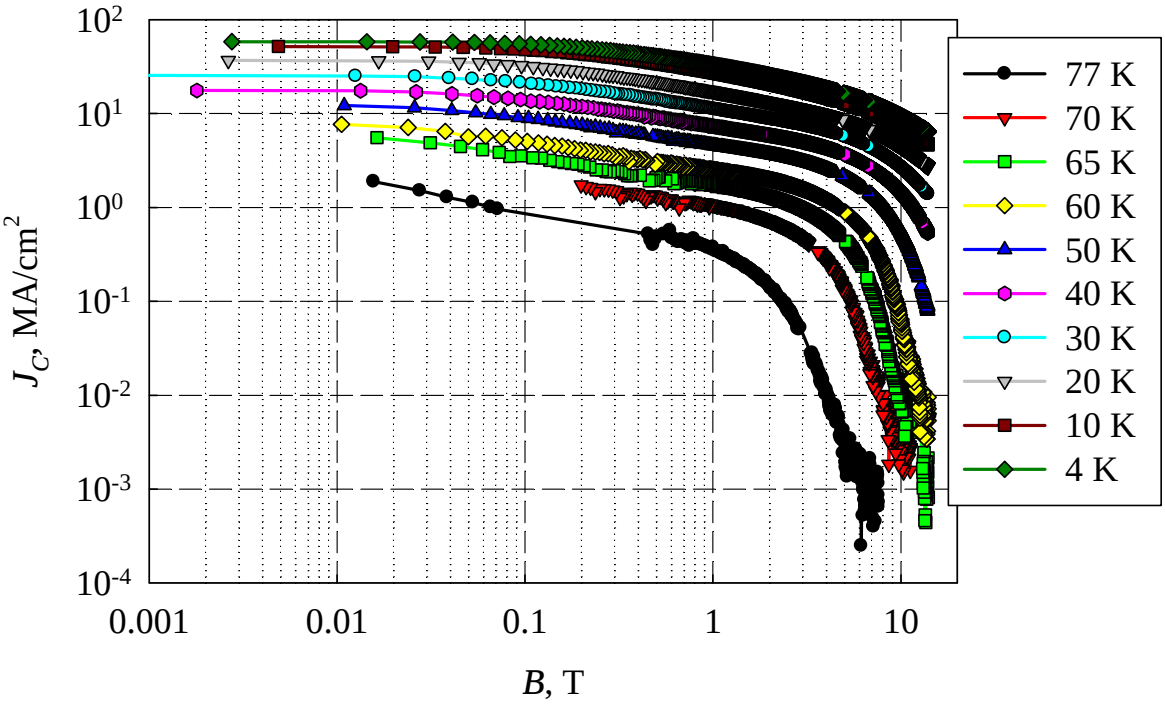

Figure 5.14. J_c vs B for TJ1601C at various temperatures.

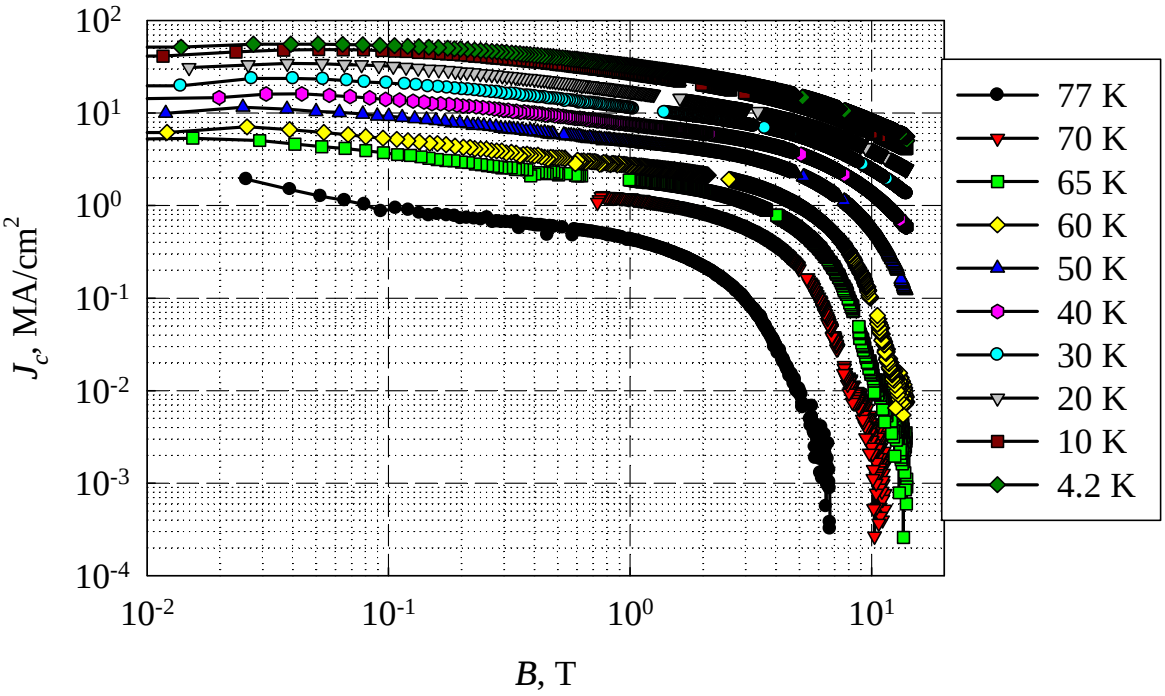

Figure 5.15. J_c vs B for TJ1595C at various temperatures.

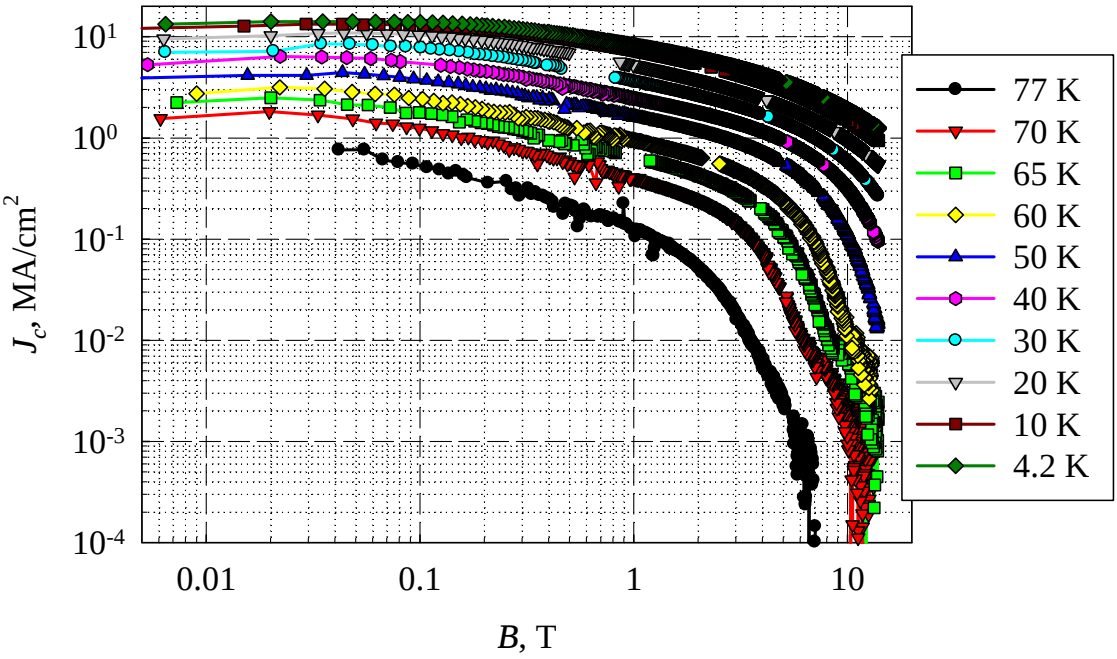

. **Figure 5.16**. J_c vs B for TJ1554C at various temperatures.

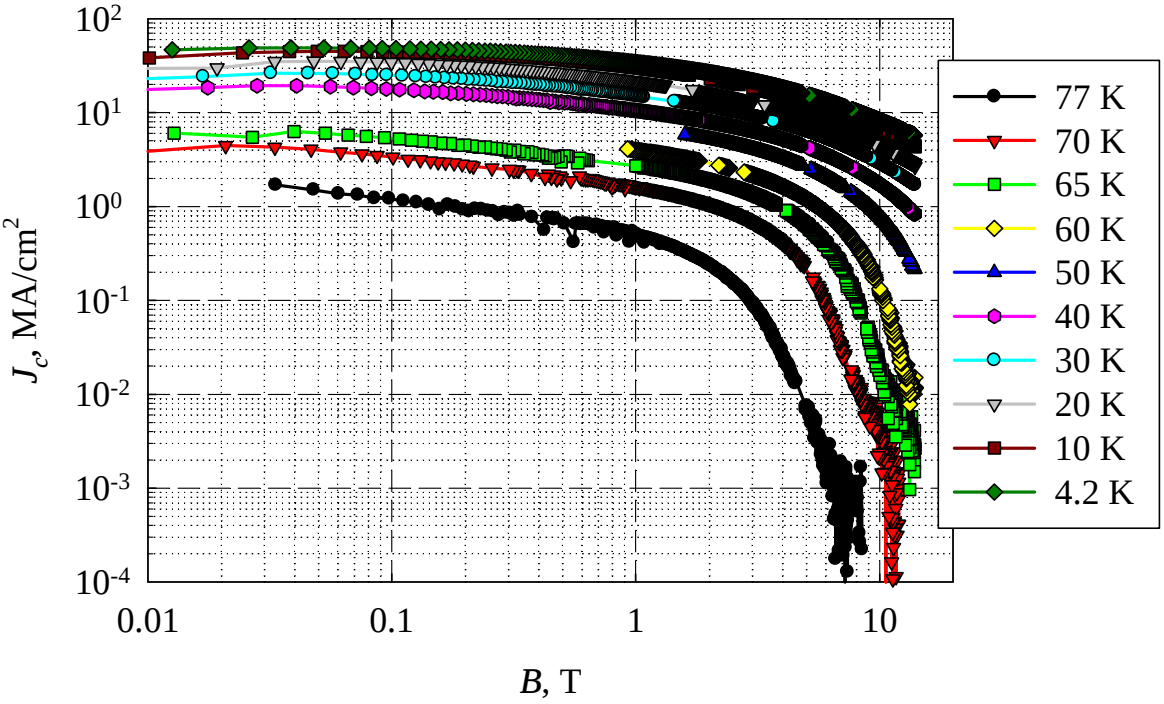

Figure 5.17. J_c vs B for TJ1533C at various temperatures.

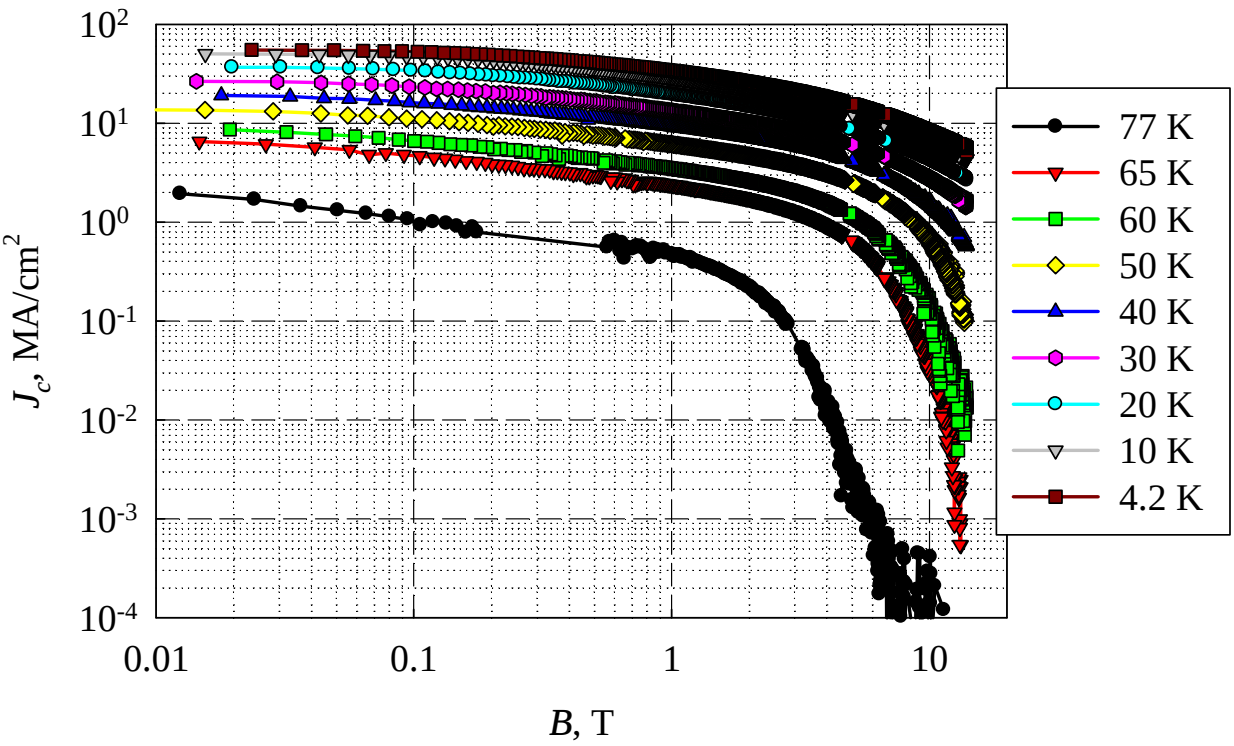

Figure 5.18. J_c vs B for TJ1551C at various temperatures

6.0 Comparisons, Summary, Future Work

Table 6.1 lists various self field and 1 T J_c values for various samples at various temperatures, as well as values of α at 77 K. The work for the analysis of the second set of samples is ongoing. However, the results are plotted in Figure 6.1 comparing the 77 K J_c results for the second set of samples. Here we see that the control samples were relatively good compared to both the BZO doped samples (TJ1625, 1622, 1619) and the Y_2O3 pinned samples (TJ1554, 1553, and 1551). At least one of each category of samples was in the top tier, but there was not a large apparent advantage to the nano-additions of either Y_2O_3 or BZO, at least for the present samples at 77 K. This can be gauged in terms both of low field J_cs as well as high field approaches to irreversibility.

Table 6.1 Summary Table

Tracer	Sample	α	←	1 T J_c, MA/cm^2		→	Zero Field, MA/cm^2	
ID	ID	(77 K)	77 K	60 K	20 K	4 K	77 K	4 K
PV119D	BSN-A	0.50	?	1.08	7.47	10.73	0.50	11.8
PV104C	BSN-B	0.30	0.235	?	6.11	8.38	0.50	8.60
J1130A	BZO-A	0.34	0.379	2.18	13.59	20.59	1.34	24.0
BSN-C	PV231-B							
PV119D	BSN-A	0.50	?	1.08	7.47	10.73	0.50	11.8

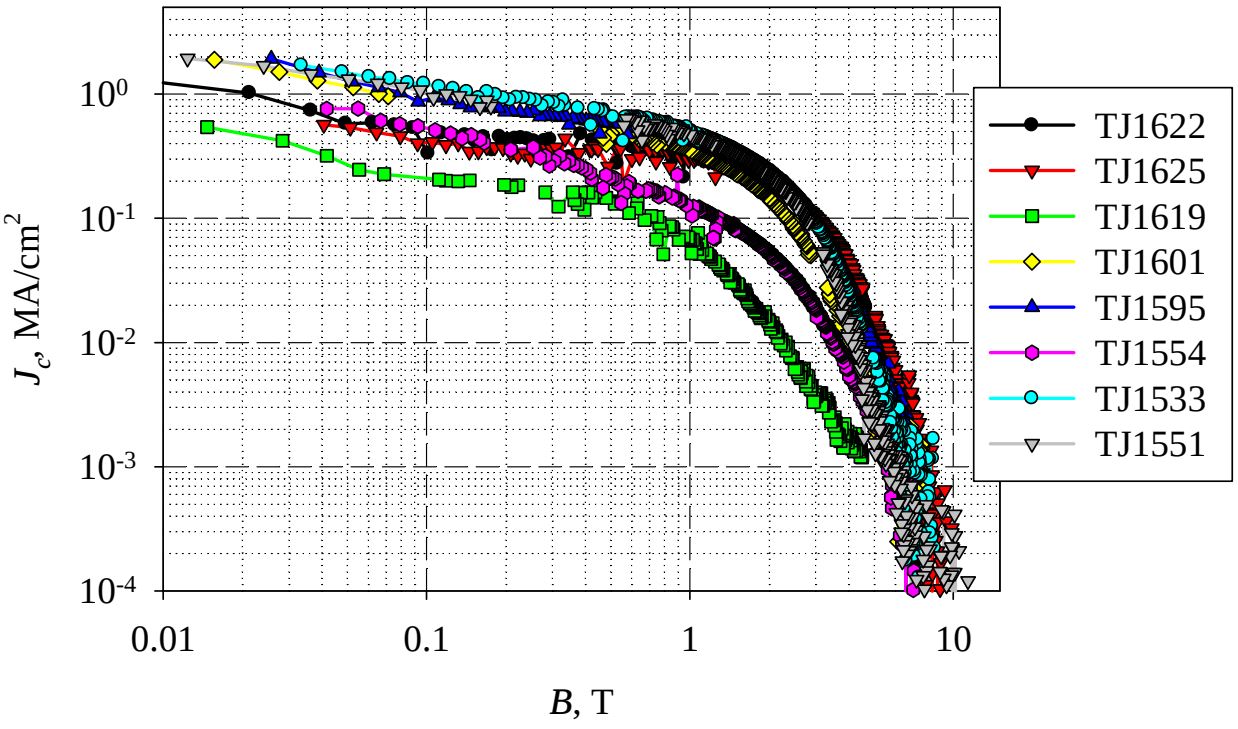

Figure 6.1. 77 K J_c for various samples.

In Figure 6.2 we see the F_p curves (at 77 K), which do suggest that perhaps the Y_2O_3 adds somewhat to pinning in mid-range fields, but the effect is not strong. BZO seems to have a lower F_p. No strong shift in the position of the F_p is obvious.

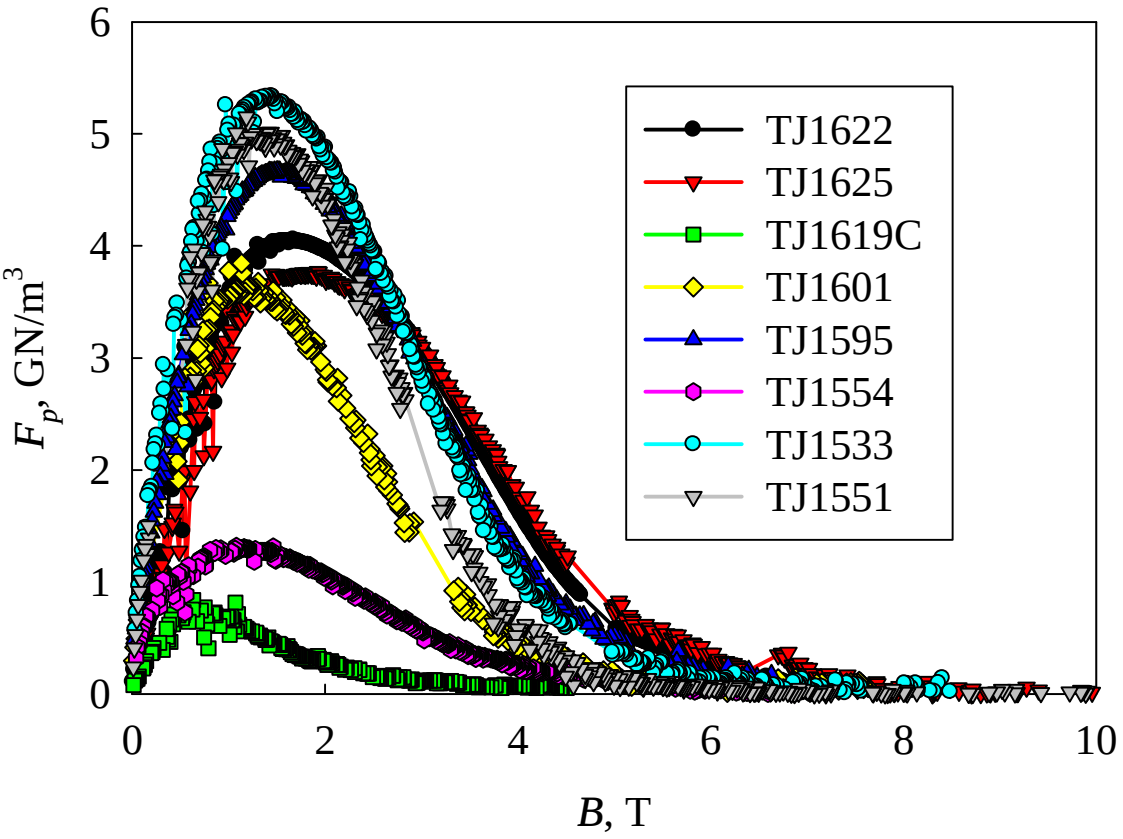

Figure 6.2. F_p vs B for various samples.

On the other hand in Figure 6.3 we see the 4.2 K J_c compared between various samples, and note that, ignoring TJ1619, which seems low, the BZO samples have a better response than the control samples, while the Y2O3 samples are lower. This suggests that some additional pinning centers may be present in the NZO samples at lower temperatures, while some small level of Y2O3 may be present at mid-ranges for higher temperatures.

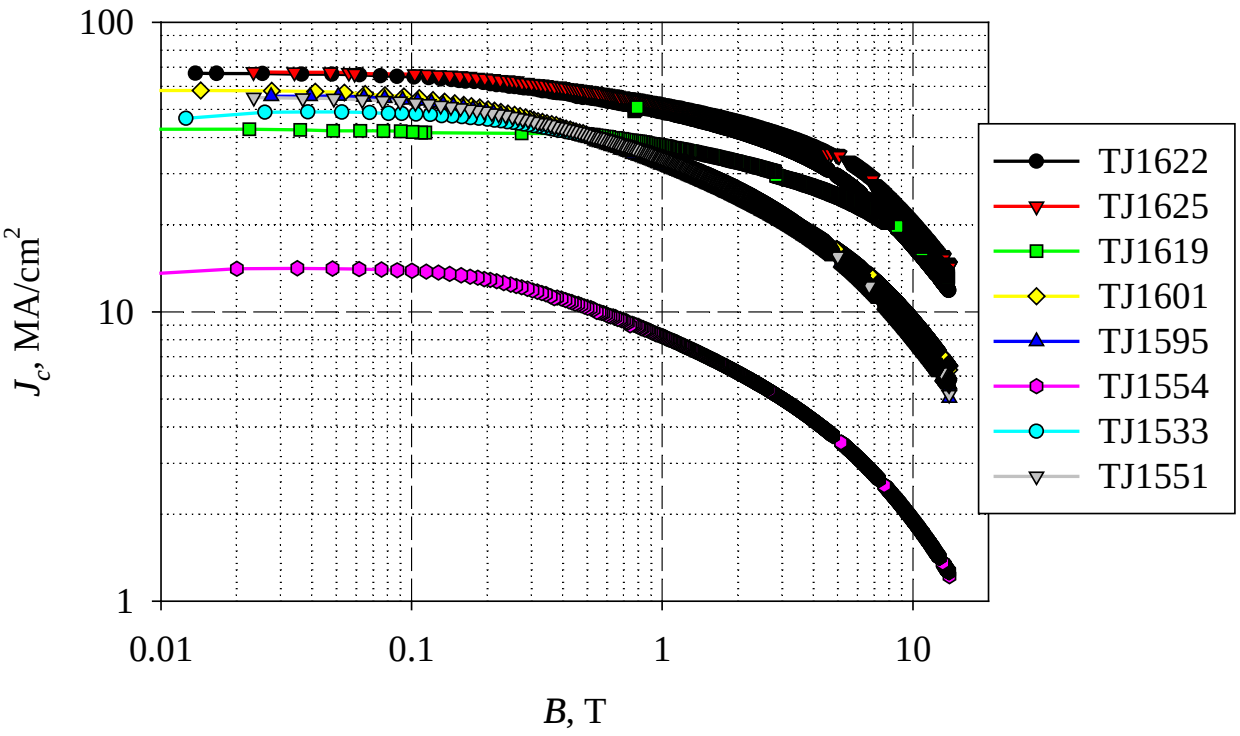

Figure 6.3. J_c vs B for 4.2 K for various samples.

7.0 Comparison to AFRL-Obtained 9 T Data

Initial measurements on two classes of samples, PV and TJ showed that while similar data was obtained for the TJ samples using a 9 T PPMS and a 14 T PMS, the same was not true for the PV samples. Extensive investigations have been carried out to clarify this situation, including repeated measurements on various samples in both machines. Initial concern centered around the centering techniques. After many discussions with the manufacturer, Quantum design, it was decided that the best centering techniques were a combination of mechanical and electrical scan techniques. These double checks, however, did not remove the difference between the PV and TJ sample responses. Temperature calibration and PPMS calibration were also checked, as well as sample magnetic field history. Also, the best field-perpendicular alignment was sought. Possible rubbing issues were also investigated. In the end, this differences persisted, but it is considered most likely that this originates from a very anisotropic magnetic response in the PV samples, centered not only about the a-b plane, as would be expected intrinsically, but also about the c-axis, correlating with columnar defects. This is now being investigated with a transverse VSM, which has very precise angular control. However, while recent results on PV samples have shown better results (i.e., higher properties) the level of certainty about PPMS measurements whether in the 9 T or 14 T PPMS should be questioned, and should probably be investigated for their angular dependence in each case.

However, the agreement between the 9 T and 14 T PPMS for the TJ samples is good, at least as good as the repeatability between various measurements on the 9 T PPMS. Below we show two measurement sets, Figure 7.1 for TJ1619C, Figure 7.2 for TJ1551A. We note in

general that the agreement between the 9 T and 14 T results is good. A second set of measurements was taken on the 9 T machine, which shows some difference at 77 and 65 K from the first. Note that these first and second run data straddle the 14 T data.

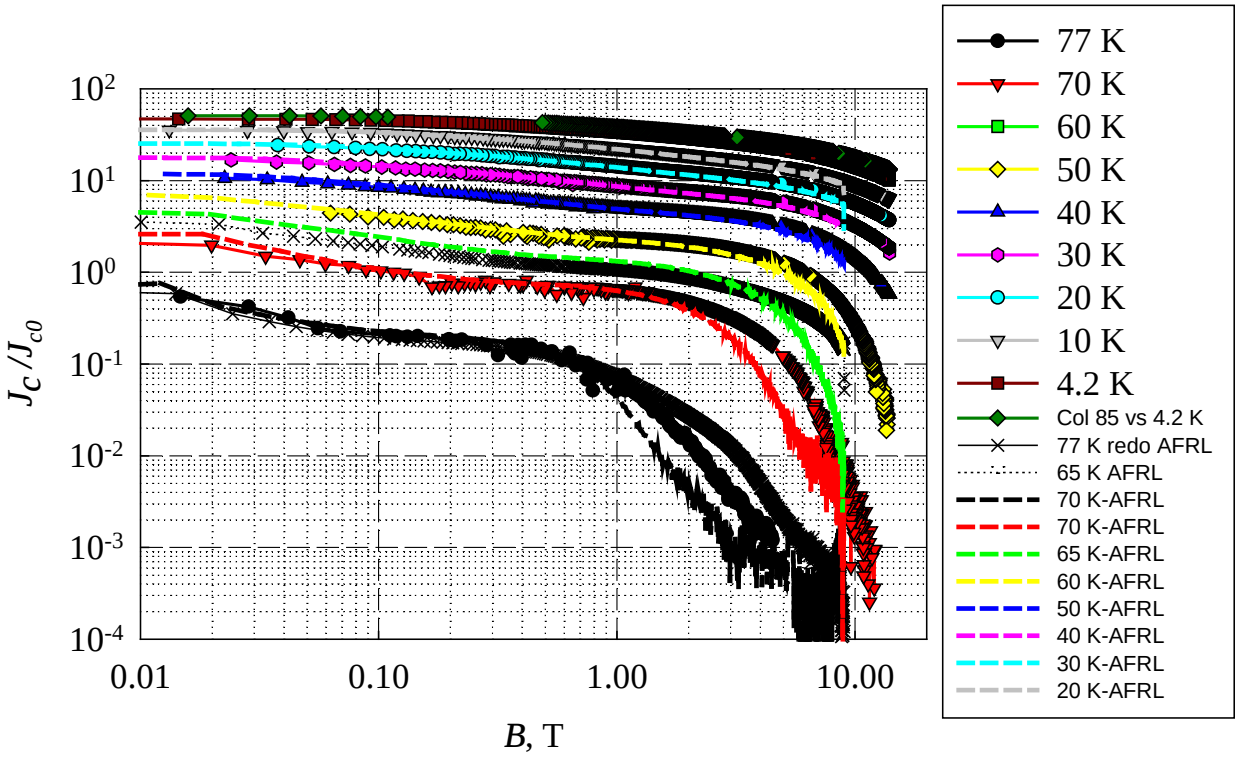

Figure 7.1. J_c comparison of 14 T and 9 T PPMS measurements on TJ 1691 C. Measurements are taken from 4.2 K to 77 K, and the field is perpendicular to the sample. Colored symbols are 14 T measurements, dashed lines are first set of 9 T results. Xs with solid lines give the second 9 T measurement at 77 K, and Xs with dotted lines the second set of measurements at 65 K. Note first the good agreement in general between the 9 T and the 14 T measurements. Note secondly the fact that the first and second 9 T results are slightly different at high fields for 77 K – and straddle the 14 T result.

The data comparison for TJ1551A is shown in Figure 7.2. Here, again the 14 T and 9 T data are in good agreement, although not perfect. It is to be recommended that more extensive comparisons be done to reduce the level of error.

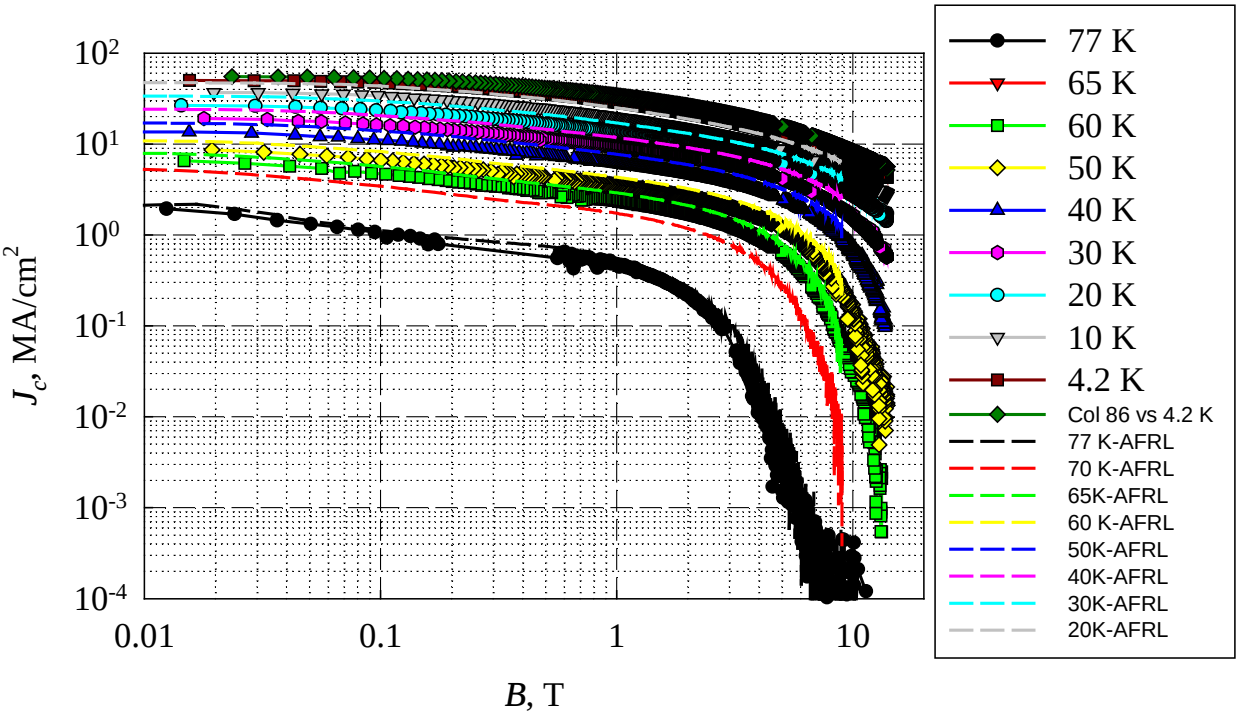

Figure 7.2. J_c comparisons between 9 T and 14 T PPMS machines for TJ1551 A. Measurements are taken from 4.2 K to 77 K, and the field is perpendicular to the sample.

8.0 Fluxon Imaging in TJ305-BV

In an attempt to image vortices in AFRL YBCO films and correlate with pinning centers and types, a YBCO samples was made. The sample was TJ305B—V, which used $LaAlO_3$ substrate. The nanoparticles were 211 phase, with a particle size of 10 nm diameter laid down in layers that were 2-5 nm thick, with 15nm 123 separating them.

The goal was to collect images that allowed us to correlate fluxons with subsurface features that pin the flux. Therefore what we would like to see is a small area scan showing groups of distinguishable fluxons congregating in areas on the surface where there are no distinguishable surface feature, as well as in regions where there are surface features.

It is important that we be able to return to the exact area scanned by the magnetic probe in order to image the same area with another technique. To this end we have placed a marker on the surface of the sample. The marker is easily found under a microscope. The SEM images below show the marker with increasing magnification (Figure 8.1). The first images observed in the nanomagnetics instrument scanning hall probe measurements are shown in Figures 8.2 and 8.3. Considerable work still remains to correlate these initial measurements with real surface pinning features.

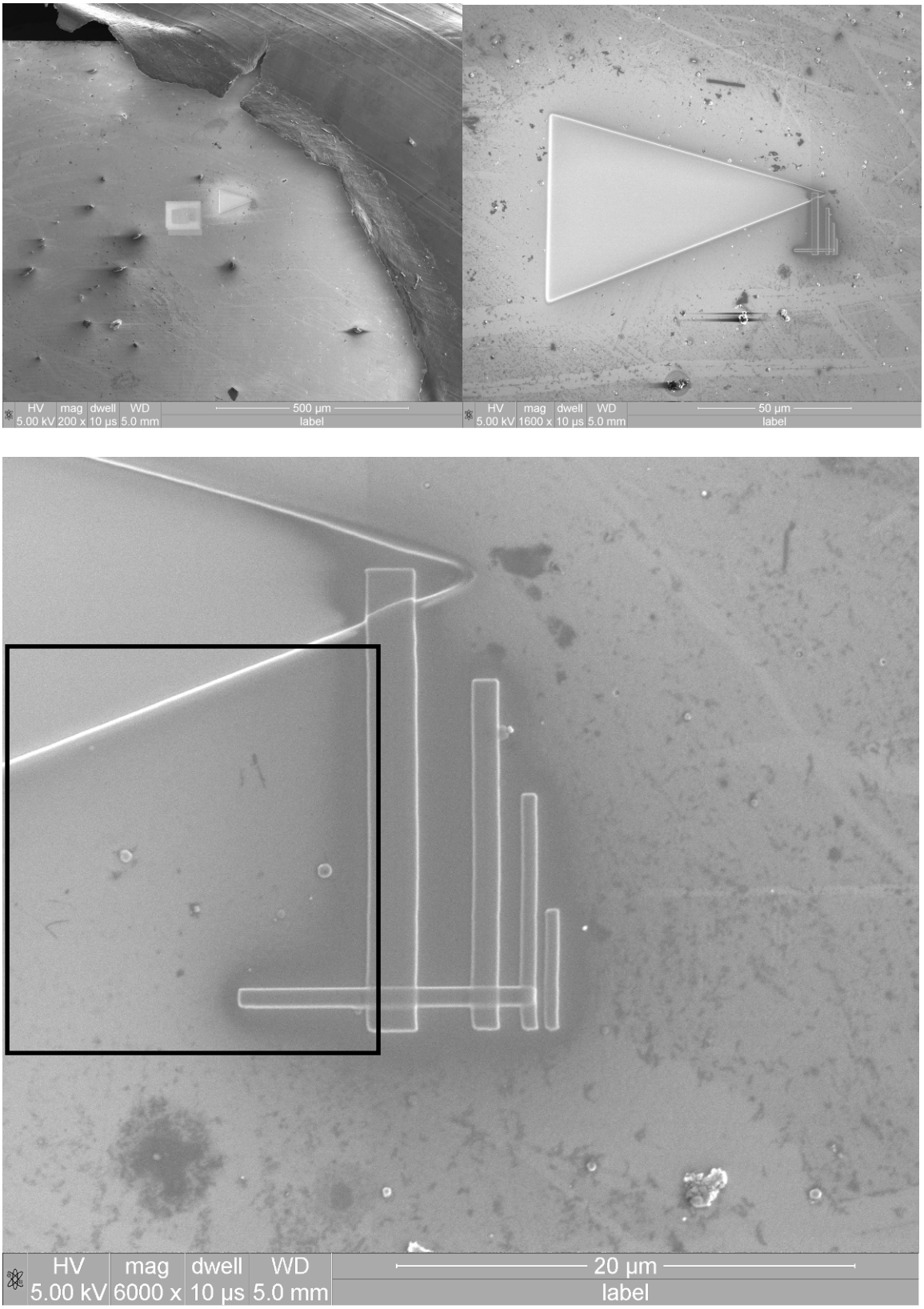

Figure 8.1. Initial target region for flux imaging, TJ305 BV.

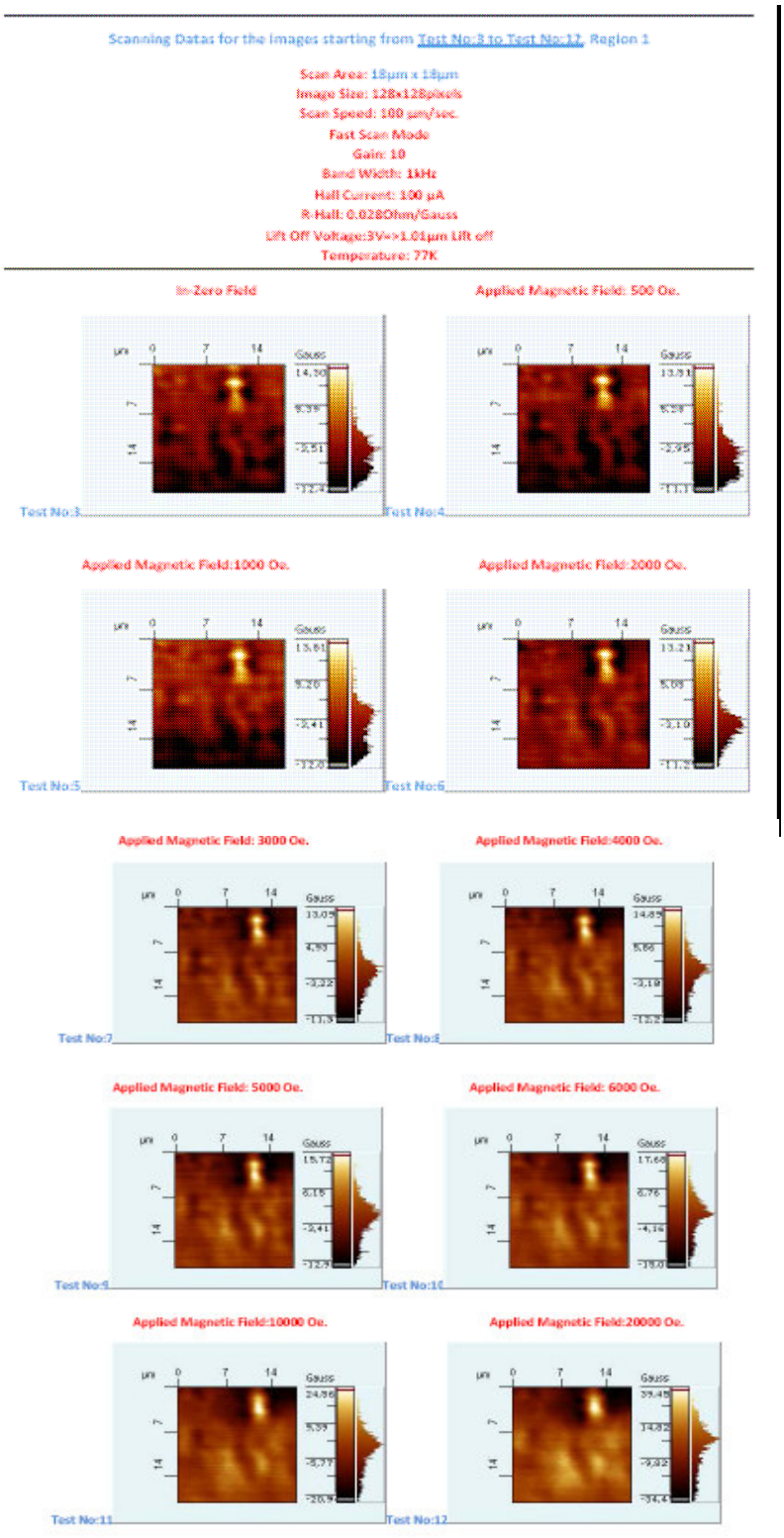

Figure 8.2. Initial Fluxon Images in TJ305 BV

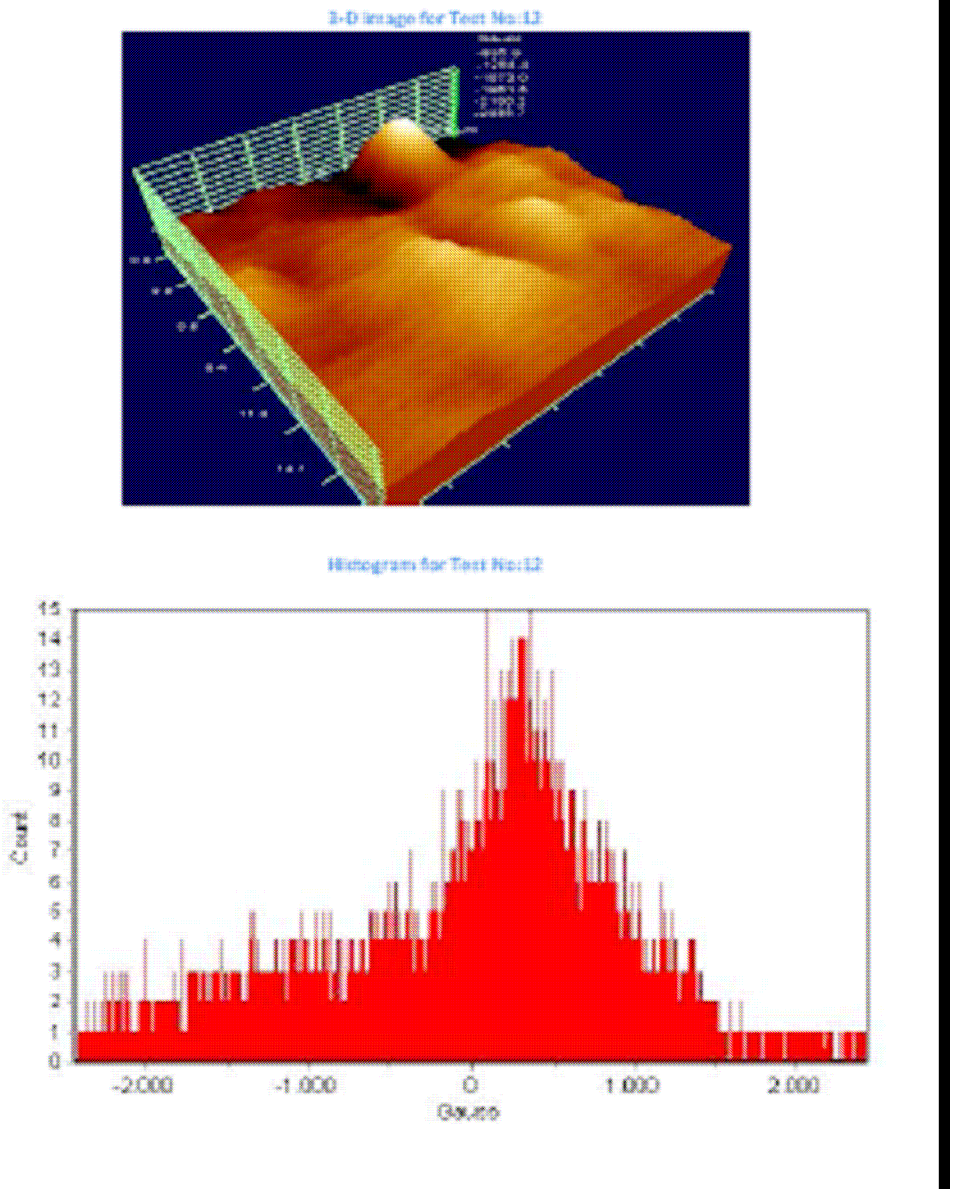

Figure 8.3. 3-D Fluxon Image Density in TJ305 BV.

9.0 Summary and Conclusions

YBCO samples with B-zirconate, Y_2O_3, and Ba-Sn-O pinning centers dopants were measured for their magnetic properties. In general, J_cs, pinning energies, α, and B^* were under study. The J_c curves are parameterized for J_{sv}, B^*, and α, and compared to previous results, including control samples. The results above showed that while good results for found in many samples, the pinning effects were not as strong as previous 123 layer pinned samples The strongest effects were seen for BZO samples at lower temperatures, while for Y2O3 samples, the mid range pinning at 77 K was seen to be somewhat higher.

APPENDIX B

Report to UTC for work performed at AFRL

BALL BEARING RACEWAY FATIGUE SPALL PROPAGATION

By

Nagaraj K. Arakere
Mechanical & Aerospace Engineering
University of Florida
Gainesville, FL 32611-6300
Email: nagaraj@ufl.edu
Tel: (352) 392-0856, Fax: (352) 392-1071

AFRL Advisor

Dr. Nelson Forster
Chief, Mechanical Systems Branch, AFRL/RZTM
Turbine Engine Division, Propulsion Directorate
Ph: (937) 255-5568, Fax: (937) 656-7176

Submitted to

Mr. Roger Rucker
Universal Technology Corporation (UTC)
937-426-2808: Tel, 937-426-0839: Fax

November 14, 2007

BALL BEARING RACEWAY FATIGUE SPALL PROPAGATION

1. Introduction

Bearing failure is the leading cause of aircraft turbine engine related Class A mishaps (defined as $1M or greater in damage or loss of life) for the DOD, and the second leading cause for the U.S. Air Force. During the past five years, the total cost to the DOD for engine bearing related Class A failures was approximately $350M. Aircraft engine and bearing manufacturers have been aggressively pursuing advanced materials technology systems solutions to meet mainshaft bearing needs of advanced military engines. Such efforts are aligned with goals for affordable high speed, high life bearings that have superior durability and corrosion resistance. Desirable near and long term attributes of an advanced mainshaft bearing, to meet the challenging requirements of future advanced military engines, include:

- Rolling contact fatigue life greater than 5X M50 steel (long life)
- Core fracture toughness greater than M50NiL (high speed, high load capability)
- Corrosion resistance greater than AISI 440C (reduced maintenance & performance debit)
- Surface durability and debris resistance greater than 5X state-of-the-art materials (reduced maintenance and damage tolerance)
- Tribological performance greater than M50 steel (increased oil out capability, lower heat generation, and performance under boundary lubrication conditions)
- Affordable life cycle cost system (performance to weight and cost benefit)
- Improved spall propagation life for single engine military fighter aircraft

These requirements have led to the development of hybrid bearings with silicon nitride balls and metal raceways made of case hardened materials such as Pyrowear 675 (P675), and M50Nil. The fatigue life performance, defined as the time until initiation of a spall, of hybrid ceramic/steel bearings has been shown to be much superior to steel bearings [1-6].

The complex processes that lead to subsurface crack nucleation and subsequent propagation resulting in a surface spall in bearing raceways, under the action of *rolling contact fatigue* (RCF), has been studied extensively. Figure 1 shows an example of a raceway spall due to RCF in an M50NiL hybrid ball bearing. Past and current bearing material research programs have only addressed fatigue life issues, i.e., the time until initiation of the failure. However, in many military aircraft engine applications, the initial raceway spall cannot always be reliably detected during operation, and the time

from fatigue spall initiation to subsequent propagation, as shown in Figure 2, leading to catastrophic bearing failure becomes an important mission critical variable. Extending spall propagation life is especially important for single engine military fighter aircraft. Bearing materials with high fatigue crack initiation resistance along with high spall propagation resistance are desirable. A systematic experimental and numerical investigation to study the complex interaction due to RCF between contact stress, microstructural changes, fracture toughness, cyclic variation in residual stresses and material plastic properties, and spall propagation rate has not been conducted.

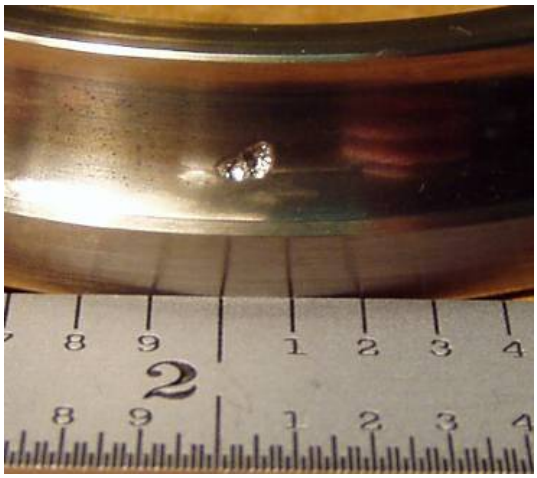

Figure 1 Example of a M50 NiL spalled ball bearing raceway.

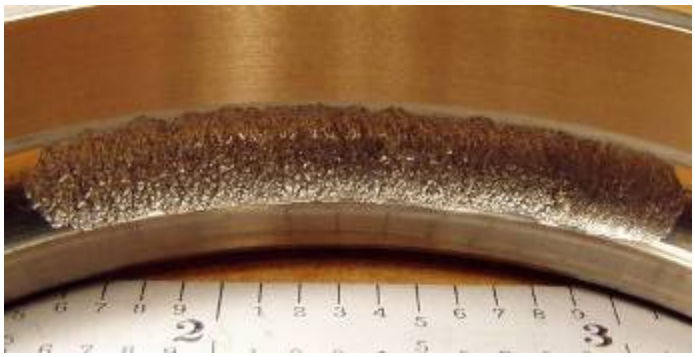

Figure 2 Example of progressive damage due to spall propagation in a ball bearing raceway.

2. Objectives for Air Force Summer Program

The overall objective of the Air Force is to develop spall propagation resistant turbine engine mainshaft bearings for improved reliability, safety, and performance margin of aircraft propulsion systems. Pyrowear 675 stainless steel case hardened material has been specifically developed to have high hot hardness (63 HRC up to 700°F) and high yield and ultimate strengths (~400 ksi). This material has been selected from a batch of candidate materials for use as bearing raceway with Si_3N_4 rolling element in hybrid bearing for insertion in to IHPTET Phase II engine. Bearings fabricated from Pyrowear 675 demonstrated improvements in subscale fatigue life in simulated engine conditions compared to the other candidate bearing steels. However, very little information is available on the propagation characteristics of the initiated surface spalls for this material. A rapid spall propagation rate can lead to catastrophic failure of the aircraft engine bearing.

Specific goals for the summer program are:

(i) Conduct a thorough literature review of research on spall propagation behavior in case hardened hybrid ball bearings, with emphasis on effects of raceway Hertz stress, evolution of compressive residual stress in the case layer with RCF cycles, and changes in micro hardness and yield stress in the neighborhood of the spall.
(ii) Understand characteristics of virgin and spalled areas of tested Pyrowear 675 and M50 NiL bearings at AFRL.
(iii) Develop a 3D linear elastic finite element model, which incorporates the full ball-raceway geometry of the 40-mm AFRL test hybrid bearing with a spall, to predict subsurface raceway stresses. Raceway stresses in the neighborhood of the spall, as the ball rolls over it will be studied in detail, to look for evidence of plastic deformation.
(iv) Submit a research paper that details the summer work, to the STLE Tribology conference.

3. Results from 3D Finite Element Modeling of the Ball Rolling Over a Spall

Military aircraft engine bearings are subjected to relatively high baseline Hertzian contact stresses in the range of 300-350 ksi. Plasticity induced in hybrid bearing raceways with silicon nitride balls can be more severe than all-metal bearings, for same peak Hertz stress value, because the ball is much harder than the raceway. Raceways made of M50NiL and P675 materials are case hardened with a strong residual compressive stress field in the case layer to a depth of about 0.050 inch. The

accumulation of cyclic plastic deformation caused by RCF can change the residual stress profile and microstructure, in a small volume of subsurface material. Yield first occurs at a point subsurface. The presence of traction forces at the contact interface causes the point of first yield to move closer to the surface. If, in the first pass, yield is initiated subsurface, residual stresses are introduced. In the second passage of the ball over the surface, the material is subjected to the combined action of the contact stresses and the residual stresses introduced in the previous pass. It is possible that after a few passes the residual stresses build up to such values that subsequent passes of the load result in entirely elastic deformation. This is the process of shakedown under repeated loading, whereby initial plastic deformation introduces residual stresses which make the steady cyclic state purely elastic. The conditions under which shakedown occurs is outlined in Melan's theorem [9]: which states if any time-independent distribution of residual stresses can be found which, together with the elastic stresses due to the load, constitutes a system of stresses within the elastic limit, then the system will shakedown. Any microstructural changes introduced by RCF will make the situation more complicated.

To examine the state of stress in the neighborhood of a spall, such as shown in Figure 1, we modeled the ball-raceway interface using 3D finite element analysis (ABAQUS version 6.1). Figure 3 shows the solid model used to represent the ball-inner ring raceway of the 40-mm test bearing. Figure 4 shows the schematic of the position of elliptical contact patch center, representing the ball-inner ring contact, as it moves over the circular spall. Figure 5 shows the stresses produced near the spall edge, as the ball approaches the spall and gradually rolls over it, for a representative case. The spall diameter is taken to be 2.6 mm, while the elliptical contact patch dimensions are chosen to be $2a$ = 2.92 mm, and $2b$ = 0.42 mm. the peak Hertz stress is 385 ksi (2.65 GPa) and the case material is assumed to have a yield stress of 390 ksi (2.69 GPa). Figure 5(a) shows the 3D solid model of the split inner ring raceway, with the ball not touching the raceway, for clarity. Figure 5(b) shows that the contact patch away from the spall with the peak von Mises stress to be 300 ksi (2.07 GPa), which is below the yield stress. Figures 5(c)-3(f) show that as the ball rolls over the spall, von Mises stresses exceed the yield stress at the spall edges, as the ball traverses over it. The peak Hertz used is representative of those likely to be seen in aircraft engine bearings. This example illustrates that for practical applications of mainshaft hybrid bearings in aircraft engines, yielding is produced at spall edges. This will result in residual stress changes, as the cyclic rolling continues, leading to work hardening, changes in yield stress and local hardness, and fatigue of spall edge material. As this process continues, it will lead to spall propagation, as shown in Figure 2.

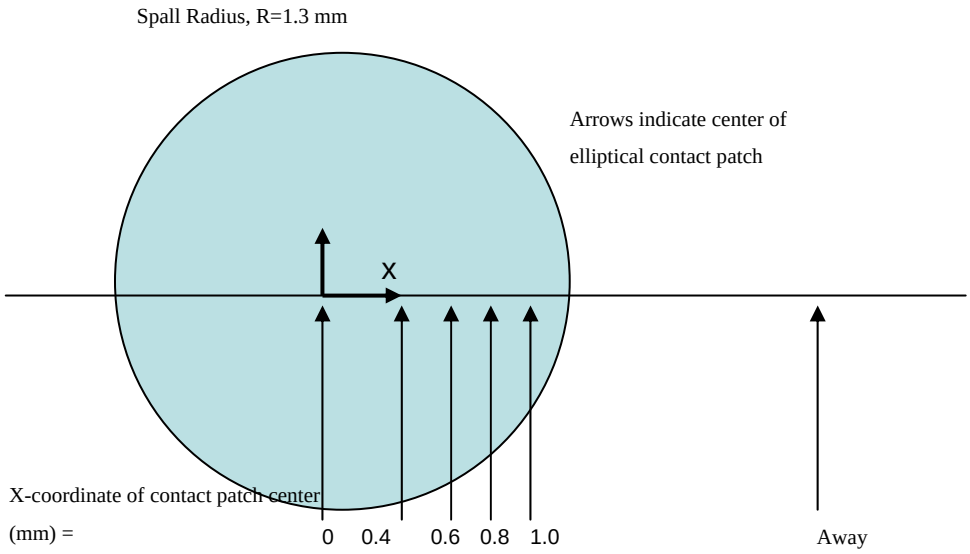

Figure 3 Schematic showing position of center of elliptical contact patch relative to the circular spall, as the ball rolls over the spall

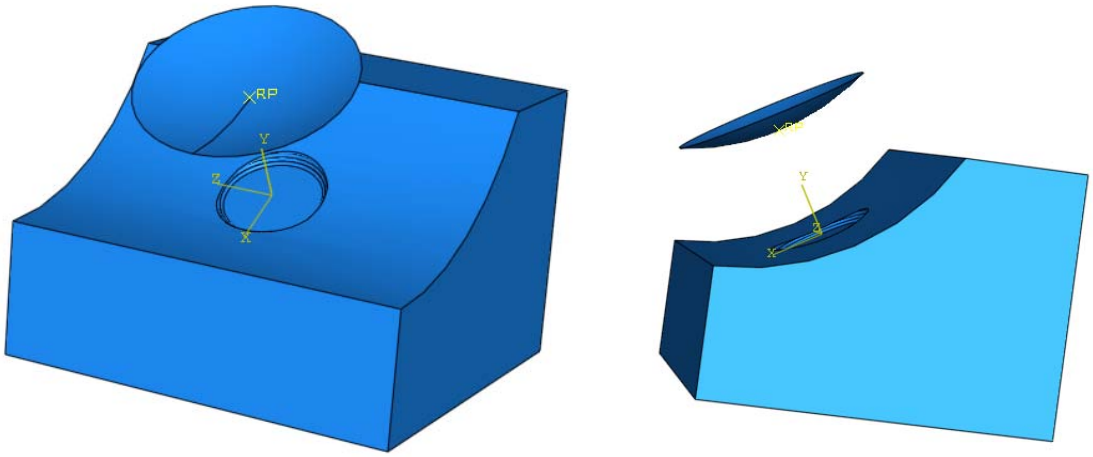

Figure 4 Solid models, used in the ABAQUS 3D finite element program, to represent the ball-inner ring contact. For clarity, the ball is not shown contacting the raceway. Ball is modeled as a rigid truncated sphere.

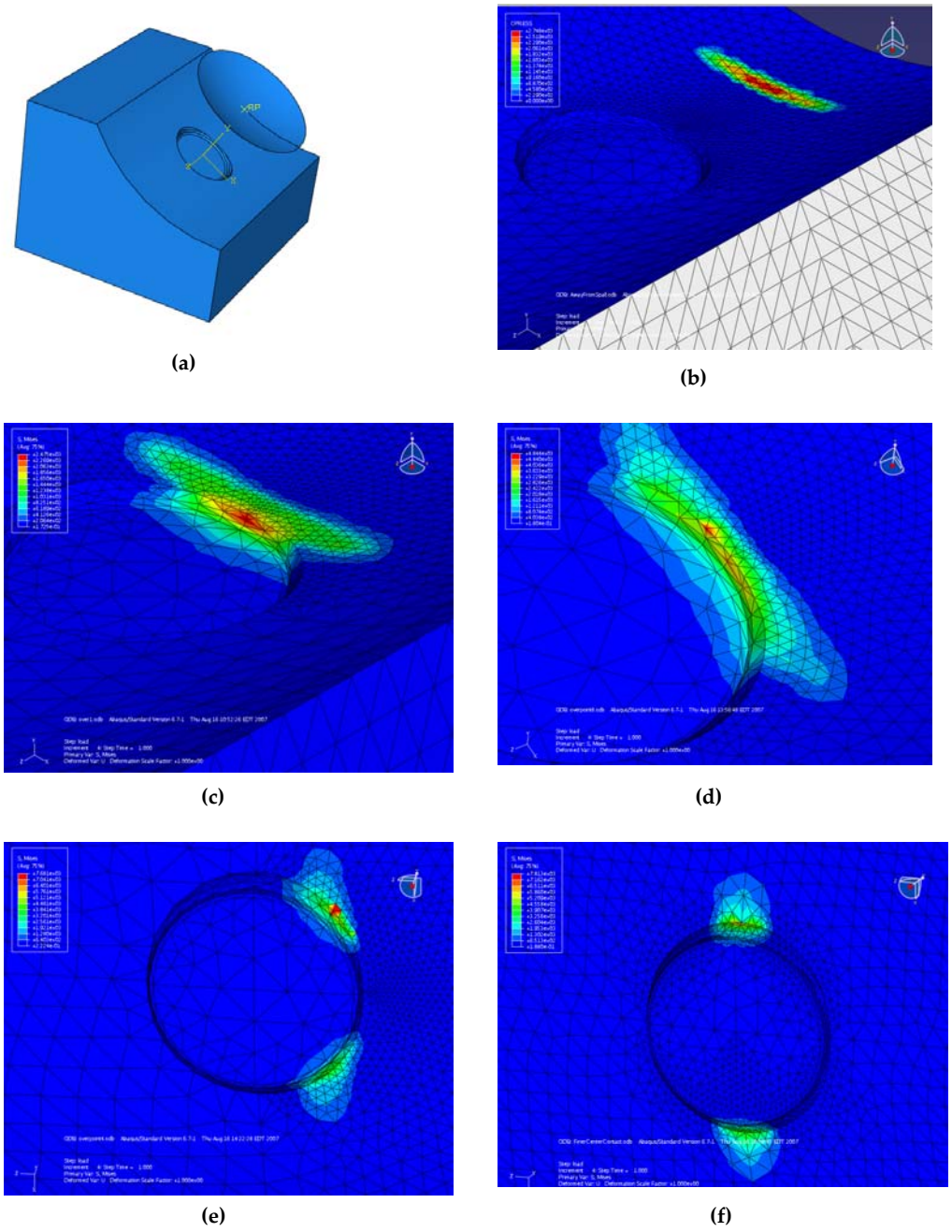

Figure 5 Representative example of peak von Mises stresses produced as a ball rolls over a circular spall. Spall diameter is 2.6 mm and the Hertzian elliptical contact patch size is given by $2a$ = 2.92 mm, and $2b$ = 0.42 mm. Peak Hertz stress is 385 ksi (2.65 GPa). Material yield stress = 390 ksi (2.69 GPa).
(a) Solid model of split inner ring raceway with ball, **(b)** Contact patch away from spall, max von Mises stress = 300 ksi (2.07 GPa), no yielding, **(c)** Contact patch close to spall (X=1), max von Mises stress = 358 ksi (2.47 GPa), no yielding, **(d)** Contact patch at inside edge of spall (X=0.8), max von Mises stress = 701 ksi (4.84 GPa), yielding, **(e)** Contact patch over spall (X=0.6), max von Mises stress = 1255 ksi (8.66 GPa), yielding, **(f)** Contact patch at inside edge of spall (X=0.0), max von Mises stress = 1132 ksi (7.81 GPa), yielding.

The 3D finite element analysis results shown in Figure 5 are based on linear elastic assumptions and hence can only predict the onset of yield, but not for predicting plastic stresses and strains. Elastic-plastic analysis with appropriate constitutive relations for M50 NiL and P675 materials is required for predicting plastic stresses and strains in the raceway contact, which will be considered in future work.

The important microstructural changes induced in the raceway material by RCF are thought to be the following [11-13]:

(i) In the first cycles of RCF, the inner ring materials experience shakedown and transformation of part of retained austenite to martensite. The subsurface volume that is plastically deformed is reduced by overrolling.
(ii) Material softening, due to decrease in yield stress, occurs in this stage, causing an increase in subsurface volume that is plastically deformed during fatigue. The probability of crack initiation increases in this stage.
(iii) Localized temperature peaks can occur in the subsurface plastic volume, due to repeated rolling, inducing carbon diffusion. As a result, underpinning and activation of other potential slip systems can occur.
(iv) The propagation of subsurface cracks, parallel to the rolling direction, is promoted by the development of a tensile residual stress in the surface normal direction. Development of an {100} <110> texture in the altered subsurface region can be seen. The onset of this stage can be the end of crack initiation/spallation phase and defines bearing fatigue life. The threshold for this stage can be assessed by measuring the percentage of retained austenite. This may not be practical for M50NiL and P675 materials since the retained austenite is only about 2% in virgin material.

4. Work Completed During Summer and Fall 2007

All the goals outlined under section 2 has been completed. An exhaustive literature review on spall propagation, elastic-plastic raceway modeling, microstructural changes induced by RCF, and subsurface crack initiation due to RCF has been completed. The initial linear elastic 3D finite element analysis of the ball-raceway contact as it rolls over the spall has been completed and representative results are shown in Fig. 5. An abstract has been submitted to STLE Tribology conference and the research paper is being written, to be submitted in November'07 [10].

5. Recommendations for Future Work

We will continue to collaborate with AFRL on spall propagation modeling, after return to the University of Florida.

To model the effects of cyclic loading due to RCF on raceway material, we plan to implement a 3D elastic-plastic finite element model using ABAQUS finite element program, with user-defined UMAT's. Kinematic hardening model will be used to simulate the inelastic behavior of raceway material subjected to cyclic loading. Here the center of the yield surface moves in stress space due to the kinematic hardening component. In addition, the nonlinear isotropic/kinematic component is incorporated so that the yield surface range may expand or contract due to the isotropic component. These features allow modeling of inelastic deformation in metals that are subject to cycles of load or temperature, resulting in low-cycle fatigue failure. These models can account for Baushinger effect, characterized by a reduced yield stress upon load reversal after plastic deformation. Cyclic hardening with plastic shakedown can also be modeled, which is characteristic of symmetric stress-or-strain controlled loading. Soft or annealed metals tend to harden toward a stable limit. Initially hardened materials, such as bearing raceway materials, tend to soften. Ratchetting behavior can also be simulated. Typically, transient ratcheting is followed by zero ratchet strain (stabilization) for low mean stresses, while a constant increase in the accumulated ratchet strain is observed at high mean stresses, which is typical of RCF loading. If the loading is unsymmetric, a relaxation of the mean stress can also manifest. Three-D simulations of this nature are computationally very intensive and complicated to perform. However, they do yield the detailed evolution of stresses and strains in the subsurface region, and in the neighborhood of the propagated spall. This information will be valuable in understanding the progressive damage due to RCF that is observed near an initiated spall.

We propose the following collaborative experimental and modeling/analysis work with AFRL, for future work:

(1) Residual stress profile in virgin case layer and in the neighborhood of a fatigue spall of failed bearings. In the case of RCF tests, Rockwell C raceway dent will be used to initiate the spall and the stress profile and its change due to accumulation of cyclic plastic deformation will be measured near the spall.
(2) Residual stress profile and microhardness mapping near a propagated raceway spall, and on the rod after RCF tests.

(3) Quantify localized modulus, yield stress, strain hardening exponent and plastic stress-strain behavior in the neighborhood of a propagated spall using instrumented micro indentation [7, 8].

(4) Analyze microstructure of the virgin raceway and near the spall.

(5) Build elastic-plastic 3D finite element model to predict subsurface raceway stresses, including effects of residual stress. Material model will include nonlinear kinematic hardening component and an isotropic hardening component, capable of simulating cyclic hardening with plastic shakedown. This model will make use of material properties measured in (3).

6. References

1. Miner, J. R., Dell, J., Galbato, A., and Ragen, M. A., (1996), "F-117-PW-100 hybrid bearing ceramic technology insertion," *ASME J of Engineering for Gas Turbines and Power*, V 118, pp. 434-442.
2. Tanimoto, K., Kajihara, K., and Yanai, K., (2000), "Hybrid ceramic ball bearings for turbochargers," *SAE Paper* 2000-01-1339, pp. 1-14.
3. Shitsukawa, et al, (1997), "Influence of lubricant on the fatigue life of ball bearings," *SAE Paper* 972710.
4. Wang, L., Snidle, R. W., and Gu, L., (2000), "Rolling contact silicon nitride bearing technology: A review of recent research," *Wear*, Vol. 246, pp. 159-173.
5. Hadfield, M., (1998), "Failure of silicon nitride rolling elements with ring crack defects," *Ceramic International*, Vol. 24, pp. 379-386.
6. Hadfield, M., and Stolarski, T. A., (1995), "The effect of test machine on the failure mode in lubricated rolling contact of silicon nitride," *Tribology International*, Vol. 28, pp. 377-382.
7. Gouldstone, A., Chollacoop, N., Dao, M., Li, J., Minor, A. M., and Shen, Y, (2007), Indentation across size scales and disciplines: Recent developments in experimentation and modeling, *Acta Materialia*, 55, pp. 4015-4039.
8. Luo, J., and Lin, J, (2007), "A study of the determination of plastic properties of metals by instrumented indentation using two sharp indenters," *International Journal of Solids and Structures*, 44, pp. 5803-5817.
9. Symonds, P. S., (1951), "Shakedown in continuous media," Trans. ASME, Series E, Journal of Applied Mechanics, vol. 18, 85.
10. Arakere, N. K., Levesque, G., Branch, N., Svendsen, V., Forster, N., "On the Rolling Contact Fatigue Life and Spall Propagation Characteristics of M50, M50 NiL and 52100 Bearing Materials, Part II - Stress Modeling," To be submitted to the STLE Tribology Conference, 2007.
11. Voskamp, A. P., Osterlund, R., Becker, P. C., and Vingsbo, O., (1980), Metals Technology, 7, pp. 14-21.
12. Voskamp, A. P. and Mittemeijer, E. J., (1997), "The effect of changing microstructure on the fatigue behavior during cyclic rolling contact loading," Z. Metallkd. 88, pp. 310-320 (translated from German).
13. Voskamp, A. P. and Mittemeijer, E. J., (1997), Metallic Materials Trans. A 27A, pp. 3445-3465.

Experimental Research Involving the Use of Pulsed Voltage to Modify Flame Speed and Flame Instability

S. D. Marcum
Department of Physics, Miami University
Oxford, OH 45056

Overview

Experiments and early results of a study designed to investigate the source(s) of pre-mixed hydrocarbon flame speed and stability modifications by the application of an external voltage source are described. A small burner and a system that allows for pulsed electrical stressing of pre-mixed hydrocarbon-air flames were constructed. Two different pulsed high voltage power systems were applied in an anode point-to-plane geometry under various flame conditions. Comparison measurements were also carried out with a DC source. Optical imaging, spectral imaging, spectroscopic and electrical diagnostics have been applied to electrically stressed pre-mixed propane/air flames at a wide variety of equivalence ratios and a range of flow speeds near 1 m/s. Observed effects on flame front geometry and flame speed and stability are evaluated in terms of two possible causative mechanisms: the ionic wind (an electric-field-dependent body force exerted on flame chemiions) or a current driven flame chemistry mechanism based upon recombination of flame chemiions at the burner head.

Introduction

Despite the rather large amount of work[1-13] that has been reported on the various effects of applied voltages on a wide variety of flames, the mechanism(s) responsible for the observed effects on the size and shape of the reaction zone of some hydrocarbon flames is still not well understood. Bradley[1] provides a good overview of the subject, as well as a thorough review of the literature in this general area up to the date of that text's publication.

The most extensive efforts to construct and test theoretical models sufficient to predict the maximum practical effects of electric fields on flames are contained in a series of publications by Lawton and Weinberg.[11-13] Their description of the basic circuit/flame interaction is generally referred to as the ionic wind, which has flame front perturbations deriving from the ***size of the imposed electric field***. The principal results of those models are summarized in Reference 1. More recently, a reaction kinetics model[14] simulating the effects of electric fields in premixed methane flames has been published, and electric fields have been used to counterbalance natural convection and simulate microgravity[15] in small diffusion flames.

We have demonstrated[16] that close coupling of the externally applied voltage to pre-mixed propane/air flames with the electric field directed generally counter to the flow can produce significant flame front perturbations with relatively small ratios[8] of voltage to the electrode separation. The close coupling[16] provides circuit current densities comparable to those previously produced using applied voltages sufficient to produce near-breakdown[1,11-13] electric fields. Modest applied voltages are capable of driving the flame[16,17] from laminar (stable, conical flame geometry) to a wrinkled laminar geometry (cellular; multiple laminar flamelets). The observed flame front perturbations in our experiments are consistent with a ***current driven***

mechanism[17] rather than any field driven effect such as the ionic wind. The effects reported earlier[16,17] differed sufficiently in magnitude and observed distribution over the flame front that an alternative explanation[17] of the observed effects based upon changes in the flame chemistry at the burner head was offered.

The term *electric pressure* [16] was used to explain the apparent difference between our results and those predicted by the ionic wind. Recent measurements suggest that the *electric pressure* acts through the manipulation of the instabilities in the flame. Sivashinksy's review[18] and the references therein, describe the development of the understanding of flame pattern formation due to coupled hydrodynamic and thermodiffusive instabilities. Hydrodynamic instabilities tend to dominate at high flow velocities (or high Reynolds numbers), and it has been shown experimentally that as the flow speed increases, so does the hydrodynamic instability of a premixed combusting flow.

Normally, the thermal-diffusive instability is dominant only under conditions where $0.8 < \varphi > 1.3$, which naturally result in lower combustion temperatures (e.g. fuel rich hydrocarbon flames or fuel lean hydrogen flames). As discussed by Sivashinsky[18] one method for increasing the strength of the thermodiffusive instability is to lower the flame global *Le* by providing a sufficient concentration of the deficient light reactant. In our work, this could be accomlished by the production of light radicals near the grounded burner head via dissociative recombination of important flame chemi-ions. Mass spectroscopic work by Goodings *et al*[19] has shown that the majority ions present in a pre-mixed hydrocarbon-air flame are H_3O^+ and HCO^+. The hydronium ion can dissociatively recombine through the four different channels shown below[20], while HCO^+ dissociatively recombines to form H + CO.

$$H_3O^+ + e^- \rightarrow \begin{matrix} H_2O + H & (N = 0.05) \\ OH + H_2 & (N = 0.36) \\ OH + 2H & (N = 0.29) \\ O + H + H_2 & (N = 0.30) \end{matrix}$$

If the chemi-derived positive ions are relocated to the immediate vicinity of the grounded burner head (pre-heat zone), the dissociative recombination of these two majority positive ions would result in a production of ground-state radicals into the pre-heat zone. Quantitative estimates on the levels of radicals necessary to produce a given flame front perturbation can be calculated by a current continuity equation,

$$n_{H_3O^+} v_{d,H_3O^+} + n_{HCO^+} v_{d,HCO^+} = \frac{j}{e}, \qquad (1)$$

where v_d represents the drift velocity of the ion, *n* is the number density, *j* is the current density, and *e* is the elementary charge. Treating the boundary between the base of the flame and the burner head as a cathode sheath allows us to substitute the Bohm velocity in place of the drift velocity. The Bohm velocity can be expressed by the following equation[21]:

$$v_B = \left(\frac{kT_e}{m_{ion}} \right)^{1/2}, \qquad (2)$$

where k is Boltzmann's constant, T_e is the electron temperature (assumed equal to the local gas temperature), and m_{ion} is the ionic mass. Using Equations 1 and 2 and the measured applied current it is possible to calculate the number densities of the light radicals that are required to produce the observed flame stability changes.

The level of light radical production based upon the above model[17] and the applied voltage induced current flow measured in our experiments (~few hundred microamperes) suggests light radical injection at the base of the flame in concentrations of the order of 10^{11} cm^3. Such levels of light radical production are difficult to measure directly a flame environment. The experiments described here thus focus upon indirect evidence that supports the light radical injection model and that runs counter to the predictions of the ionic wind.

Results and Discussion

The bulk of the experimental apparatus used to develop the results discuss here has been discussed in detail elsewhere[16,17]. A block diagram of the overall setup is shown in Figure 1., with modifications for this work primarily involving various anode and cathode geometries, and the DC power supply was at times short pulsed (~100 ns, up to 20 kV @ 1 kHz), long pulsed (~1 ms, up to 3 kV, low duty cycle) or DC (up to 5 kV).

Using the original burner/disk anode[16,17] system with a long pulsed-DC power supply allowed the capture of the two sequences of images shown in Figure 2. The time evolution of the effect of a long square pulse (> 10 ms) bias at ~ 2 kV (~ 200 μA), on a pre-mixed propane/air flame at near stoichiometric conditions (time between frames = 1 ms) is shown. The flame speed increase (**top set**) is ***initiated at the base*** of the reaction zone where close attachment of the flame to the screen cathode would allow flame chemi-ions to (dissociatively) recombine producing light flame radicals such as H atoms, hydroxyl radicals, etc. As the upper sequence suggests, injection of the flame-speed-enhancing radicals spreads radially inwards toward the burner axis as the flame front's proximity to the burner head (cathode) expands. When the ***current pulse*** is terminated (**lower set**) the normal (slower) flame chemistry resumes, and the **signal** that the lower (zero-current) flame speed has resumed **propagates downstream** with the **steady** input flow. The result is that the flame front geometry recovers as shown. The location (at the burner head) and extent (area) of the cathode (sheath) thus combine with the ion current to the burner head to produce the observed acceleration and deceleration of the flame.

Such image sequences are consistent with the applied voltage induced current flow acting to enhance the flame speed at the base of the flame. The electric field driven view of the ionic wind would predict a body force acting everywhere along the flame front dependent upon the local chemiion production and electric field. Modification of the anode geometry from the original perforated disk to that of a downward pointing sharp rod (3-mm diameter rod tapering to a point over 7-mm) provided a highly non-uniform electric field that was strongest near the tip. The anode point-to-plane electrode geometry was chosen to enhance any ionic wind effects, and further cause them to be sensitive to the placement of the point anode. Using initially a steady DC bias the results shown in Figure 3 were recorded.

The images of Figure 3 show the ***independence*** of the point **anode's** position on the flame speed increase for DC anode point-to-plane biasing of a propane/air flame (ϕ = 1.1, flow speed = 1.3 m/s). A small DC current causes a laminar flame to go unsteady and decrease somewhat in height due to the increased flame speed. The circuit current was adjusted to provide ~ 20% increase in for the case shown. The upper left direct reference image shows the initial electrode geometry. The subsequent images were taken through 10-nm bandpass filters centered at 430 nm (CH(A-X)), with the electrode tip position indicated by an arrow. The top middle image is with no bias, and all but the last were taken with a 1.5-kV bias between the electrode tip and the *grounded burner head*. The final image, which shows no flame speed increase, also used a 1.5 kV bias, but employed a ***ring cathode*** at the position shown (burner head floating) rather than the burner head as the cathode. The ***cathode position dependence*** is clearly demonstrated. The current drawn was essentially constant for all conditions shown (~150 μA, or roughly ¼ Watt input power). These results are fully supportive of the current driven recombination chemistry mechanism given the essential dependence upon cathode placement shown in the last image. Injection of radicals into the flame at the position of the ring would add only a very low flux of light radicals in a region of the flame where the radical density is already quite high – thus no observable effect. In addition, the independence of the point anode's position speaks against any field driven effect.

For the next three figures, the long-pulsed DC power supply used for the initial results (Figure 2). Figure 4 is a sequence of images showing the effect of a 3 kV, 2 ms excitation pulse on a flame using an anode point-to-plane geometry. The anode tip (not shown) was centered just above the unperturbed flame cone tip. The images were taken at 1 ms intervals, and the flame conditions were ϕ = 1.1with a flow velocity 1.3 m/s. The images were recorded through a 10-nm bandpass filter centered at 430 nm (CH(A-X)). Each image was made by summing twenty 60-μs exposures. That sequence of images clearly demonstrates that the flame speed enhancing mechanism is initiated at the cathode where the flame is attached to the burner head.

Figure 5 shows a similar set of images where the flame conditions were identical those of Figure 4 except for a lower flow velocity of 0.8 m/s. Together these results show that the speed of the disturbance toward the tip of the inner cone is determined by the flow speed of the input mixture.

Figure 6 shows a similar sequence of images like those of Figure 4 except using a horizontal 3-mm-diameter rod as the anode passing through the reaction zone (not shown). The anode rod was oriented perpendicular to the page and to the right of the reaction zone. Those results also show that the flame response to the applied voltage induced current is independent of the placement and shape of the anode.

The remaining results that are presented here used a short-pulsed (<100 ns) high voltage (up to 20 kV) power supply at higher repetition rates (500 Hz – 1 kHz). Figure 7 shows the development of an anode point-to-plane corona discharge in a stoichiometric propane/air mixture (flow velocity < 1 m/s) excited by a 10 kV short-pulse (< 100 ns) @ 1 kHz. Each photo is an accumulation of 500 10-ns exposures and each successive image is delayed by 10 ns. All images were taken through a 10-nm bandpass filter centered at 340 nm (N_2(C-B)). The corona discharge

has no observable effect on the flame front even in a situation that is optimized for the ionic wind.

A false color version of one of the images in the previous sequence is shown in Figure 8. Although the corona discharge has no observable effect on the flame front, the resulting intensity distribution suggests possible application of such discharges to the imaging of gas density distributions in high speed flows. Figure 9 shows current/voltage/power characteristics for the pulsed anode point-to-plane corona discharge used to produce the images contained in the previous 2 figures. Typical time resolved emission from the discharge from N_2(C-B) emission at 337 nm is shown with a discharge current pulse in the lower plot.

The final results presented here are the sequence of images of a *transverse* anode point-to-plane corona discharge into a stoichiometric propane/air mixture (flow velocity < 1 m/s) excited by high voltage, short-pulse (< 100 ns) discharge @ 500 Hz. In Figure 10, the top left comparison image was taken through a 10 nm bandpass filter centered at 430 nm (CH(A-X)) with the discharge off. Each subsequent photo is an accumulation of 400, 100-ns exposures imaged through a long pass filter (400 nm cutoff). They are arranged in order of increasing discharge voltage in 1 kV steps (1 through 9 kV). The corona discharge has no observable effect on the flame front using this discharge geometry.

Conclusions

The results of this study solidly support the conclusion that an applied voltage induced current based mechanism such as that described in detail elswhere[16,17] is much more likely to be responsible for the observed flame speed and stability modifications that is the ionic wind.

References

1. D. Bradley, in Advanced Combustion Methods, F.J. Weinberg, Ed., Academic Press, New York, 1986, p. 331.
2. A.P. Chattock, Phil. Mag **48** (1899) 401-403.
3. H.F. Calcote and R.N. Pease, Ind. Eng. Chem. **43** (1951) 2726-2731.
4. H.F. Calcote and C.H. Berman, in Fossil Fuels Combustion Symposium PD-Vol. 25, S.N. Singh, Ed., ASME Book No. H00453, 1989, p. 25.
5. D. Bradley and S.H. Nasser, Combust. Flame **55** (1984) 53-58.
6. D. Bradley and S.M.A. Ibrahim, Proc. Combust. Inst. **15** (1974) 1023-1029.
7. H.C. Jaggers and A.von Engel, Combust. Flame **16**, (1971) 275-285.
8. D.S. Maclatchy, R.M. Clements and P.R. Smy, Combust. Flame **45**, (1982) 161-169.
9. M. Kono, F.B. Carleton, A.R. Jones and F.J. Weinberg, Combust. Flame **78** (1989) 357-363.
10. G.A. Gulyaev, G.A. Popkov and Yu.N. Shebeko, Phys. Combust. Explosion **21** (1985) 23-25.
11. J. Lawton and F.J. Weinberg, Proc. Roy. Soc. **A227** (1964) 468-497.
12. J. Lawton, P.J. Mayo and F.J. Weinberg, Proc. Roy. Soc. **A303** (1968) 275-298
13. J. Lawton & F.J. Weinberg, Electrical Aspects of Combustion, Clarendon Press, Oxford, 1969, pp. 285-336.

14. T. Pedersen and R.C. Brown, Combust. Flame **94** (1993) 433-448.
15. B.A. Strayer, J.D. Posner, D. Dunn-Rankin and F.J. Weinberg, F.J., Proc. R. Soc. Lond. A, Math. Phys. Eng. Sci. **458** (2002) 1151-1166.
16. S. D. Marcum, B. N. Ganguly, Combust. Flame **143** (2005) 27-36.
17. D. L. Wisman, S. D. Marcum and B.N. Ganguly, "The Effects of Electric Fields on the Thermodiffusive Instability in Hydrocarbon-Air Flames," Paper AIAA-2007-1383, 45th AIAA Aerospace Sciences Meeting, January 01-11, 2007, Reno, NV. Ibid, see also accepted for publication by Combustion and Flame, September 2007, "Electrical Control of the Thermodiffusive Instability in Pre-Mixed Propane-Air Flames"
18. G.I. Sivashinsky, Annu. Rev. Fluid Mech. **15** (1983) 179-199.
19. J. M. Goodings, D. K. Bhome, C. Ng, Comb. Flame **36** (1979) 27-43.
20. L. Veiby-Christensen, L. H. Andersen, O. Heber, D. Kella, H. B. Pedersen, H. T. Schmidt, D. Zajfman, The Astrophys. Journal **483** (1997) 531-540.
21. K. Riemann, J. Phys. D: Appl. Phys. **24** (1991) 493-518.
22. S. M Starikovskaia, J. Phys D: Applied Physics **39** (2006) R265-R299.
23. Special Issue on Plasma Assisted Combustion, IEEE Transactions on Plasma Science **34**, December 2006.

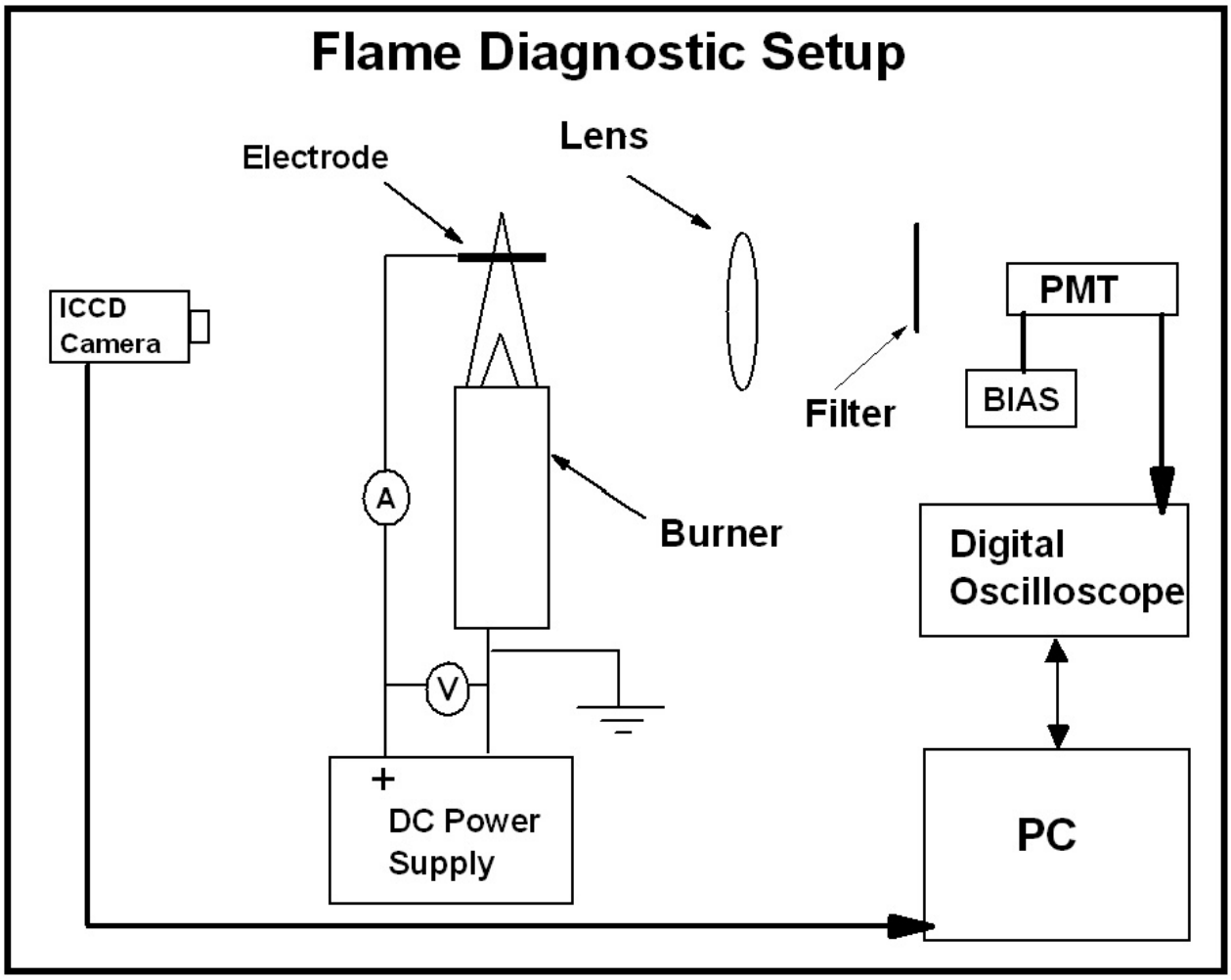

Figure 1: The general setup used for this study is shown above. Various anode and cathode geometries were used, and the DC power supply was at times short pulsed (~100 ns, up to 20 kV @ 1 kHz), long pulsed (~1 ms, up to 3 kV, low duty cycle) or DC (up to 5 kV).

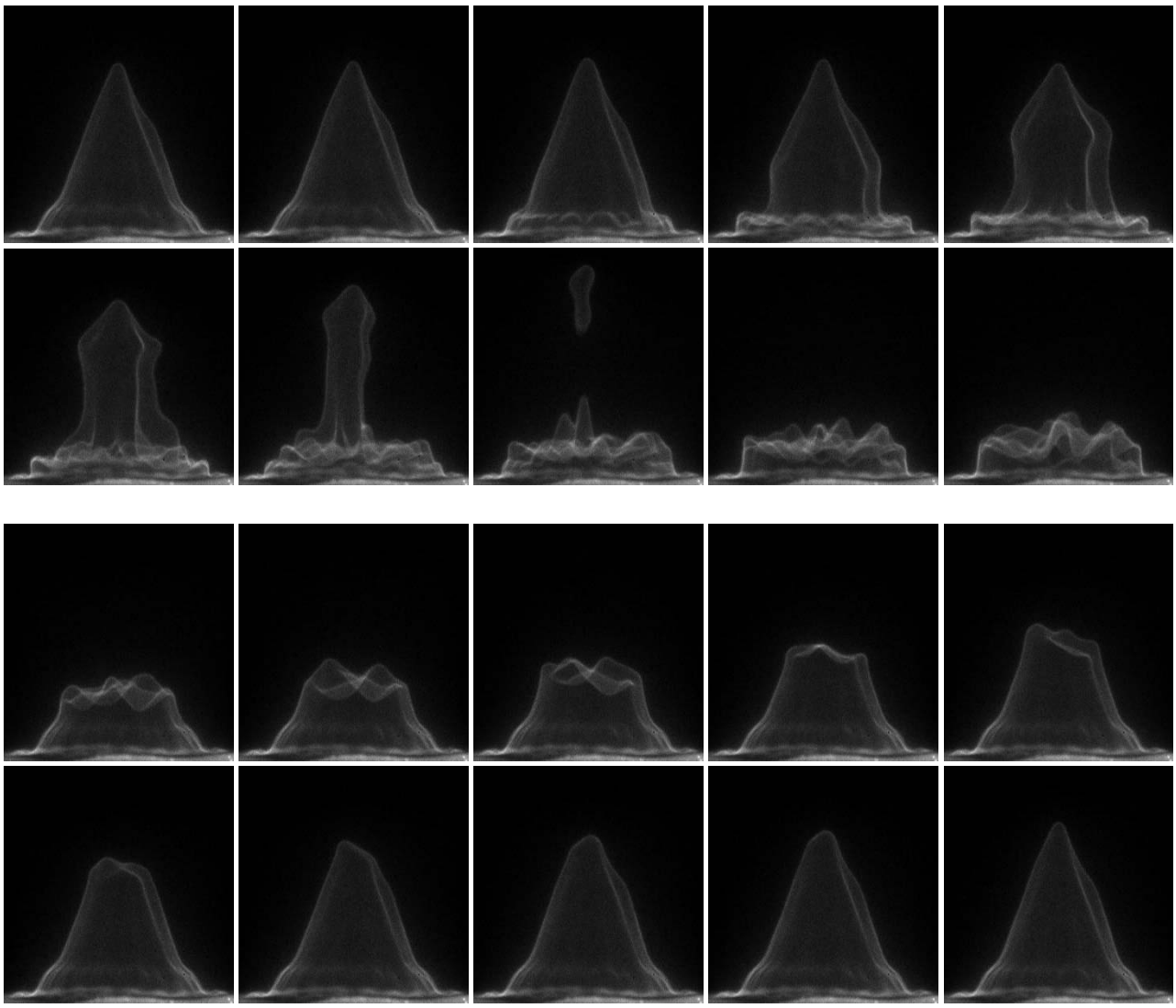

Figure 2: Using a disk anode, the time evolution of the effect of a long square pulse (> 10 ms) bias at ~ 2 kV (~ 200 μA), on a pre-mixed propane/air flame at near stoichiometric conditions (time between frames = 1 ms) is shown. The flame speed increase (**top set**) is ***initiated at the base*** of the reaction zone where close attachment of the flame to the screen cathode would allow flame chemi-ions to (dissociatively) recombine producing light flame radicals such as H atoms, hydroxyl radicals, etc. As the upper sequence suggests, injection of the flame-speed-enhancing radicals spreads radially inwards toward the burner axis as the flame front's proximity to the burner head (cathode) expands.
When the ***current pulse*** is terminated (**lower set**) the normal (slower) flame chemistry resumes, and the **signal** that the lower (zero-current) flame speed has resumed **propagates downstream** with the **steady** input flow. The result is that the flame front geometry thus recovers as shown. The location (at the burner head) and extent (area) of the cathode (sheath) thus combine with the ion current to the burner head to produce the observed acceleration and deceleration of the flame.

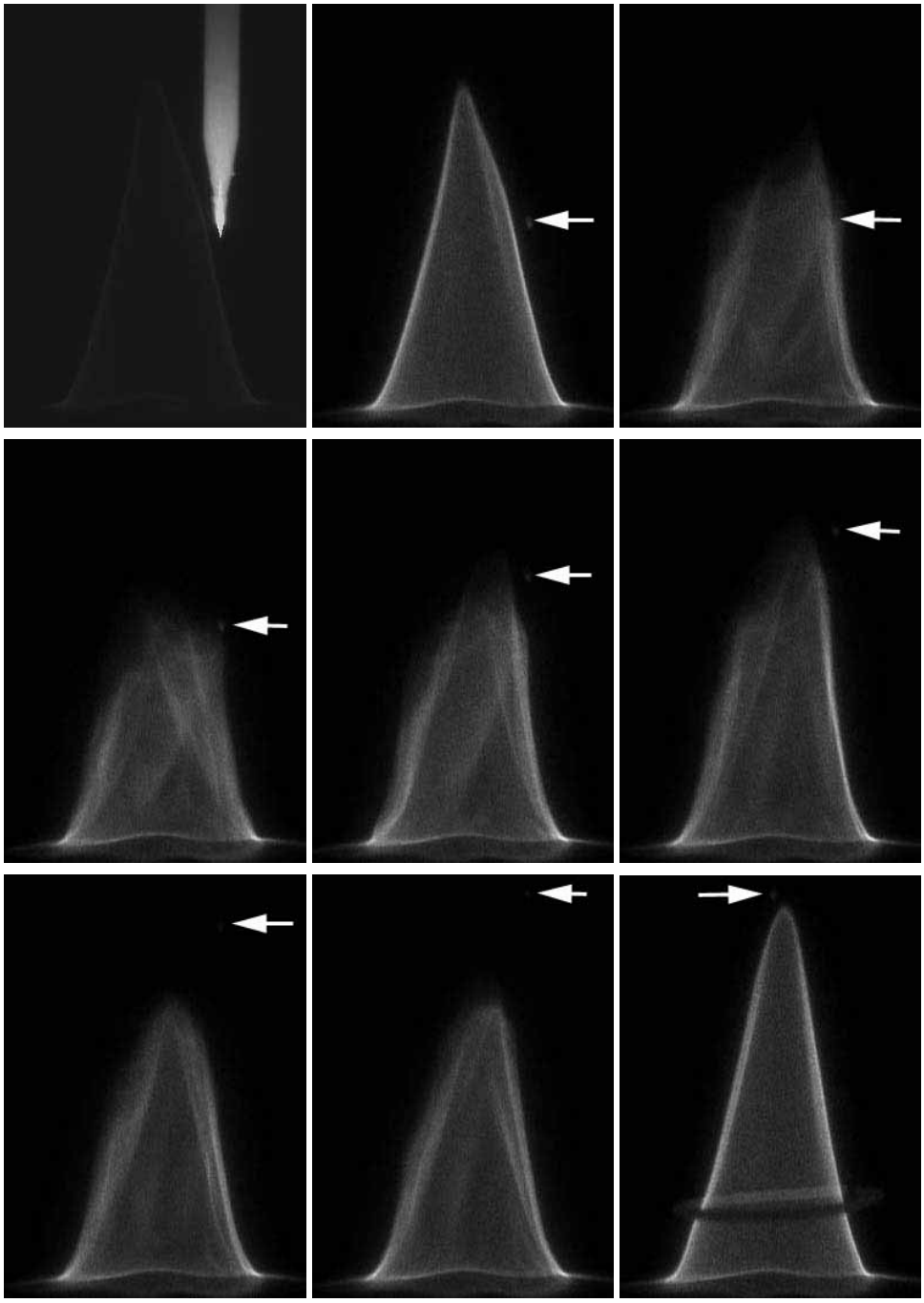

Figure 3: Images showing the ***independence* of the point <u>anode's</u> position** on the flame speed increase for DC anode point-to-plane biasing of a propane/air flame (ϕ = 1.1, flow speed = 1.3 m/s). The upper left direct reference image shows the initial electrode geometry. The subsequent images were taken through 10-nm bandpass filters centered at 430 nm (CH(A-X)), with the electrode tip position indicated by an arrow. The top middle image is with no bias, and all but the last were taken with a 1.5-kV bias between the electrode tip and the *grounded burner head*. The final image, which shows no flame speed increase, also used a 1.5 kV bias, but employed a ***ring <u>cathode</u>*** at the position shown (burner head floating) rather than the burner head as the cathode. The ***cathode position dependence*** is clearly demonstrated. The current drawn was essentially constant for all conditions shown (~150 μA, or roughly ¼ Watt input power).

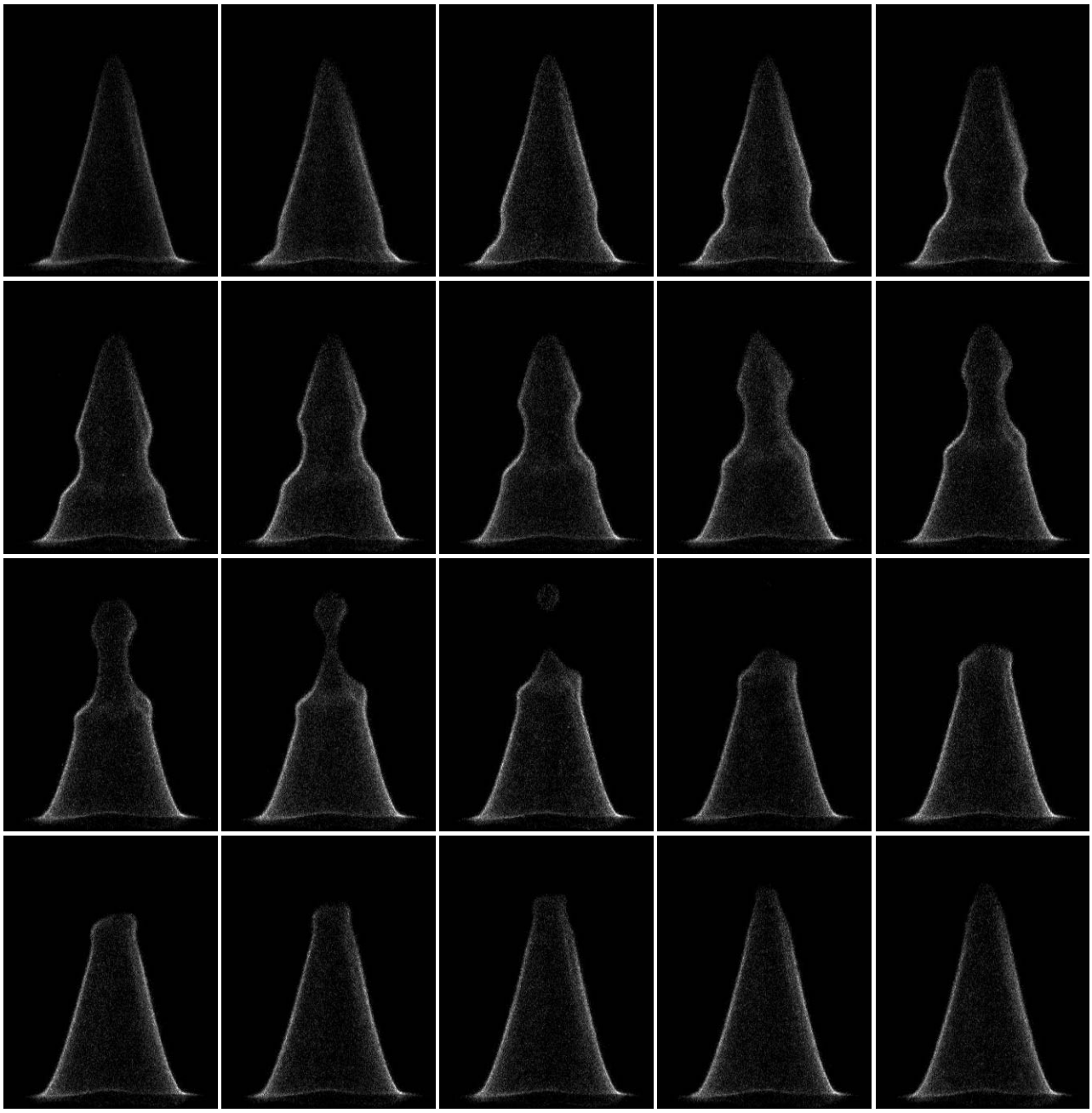

Figure 4: Sequence of images showing the effect of a 3 kV, 2 ms excitation pulse on a flame using an anode point-to-plane geometry. The anode tip (not shown) was centered just above the unperturbed flame cone tip. The images were taken at 1 ms intervals, and the flame conditions were ϕ = 1.1with a flow velocity 1.3 m/s. The images were recorded through a 10-nm bandpass filter centered at 430 nm (CH(A-X)). Each image was made by summing twenty 60-μs exposures.

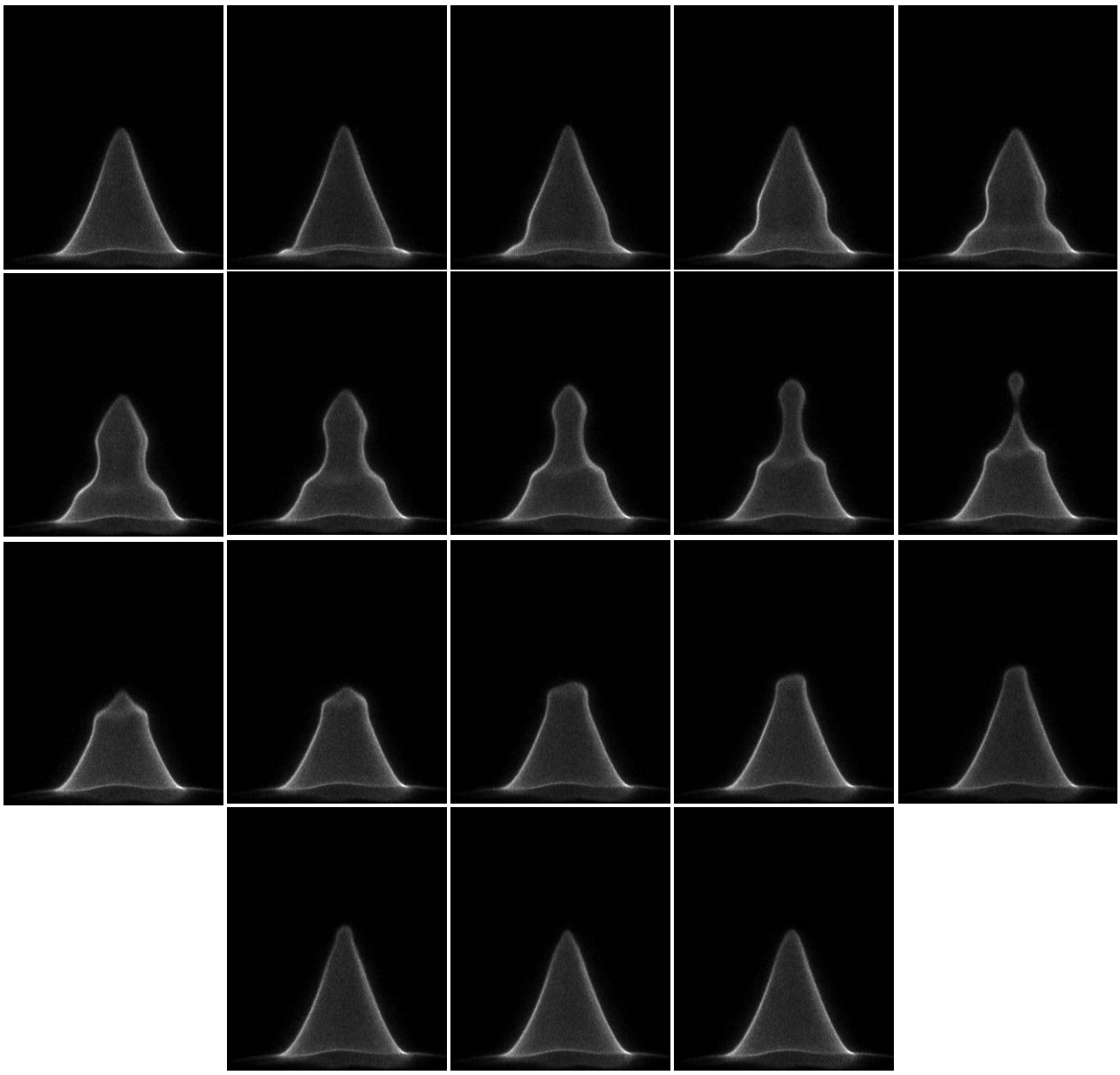

Figure 5: Sequence of images showing the effect of a 3 kV, 2 ms excitation pulse on a flame using an anode point-to-plane geometry. The anode tip (not shown) was centered just above the unperturbed flame cone tip. The images were taken at 1 ms intervals, and the flame conditions were ϕ = 1.1with a flow velocity 0.8 m/s. The images were recorded through a 10-nm bandpass filter centered at 430 nm (CH(A-X)).

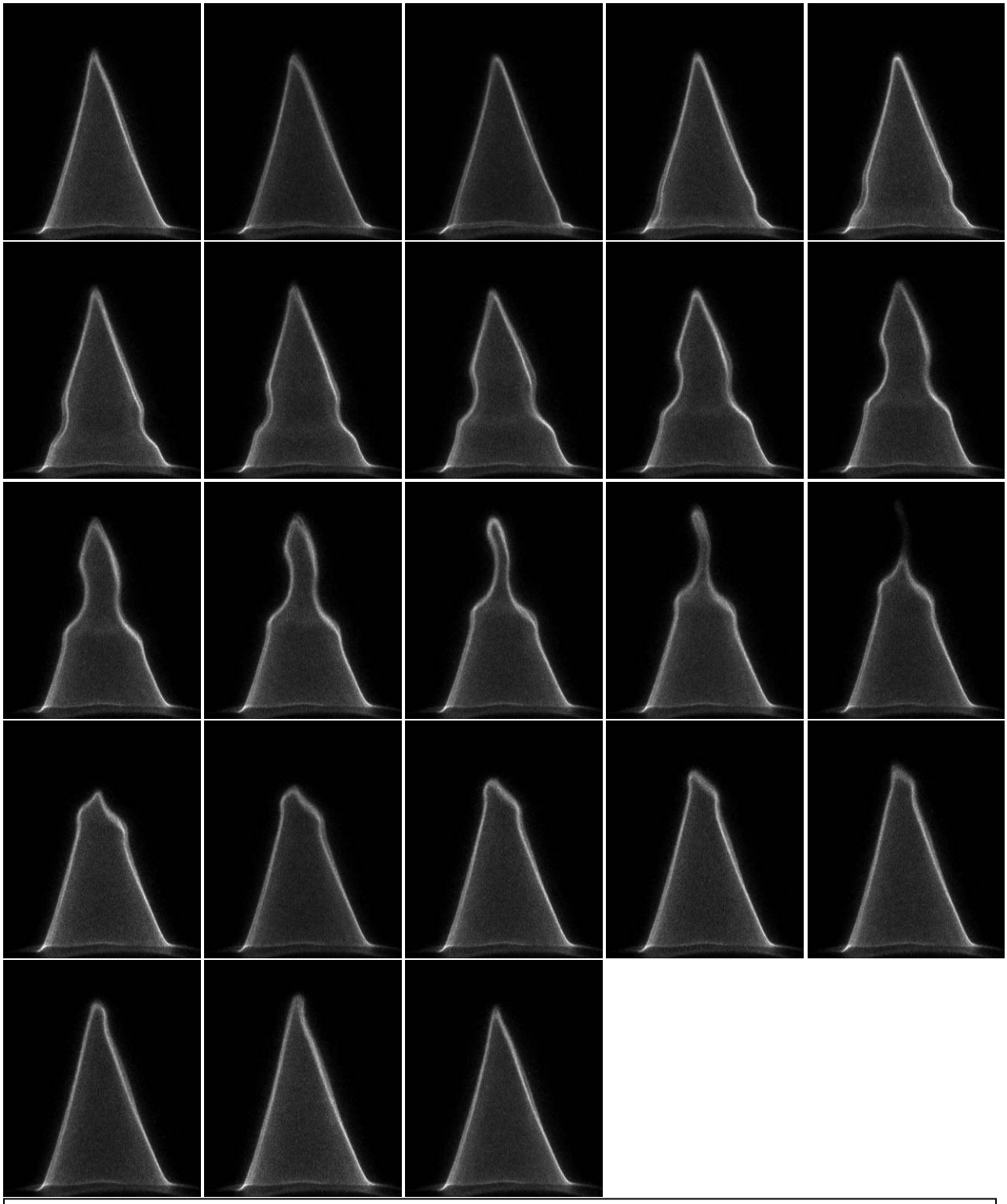

Figure 6: Sequence of images showing the effect of a 3 kV, 2 ms excitation pulse on a flame using a horizontal 1/8”-diameter rod as the anode passing through the reaction zone (not shown). The anode rod was oriented perpendicular to the page and to the right of the reaction zone. The images were taken at 1 ms intervals, and the flame conditions were propane/air , ϕ = 1.1 with a flow velocity > 1 m/s. The images were recorded through a 10-nm bandpass filter centered at 430 nm (CH(A-X)).

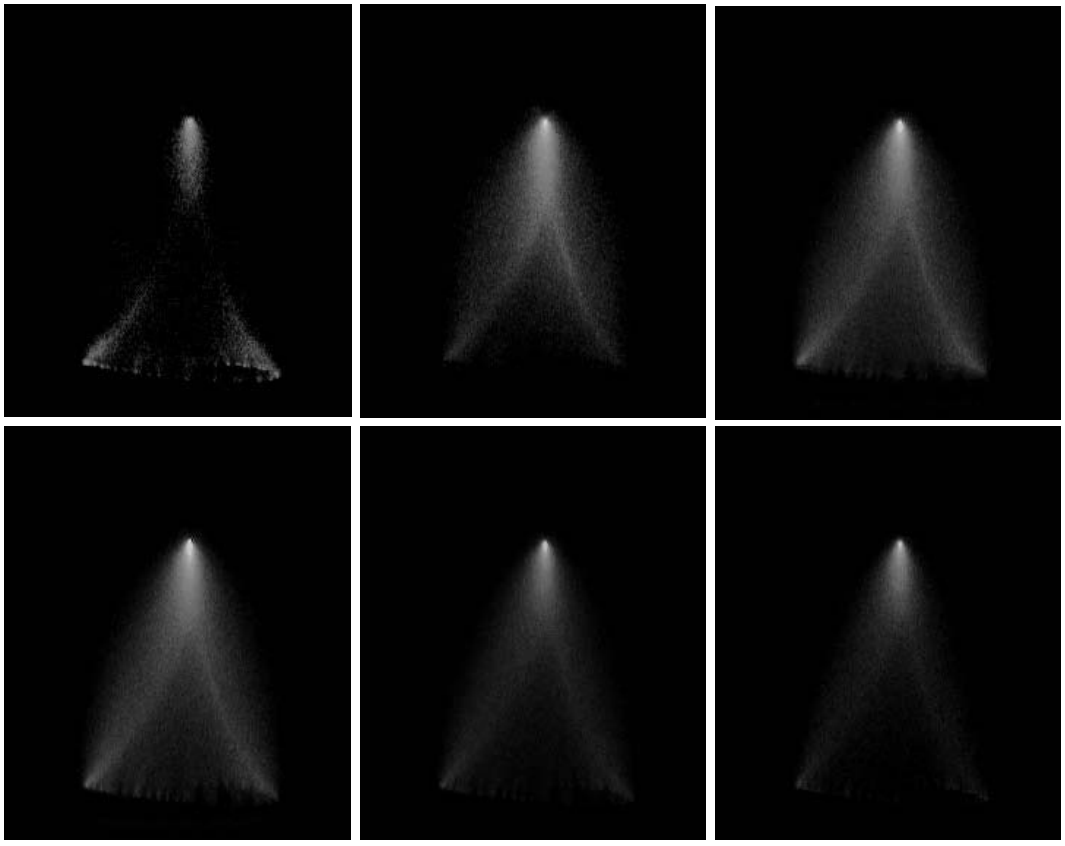

Figure 7: Development of an anode point-to-plane corona discharge in a stoichiometric propane/air mixture (flow velocity < 1 m/s) excited by a 10 kV short-pulse (< 100 ns) @ 1 kHz. Each photo is an accumulation of 500 10-ns exposures and each successive image is delayed by 10 ns. All images were taken through a 10-nm bandpass filter centered at 340 nm (N_2(C-B)). The corona discharge has no observable effect on the flame front (see comparison image below).

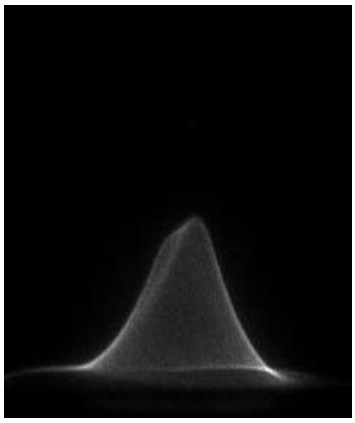

Figure 7a: Comparison image of the flame imaged above without the corona discharge and using a 10-nm bandpass filter centered at 430 nm (CH(A-X)).

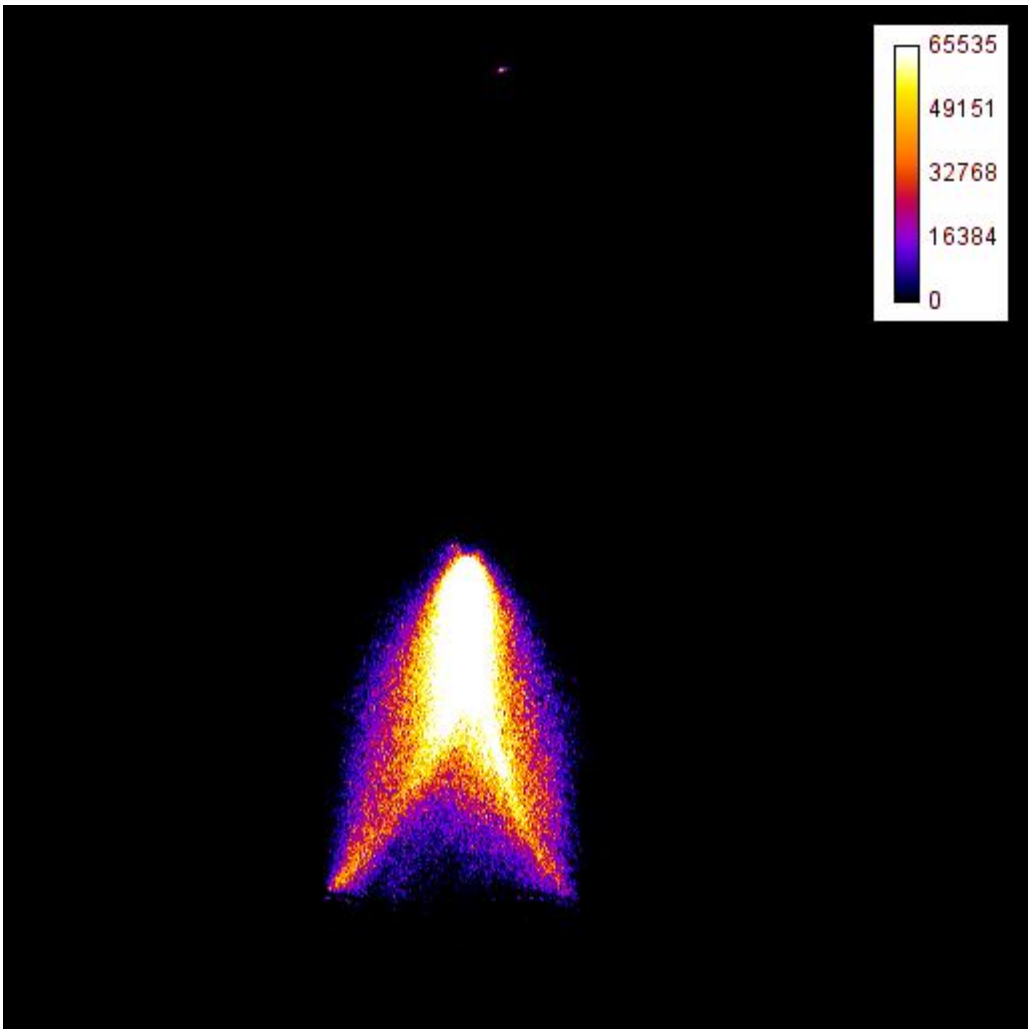

Figure 8: False color image of an anode point-to-plane corona discharge in a stoichiometric propane/air mixture (flow velocity < 1 m/s) excited by a 10 kV short-pulse (< 100 ns) @ 1 kHz. The photo is an accumulation of 500 10-ns exposures and was taken through a 10-nm bandpass filter centered at 340 nm (N_2(C-B)). Although the corona discharge has no observable effect on the flame front, the resulting intensity distribution suggests possible application of such discharges to the imaging of gas density distributions in high speed flows.

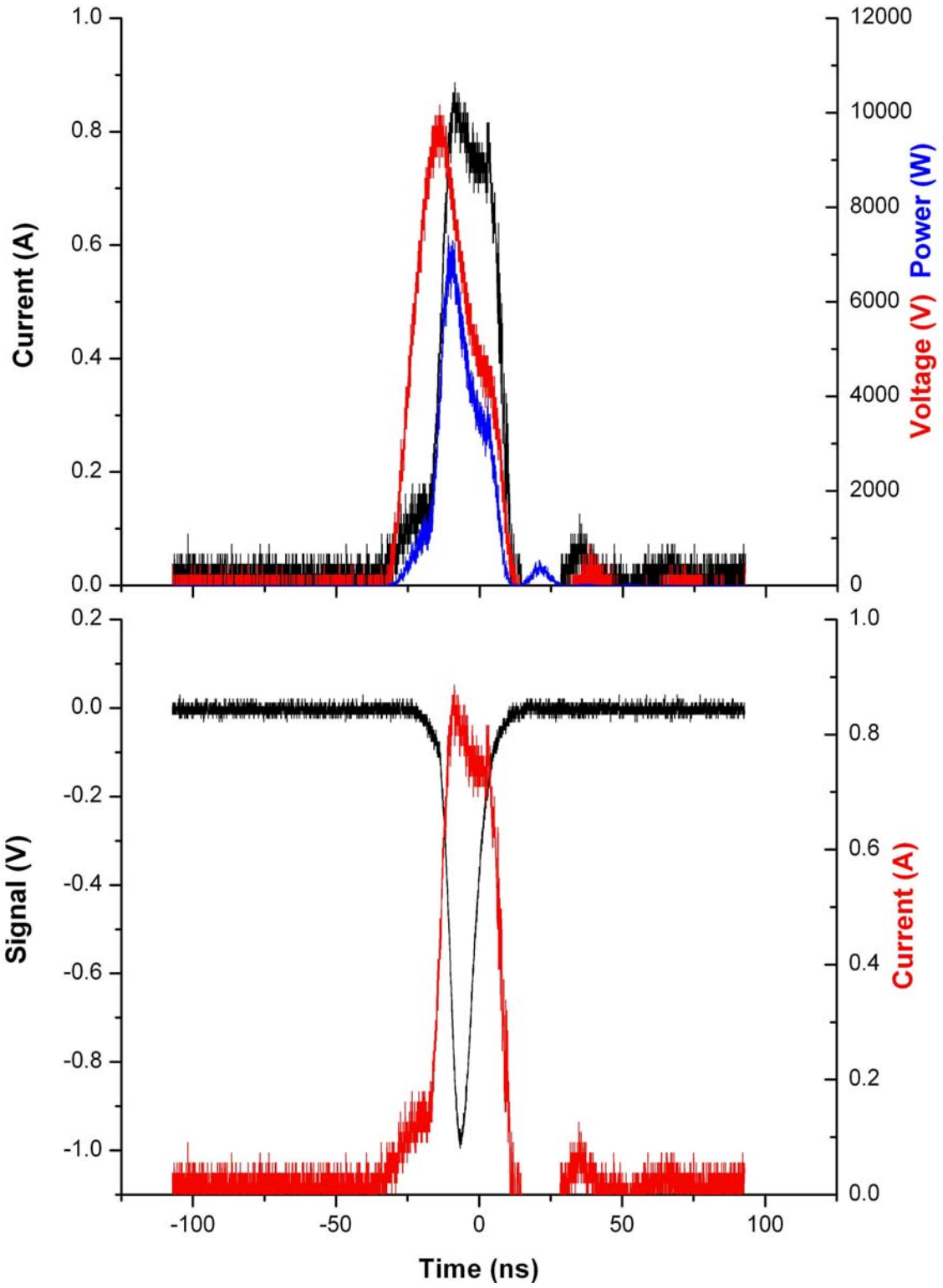

Figure 9: Current/voltage/power characteristics (top) for the pulsed anode point-to-plane corona discharge used to produce the images contained in the previous 3 figures. Typical time resolved emission from the discharge from N_2(C-B) emission at 337 nm is shown with a discharge current pulse in the lower plot.

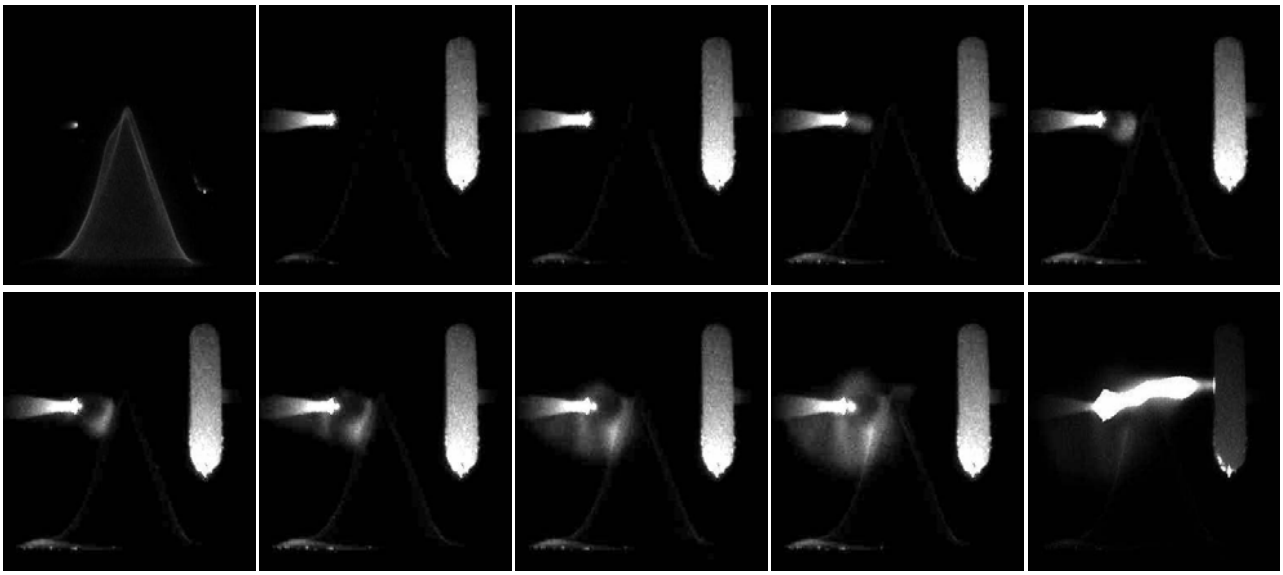

Figure 10: Images of a transverse anode point-to-plane corona discharge into a stoichiometric propane/air mixture (flow velocity < 1 m/s) excited by high voltage, short-pulse (< 100 ns) discharge @ 500 Hz. The top left comparison image was taken through a 10 nm bandpass filter centered at 430 nm (CH(A-X)) with the discharge off. Each subsequent photo is an accumulation of 400, 100-ns exposures imaged through a long pass filter (400 nm cutoff). They are arranged in order of increasing discharge voltage in 1 kV steps (1 through 9 kV). The corona discharge has no observable effect on the flame front using this discharge geometry.

Air Force Summer Faculty Fellowship Program Final Report
Summer 2007

AN ENERGY-BASED FATIGUE LIFE ESTIMATION METHOD FOR COMMON GAS TURBINE ENGINE MATERIALS

by

Onome Scott-Emuakpor, Graduate Student
Department of Mechanical Engineering
The Ohio State University
206 W. 18th Ave.
Columbus, Ohio 43210

Host Adviser:
Dr. Charles Cross
Turbine Engine Division
Propulsion Directorate
Air Force Research Laboratory
1950 Fifth Street, Bldg. 18
Wright-Patterson AFB, OH 45433-7251

Tenure: [June 4, 2007] to [July 31, 2007]

Submitted [September 17, 2007] to:
Universal Technology Corporation
Roger Rucker

ABSTRACT

An energy-based method for predicting fatigue life of half-circle notched specimens, based on the nominal stress amplitude, has been developed. The developed method is based on the understanding that the total strain energy dissipated during a monotonic fracture and a cyclic process is the same material property, where the density of each can be determined by measuring the area underneath the monotonic true stress-strain curve and the area within a hysteresis loop, respectively [1]. Using this understanding, the criterion for determining fatigue life prediction of half-circle notched components is constructed by incorporating the stress gradient effect through the notch root cross-section. The validation of this method is carried out by comparison with both notched and unnotched experimental fatigue life of Aluminum 6061-T6 specimens under tension/compression loading at the theoretical notch fatigue stress concentration factors of 1.75 and 1.975. The comparison shows encouraging agreement, thus validating the capability of the framework to produce accurate fatigue life predictions of half-circle notched components.

1. INTRODUCTION:

One of the many reasons for catastrophic failure in commercial and military aircrafts is due to foreign object damage (FOD) in gas turbine engines. FOD is defined as the premature fatigue damage to aircraft engines due to the increased stress concentration from the intake of debris in the surrounding environment. There are several different methods to account for stress concentration in components of aircraft engines, such as shot peening, fracture mechanics of cracks, and a prestraining method that induces

residual stress [2,3]. However, several design and experimental procedures regarding FOD shows that it is better to model the stress concentration as a notch [4].

The stress concentration factor used during notch evaluation is K_t. The factor K_t is defined as the theoretical elastic stress concentration factor, which for the case of notches is the ratio of actual maximum local stress versus the nominal stress at the net cross-section of the specimen [5]. K_t, however, is only applicable to static loading. In order to account for cases involving fatigue, the stress concentration factor K_f is used. K_f is defined as the ratio of the fatigue life of an unnotched member versus the fatigue life of the notched version of the same member [5]. Unlike the factor K_t, K_f for High Cycle Fatigue (HCF) is a function of the material under analysis [5]. The material influence is accounted for by the incorporation of the notch sensitivity index (q), which is used in the correlation between K_f and K_t. With the use of Equation 1 and several theoretical references on geometry and notch sizes, each stress concentration factor can be determined with good precision.

$$K_f = q(K_t - 1) + 1 \qquad (1)$$

Despite the theoretical stress concentration knowledge, there still doesn't exist, a method for predicting the fatigue life of notched components based on the nominal amplitude stress. This conclusion has led to the analysis of strain energy gradient at the notch root of components under cyclic loading.

APPENDIX D

Though there are some well-publicized design rules that make use of stress gradient at the notch root of components to predict fatigue stress, these rules fall short of the goal to predict the fatigue life based on nominal stress amplitude and the effect of the total strain energy through the net cross-section. In order to correlate strain energy gradient to the nominal stress amplitude during cyclic loading, an understanding of the connection between strain energy and fracture/fatigue mechanics is essential.

Curiosity of the correlation between energy and fracture/fatigue can be dated back as early as the 1920's [6]. However, in the 1940's and 50's, a number of well-publicized attempts to relate strain energy per cycle to the number of cycles for failure were considered and initially resulted in minimal success [7]. However, success in this area was later achieved by introducing the hypothesis that implied; under cyclic loading there exists a critical energy value for which failure occurs [8]. This hypothesis was later justified by displaying agreement between the theoretical and the experimental results on an S-N curve. Further investigation of the assumption made in [8] led to the introduction of a more sufficient correlation between the fatigue life of a material and the strain energy dissipation during the fatigue process. It has been suggested that the strain energy required to fracture a material monotonically is the same as the strain energy accumulated during a cyclic fatigue procedure [7,9]. Thus, the critical energy value for each material is the monotonic strain energy. Based on this understanding, an improved energy-based criterion has been developed to allow one to systematically determine uniaxial fatigue life based on the amount of energy loss per fatigue cycle [1]. This previously developed energy-based theory shows the capability of accurately predicting uniaxial fatigue life of

Aluminum 6061-T6 specimens. Therefore, in order to extend the theory to the case of notch fatigue assessment, the incorporation of the stress gradient at the notch root in the energy-based criterion is required along with an effective cyclic stress expression.

2. PREVIOUS RESEARCH SCOPE

Though several energy-based methods for predicting tension/compression fatigue life have been developed [7,9], an improved energy-based criterion for tension/compression with the capability to easily incorporate the effects of stress gradient on fatigue life was essential for the future possibility of developing a general prediction criterion to address fatigue in the bending case. This improved energy-based criterion was developed from the stress-strain representation of the monotonic (Equation 1 & 2) and cyclic (Equation 3) loading behavior shown in the following equations, where Equation 1 and 2 represent the stress-strain relation prior to and after the necking phenomenon, respectively [1,9].

$$\varepsilon = \frac{\sigma}{E} + \varepsilon_o \sinh\left(\frac{\sigma}{\sigma_o}\right) \quad (1)$$

$$\sigma = \beta_1 \varepsilon + \beta_o \quad (2)$$

$$\varepsilon_{cycle} = \frac{\sigma_{pp}}{E} + \frac{1}{C}\sinh\left(\frac{\sigma_{pp}}{\sigma_c}\right) \quad (3)$$

The parameters displayed are defined as follows: σ is the value for stress at the surface of the specimen (in the bending case, max stress), ε is the strain corresponding to the stress σ, β_1 & β_o are the respective slope and intercept of the stress-strain relationship in the necking region (From ultimate tensile to point of fracture), σ_{pp} is the generalized stress value corresponding to the generalized cyclic strain ε_{cycle} (i.e. the minimum fully reversed point is observed as the origin), E is the modulus of elasticity, and the variables σ_c, σ_o, ε_o,

and C are curve fit parameters [1]. These curve fit parameters for the cyclic and monotonic representations (Equation 1-3) are statistically acquired by comparison between low cycle experimental results and experimental monotonic results, respectively [1].

Fatigue life is systematically determined for the improved criterion by taking the total monotonic strain energy density and dividing it by the strain energy density for one cycle. The total strain energy dissipated during a monotonic process is determined as the area underneath the curve constructed by Equations 1 & 2 and the strain energy density for one cycle is represented by the area within the hysteresis loop formed by Equation 3. Therefore, the expression of the improved criterion for systematically determining fatigue life at a specified stress amplitude level (σ) is given as Equation 4 [1].

$$N = C\frac{\sigma_n\left(\varepsilon_n - \frac{\sigma_n}{2E}\right) - \varepsilon_o\sigma_o\left[\cosh\left(\frac{\sigma_n}{\sigma_o}\right) - 1\right] + \frac{\beta_1}{2}\left(\varepsilon_f^2 - \varepsilon_n^2\right) + \beta_o\left(\varepsilon_f - \varepsilon_n\right)}{2\sigma_c\left\{\frac{\sigma}{\sigma_c}\sinh\left(\frac{2\sigma}{\sigma_c}\right) - \left[\cosh\left(\frac{2\sigma}{\sigma_c}\right) - 1\right]\right\}} \qquad (4)$$

Where σ_n is the necking stress, ε_f is the facture strain, and ε_n is the necking strain. The results from Equation 4 are compared to previously acquired fully-reversed axial test results and the corresponding linear regression curve on the S-N plot of Figure 5. The comparison shows that the criterion provides good life estimations for tension/compression fatigue results. To further validate the accuracy of the comparison, strain energy density per cycle is calculated from low cycle experimental results and matched with the experimental linear regression cycles to failure. These results are then compared with the energy-based predicted cyclic strain energy density and the related cycles to failure, which are all displayed in Figure 6. It has been previously presented

that the logarithmic slop of this comparison is roughly -0.6 [10]. Though the experimental results of Figure 6 concur with this belief, further analysis of the cyclic strain energy density calculation method is conducted to provide reasoning for this agreement. Conclusion of this analysis shows that the variation between experimental and analytical results is more obvious in test data with a higher standard deviation of the hysteresis loop curve fit constructed by Equation 3. Due to a more sensitive stress-strain comparison, minor changes in the standard deviation of the curve fit causes major variation in strain energy density calculation. Based on this sensitivity issue, the cyclic curve fit parameters that provided minimal standard deviation where used in Equation 4 for prediction-experimental comparison. This comparison, as stated, validated the encouraging output of the criterion. Therefore, the chosen cyclic curve fit parameter provides an assuring comparison between the experimental results and the predicted curve.

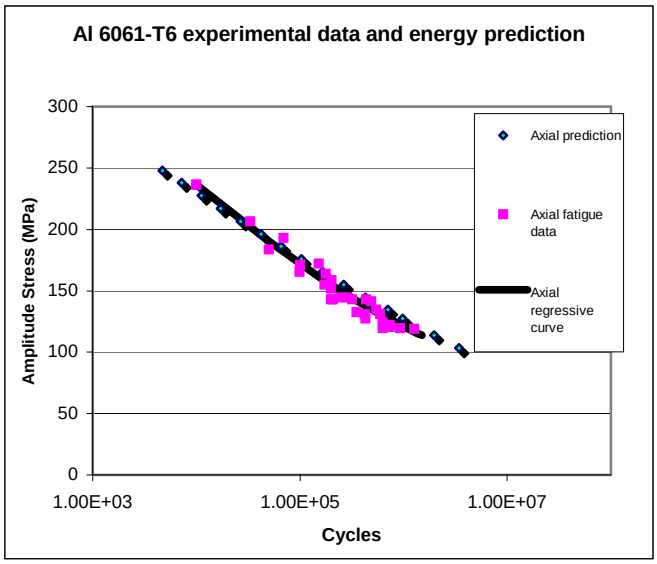

Figure 5. Comparison of prediction and experimental results [1]

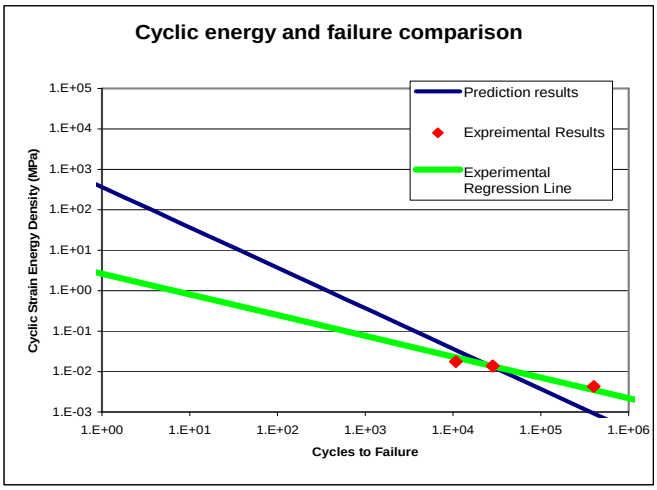

Figure 6. Cyclic strain energy versus cycles to failure plot

TASK #1: INCORPORATION OF ENERGY-BASED METHODOLOGY TO CONVENTIONAL ENERGY DISTORTION THEORY

Fatigue prediction analysis for multi-axially loaded structures is a tumultuous task. In fact, there is no fatigue life calculation technique that can be directly applied to a multi-axial fatigue analysis without simplification of the total stresses acting on the multiple axes. The most popular simplified multi-axial fatigue life calculation method is the equivalent stress analysis [5]. This particular analysis is conducted by studying the 3-D stresses on an infinitesimal element from the fatigue zone under observation, followed by the use of von Mises stress and the Goodman diagram relation to determine a single equivalent stress value [5]. This process, however, cannot be adopted by the constitutive stress-strain law of Equation 3; due to the unconventional incorporation of plastic effect. Therefore, the Distortion Energy Theory is observed with the assumption that the displacements are functions of nonlinear external loads.

The distortion energy theory is based on the understanding that the total strain energy is stored in two parts: (1) energy from the change in volume, and (2) energy from the change in shape [5]. Equation 11 and Figure 7 displays the expression and illustration for this understanding, respectively.

$$U_T = U_v + U_D \tag{11}$$

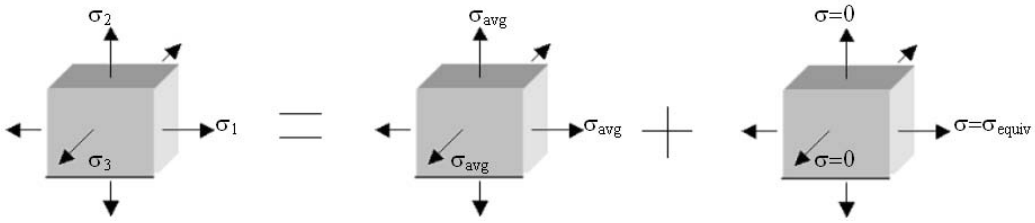

Figure 7. Energy distortion theory for equivalent stress analysis

The parameters for Equation 11 are defined as follows: U_T is the total strain energy, U_v is the strain energy of the change in volume, and U_D is the strain energy for the change in shape. The strain energy of the change in volume (Uv) is better known as strain energy caused by hydrostatic stress. The effect of this stress is an even volumetric expansion of the infinitesimal element under observation on all sides. Therefore during one cycle of a cyclic loading procedure, the hydrostatic stress returns to zero and the corresponding strain energy (Uv) becomes zero. This minimizes Equation 11 to Equation 12 and shows that the total energy within a hysteresis loop is purely distortion energy.

$$U_T = U_D \tag{12}$$

Furthermore, if it can be justified that the total monotonic strain energy density of an infinitesimal element subjected to multi-axial loading is the summation of the six areas under the curves formed by the respective stress-strain relationships, it can then be implied that the total strain energy density in one multi-axial cycle is the summation of the directional (3 for principle-axes and 6 for Cartesian-axes) hysteresis loops acting on an infinitesimal element as well. Therefore to acquire an equivalent stress value from Equation 11, this implication is displayed for principle axes only by Equation 13; where ε_E & ε_i are functions of stress. These functions are further shown in their trigonometric and exponential form by Equation 14 and 15 respectively: where $\sigma_{pp,E}$ & $\sigma_{PP,i}$ are the generalized stress values corresponding to the generalized cyclic strains ε_E and ei (i.e. the minimum fully reversed point is observed as the origin), and i denotes the principle direction, which are values from 1-3.

$$\sigma_{PP,E}\varepsilon_E - 2\int_0^{\sigma_{PP,E}} \varepsilon_E d\sigma_{PP,E} = \sum_{i=1}^{3} \sigma_{PP,i}\varepsilon_i - 2\int_0^{\sigma_{PP,i}} \varepsilon_i d\sigma_{PP,i} \tag{13}$$

$$\frac{\sigma_{PP,E}}{C}\sinh\left(\frac{\sigma_{PP,E}}{\sigma_c}\right) - \frac{\sigma_c}{C}\int_0^{\sigma_{PP,E}} \sinh\left(\frac{\sigma_{PP,E}}{\sigma_c}\right) d\sigma_{PP,E} = \sum_{i=1}^{3} \frac{\sigma_{PP,i}}{C}\sinh\left(\frac{\sigma_{PP,i}}{\sigma_c}\right) - \sum_{i=1}^{3}\int_0^{\sigma_{PP,i}} \sinh\left(\frac{\sigma_{PP,i}}{\sigma_c}\right) d\sigma_{PP,i} \tag{14}$$

$$e^{\frac{2\sigma_E}{\sigma_c}} + e^{-\frac{2\sigma_E}{\sigma_c}} + 1 = \sum_{i=1}^{3}\left(e^{\frac{2\sigma_i}{\sigma_c}} + e^{-\frac{2\sigma_i}{\sigma_c}} + 1\right) \tag{15}$$

Between the process of acquiring Equations 14 & 15 from Equation 13, some simplifications where made based on cancellation from the solving process and scientific assumptions. First, since the effect of poisson's ratio is used in defining the experimental stress acting on an observed fatigue zone, it is not carried over to any of the energy-based calculations. Furthermore, proceeding evaluation of Equation 13, the expression for Equation 14 was solved and further validates the belief previously stating that hydrostatic stress is eliminated from total strain energy density calculation. To simplify this expression for use in determination of equivalent stress, the summation of the integrated expression on the right side of Equation 14 is assumed to be equal to the integrated portion of the equivalent stress calculation on the left side. Therefore, following integration of both sides and replacing hyperbolic trigonometry with exponential functions, the expression in Equation 15 is acquired.

Upon further analysis of Equation 15, two assumptions are made: (1) the numerical portion has a minimal effect in the equation, and the exponential functions of similar signs on both sides of the equation are equivalent. In other words, Equation 16 is assumed to be a true expression. Therefore the resulting expression for calculating an effective cyclic multi-axial stress using the energy-based methodology is displayed by Equaiton 17.

$$e^{\frac{2\sigma_E}{\sigma_c}} = \sum_{i=1}^{3} e^{\frac{2\sigma_i}{\sigma_c}} \tag{16}$$

$$\sigma_E = \frac{\sigma_c}{2} \ln\left(\sum_{i=1}^{3} e^{\frac{2\sigma_i}{\sigma_c}} \right) \tag{17}$$

REFERENCE

[1] Scott-Emuakpor, O., Shen, M.-H. H., Cross, C., Calcaterra, J., and George, T., "Development of an Improved High Cycle Fatigue Criterion," 2007, Journal of Engineering for Gas Turbines and Power, Vol. 129, Issue 1, pp. 162-169.

[2] George, T., Shen, M.-H. H., Scott-Emuakpor, O., Nicholas, T., Cross, C., and Calcaterra, J., "Goodman Diagram via Vibration-Based Fatigue Testing," 2005, Journal of Engineering Materials and Technology, Vol. 127, Issue 1, pp. 58-64.

[3] Scott-Emuakpor, O., **"**Development of an Improved Energy-Based Criterion for Fatigue Life Assessment", Thesis (M.S.), The Ohio State University, 2004.

[4] Lanning, D., Nicholas, T., and Haritos, G., "Effect of Plastic Prestrain on High Cycle Fatigue of Ti-6Al-4V," International Journal of Fatigue 2002; 34: 127-134.

[5] Collins, J., *Mechanical Design of Machine Elements and Machines*, John Wiley & Sons, Inc, 2003.

[6] Jasper TM, "The Value of the Energy Relation in the Testing of Ferrous Metals at Varying Ranges of Stress and at Intermediate and High Temperatures," Philosophical Magazine, Series. 6, Oct. 1923; 46: 609-627.

[7] Feltner, C. E., and Morrow, J. D., 1960, "Microplastic Strain Hysteresis Energy as a Criterion for Fatigue Facture," ASME Paper No. 60-MET-2.

[8] Enomoto, N., 1955, "On Fatigue Tests Under Progressive Stress," ASTM, Vol. 55, pp. 903.

[9] Stowell, E., 1966, "A Study of the Energy Criterion for Fatigue," Nuclear Engineering and Design, pp. 32-40.

[10] Garud, YS, "A New Approach to the Evaluation of Fatigue Under Multiaxial Loading," *Proceeding of Symposium on Methods for Predicting Material Life in Fatigue*, ASME, New York, 1979; 247-264.

Summer 2007 Final Report

Physics of Electric Discharge

During the summer of 2007, I was stationed in building 450 in Area B at Wright-Patterson Air Force Base in the Dayton, Ohio area. While on base, I assisted Dr. Charles DeJoseph, Jr. and Dr. Vladimir Demidov with research involving pulsed systems. The pulsed systems involved using mixtures of Argon/Oxygen gas as well as pure Argon within the Base vacuum chamber. This pulsed system was important in our experiment to find out ways to control different plasma parameters in the afterglow of the pulsed discharge. The afterglow occurred during the shut-off period of the Radio-Frequency Pulse system. During the pulse, RF signals excited the electrons which in turn produced an Inductively Coupled Plasma inside the Discharge Chamber of the experimental apparatus. We were able to affect the density of electrons produced during the afterglow by altering the pulse length of the RF-signal before shut-off.

In order to affect the afterglow, we used the three-level model which is used for inert gases. The three-level model describes the build-up of electrons in the system as they go through the metastable level as well as through ionization. Through calculations and experiments, we were able to recognize that the metastable atoms produced through Argon/Oxygen plasma would follow the three-level model, building up the metastable atom density at a slower rate in comparison to an inert gas three-level system.

By changing the pulse length of the discharge, the Argon/Oxygen metastable rate would be affected (increasing or decreasing) allowing us to affect the plasma density of the afterglow and control a plasma parameter.

This research is currently still under development and will be presented at both the October 2007 Gaseous Electronics Conference (GEC) in Arlington, VA as well as the American Physics Society Plasma Conference in November 2007 in Orlando, Florida.

Jon C. Blessington
WVU Graduate Student
9-4-2007

Modeling spall growth in ball bearing raceways

Final Report

Nathan Branch

George Levesque

University of Florida graduate students

Propulsion Directorate

Air Force Research Labs

Wright Patterson Air Force Base

Dayton, Ohio

Summer 2007

Background

Bearings in military jet aircraft engines can support relatively large loads and high rotating speeds. Due to this, the surfaces of the bearing's ball and raceway experience a large number of loading cycles. The consequence of this large number of loading cycles is called fatigue. Fatigue failure is the dominant source of engine failure for this type of engineering application.

As the balls and bearing raceway are rolling relative to one another, large subsurface shear stresses are experienced just below the point of contact. Repeated loading of this shear stress leads to the initiation of subsurface fatigue cracks. After further loading these fatigue cracks tend to grow towards the surface forming a pit or crater. These pits and craters are termed "spalls." Fatigue cracks can also be initiated by foreign particles that get pinched between the ball and raceway. These particles can leave an indention on the raceway which acts as a stress riser.

unspalled raceway

one spall

grown spall

Spalls are a common failure mode in bearings. Spalls can cause excessive vibrations, excess heat generation, and higher loads on balls. Vibrations cause erratic loading conditions in the bearing. Excess heat leads to undesired higher operating temperatures in engine components. When one or multiple balls are unsupported by the spall's void, the other balls experience higher loads. All of these consequences lead to catastrophic failure of the bearing and loss of engine and aircraft. Worse still, spalling is a relatively unpredictable phenomenon with dire consequences.

Many different design issues are used to prevent spalls. The bearing geometry, applied loads, type of material, and time of operation are controlled to try to prevent the formation and propagation of spalls. Due to the ever increasing demands of aircraft technology, bearings are desired to endure very high thrust loads and function properly

for an infinite amount of time. To achieve this, the designer is only left with direct control over the material selection and the geometry of the bearing.

This summer's research will be entirely focused on spalls that occur in the bearing raceway and not the ball. Different raceway materials cause different characteristics of spalls. The spall's depth, size, texture, and growth rate are heavily dependent on the raceway's material type. Designers have to optimize the material properties in order to reduce the severity of the spalls. This project will be devoted to how raceway material type affects the propagation of spalls.

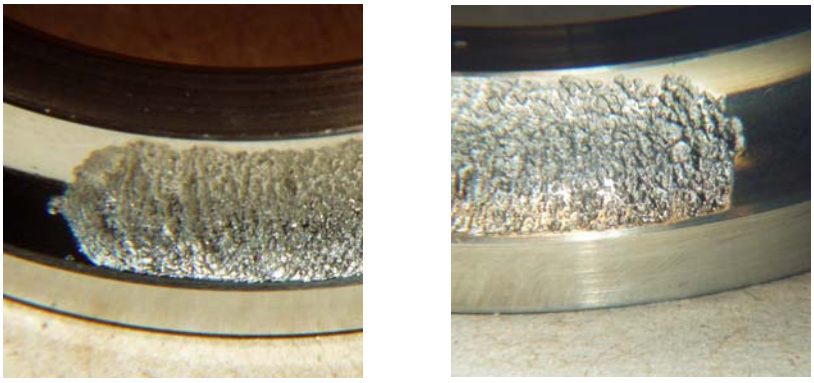

Spall size and texture dependent on material of raceway; left: M50; right M50NiL

Ongoing Research

Spall research is being done at the Air Force Research Labs located in the Wright Patterson Air Force base in Dayton, Ohio. Numerous test rigs have been designed and implemented to study the factors that control spall formation and propagation. These test rigs allow the designer to control the applied thrust load and bearing raceway material. Various instrumentation alerts the engineer when a spall has formed and the rate of spall growth can be recorded.

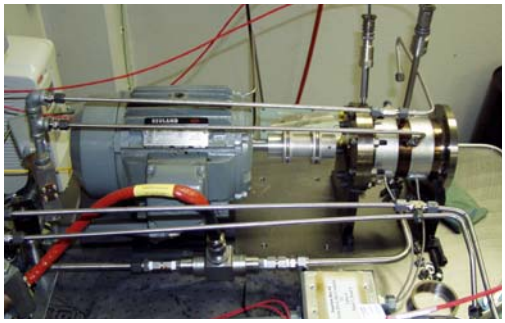

Experimental test rig

In order to reduce the amount of experimental time, spalls are artificially initiated. They are initiated by Rockwell C indentions purposefully placed on the raceway. These indentions behave as stress risers and fatigue crack initiation sites. The balls used in these test are ceramic, silicon nitride balls. These balls are much harder and have a higher elastic modulus than the steel raceways under study. The occurrence of spalls on the ceramic balls *in this test* is extremely rare.

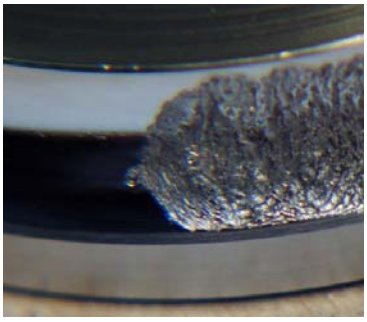

Spall initiated from Rockwell C indention

The two raceway materials to be studied this summer are M50 steel and M50 NiL steel. M50 steel is a very hard material with a relatively low fracture toughness. M50 NiL steel conversely has a low hardness but a high fracture toughness. To compensate for this design discrepancy the M50 NiL steel is case carburized to increase the hardness of the surface that interacts with the ball. The benefit of this is that a case hardened M50 NiL material has the same hardness as regular M50, plus a higher fracture toughness below the case hardened layer.

This does raise one problem. No one is sure what the fracture toughness is for the case carburized layer of M50 NiL. In M50 NiL, spalls are formed and propagated entirely within the case carburized layer. Since the fracture toughness of this region is unknown, spall growth analysis cannot be completed. Determining this mystery fracture toughness was not the goal of this summer's work.

				Fracture
		Hardness		**Toughness**
Material		HRC	Position	MPa√m
M50		60-64	Through	19.78 – 21.97
M50 NiL		60-64	Within Case	**?**
		46	Below Case	54.94 - 57.14
ASTM E399				

Goals of summer work

The purpose of our summer internship is to research ways to predict spall growth characteristics using computer models. This summer, ABAQUS finite element analysis software and Franc3Dng crack growth software were both used as tools to analyze this problem. Computer software allows the designer to vary different aspects of design, and see how it affects the results of the analysis without having to implement time consuming experiments.

The goals of this summer's work were to model contact stresses for a ball near or on a spall, find the critical stress location around a spall where a fatigue crack is likely to initiate, build a computer model that can grow a spall subjected to rolling contact fatigue, predict different spall characteristics by varying material properties and residual stresses, and finally to automate the entire process to reduce the amount of work required per analysis.

Details of computer software

ABAQUS is a finite element analysis software that will be calculating the stress and displacement parameters of our computer models. Franc3Dng will grow the crack a calculated amount in a determined direction. Franc3Dng also remeshes the model after crack growth.

Franc3Dng (also called "Franc") is a three dimensional crack growth software developed by the Cornell University Fracture Group. Franc was once compatible solely with ANSYS FEA software, but is now compatible also with ABAQUS. Franc is not a predefined crack path software. Crack insertion and remeshing, once tedious and difficult to do in ABAQUS, is very user-friendly to do in Franc.

Crack growth direction is determined by specified planer extension, the maximum stress criterion, or the maximum strain energy release rate criterion. Crack extension is calculated by da/dn vs ΔK data, Paris Law constants, or a user specified amount. Calculations to find stress intensity factors (SIF's) are done by a computer algorithm called the M-Integral.

Submodeling in ABAQUS

Submodeling is a technique in ABAQUS that allows the modeler to greatly reduce the run time and memory of a finite element model. Certain locations on a smaller, submodel can be specified to imitate the behavior of other certain locations in the larger, "global" model. For this application, a submodel is the region around a spall where the fatigue crack has been initiated and where it will grow.

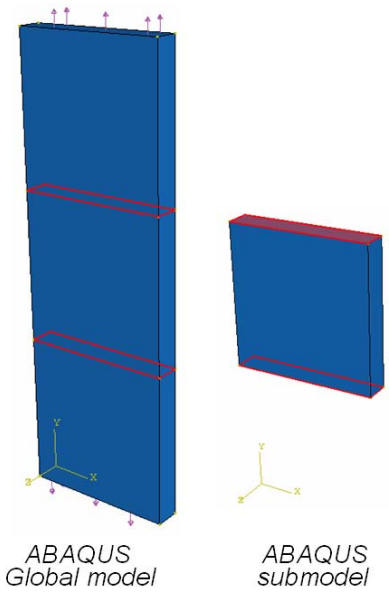

Top and bottom faces reference highlighted faces in global model;
Submodel behaves just like middle region in global model

Verifying Franc and ABAQUS

Before one can begin a full analysis of spall growth, the tools used must be verified and checked for accuracy for simple cases. The most relevant test case explored this summer was the crack growth of an angled crack in a biaxial stress state. The solution to this problem was verified three different ways by using an analytical approach, fracture analysis in ABAQUS, and finally calculations done by Franc.

The 3D computer model was a 6 x 6 x 0.5 inch steel block subjected to a 100 psi stress on the top and bottom sides, and a 75 psi stress on the right and left sides. The specimen has a center crack that is angled at 45 degrees from the horizontal. The stress intensity factors and crack turning angles calculated are represented in the picture below.

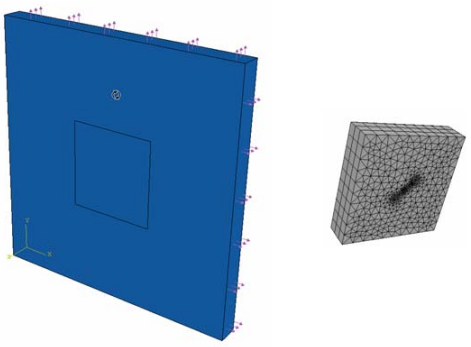

global model *submodel remeshed by Franc*

ABAQUS	K1=79.5;	K2=10.9;	α= -15 deg
Franc	K1=72.6;	K2=10.8;	α= -16.4
Analytical	K1=77.8;	K2=11.1;	α= -16
K(psi√in)			

Three methods verify same crack turning properties in biaxial stress state

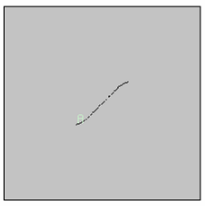

Grown crack in FRANC

This experiment verifies that crack growth calculations done by Franc with submodeling in ABAQUS are accurate for simple cases.

Current computer models

Our computer models accurately recreate the interaction between a ball bearing and its raceway. This interaction is better described as the magnitude and distribution of contact stresses between the bodies. This distribution of stresses is termed the "contact patch." The magnitude and distribution of contact stresses can be determined by analytical approaches and also through calculations by ABAQUS.

To simplify the finite element model, a portion of the curved raceway will be modeled as a flat block. If a ball bearing were to indent this flat block, a different magnitude and distribution of contact stresses would result. In order to preserve the same contact patch size and magnitude, a different indenter other than the ball must be designed and used.

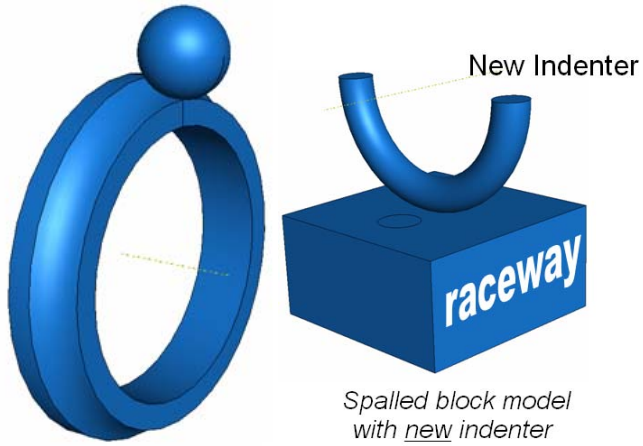

Spalled block model with new indenter

This new indenter is deemed to be analytically rigid in ABAQUS. Since it is analytically rigid it will not deform regardless of the load applied to it. Thus there is no need to assign material properties or a mesh to the indenter. This rigid nature simulates a rigid silicon nitride ball on a steel raceway. Better contact solutions are obtained in ABAQUS when this rigid indenter is used.

In general the finite element mesh should be finer where the ball will contact the raceway and around the spall. Any spall size can be modeled. For the current models, the spall is assumed to be as big as the contact patch. The current contact patch dimensions for a 350 ksi maximum contact stress are 2.64 mm by 0.35 mm. It is also important to note that hexahedral elements give better results than tetrahedral elements.

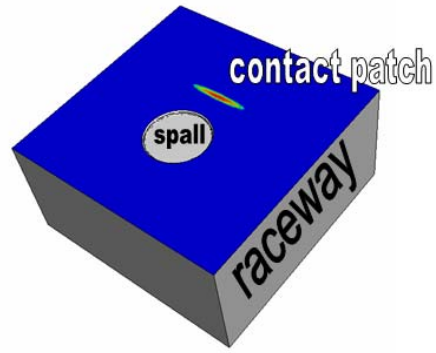

Contact pressure

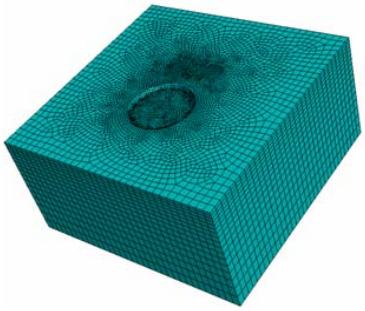

"Hex" model

This analysis is assumed to be static and elastic. In reality there are dynamic effects of the ball hitting the edge of spall. This may not be captured by this current model. There are also plasticity effects of the material that are not accounted for in this model.

Although fatigue crack initiation is not the primary issue regarding this analysis, an initial fatigue crack must be put somewhere in order to grow a spall. There are many such theories that try to predict how and where a fatigue crack would start. For our purposes we will look at various critical points around the edge of the spall where the stresses appear to be high. From there we will look at the imaginary planes that pass through these points to find the worse combination of shear and tensile stresses on a per plane basis. The location of the point and the critical orientation of the plane will indicate where a fatigue crack will likely initiate.

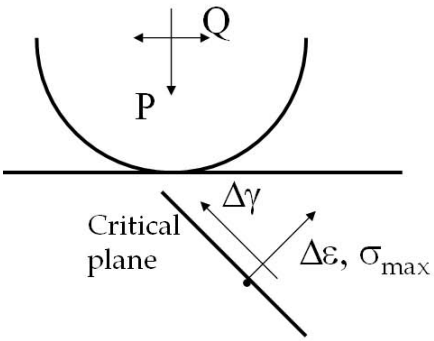

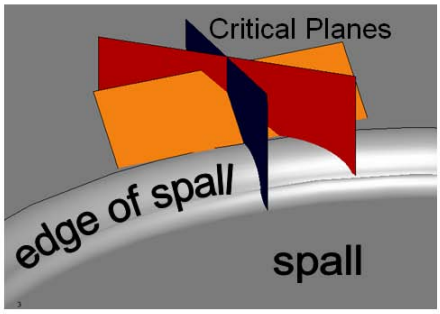

Process for growing a spall

Even though there was not enough time this summer to actually grow a spall, a process to grow a spall was developed. This process was verified to work accurately for simple test cases. The process is as follows:

1. create the ball on block model in ABAQUS (“global model”)
2. create the submodel, where the crack will initiate and grow
3. send the submodel to Franc for crack insertion and remeshing
4. send this newly meshed submodel back to ABAQUS for analysis
5. in ABAQUS, assign submodel boundary conditions and run job
6. send the file containing the nodal displacements back to Franc
7. Franc uses the original and displaced nodal positions to calculate SIF’s
8. in Franc, grow crack one increment and remesh
9. repeat steps 4 through 9 until spall occurs

Model information is sent back and forth between ABAQUS and Franc in the form of an inp file. Inp files contain information of the geometry and material properties

of the material. Every time the geometry is changed, i.e. the crack grows one increment, a new inp file has to be created. The nodal displacements are stored in the fil file. A fdb file is created when a newly cracked and remeshed block is saved in Franc. To calculate the stress intensity factors the fdb file and fil file must be opened together for a specific model.

Problems encountered in Franc and ABAQUS

No software is perfect and some idiosyncrasies cannot be avoided or have to be corrected in order to make sufficient progress. For instance, submodel boundary conditions are not retained in the file transfer between ABAQUS and Franc. The contact interaction defined by Franc is not complete by ABAQUS's standards. The contact definition is not assigned correctly by ABAQUS as seen by the direction of the unit normal vectors at the crack tip. When model surfaces are remeshed by ABAQUS, the corresponding set name is deleted. "Encastre" boundary conditions defined in ABAQUS are not fully carried over after the file transfer with Franc. Any user specified Step type and name is mistakenly changed by Franc.

The aforementioned problems can be corrected by the respective software's distributor. As of now python scripts are being created to fix all of these issues on a per model basis.

Future Work

Future work includes automating the crack growth process between ABAQUS and Franc. Residual stresses and the case hardened layer will be modeled as well as surface traction effects on crack turning. Nonplanar crack insertion and growth is a long term goal of this project. A dynamic model will also be built in order to better capture the physics of the problem.

Conclusion

This summer George Levesque and Nathan Branch mastered submodeling in ABAQUS, learned the new software Franc, verified Franc's accuracy and capabilities, modeled contact stresses near a spall, and developed a process for growing a spall.

MFL-KAS-07-02

DOUBLE-PULSED DIGITAL HOLOGRAPHIC DIAGNOSTICS FOR AERATED LIQUID JETS IN CROSSFLOW

By

D. Olinger, J. Lee, and K.A. Sallam

College of Engineering, Architecture and Technology
School of Mechanical and Aerospace Engineering
Oklahoma State University
Stillwater, Oklahoma 74078-5016

APPENDIX G

MFL-KAS-07-02

DOUBLE-PULSED DIGITAL HOLOGRAPHIC DIAGNOSTICS FOR AERATED LIQUID JETS IN CROSSFLOW

By

D. Olinger, J. Lee, and K.A. Sallam

Final Report
1 July 2007 – 3 August 2007

20 December 2007

Award Ref. No. AA-5-19858
Taitech, Inc. for United States Air Force
AMC P.O. Box 33630
Wright-Patterson AFB, OH 45433-0630

Abstract

The breakup of aerated liquid jets in crossflow was investigated by digital holographic microscopy (DHM). The experiments were performed in test cell 18 at Wright-Patterson Air Force Base. Test conditions were as follows: M=0.3 and M=0.6, q=10, GLR=0%, 2%, 4%, and 8%, with water as the test liquid. Holograms were recorded of the jet core and followed the upstream edge of the spray using two frequency doubled YAG lasers were used to illuminate the spray field (Continuum Surelite I, operating at 10Hz, 532 nm wavelength, and nominally 200mJ/pulse). The two lasers were triggered using a Labsmith LC880 pulse generator. The two laser beams expanded with an objective lens, pass directly through the test section of the wind tunnel (windows GE type 124 quartz ground and polished to 80/50 scratch/dig) to the CCD sensor (Redlake EC1600, 4872 x 3248 pixels). Double-pulsed holograms (timed to the two lasers) were captured to enable velocity measurements. Numerical reconstruction of 2048 x 2048 pixels area of the recorded holograms was obtained successfully. Digital holograms of a resolution target were recorded. The results show that the presence of the window affects the background noise but not the resolution.

Acknowledgements

This research was sponsored by Taitech, Inc., of Beavercreek, Ohio, under a subcontract from the Taitech base contract with the Air Force. K.-C. Lin of Taitech, Inc., and C.D. Carter of the Air Force Research Laboratory, Wright-Patterson AFB, Ohio, were fully engaged collaborators in this study. The work was performed in test cell 18 at Wright-Patterson Air Force Base, Ohio. The technical help received from the staff of test cell 18: Paul Kennedy, Steven Enneking, Matt Streby, Dominic Barone, and Bill Terry is gratefully acknowledged.

TABLE OF CONTENTS

I. INTRODUCTION.....6

II. EXPERIMENTAL METHODS 9

III. RESULTS.....14

VI. SUMMARY, CONCLUSIONS AND FUTURE WORK.....21

REFERENCES 23

1. Introduction

1.1 Background and Previous Work

A good understanding of the phenomena of liquid jet breakup is essential for successful design of fuel injection systems. The objective of most injectors is to atomize a liquid jet into a fine spray. Pressure atomizers, such as plain orifice nozzle injector, accomplish this objective by using very small orifice diameter and/or very high injection pressure. In many applications, this solution is not feasible, however, because small orifice diameters tend to get clogged easily and high injection pressure is not always available. Aerated liquid injector (also known as effervescent atomizer), on the other hand, can easily provide dense sprays of fine droplets with low injection pressures and large orifice diameter by mixing liquids and gases inside an injector. These injectors find applications in ramjet engines and scramjets engines of interest to the Air Force. Aerated liquid fuel injection is of interest to the Air Force due to its demonstrated capability to generate large plumes of finely atomized sprays for scramjet engine applications (Lin et al., 2002, 2001, 2000, 1999).

In order to understand how to control the atomization quality of aerated-liquid jets injected into crossflows, it is essential to understand the breakup mechanisms in the near injector region of a spray. Unfortunately, this optically-challenging area is typically opaque for PDA diagnostics (Lee et al., 2002, Trolinger et al., 1969). Traditional film-holography has long been used for 3-D measurements in particle fields such as sprays (Ewan et al., 1980, Ewan et al., 1979, Thompson et al., 1974, Menzel et al., 1970, Trolinger et al., 1969). It has also been successfully used to visualize sprays in supersonic crossflows (Sallam et al., 2006). With the advent of digital holography (Pu et al. 2005, Burke et al., 2003), this technique has become more popular since the need for chemically processing the holographic film has been eliminated. Recently, much work has gone into digital holographic PIV so that the holograms may be recorded and reconstructed digitally (Meng et al., 2004, Pan and Meng, 2002, Hinsch 2002, Bryanston-Cross et al., 1992).

Digital holographic microscopy was proved to be a promising technique at Oklahoma State University; where, aerated liquid jets injected in subsonic crossflows (65 m/s) were probed to obtain drops sizes and velocities at downstream distances of x/d_{inj} = 5, 10, 25 and 50. Miller et al. (2008) have successfully used digital holography to probe the droplets sizes of aerated liquid jet in crossflow at downstream distances between $x/d_0 = 25$ and $x/d_0 = 50$ using single laser beam. They used two methods which are digital inline holography (DIH) and digital holographic microscopy (DHM) (also known as digital microscopy holography), and demonstrated that two methods are suitable for measuring the properties of the dense spray region and insensitive to the non-spherical droplets. They concluded DHM is the best method for providing valuable information about the small droplets encountered in the spray because of its ability to resolve very small details.

Lee et al. (2008) extended the work of Miller et al. (2008) by using double-pulsed digital holography to probe both droplets sizes and velocities in very dense spray region ($x/d_0 < 25$) of aerated liquid jet injected in subsonic crossflow. New size and velocity data in the dense spray region of aerated liquid injectors was obtained by using digital holographic microscopy (DHM). Test conditions included: nozzle exit diameter (d_0) of 1mm, Gas to liquid ratio (GLR) of 8%, and jet/freestream momentum flux ratio (q_0) of 0.74 at the near-injector region ($x/d_0 = 0 \sim 22.5$ and $y/d_0 = 0 \sim 27$). The measurements included droplets locations, Sauter mean diameter (SMD), sphericity, and three-dimensional droplet velocities, mass-averaged velocities distributions, drop sizes distributions. The measurements were obtained by slicing the holograms into multiple two-dimensional images within the span wise distance of $z/d_0 = -13 \sim 13$. To overcome the limited field of view, the spray maps was be constructed by patching several holograms.

The results of the currently-active investigation at Oklahoma State University were documented in the following publications:

1) B. Miller, K.A. Sallam, M. Bingabr, K.-C. Lin and C. Carter (2008), “Breakup of Aerated Liquid Jets in Subsonic Crossflow,” J. Prop. Power, in press.

2) J. Lee, K.A. Sallam, K.-C. Lin and C. Carter, “Spray Structure in Near-Injector Region of Aerated Jet in Subsonic Crossflow,” AIAA paper No. 2008-1043, 46th AIAA Aerospace Sciences Meeting, Reno, Nevada, January 2008.
3) J. Lee, B. Miller, K.A. Sallam, K.-C. Lin, and C. Carter, “Velocity and Size Measurements of Aerated Spray using Digital Microscopic Holography,” ILASS-AMERICAS 2007, May 15-18, 2007 - Chicago, Illinois.
4) B. Miller, K.A. Sallam, M. Bingabr, K.-C. Lin and C. Carter, “Secondary Breakup of Aerated Liquid Jets in Subsonic Crossflow,” AIAA paper No. 2007-1342, 45th AIAA Aerospace Sciences Meeting, Reno, Nevada, January 2007.
5) B. Miller, K.A. Sallam, K.-C. Lin and C. Carter, “Digital Holographic Spray Analyzer,” ASME paper No. FEDSM2006-98526, ASME Joint U.S.-European Fluids Engineering Summer Meeting, Miami, Florida, July 2006.

1.2 Research Objectives

The objectives of the present project were as follows:

1) Construct single-pulsed digital holographic microscopy optical setup in test cell 18. Calibrate CCD sensors and Nd:YAG laser using Air Force Target.
2) Construct double-pulsed digital holographic microscopy optical setup. Complete spatial and temporal calibration.
3) Construct double-pulsed digital holographic microscopy optical setup. Complete measurements of drop size and velocity distributions downstream of the fuel injector at locations inaccessible to PDPA (x/d_{inj} = 10 and 20) at locations accessible to PDPA (x/d_{inj} = 50) to validate the present diagnostic.
4) Investigate the spatial limit (x/d_{inj}) of the present diagnostic by recording holograms of the spray structure at $x/d_{inj} < 10$.
5) Use phenomenological analyses to correlate the drop sizes and velocities measurements. Quantify the effects of the secondary breakup on the spray structure.
6) Write the final report.

2. Experimental Methods

2.1 Experimental Apparatus

The experiments were performed in test cell 18 at Wright-Patterson Air Force Base. Water was used as the test liquid. Digital holographic microscopy (DHM) was used to visualize the spray structure of aerated jets. The injector internal structure is shown in Fig. 2.1. The schematic of double pulsed digital holographic microscopy is shown in Fig. 2.2. Two frequency doubled YAG lasers were used to illuminate the spray field (Continuum Surelite I, operating at 10Hz, 532 nm wavelength, and nominally 200mJ/pulse). The two lasers were triggered using a Labsmith LC880 pulse generator. The setup consists of two laser beams expanded with an objective lens, and then they pass directly through the test section of the wind tunnel (windows GE type 124 quartz ground and polished to 80/50 scratch/dig) to the CCD sensor (Redlake EC1600, 4872 x 3248 pixels) shown in Fig. 2.3. Double-pulsed holograms (timed to the two lasers) were captured to enable velocity measurements. The holograms were reconstructed numerically.

The resolution of the digital hologram depends on the distance from the object to the CCD, the wavelength of the light, and the pixel size of the CCD. The resolution of the hologram is determined by Schnars and Jueptner (2005) as follows:

$$\Delta\xi = \frac{\lambda d}{N\Delta x} \tag{2-1}$$

where ($\Delta\xi$) is the resolution, (λ) is the wave length, (d) is the recording distance, i.e. the distance from the object to the CCD, (N) is the number of pixels, and (Δx) is the pixels size. The distance between the objective lens and aerated jet was minimized for good resolution, and the distance between the aerated jet and CCD sensor was minimized for large field of view.

2.2 Test Conditions

Experiments were performed at M=0.3 and M=0.6, q=10, and GLR=0%, 2%, 4%, and 8%. Water was used as the test liquid. Holograms were recorded of the jet core and followed the upstream edge of the spray.

2.3 Instrumentation

When the digital hologram is stored on the CCD sensor, it can be reconstructed by a numerical algorithm (Schnars and Jueptner, 2005). After the reconstruction process, three-dimensional volume information is expressed by many reconstruction holograms focused on each two-dimensional plane. Because of the expanding laser beam used for DHM, the spatial calibration is continuously changing for each one of these two-dimensional planes. To conduct the spatial calibration, one needs at least three pins placed at three different distances form the CCD sensor. Because of expanding laser beam diameter, the reconstructed image of each of the identical pin had different diameter. The linear spatial calibration is as follows:

$$Y = aX + b \qquad (2\text{-}2)$$

where Y is the ratio of pin diameters (μm/pixels), X is the reconstruction distance (mm) and a and b are constants depending on the geometry of the actual setup. Thus, this equation becomes very useful for getting the actual distance in each reconstruction two-dimensional plane.

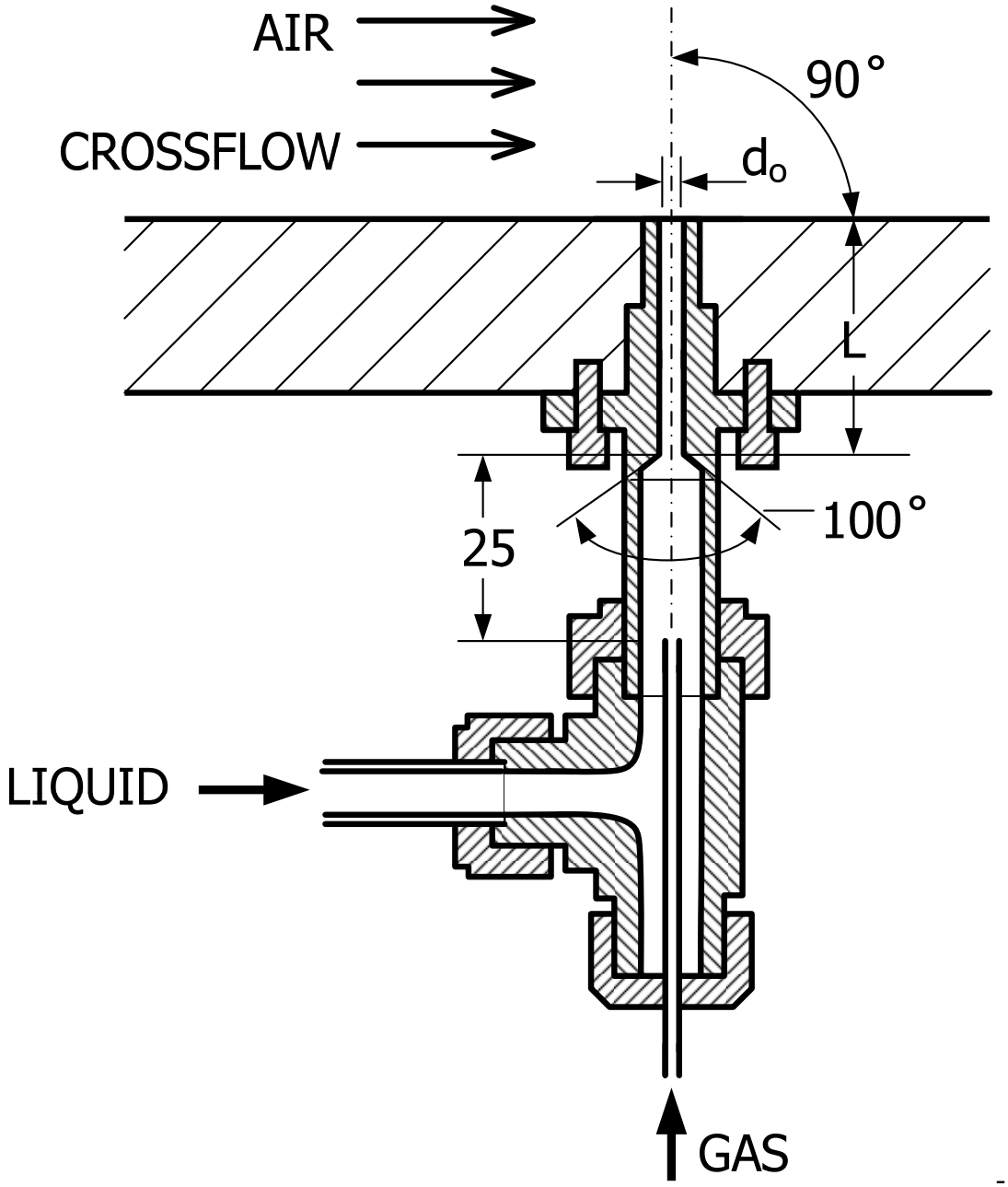

Fig. 2.1 Schematic of aerated injector.

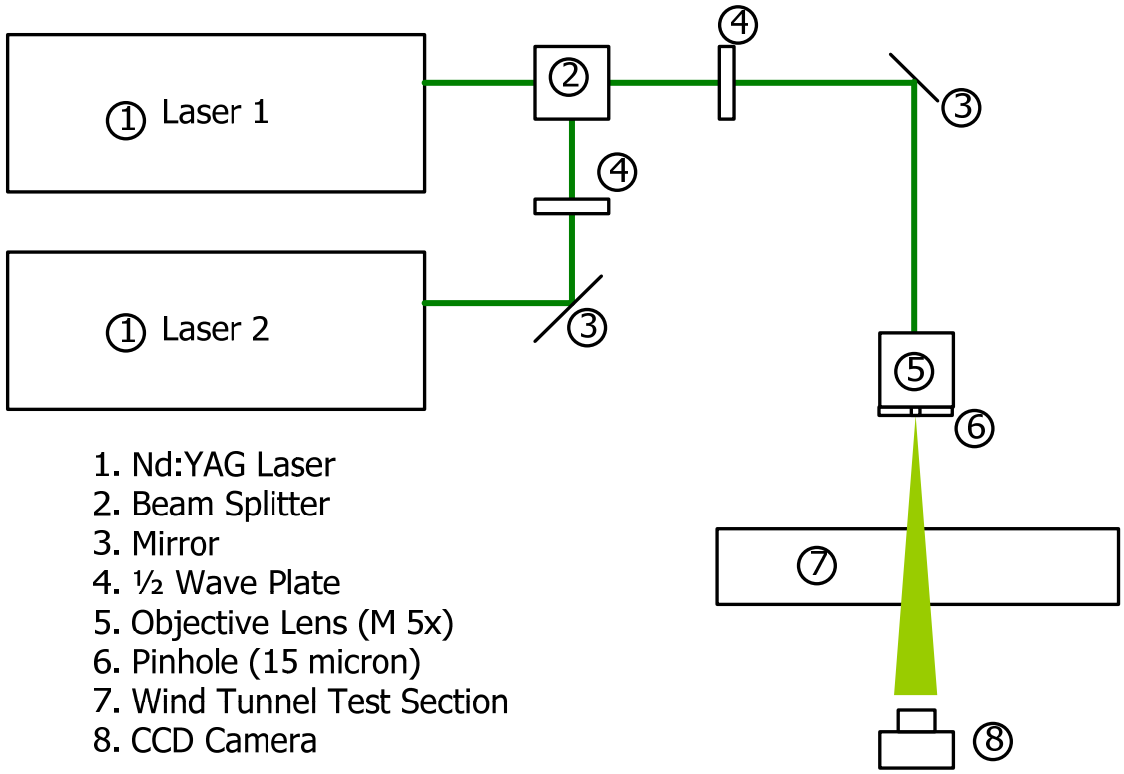

Fig. 2.2 Schematic of aerated injector.

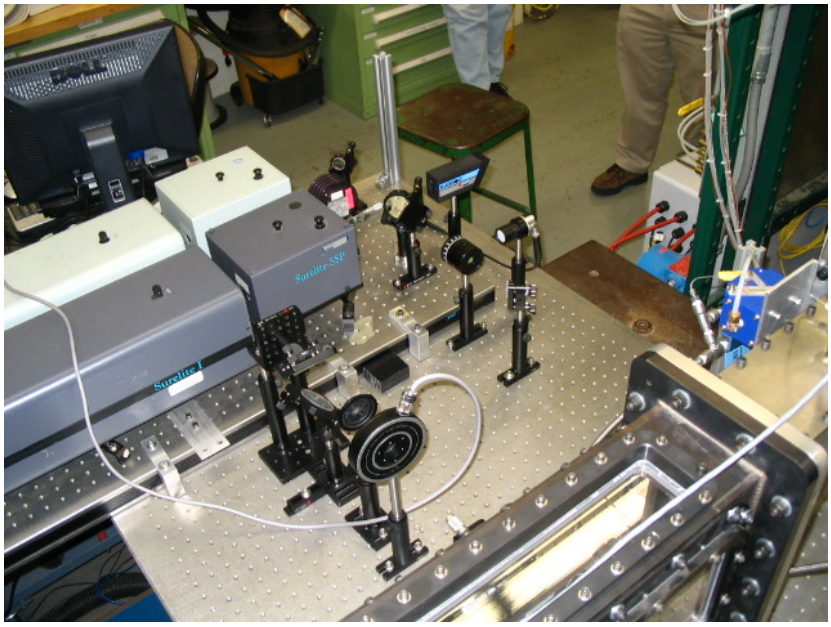

(a)

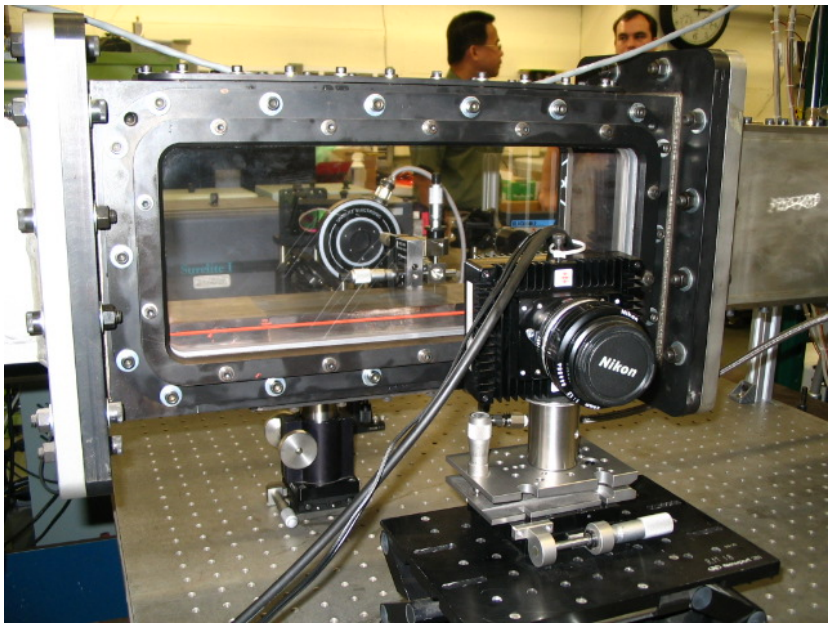

(b)

Fig. 2.3 Optical setup: (a) sending optics, (b) receiving optics (Camera flipped for clarity).

3. Results

Digital holographic microscopy (DHM) was used for probing the dense spray region near the injector of the aerated liquid jets. A recorded pulsed hologram using Red lake CCD camera (4872 x 3248 pixels) of a resolution target in the presence of the wind tunnel windows is shown in Fig. 3.1. The background noise is mainly due to the presence of the window. To quantify its effect on resolution, two holograms without and with the windows are shown in Figs. 3.2 and 3.3, respectively. Although the windows increase the background noise, it has little effect on resolution. The present setup in the presence of the wind tunnel windows managed to resolve the 5^{th} element of 6^{th} group (101 lp/mm) as shown in Fig. 3.4. This resolution should be adequate to resolve the droplets and the ligaments resulting from the breakup of aerated liquid jets in crossflow as shown in Fig. 3.5. Several attempts to obtain clear holograms were made at different location along the outer boundary of the spray as shown in Fig. 3.6. The background noise, however, is of the same order of magnitude as spray droplets and would be problematic when droplets recognition is performed for size and velocity measurements.

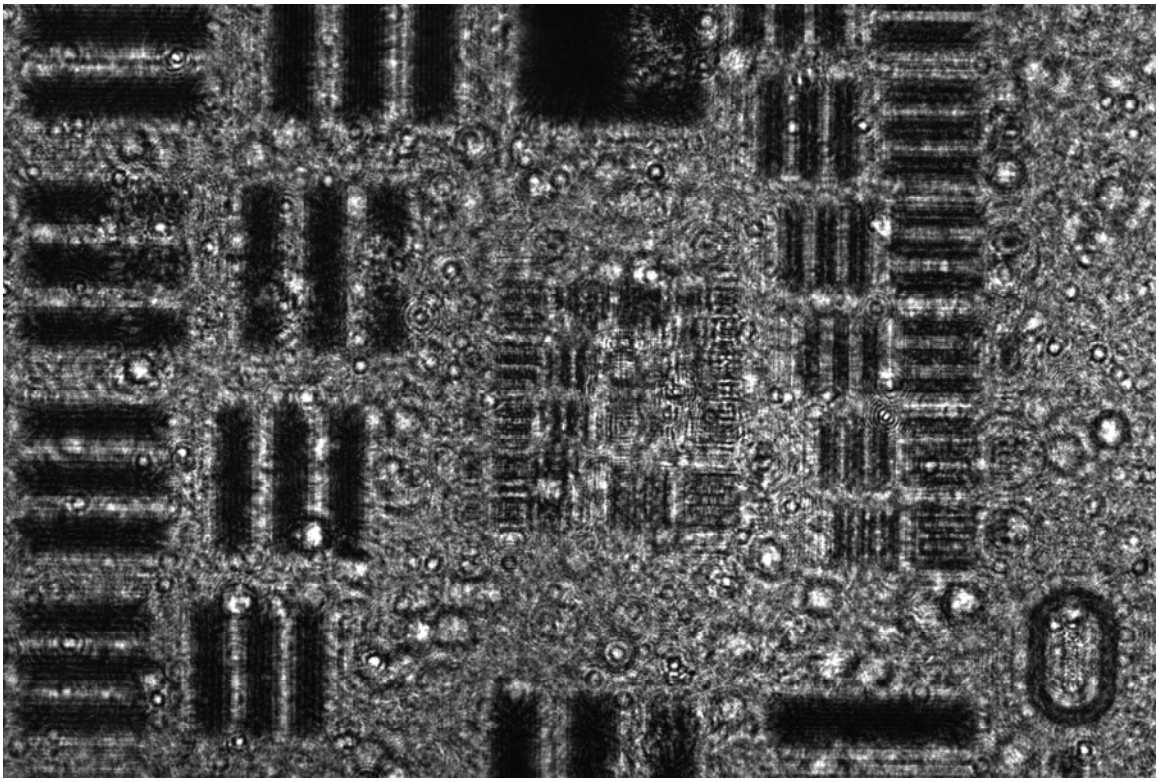

Fig. 3.1 Recorded hologram using Red lake CCD camera (4872 x 3248 pixels).

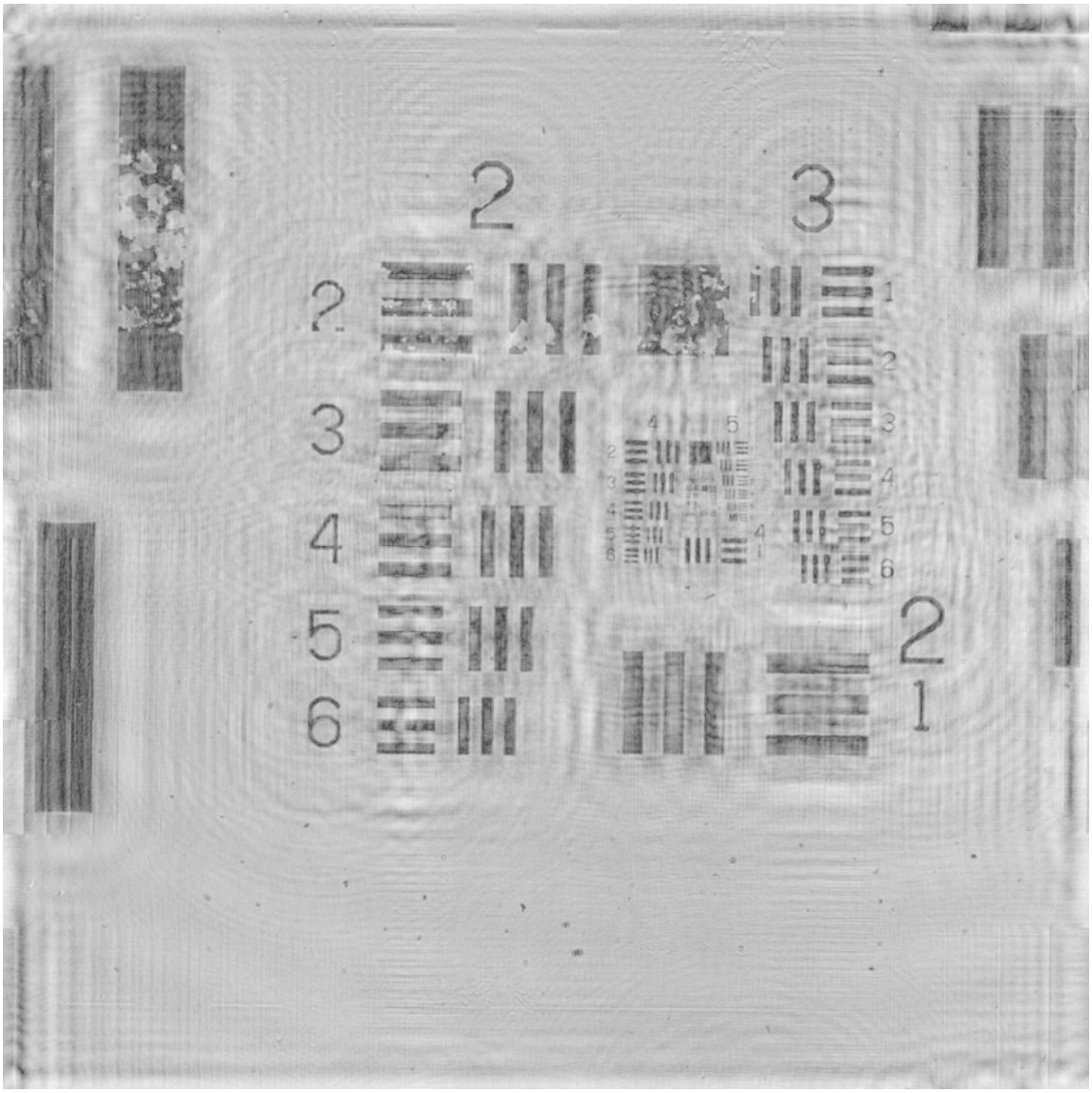

Fig. 3.2 Reconstructed pulsed hologram without wind tunnel windows. Only 2048 x 2048 pixels were reconstructed from the original 4872 x 3248 array.

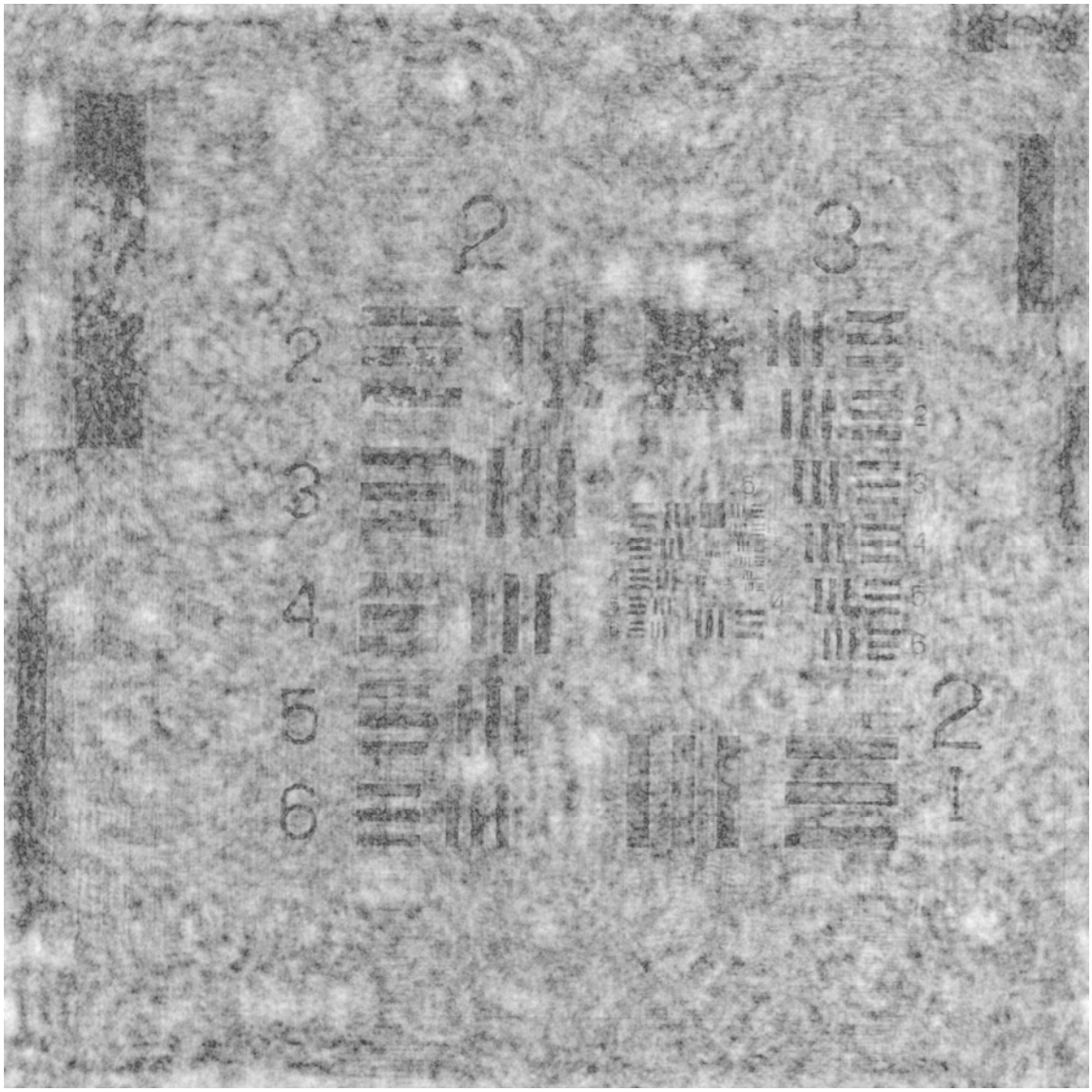

(b)

Fig. 3.3 Reconstructed pulsed hologram with wind tunnel windows. Only 2048 x 2048 pixels were reconstructed from the original 4872 x 3248 array.

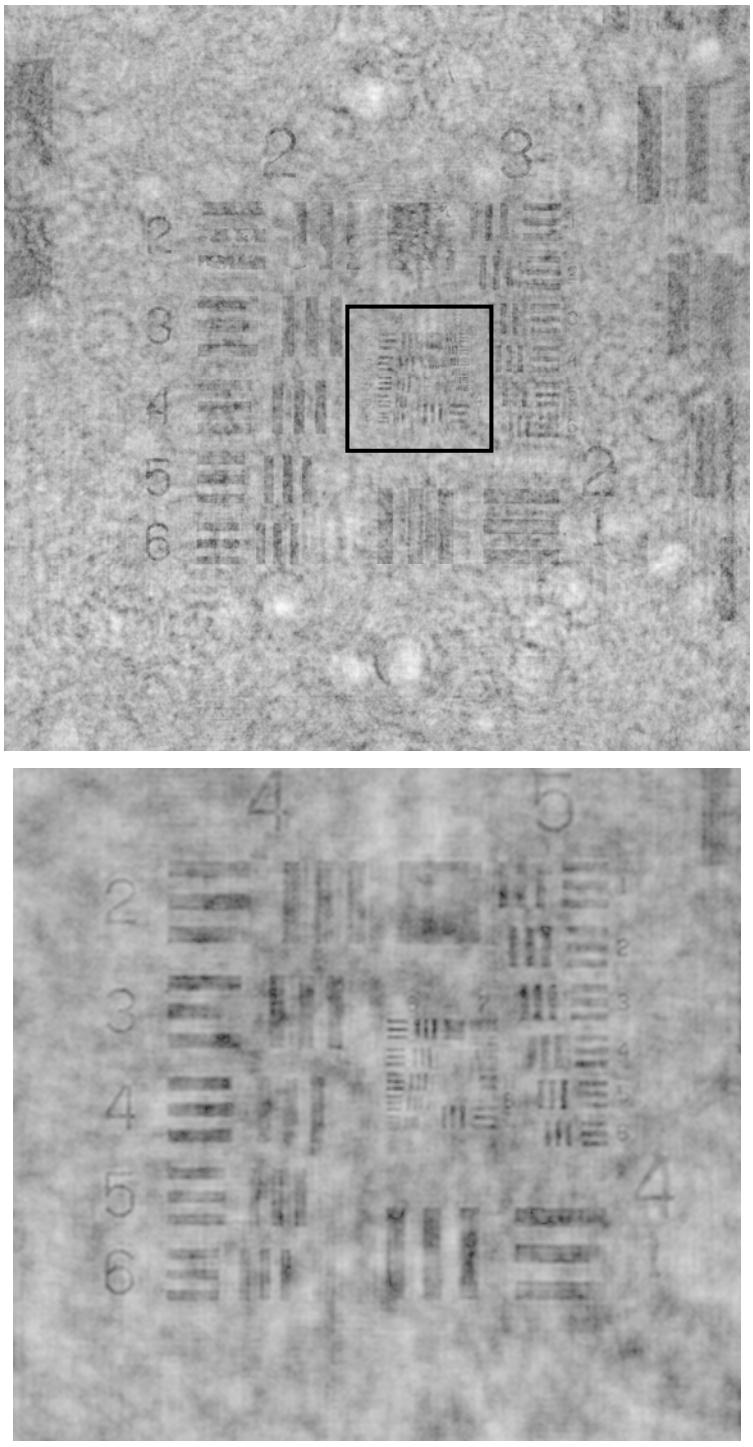

Fig. 3.4 Reconstruction in the presence of the window showing (Top) the 2nd and 3rd groups resolved and (Bottom) zoom-in area showing the 4^{th}, 5^{th} and 6^{th} group resolved. The hologram was made using 20x objective lens and 15 micron pin hole.

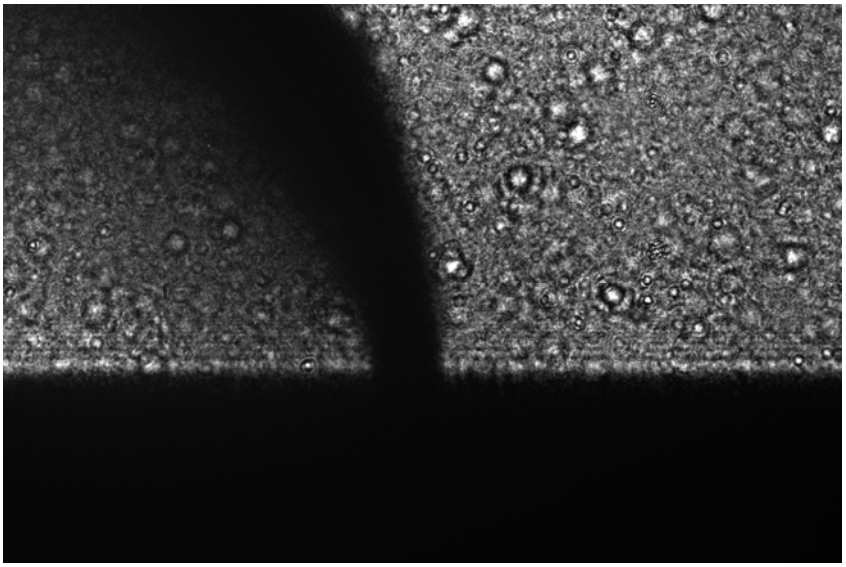

Fig. 3.5 Recorded Hologram at M=0.6, q=10, GLR=0%.

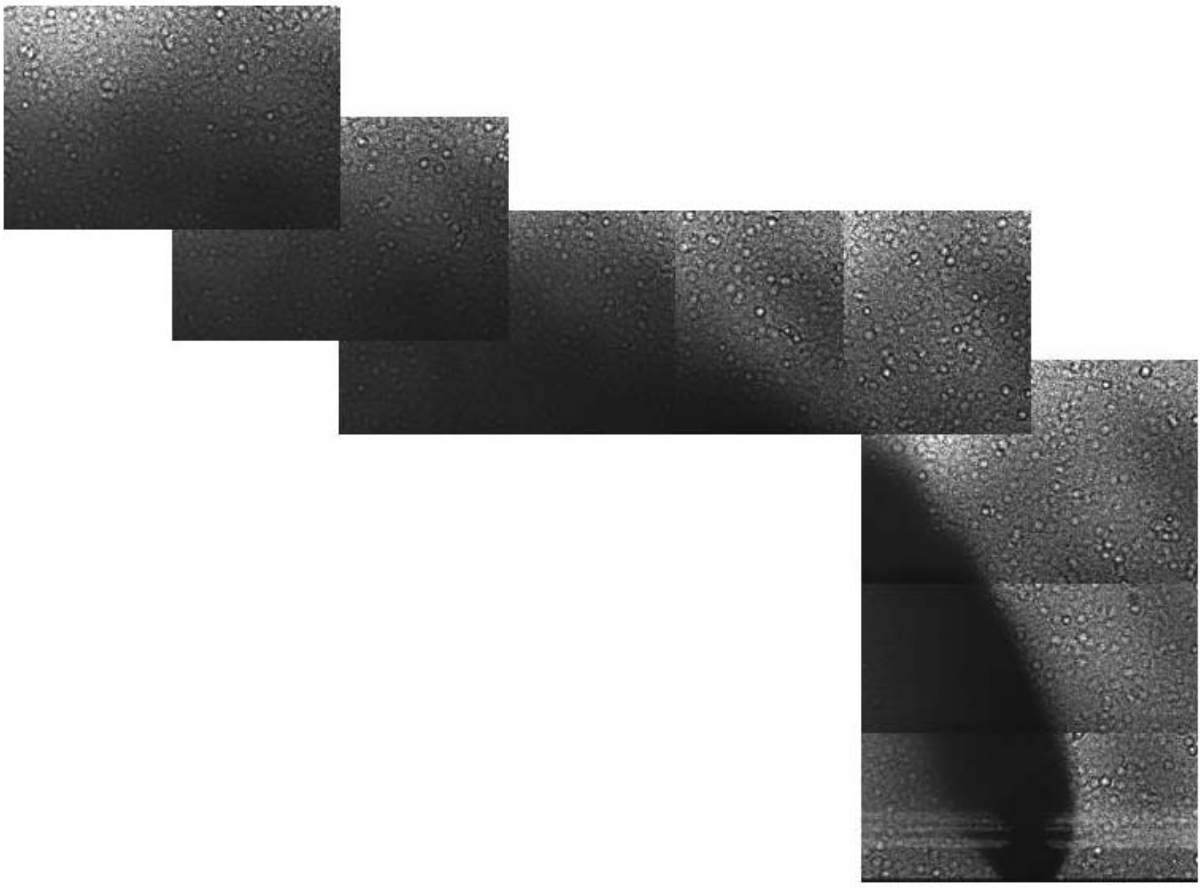

Fig. 3.6 Recorded holograms at M = 0.3, q = 10, GLR = 2%.

4. Summary, Conclusions and Future Work

4.1 Summary and Conclusions

The dense spray region of aerated liquid jet in subsonic crossflow has been investigated by double-pulsed digital holographic microscopy (DHM) at test cell 18, WPAFB. To visualize the entire structure of aerated liquid jet the spray map was constructed by patching several reconstructed holograms with high resolution (101 lp/mm). To quantify the effect of the windows of the wind tunnel on resolution, two holograms without and with the windows were compared. The conclusions of the present study were as follows:

1. Digital holographic microscopy is suitable for probing the dense spray near-injector region for aerated liquid jets in subsonic crossflow. The present optical setup is relatively simple and does not require a collimating lens or relay lens unlike digital in-line holography, which helps increase the resolution of the technique.
2. Large field of view can be obtained by simply patching several high resolution holograms reconstructed in the same span wise distance.
3. Although the windows increase the background noise, it has little effect on the resolution. This background noise, however, are of the same order of magnitude as spray droplets and would be problematic when droplets recognition is performed for size and velocity measurements.
4. It is therefore recommended that one should attempt to remove background noise before size and velocity measurements would be performed.

4.2 Future Work

To reduce the background noise, new windows will be installed in the wind tunnel. The testing of the optical setup is scheduled in January 2008.

1. Spatial calibration of the optical setup using resolution target without and with the wind tunnel window. Evaluate the effect of the windows on resolution and background noise.

2. Testing the setup in the single-pulse mode using aerated jet injection in crossflow starting at upwind side to reduce multiple scattering. Investigate other areas in the spray.
3. Testing the setup in the double-pulse mode to yield velocity information. Construct a dataset of 3D maps of size and velocity measurements in the near injector region ($0<x/d<50$) of aerated spray in crossflow.

References

Bryanston-Cross, P. J., Funes-Gallanzi, M., Quan, C., and Judge, T. R., Optics & Laser Technol., Vol. 5, pp. 251-256, 1992.

Burke, J., Hess, C. F., and Kebbel, V., Part. Syst. Charact., Vol. 20, pp. 183-192, 2003.

Ewan, B.C.R, Appl. Opt., Vol. 18, pp. 3156-3160, 1979.

Ewan, B. C. R., Appl. Opt., Vol. 19, pp. 1368-1372, 1980.

Hinsch, K. D., Meas. Sci. Technol., Vol. 13, pp. 61-72, 2002.

Lee, C. S., and Park, S. W., Fuel, Vol. 81, pp. 2417–2423, 2002.

Lee, J., Sallam, K.A., Lin, K.-C., and Carter, C., AIAA paper No. 2008-1043.

Lin, K.-C., Kennedy, P. J., and Jackson, T. A., AIAA Paper No. 99-2374 (1999).

Lin, K.-C., Kennedy, P. J., and Jackson, T. A., AIAA Paper No. 2000-0194 (2000).

Lin, K.-C., Kennedy, P. J., and Jackson, T. A., AIAA Paper No. 2001-0300 (2001).

Lin, K.-C., Kennedy, P. J., and Jackson, T. A., AIAA Paper No. 2002-3178 (2002).

Meng, H., Pan, G., Pu, Y., and Woodward, S. H., Meas. Sci. Technol., pp. 673-685, 2004.

Menzel, R., and Shofner, F. M., Appl. Opt., Vol. 9, pp. 2073-2079, 1970.

Miller, B., Sallam, K.A., Bingabr, M., Lin, K.-C., and Carter, C., J. Prop. Power, in press (2008).

Pan, G., and Meng, H., *ASME International Mechanical Engineering Congress & Exposition,* New Orleans, Louisiana, Nov 2002.

Pu, S. L., Allano, D., Patte-Rouland, B., Malek, M., Lebrun, D., and Cen, K. F., Exp. In Fluids, Vol. 39, pp.1-9, 2005.

Sallam, K.A., Aalburg, C., Faeth, G.M., Lin, K.-C., Carter, C.D., and Jackson, T.A., *Atom. Sprays* 16:657-672 (2006).

Schnars, U., and Jueptner, W., "Digital Holography: Digital Hologram Recording, Numerical Reconstruction, and Related Techniques," Springer, Berlin (2005).

Thompson, B. J., J. Phys. E, Vol. 7, pp. 781-788, 1974.

Trolinger, J. D., Belz, R. A., and Farmer, W. M., Appl. Opt., Vol. 8, pp. 957-961, 1969.

Flow Loop Experiments Using PAO/CNT Nanofluids

David Huitink[1], Debjyoti Banerjee, Ph.D.[1,*], Sabyasachi 'Raj' Ganguli, Ph.D. [2], and Kirk Yerkes, Ph.D.[2]

[1]*Dept. of Mechanical Engineering, Texas A&M University, College Station, TX;* [2]*Air Force Research Laboratory, Wright-Patterson AFB, OH;* [*]*Author for correspondence (Tel.: 979-845-4500; E-mail: dbanerjee@tamu.edu)*

Keywords: nanofluids, carbon nanotubes, convective heat transfer, thermal property enhancement

Abstract

Experiments were performed using a flow loop apparatus to explore the performance of nanofluids in electronic cooling applications for forced convective heat transfer applications. The experiments were performed using 0.5% by weight carbon nanotubes (CNT) suspended in Poly Alpha Olefin (PAO). The CNT were chemically functionalized to enable their homogeneous dispersion in PAO. The experimental set-up consisted of a test section containing plain offset-fin cooler apparatus which was connected to a flow loop consisting of a gear pump, a compact heat exchanger (which was cooled by a constant temperature bath chiller) and a reservoir. The thermal performance of the nanofluid was compared to that of PAO. The performance data was obtained by parametrically varying the operating conditions (heat flux and flow rates). The change in surface morphology of the offset-fins was investigated using Scanning Electron Microscopy (SEM). The nanofluids properties were measured using rheometry for viscosity and Differential Scanning Calorimetry (DSC) for specific heat. Observations from this and past studies suggest that the formation of "nanofins" on the surface of the heater from deposited nanoparticles enhances the surface characteristics of the heater, resulting in improved heat rejection.

Introduction

In commercial systems, heat fluxes approaching 300 W/cm^2 are projected for electronic chips and optoelectronic devices in the next 10 years (ITRS, 2002). This technical need for high heat flux thermal management will significantly affect the growth of chip interconnect and electronic packaging industries. The estimated annual sales for these industries are currently approaching ~$16 billion worldwide and are expected to increase exponentially in the next 10 years (Thermacore Inc, 2003). Hence, investigation of single-phase convective heat transfer enhancement in nanofluids is motivated by a number of contemporary thermal management applications, which include: (i) Electronics cooling: of next generation computing platforms and data servers, aircraft on-board electronics components, cabinets, circuit boards, power modules (e.g., in aircraft and ship systems), RF devices, power transmission devices (e.g., IGBT) and satellite systems; (ii) Improving energy efficiency of HVAC (Heating,

Ventilation and Air Conditioning) equipment: chillers and refrigerators requiring higher COP (Coefficient of Performance); (iii) Propulsion systems for defense applications: next generation systems requiring better thermal efficiencies for reducing thermal signatures; (iv) other systems (typical waste heat ~100 MW): electromagnetic rail guns and catapults, direct energy weapons (DEW), all electric aircraft and ship technologies, thermal busses, and heat sinks (e.g., through the hull cooling). In order to meet the rising demands of thermal management, better coolants and heat transfer fluids are required. Ideally, a high conductivity, low viscosity fluid is envisioned for compact heat exchangers which would result in enhanced heat transfer and reduced weight.

Nanofluids have recently gained attention for enhancing heat transfer in thermal management systems. Being defined as colloidal solvents containing dispersed nanometer (~10-100 nm) sized particles (Choi, 1999), nanofluids have been discovered to possess many of the qualities desired in a revolutionary heat transfer fluid. Fluids doped with these nanoparticles have been shown to enhance the conductivity of solvents at low concentrations (< 4%) as the sizes of the particles are decreased (Keblinski, 2005). Eastman et al. found that a 4% volume suspension of CuO and Al_2O_3 nanoparticles in ethylene glycol yielded a 20% increase in thermal conductivity (Lee, 1999), while a 0.3% volume concentration of CuO yielded the greatest enhancement of 40% (Eastman, 2001). An aqueous suspension of 26nm diameter SiC nanoparticles at 4.2% volume fraction led to the increase of thermal conductivity by 15.8% (Xie, 2002). Additionally, the suspension of multi-walled carbon nanotubes in oil (PAO) was shown to enhance thermal conductivity by up to 150% (Choi, 2001) when evaluating using the transient hot-wire method. Choi proposed that the observed nonlinear thermal conductivity variation with concentration is affected by the aspect ratio of the tubes in addition to the number density of the tubes in the suspension.

The enhancements in thermal conductivity of the nanofluids predicted by the classical theories were found to underestimate the observed improvements (Maxwell, 1881; Hamilton, 1962), explained by the fact that these theories were proposed for heterogeneous colloidal mixtures of micron-scale particles in solvents. Hamilton and Crosser's analytical model (Hamilton, 1962) for predicting the thermal conductivity of two component mixtures underestimated the enhancements seen in these experiments by up to an order of magnitude, explained by lacking the particle size dependence in the model. Large variations in thermal conductivity have been reported in the literature for various nanofluid compositions, i.e., solvent type, pH of aqueous solvents, stabilizers (e.g., surfactants), material of the nano-particles, concentration of the nano-particles, size and aspect ratio of the nano-particles (Wang, 2007). Several mechanisms have been proposed to account for the aberrant (or anomalous) behavior of thermal conductivity of nanofluids (Keblinski, 2005; Wang, 2007).

A review of the recent literature data and of the recently proposed theories suggests that localized Brownian convection is potentially the dominant mechanism responsible for the observed increase in thermal conductivity (Prasher, 2006). Comprehensive examination of the literature data for aqueous nanofluids also shows a potential trend for maxima in the thermal conductivity 10nm-50nm diameter spherical nano-particles (Prasher, 2006; Putnam, 2006). This maxima is primarily governed by the competing effects of two transport resistances: (1) convective-conductive resistance arising from Brownian convection (Prasher, 2006), and (2) liquid-

solid interfacial resistance (Putnam, 2006) on the surface of the nano-particles. The former resistance dominates for bigger sized particles (> 10nm) while the latter resistance dominates for the smaller sized particles (< 10nm). The competing resistances at different size ranges help to explain the maxima in thermal conductivity observed in nanofluids. An additional effect in conductivity measurements could be due to surface coating of the measurement probes caused by precipitation of nano-particles. The measurements for thermal conductivity of nanofluids reported in the literature have largely ignored this effect. Proper design of experiments is needed to account for this effect on thermal conductivity measurements due to surface precipitation of nano-particles.

Nanofluids were also reported to enhance single-phase (forced convection and natural convection) as well as two-phase (pool boiling) convective heat transfer (Keblinski, 2005; Prasher, 2006). The critical heat flux (CHF) was reported to increase by 300% during pool boiling of nanofluids while the required wall superheat for a given heat flux was also found to increase for nanofluids compared to the pure solvent (You, 2003; Vassalo, 2005). There are contradicting reports in the literature since a reduction in the pool boiling heat transfer coefficient was also reported for nanofluids (Das *[IJHMT]*, 2003; Das *[IJMF]*, 2003; Li, 2003). The observed enhancement is possibly due to increase in the number of nucleation sites, the size of the nucleation cavities and the associated nucleation site density arising from the precipitation of the nano-particles. Nanofluids are also known to have different wetting behavior (Wasan, 2003). In contrast, enhanced fouling of the heater surface due to rapid precipitation of the nano-particles could also cause degradation of the pool boiling performance.

While limited precipitation of nano-particles can enhance boiling heat transfer by increasing the nucleation site density and changing the wettability of the nanofluid on the heater surface, in single phase flows such precipitations can enhance heat transfer by forming enhanced heat transfer surfaces ("nano-fins"). Liquid thermal conductivity is ~100-1000 times smaller compared to solid materials (Mills, 1995). Hence, seeding liquids with solid particles for enhancing the effective liquid conductivity has been subject of scientific interest for more than a century (Maxwell, 1881). The consideration of nanofluids as heat exchanger fluids is primarily because the stable colloidal suspensions that can be derived from dispersing the nanoparticles into the fluids are much more effective when compared to earlier attempts reported in the literature where unstable colloids were derived from micron-sized particles. Initial motivation for use of nanofluids was mediated by the high surface to volume ratio of such nano-particles which was expected to enhance their thermal conductivity at low concentrations (Lee, 1999). Such low concentrations of the nano-particles were also expected to minimize the pressure penalty and wall abrasion from the nano-particles.

However, for evaluating the convective heat transfer enhancement - in addition to thermal conductivity other thermo-physical properties, such as, thermal diffusivity, specific heat and dynamic viscosity - as well as flow conditions, such as surface roughness and Reynolds number are important factors that should be accounted for or measured experimentally. Review of literature data (Keblinski, 2005; Wang, 2007) for forced convection using nanofluids suggests that heat transfer was increased by 8-15% for the same Reynolds number. Thus, there is less variability in forced convective heat transfer data of nanofluids compared to data for thermal conductivity or pool boiling (Keblinski, 2005; Wang, 2007). However, it was found that majority of these results were

reported using "effective" thermo-physical properties of the nanofluids rather than experimental measurements for these properties (e.g., volume expansion coefficient for natural convection experiments, as well as specific heat, thermal conductivity and viscosity for forced convection experiments). Also, only a limited number of studies characterized the surface roughness of the heater surfaces before and after the experiments were performed using the nanofluids.

Pak and Cho (Pak, 1998) used γ-Al_2O_3 and TiO2 nanofluids in water where the particle sizes were 13 and 27 nm, respectively, for studying convective heat transfer in a pipe of internal diameter 1.07 cm and 480 cm length. The viscosity values for these nanofluids were found to be 200 times higher for γ-Al_2O_3 and 3 times higher for TiO_2 (than for water) at 10% volume concentration each. The viscosity of the γ-Al_2O_3 nanofluids showed shear thinning behavior for volume concentrations exceeding 3%. The viscosity of TiO_2 nanofluids showed shear thinning behavior for volume concentrations exceeding 10%. The Reynolds number (Re) and Prandtl number (Pr) were varied from 104 – 105 and 6.5 – 12.3, respectively in these experiments. The specific heat and thermal conductivity were estimated using empirical formulas and were not measured in these studies. The Darcy friction factor for nanofluids (volume fractions less than 3%) was measured to be within 3% of that for water for the same Reynolds number. This result is similar to friction factor for 100nm Copper nanofluids in water where the friction factor was measured to be the same as for water at same Reynolds number (Xuan, 2003). However, due to the significant increase in viscosity – comparisons for the same average velocity of the fluids showed that the pressure drop in nanofluids (2.78% γ-Al_2O_3) was 28% higher, the pumping penalty was 31% higher and the frication factor was 36% higher, than for water. Based on the heat flux data, the authors proposed a new correlation for turbulent flow of nanofluids in a pipe to be:

$$\mathrm{Nu} = 0.021\ \mathrm{Re}^{0.8}\ \mathrm{Pr}^{0.5}. \qquad (1)$$

The heat flux for the same average velocity was found to be 12% lower. The authors concluded that the convective heat transfer for the nanofluids could be increased by using larger sized nano-particles and higher thermal conductivity materials. In retrospect, the authors of this study probably could have obtained better results at lower volume concentration of the nano-particles. In a subsequent study, CuO nanoparticles in water at 0.9% volume concentration were found to augment forced convection heat transfer coefficient by more than 15% (Eastman, 1999). Copper nanoparticles with size less than 100 nm and volume fractions up to 2% were suspended in water and their convection properties were studied by Xuan and Li (Xuan, 2003) for flow inside a 10 mm diameter brass tube, 800 mm long. The friction factors were found to be identical to that of water for Reynolds number in the range of 10,000 – 25,000. The Nusselt number variation of the nanofluids was found to be significantly under predicted by the Dittus Boelter correlation (Mills, 1995). The authors did not measure the associated thermo-fluidic properties but used an estimated value by using the effective thermal conductivity, diffusivity and viscosity of the nanofluid. The Nusselt number of the nanofluids was found to be enhanced by up to 60% than water for the same Reynolds number at 2% volume concentration of the nanoparticles. Based on these measurements the authors proposed a correlation for convective heat transfer of the nanofluids:

$$Nu = c_1\left(1.0 + c_2\phi^{m1}Pe_d^{m2}\right)\mathrm{Re}_{nf}^{m3}\ \mathrm{Pr}_{nf}^{0.40} \qquad (2)$$

where, the subscript nf denotes "effective" nanofluid properties, φ is the volume fraction, Pe is the Peclet number (Mills,

1995) based on the diameter of the nanoparticle, and the constants for the correlation are denoted by c_1, c_2, m_1, m_2, and m_3. At low volume fractions of the nano-particles the pressure drop was found to be identical to that of water and the authors did not find any pressure penalty associated with the nanofluids. Heat transfer was enhanced locally by up to 47% for γ-Al_2O_3/water nanofluid (~27-56 nm size nano-particles, volume fractions up to 2%) in the entrance region of a 4.5 mm diameter tube, 970 mm long. The local enhancement was found to decrease with the axial distance from the entrance (Wen, 2004). The authors proposed that the enhancement was due to particle migration which resulted in non-uniform distribution of thermal conductivity and viscosity as well as due to reduced thickness of the thermal boundary layer. Such transient disruptions in viscosity, thermal conductivity and boundary layer profile can also be expected due to precipitation of nano-particles on the tube walls. The effective viscosity was estimated using empirical equations and the thermal conductivity was measured. The effective values specific heat and density for the nanofluids were also estimated empirically in this study (Wen, 2004). Laminar forced convection heat transfer was enhanced using Al_2O_3/ water (~20 nm particle size) and CuO/ water (~50-60 nm particle size) nanofluids with volume fractions of 0.2%-3% under constant temperature conditions (Heris, 2006). The viscosity of the nanofluids was measured using a rheometer. The effective density, specific heat and thermal conductivity were estimated from empirical equations in this study. The heat transfer coefficient was found to be enhanced by up to 40% compared to the theoretically predicted values for a given Peclet number. The enhancement was found to increase with particle concentration. Higher enhancement was observed for Al_2O_3 than for CuO. Laminar forced convection heat transfer was enhanced using γ-Al_2O_3/ water (~20 nm particle size) nanofluids with volume fractions of 0.5%, 0.75% and 1% under constant wall heat flux conditions (Lai, 2006). The experimental apparatus consisted of a tube of 1.02 mm diameter and 20 cm length and the flow rate was varied to achieve a maximum Reynolds number of 270. The heat transfer coefficient was found to decrease with axial length until fully developed conditions were reached. The entrance length was found to agree with analytical formulations in the literature. The heat transfer enhancement was found to depend on Reynolds number and particle volume fraction. At Reynolds number of 270 the heat transfer coefficient was enhanced by 8% for volume fraction of 1% and by only 3% for volume fraction of 0.5%. The authors attributed the enhancement to Brownian convection of the nanoparticles and interaction of the nano-particles with molecules of the base fluid as well as potentially due to formation clusters of the nanoparticles.

Interesting results were reported on the effect of the nano-particle aspect ratio on the performance of the nanofluids for forced convective heat transfer augmentation (Yang, 2005; Ding, 2006). The former study (Yang, 2005) explored the effect of flow Reynolds number, temperature, nano-particle loading, nano-particle source, and the choice of base fluid on heat transfer enhancement. Graphite nano-particles of 20-40 nm thickness and 1-2 microns diameter (length to diameter - aspect ratio ~ 0.02) were suspended in two types of base fluids at concentrations of 2% and 2.5% by weight (Yang, 2005). The first base fluid was a commercial grade automatic transmission fluid (ATF) while the second base fluid was a mixture of synthetic “base oils” with commercial additive packages. The relevant liquid thermo-physical properties were measured experimentally (e.g., density, viscosity, specific heat and thermal

conductivity) for the base fluids and the nanofluids. The thermal conductivity was found to be enhanced by 56%. The density and specific heat were not found to show much change. Depending on the concentration, base fluid and nanofluids concentration, the viscosity was found to be enhanced by as much as 10% or was found to be reduced by up to 12%. The viscosity for both the base fluids and nanofluids was found to decrease with temperature. The heat transfer coefficient was enhanced by 22% for 2.5% weight concentration at 50ºC and by 15% at 70 ºC. The data was normalized on the basis of Sieder-Tate correlation (Sieder, 1936) as

$$\Omega = Nu \cdot \mathrm{Pr}^{-1/3}\left(\frac{L}{D}\right)^{1/3}\left(\frac{\mu_b}{\mu_w}\right)^{-0.14} = 1.86\,\mathrm{Re}^{1/3} \quad (3)$$

Hence, the data was normalized as

$$\Omega = a\,\mathrm{Re}^{b} \quad (4)$$

where a and b are constants for fitting the correlations to the experimental data. It was found that the values of a obtained from fitting the experimental data were fairly higher (~2-3) than the theoretical value of 1.86 while the values of b obtained from experimental data were fairly close to 0.33 (except for a few cases), for majority of the experimental data. However, comparison of the heat transfer coefficients (as ratio of nanofluids to base fluids) showed that the enhancement was lower than that predicted by theory by 10%-20%. The authors identified a number of effects for this behavior which include: (i) rapid alignment of nano-particles in lower viscosity fluids which lead to less interaction between the nano-particles and therefore reduced heat transfer, (ii) depletion of the nano-particles near the wall – leading to an intrinsically lower thermal conductivity. Subsequently, while analyzing this data(Yang, 2005) other authors (Ding, 2006) noted that the low aspect ratio (~0.02) of the graphite nano-particles could also be a factor responsible for the reduction of the ratio of heat transfer coefficient compared to the theoretical values. Since Carbon Nanotubes (CNT) have aspect ratios (length to diameter) more than 100 – CNT suspensions have also been investigated as convective nanofluids. Ding et al. used gum Arabic (GA) as a surfactant to stabilize MWNTs in aqueous solution which was found to have an 80% increase in thermal conductivity for 1% weight concentration and a maximum heat transfer enhancement of 350% over the base fluid when containing 5% weight concentration CNTs at a Reynold's number of 800 (Ding, 2006). The authors argued that as a percentage value the enhancement in thermal conductivity for CNT/ water nanofluids was found to be lower than CNT suspension in PAO (poly alpha olefin) (Choi, 2001), probably because PAO oils have lower thermal conductivity – hence the absolute enhancement in thermal conductivity was actually lower in PAO than in water. The viscosity of the CNT/water nanofluids was measured and shear thinning behavior was observed (Ding, 2006). This suggests that the effective viscosity of the CNT nanofluid is lower near the wall due to the high shear rate in the momentum boundary layer. Confirmatory tests for rheological behavior of the GA solution showed that the viscosity of the GA solution was an order of magnitude smaller than the CNT nanofluids. Also, shear thinning behavior at low shear rates and shear-thickening behavior at high shear rates (> 200/s) was observed for the GA solution. This was also reflected in the rapid increase in the enhancement for heat transfer coefficient at Reynolds number exceeding 1,100 (which corresponds to shear rates in excess of 500/s). The authors conjectured that shear thinning behavior would lead to higher effective thermal conductivity in the thermal and momentum boundary layers (i.e., higher Peclet numbers); and furthermore, that the shear thinning may

cause the CNT nanoparticles to interact in a more complex manner by forming larger nano-structures such that the effective particle size was greater than the volume based equivalent particle diameter – also resulting in higher effective conductivity of the nanofluids. This was also reflected in the entrance length of the flow. The convective heat transfer coefficient was found to decrease with axial length. However, the decay was much quicker for water than CNT nanofluids – suggesting that the boundary layer development was affected by the CNT. The authors attributed this to microscopic effects – such as particle migration and rearrangement due to non-uniform shear rate resulting in non-uniformity of viscosity as well thermal conductivity of the nanofluid at different pipe locations and cross-sections. Such non-uniformity has been shown theoretically to enhance the Nusselt number in pipe flow (Wen, 2005). The nanofluid concentrations used in the experiments were 0.1%, 0.25% and 0.5%. The potential mechanisms responsible for the observed enhancement could not be attributed simply due to enhanced thermal conductivity of the CNT nanofluid and were identified by the authors as: particle rearrangement, shear induced thermal conduction enhancement, reduction of thermal boundary layer due to the presence of nanoparticles and the high aspect ratio of CNT leading to enhanced inter-particle interactions for augmenting heat transfer.

The objective of this study was to study the heat transfer enhancement in CNT type nanofluids (compared to the base fluid) from a plain array fin cooler as well as investigating possible performance enhancements in a compact heat exchanger (Lytron). The motivation of the study was to produce preliminary data for exploring applicability of nanofluids to various US Air Force thermal management applications such as: liquid-to-air heat exchangers, all electric aircraft technologies, DEW Power Thermal Management (PTM), and Aircraft PTM. The expected thermal enhancements could enable reduction of aircraft components sizes and weight. Other benefits include development of the technical knowledge and capability to produce engineered (customized) coolants for retro-fitting in future USAF air platforms. Multi-walled carbon nanotube (MWNT) nanoparticles suspended in PAO was used as the nanofluid for concentration of 0.5% by weight with tube diameters of 50 nm and aspect ratios ranging from 10 to 4,000. The thermal diffusivity, density, specific heat, and viscosity of the nanofluid were measured in the experiments. The surfaces of the plain fins were characterized before and after the experiments using Scanning Electron Microscopy (SEM). The elemental chemical compositions of the deposited particles were characterized using EDX spectra (Energy Dispersive X-Ray). The deposited nanotubes are believed to act as enhanced heat transfer surfaces (“nano-fins”).

Experimental Apparatus and Procedure

Nanofluid Preparation

The MWNTs used in this study were obtained from Ahwahnee, which had nominal tube dimensions of 50 nm in diameter with aspect ratios ranging from 10 to 4,000. The tubes were chemically functionalized for encouraging the covalent bonding of the tubes to the PAO using 3-isocyanopropyltriethoxysilane (“silane”) in a similar manner to work done by Castaño, et al (Velasco-Santos, 2002). It was desired to use a silicon ester silane compound for the highest level of bonding with the PAO; however, the chemical was not readily available at the time of the experiment, thus the substitution was made. To accomplish the functionalization, the tubes needed to be oxidized, which was verified by X-ray

Photoelectron Spectroscopy (XPS). The CNTs were mixed into an ethanol-silane solution (2.5% by weight silane) for one hour in a heated bath (>80°C) where the mass of silane in the solution is equal to the mass of CNT to be functionalized. After the period of stirring at this elevated temperature, the volume of the solution was doubled using water/ethanol mixture such that the final concentration of the water in the complete solution was 5%. The mixture was percolated with nitrogen and stirred over heat for five hours. The experimental setup is pictured in Figure 1. Afterward the MWNTs were filtered from the solution using Whatman filter paper and subsequently freeze-dried. The tubes were then mixed with the PAO at 0.5% weight concentration by ultrasonicating the suspension for 2.5 hours in separate batches before the final mixing.

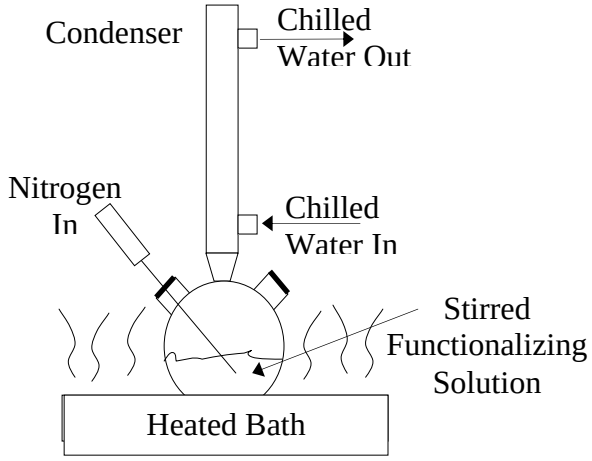

Figure 1. Functionalization Bath Schematic.

Heat Transfer Flow Loop

A flow-loop experimental set-up was used in this study. The experimental set-up was modified from a system originally designed for the measurement of heat transfer and pressure drop in plain fin array coolers (Lin, 2002; Lin *[AIAA]*, 2002). A schematic of the experimental setup is shown in Figure 2. The experimental set-up consists of a reservoir which connects to a flow meter. A positive displacement flow meter for high viscosity fluids was used (Model: FPD1004-D-R-A, with Display, Reed Switch, Output 4-20mA, Supplier: Omega). A magnetically coupled gear pump was used to pump the test fluid at flow rates up to 1.5 gpm (0.095 L/s). The test fluid passed through a compact heat exchanger apparatus before entering the test section (cooling chamber) in order to obtain a constant inlet temperature to the cooler test section. The cooler apparatus housed a

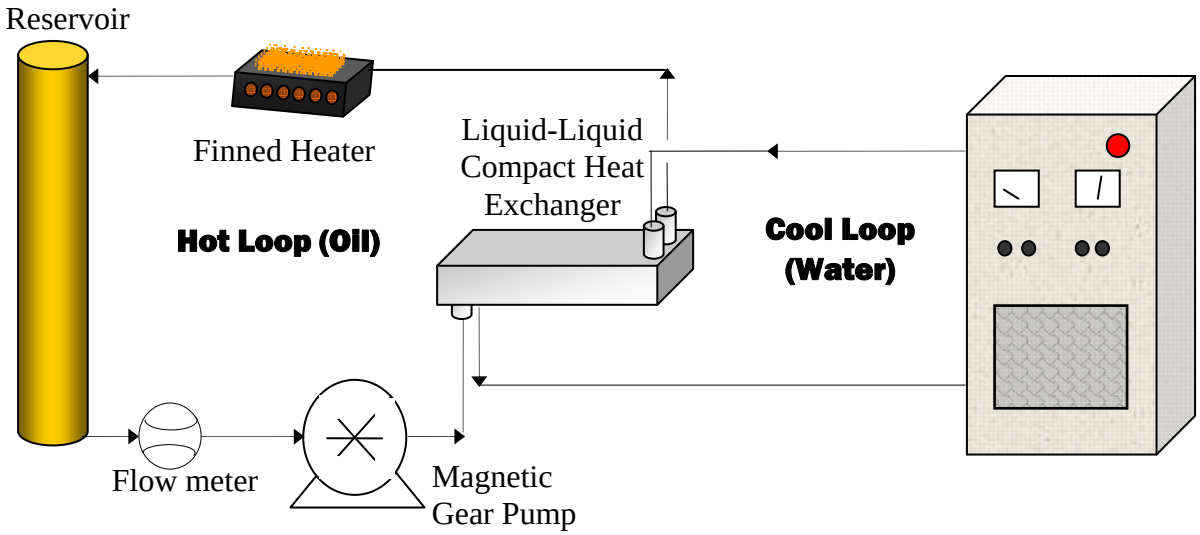

Figure 2. Schematic of Experimental Test Setup.

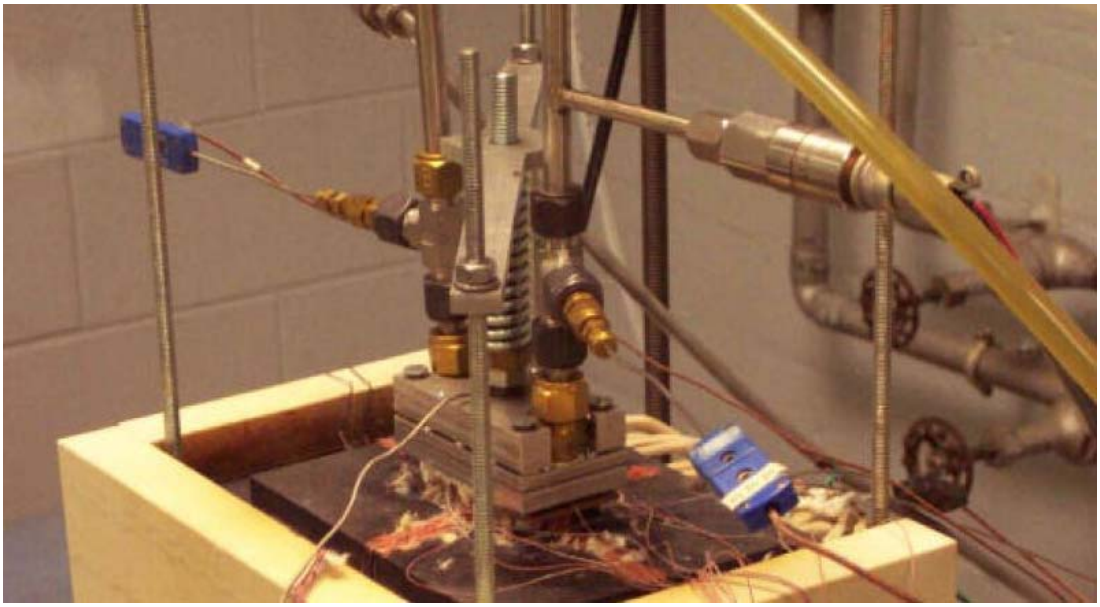

Figure 3. Photograph of Experimental Setup (Lin, 2002; Lin *[AIAA]*, 2002).

copper heat focusing block. Seven cartridge heaters and 8 thermocouples were embedded in the heat focusing block. The heater apparatus was connected to a DC power supply and was used to heat the coolant in the cooler apparatus. The thermocouples were placed in the upper part of the heat focusing block and were arranged in four pairs in two horizontal planes. These thermocouples were used to measure the heat flux into the cooler at different locations (marked as: E, W, N, S). The distance between each pair of thermocouples was 5.1 mm. The heater and cooler were insulated with fiberfax. Figure 3 shows a photograph of the experimental heating chamber apparatus (Lin, 2002; Lin *[AIAA]*, 2002).

An array of plain fins (offset and gapped by 1 mm) was attached to the heater block (Figure 4). Offset gap fins were chosen for this study since in prior studies this configuration was observed to have the best cooling capability (Lin, 2002; Lin *[AIAA]*, 2002). The fin array contained fourteen rows of twenty copper fins and was soldered onto a substrate.

An intermediate plate (thickness 0.8 mm) was mounted between the heater and fin array in the cooler. Machined slots in the plate were used to house ten T-type thermocouples (0.3 mm bead diameter) for measuring the temperature on the bottom of the cooler substrate, as seen in Figure 5. The thermocouples were electrically insulated and mounted in the slots using epoxy glue. Thermal grease (Omegatherm, manufacturer: Omega) was used to minimize the thermal resistance between the intermediate plate, the heater and cooler in the sandwich assembly which was held together by a compression mount. The location of the thermocouples was used to estimate the temperature distribution in the cooler apparatus. The temperatures on the bottom surface were measured by the thermocouples and were used to calculate the surface temperatures at the base of the fins by:

$$T_{b,m} = T_{s,m} - \frac{q_{ts}}{k_s} \qquad (8)$$

Fig. 5 shows an exploded layout of the base of the cooler apparatus. In the cooler apparatus the coolant flowed downwards into the cooler turned 90° to the fin channels, crossed the fin array, and the left the cooler at right angles to the substrate. The coolant inlet temperature was maintained at a constant temperature using the heat exchanger

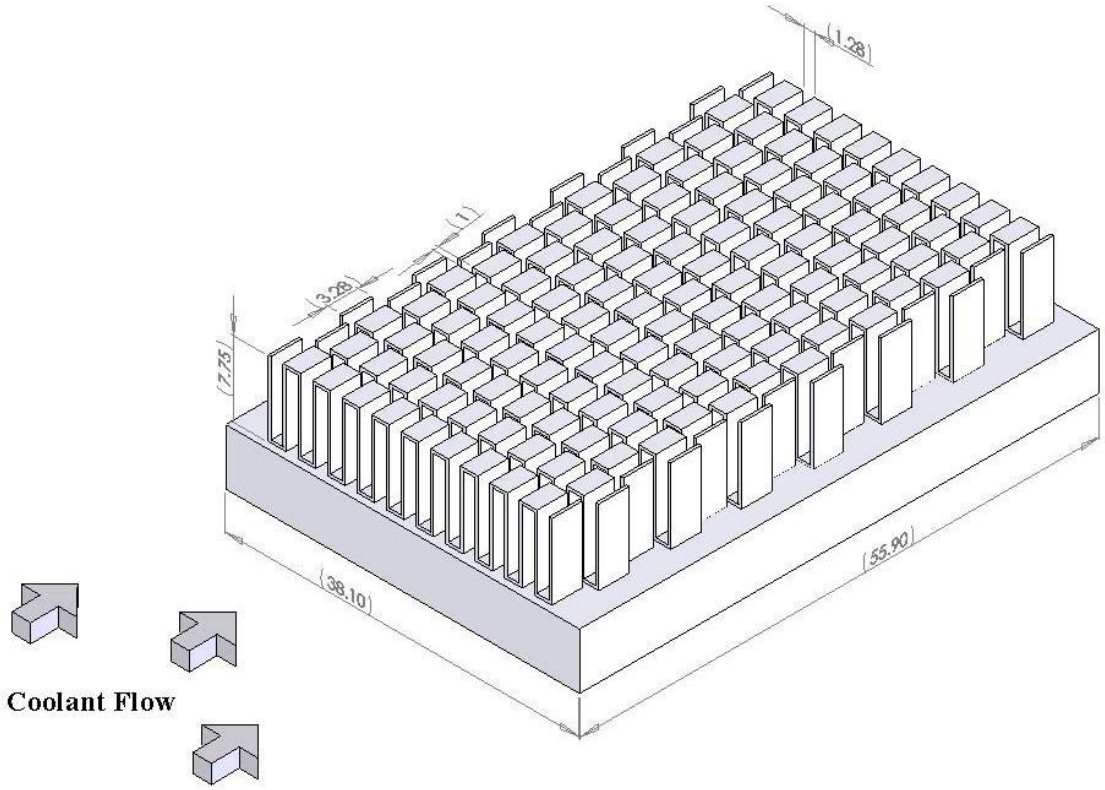

Figure 4. Schematic of the offset gap plain fin array used in this study.

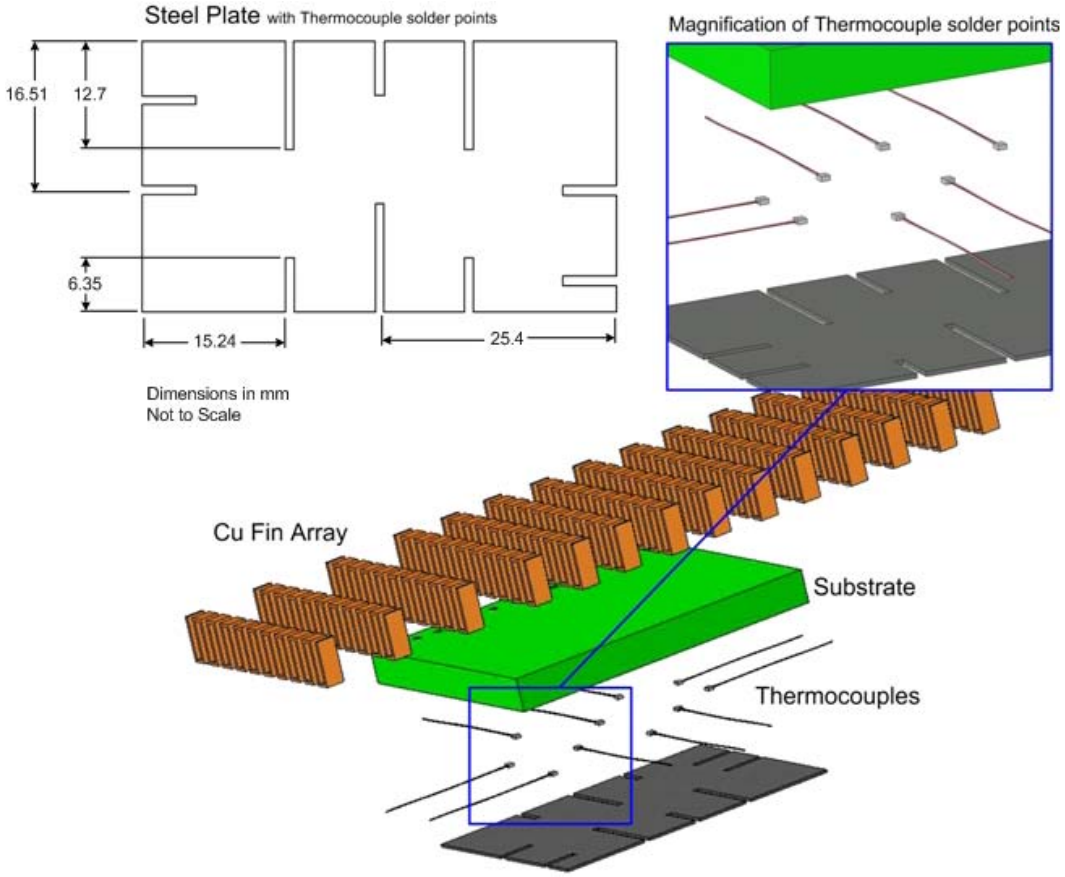

apparatus which was connected to a constant temperature bath. The test fluid inlet and outlet temperatures from the cooler were measured using two probe thermocouples. The mean temperatures ($T_{l\text{-}m}$) for the test fluids were calculated using the arithmetic mean of the inlet and outlet temperatures of the cooler (Lin, 2002; Lin *[AIAA]*, 2002). The test fluid properties were calculated using the mean temperature of the test-fluids. The dimensions of the offset fins used in the experiments are listed in a separate reference (Lin, 2002; Lin *[AIAA]*, 2002).

The coolant inlet temperature was held constant at 75 °C for these experiments in order to cross-check the baseline data for pure solvent, (i.e., PAO) with previous data reported using the same experimental set-up (Lin, 2002; Lin *[AIAA]*, 2002). The nanofluid concentration used in these experiments was 0.5% by weight of multi-walled carbon nanotubes (MWNT) in PAO. The MWNTs were functionalized using a cyano-urate silane to encourage dispersion in the PAO. During the test, the experimental conditions were varied in the following range:

- Input Power: 100 W to 500 W
- Coolant Flow Rate: 0.033 L/s (0.52 gpm) to 0.095 L/s (1.5 gpm).

Uncertainty Measurement

A Hewlett Packard 3852A data acquisition system was used to record the experimental parameters (electrical output signals from the measuring instruments for temperature, flow rate, and pressure). The resolution for temperature measurement for the data acquisition system was 0.02 °C and the accuracy of the measured temperature was reported to be 0.2 °C (Lin, 2002; Lin *[AIAA]*, 2002). The machining and positioning accuracy between any two thermocouples for heat flux measurement was reported to be 0.3 mm. The uncertainty for the positive displacement flow meter was 6.3 × 10-4 L/s. After steady state conditions were reached, all of the experimental data (including temperature and flow rates) were acquired 50 times in an interval of 1 minute and the average values were recorded. The thermo-physical property values for PAO were evaluated at the mean temperature using correlations obtained from the literature (Ghajar, 1994). A basic Kline-McKlintock uncertainty analysis was performed for the heat rate calculation, which determined the maximum observed uncertainty to be ±6%.

Results and Discussion

CNT Functionalization

To verify that the CNTs were chemically functionalized, the sample was evaluated by XPS post processing, for which the presence of the silane compound was confirmed. The XPS spectra from before and after the functionalizing process are shown in Figure 6. The slight peaks of silicon (100 and 150 eV) and nitrogen (400 eV) in the post processed sample indicates the presence of the silane as opposed to the sole peaks of carbon and oxygen in the original state.

Additionally, a thermal gravimetric analysis (TGA) of the post-functionalized tubes verifies the silane presence by the breakdown of the silane compound near 400 °C, as seen in Figure 7. The chemical decomposition of the silane results in a drop in weight of the sample, further showing that the CNT sample was functionalized by roughly 4% weight. This is reasonable considering that the silane only bonds with oxygen on tube imperfections, for which XPS data showed a molecular composition of 11% oxygen in the CNT sample's original state.

Unfortunately, after the CNTs were dispersed in the PAO, significant settling was observed despite the functionalization. It is likely that a more desirable dispersion could have been

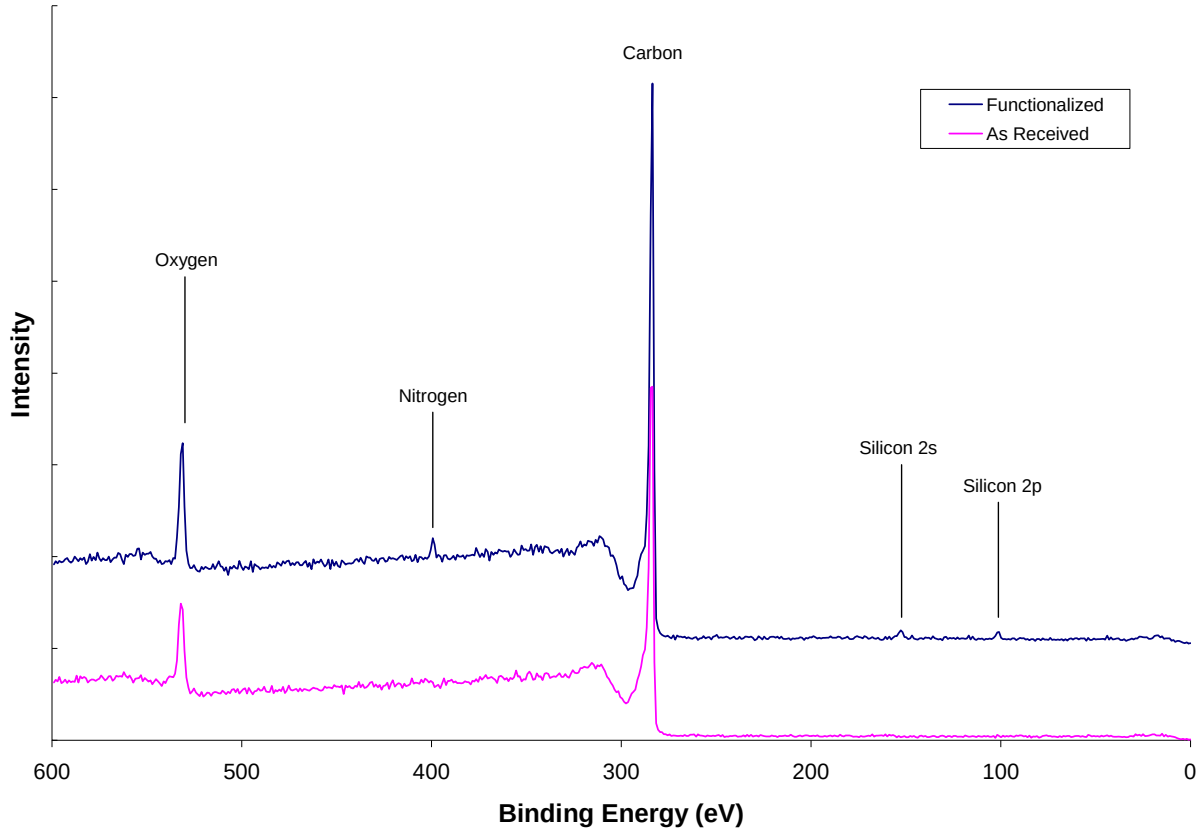

Figure 6. XPS Comparison of Functionalized and As Received MWNTs.

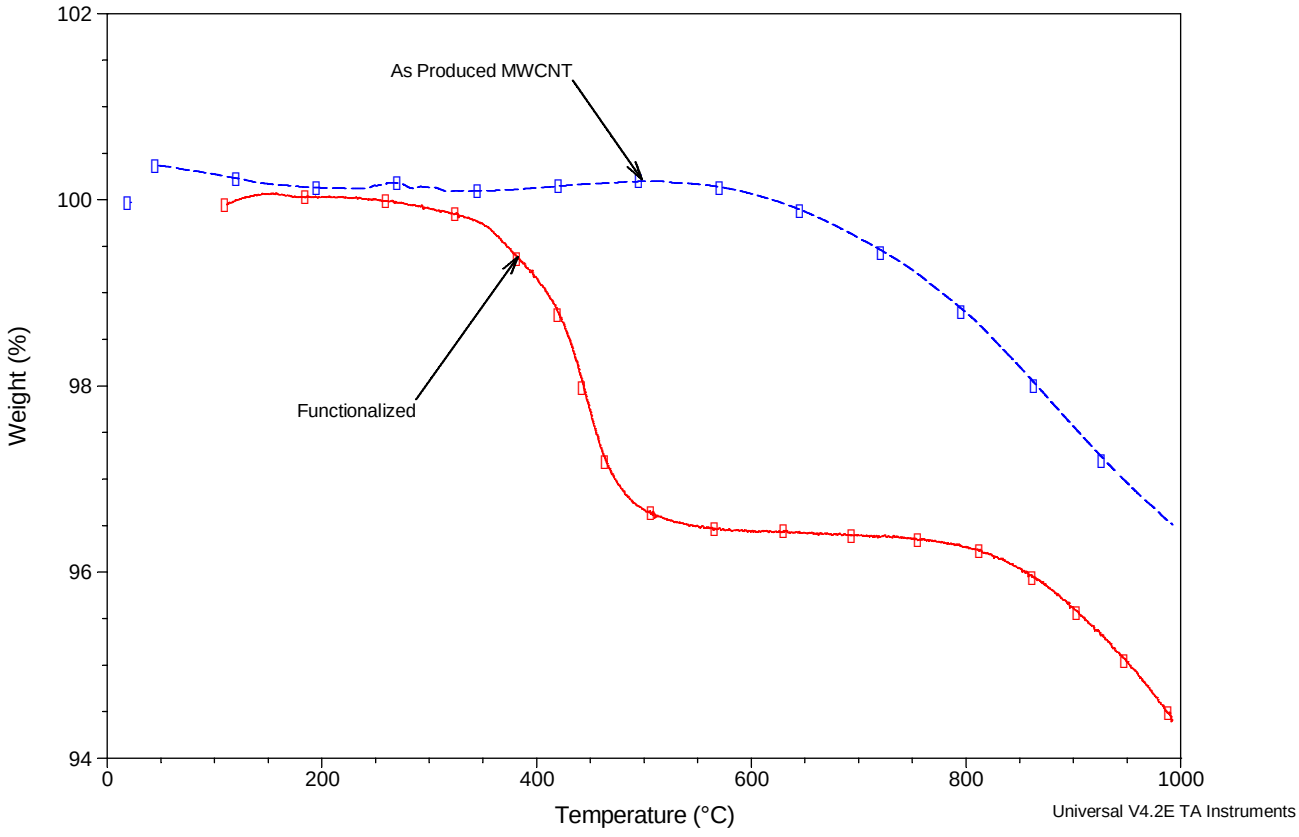

Figure 7. TGA Analysis of Functionalized and As Received MWNTs.

obtained using the intended silane ester compound for functionalizing the nanotubes.

Thermo-Physical Property Measurements for PAO Nanofluids

The thermo-physical properties that are required to evaluate the forced convective heat transfer performance of nano-fluids in these experiments are: specific heat capacity (Cp), density (ρ), viscosity (μ) and thermal conductivity (κ), or thermal diffusivity (α). These properties were needed as a function of temperature for the temperature range of the experiments (75 °C – 125 °C) and are provided in Table 1.

Specific Heat Capacity (Cp): The specific heat of nano-fluids and PAO were measured as a function of temperature using Differential Scanning Calorimetry (DSC) and is plotted in Figure 8. The results show that the specific heat for PAO increases

Table 1. Thermophysical Properties

Property Data (75 °C)	PAO	PAO Nanofluid
Density (kg/m^3)	737	782
Viscosity (Pa·s)	0.0016	0.0018 (?)
Specific Heat (kJ/°C kg)	2.33	2.75

marginally with temperature whereas the nanofluid remains fairly constant except for a slight peak that occurs near 100°C. This may be an effect of the CNTs unlinking at higher temperatures leading to a more uniform dispersion. At any rate, there is marked increase in specific heat of nano-fluid over the base fluid. The specific heat capacity of the nanofluid was found to be enhanced by ~100% compared to PAO at 0.5% concentration by weight for the operating temperatures.

Viscosity (μ): The viscosity of nanofluid

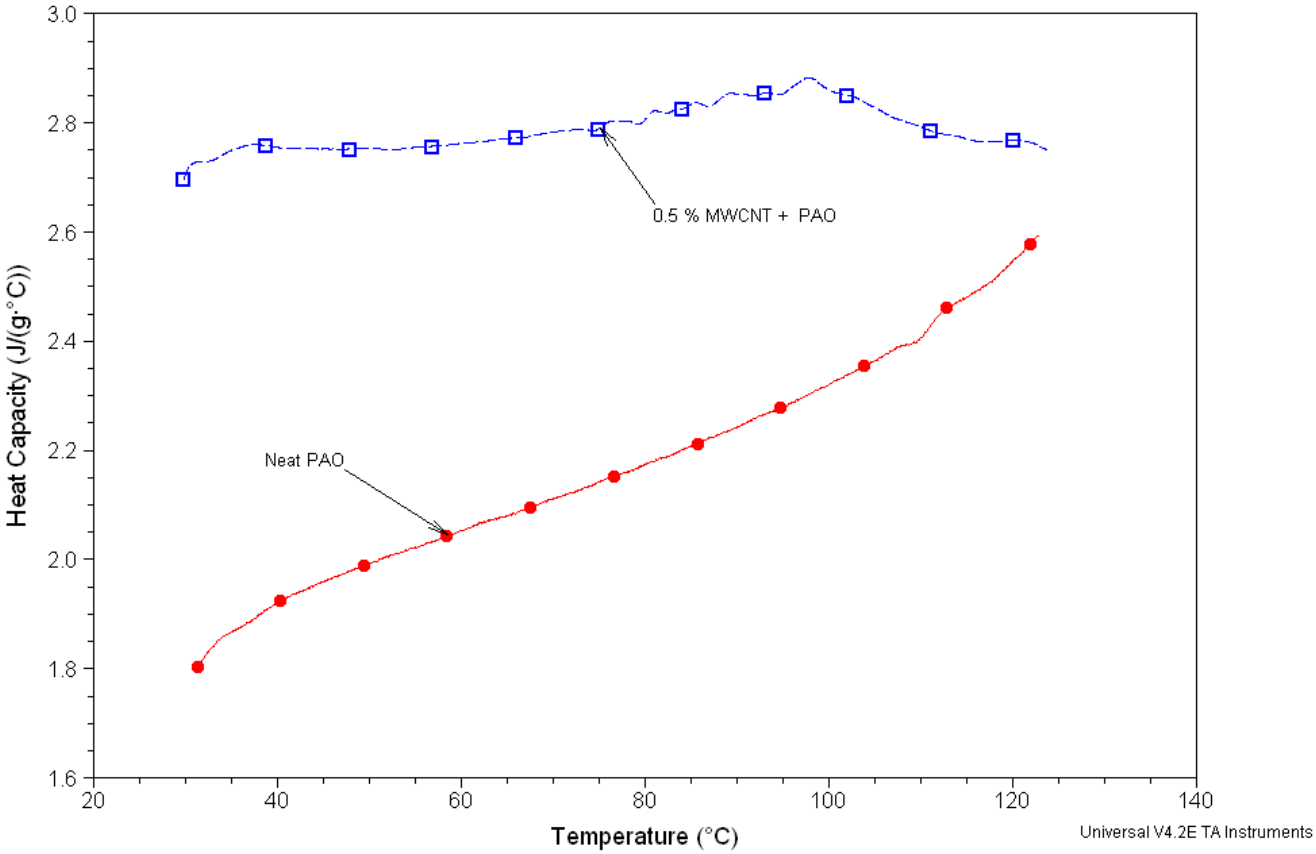

Figure 8. Variation in Specific Heat with Temperature for PAO and Nanofluid.

(0.5% concentration) was measured using rheometry and was observed to be 11% higher than PAO. Because of instrumentation problems, the viscosity as a function of temperature was not able to be determined for the nanofluid. Room temperature measurements were taken to get a general idea of the viscosity values, but eventually, a more precise measurement will be taken to accurately describe the nanofluid behavior. The value listed in Table 1 is an estimated value based on the room temperature measurement.

Thermal Diffusivity (α) and Thermal Conductivity (κ): Although measurements were not made during the past weeks for these properties due to lacking the availability of the equipment, the diffusivity and conductivity of the nanofluid will be measured at Texas A&M facilities within the coming month. A laser flash apparatus will be used such that the nanofluid can be compared to the PAO. For the calculations performed in this study, the conductivity of the nanofluid will be assumed to be the same as the similar fluid used by Choi, et al (Choi, 2001).

Density (ρ) of the nanofluid was measured to be 782 kg/m^3 at operating temperature (~350K).

Convective Heat Transfer

Experimental results were obtained for a range of heat fluxes from 6 to 30 W/cm^2 with reference to the heating area (Ah). The Reynolds number (Re) variation for PAO in these experiments was from 130 to 450. The Reynolds number variation for nanofluid could not be determined in the absence of appropriate property data. The heat transfer coefficient was implicitly expressed in the following equations as (Mills, 1995; Lin, 2002). (for details about the nomenclature please see Ref. Lin, 2002):

$$Q = \left[n_f n_{st} \sqrt{hPk_f A_c}\, \tanh(sl_1) + A_b h \right] \left(T_{b,m} - T_{l,m} \right) \quad (9)$$

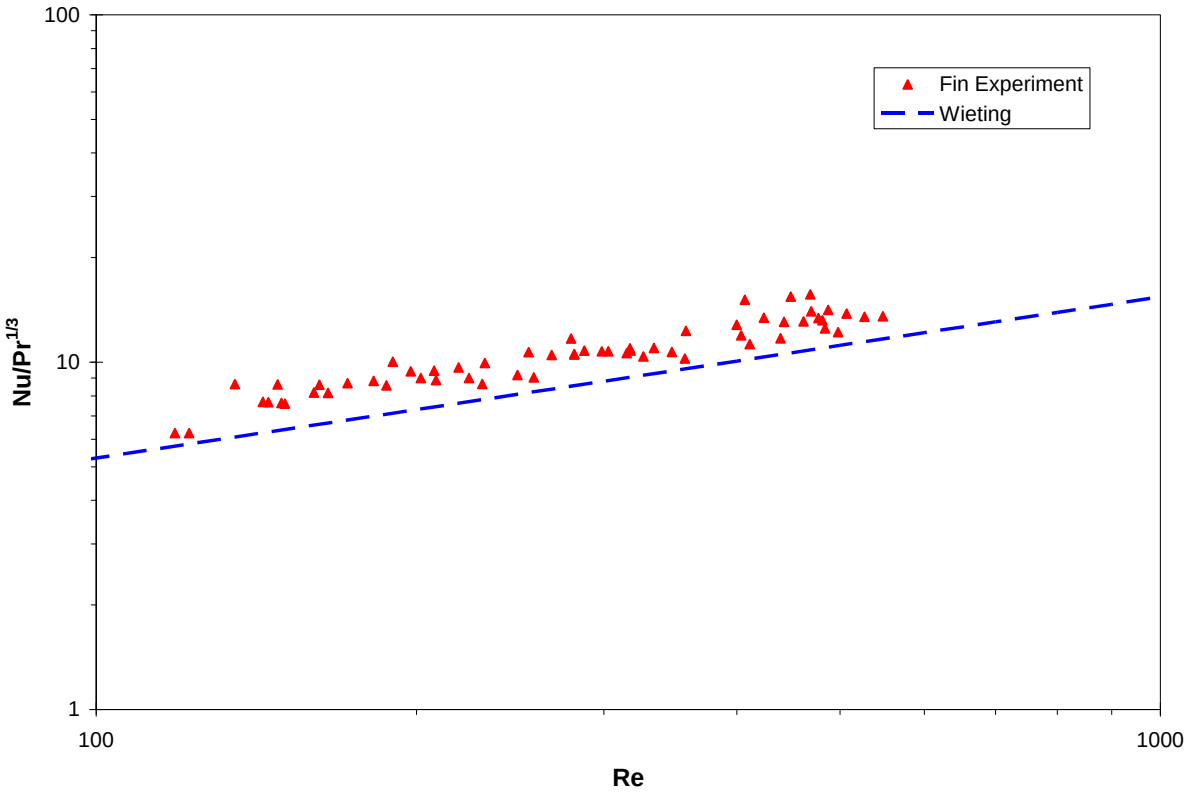

Figure 9. Baseline Experiment Results for Finned Heater Performance. Wieting's Correlation (Wieting, 1975; Joshi, 1987) is presented for reference.

where,

$$s = \sqrt{\frac{hP}{k_f A_c}} \qquad (10)$$

The heat transfer coefficient (h) was iteratively obtained from experimental data for PAO by using Equation (9).

Baseline Experiments with PAO

The heat transfer data for PAO was expressed by plotting $Nu/Pr^{1/3}$ as a function of Re (Figure 9 on the previous page). The data for gap fins show an enhancement in heat transfer coefficient compared to the Wieting correlation. This consistent with earlier observation (Lin, 2002; Lin *[AIAA]*, 2002) where the heat transfer coefficient was also reported to be higher for offset fin strip layout with gaps greater than 1mm. These experiments were performed to establish the base line data for comparison with nanofluids. The data also helped to establish any instrument bias compared to prior experiments reported in the literature using the same experimental apparatus (Lin, 2002; Lin *[AIAA]*, 2002).

Finned Heater Results

The flow loop experiments were conducted by parametrically increasing the heat input from the cartridge heaters for given flow rates. The results from these experiments are plotted for different values of heat input to the cartridge heaters (Figure 10). For each heat input, the results show that the heat rejection rate for the nanofluid (indicated in red) was consistently higher than the plain PAO (indicated in blue) by 15 – 30 % at flow rates less than 1 gpm, above which the performance of both fluids were similar. The enhancement seen appears to be slightly less in the highest two heat inputs, which may indicate that the performance of the fluid has some dependence on temperature.

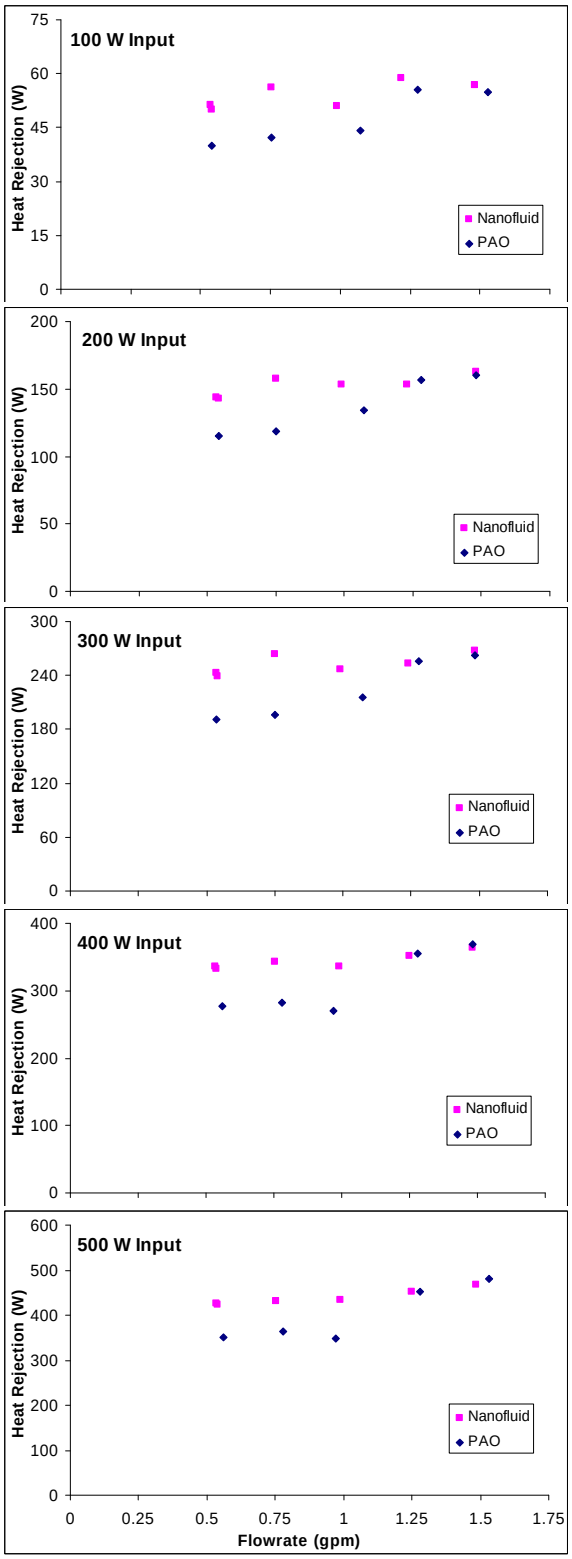

Figure 10. Comparison of Heat Removal Rates from Fin Array for Varying Flow rate and Heat Input.

Heat Exchanger Results

Additionally, the performance of the compact heat exchanger was monitored for both the nanofluid and the PAO. As in the results from the fin array, the flow rates were varied parametrically with the heat input into the system from the cartridge heaters to obtain different inlet conditions on the oil side of the heat exchanger. The water side of the heat exchanger was supplied at a constant flow rate and temperature (75°C). Figure 11 shows the heat exchange rate for varying flow conditions when given differing inlet temperatures. Note that Figure 11.a and 11.b are at inlet conditions less than the water temperature, indicating heat transfer into the oil, while Figure 11.c and 11.d have higher inlet temperatures, indicating a heat rejection from the nanofluid/PAO. In the heat absorption mode, the results echo those seen in the fin heater array where the flow rates less than 1 gpm see a 20 – 50 % enhancement in the nanofluid over the plain PAO, while showing little significant difference at the higher flows. In the heat rejection mode, however, the results are somewhat different. Here it is observed that the rejection rates for both the PAO and the nanofluid are quite similar across the flow spectrum, with perhaps a slight enhancement around 10%. This could be attributed to possible temperature dependent effects in the nanofluid as alluded to in the finned heater results.

Pressure Drops across Heating Elements

While increasing thermal properties and enhancing convective heat transfer with nanofluids is important, excessive increases in pumping requirements because of significant pressure drops can completely invalidate the use of nanofluids. Using differential pressure transducers (Omega), the

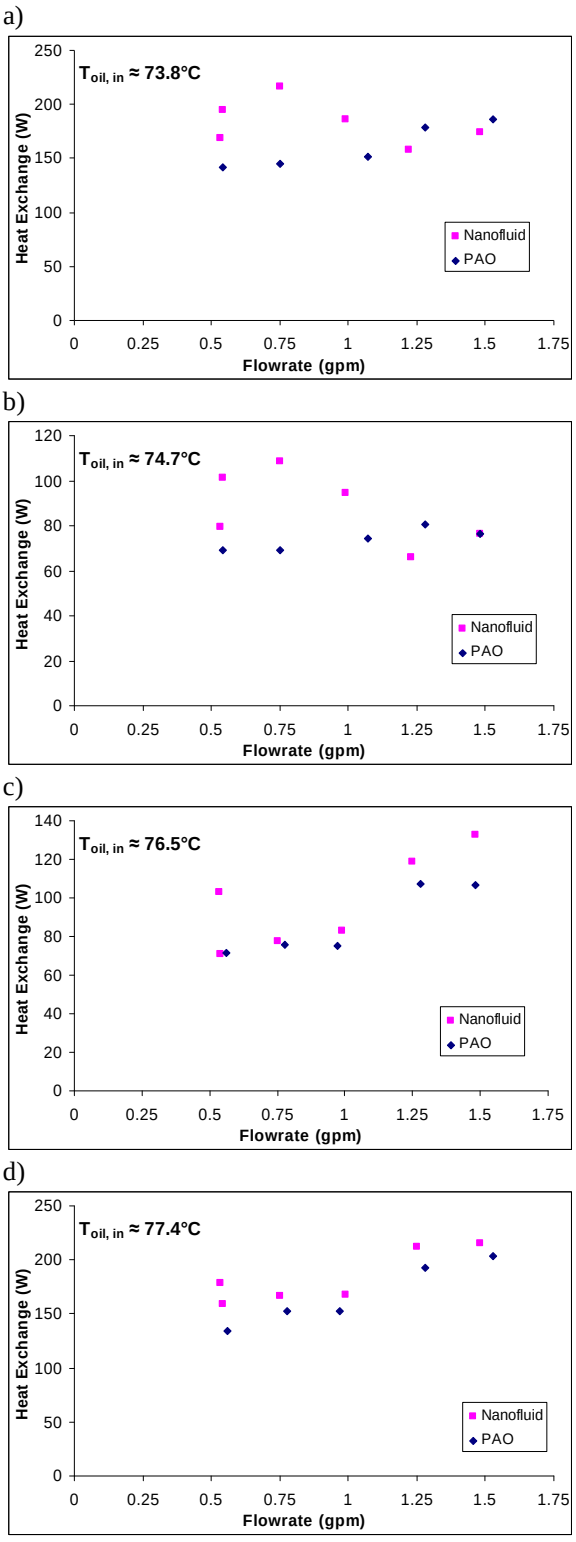

Figure 11. Comparison of Heat Exchange Rates in Compact Heat Exchanger for Varying Flow rates and Oil Temperature Inlet Conditions.

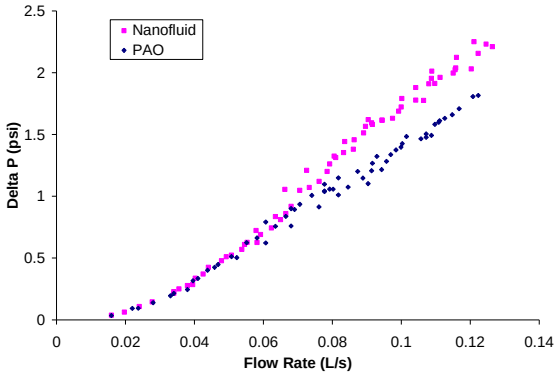

Figure 12. Pressure Drop across Gap-Fin Heater Element for PAO and Nanofluid.

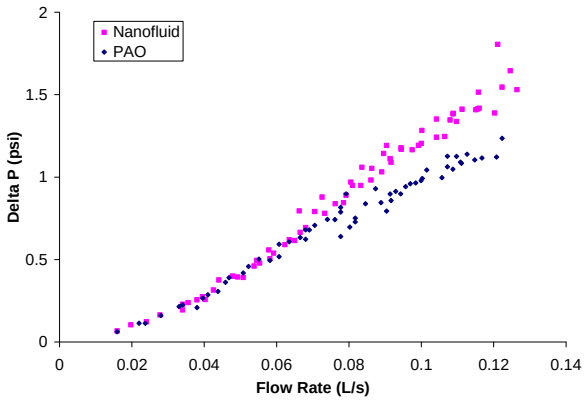

Figure 13. Pressure Drop across Compact Heat Exchanger for PAO and Nanofluid.

pressure drops across the finned heater and the heat exchanger were observed for a range of flow rates at the operating temperature. These readings for both neat PAO and the nanofluid are presented in Figures 12 and 13. As can be seen in the charts, both elements exhibit similar pressure drops at low flow rates (less than 0.07 L/s or 1 gpm) for the nanofluid and the PAO. However, a difference becomes evident as the flow rate increases where the pressure drop for the nanofluid across both the gap-fin heater and the heat exchanger is roughly 25% higher for the maximum flow conditions. The water side of the heat exchanger was maintained at a constant flow, resulting in a constant pressure drop of 1.1 psi.

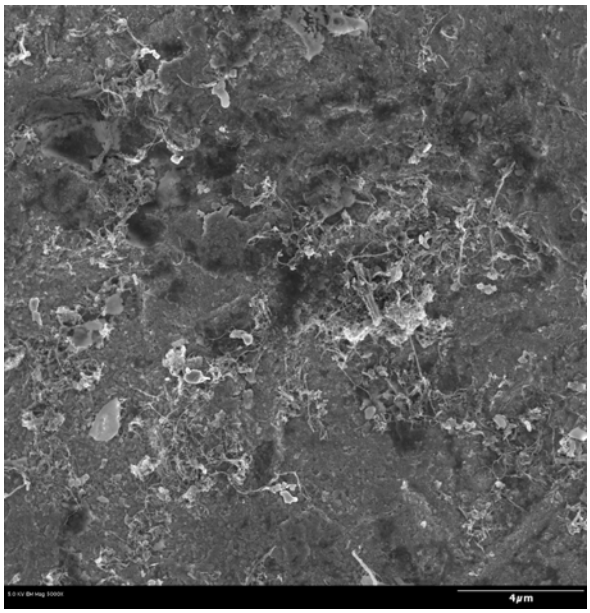

Figure 14. Micrograph Overview of Fin Surface

Scanning Electron Micrography (SEM)

To explore the reason behind the enhancement on heat flux for nanofluids it was hypothesized that the nanofluids deposit nano-particles on the surfaces inside the flow loop (possibly due to electro-static interactions). These nano-particles act as "*nano-fins*" which enhance the effective surface area of the walls and therefore act as enhanced heat transfer surfaces. To test this hypothesis a fin surface was observed under a scanning electron microscope. Figure 14 shows a representative micrograph of the fin surface at a relatively low magnification. Her it can be seen that the surface of the fin is coated with nano-particulate matter in varying concentrations across the surface, likely due to flow patterns over the fin array. A closer examination of surface revealed the substantial presence of CNTs deposited on the surface. Figure 15 a and b respectively show high magnification images of CNTs present on the surface in both densely populated areas and less dense areas. It was additionally observed that the tubes in many locations had bundled together such that in some areas they formed columns of tubes

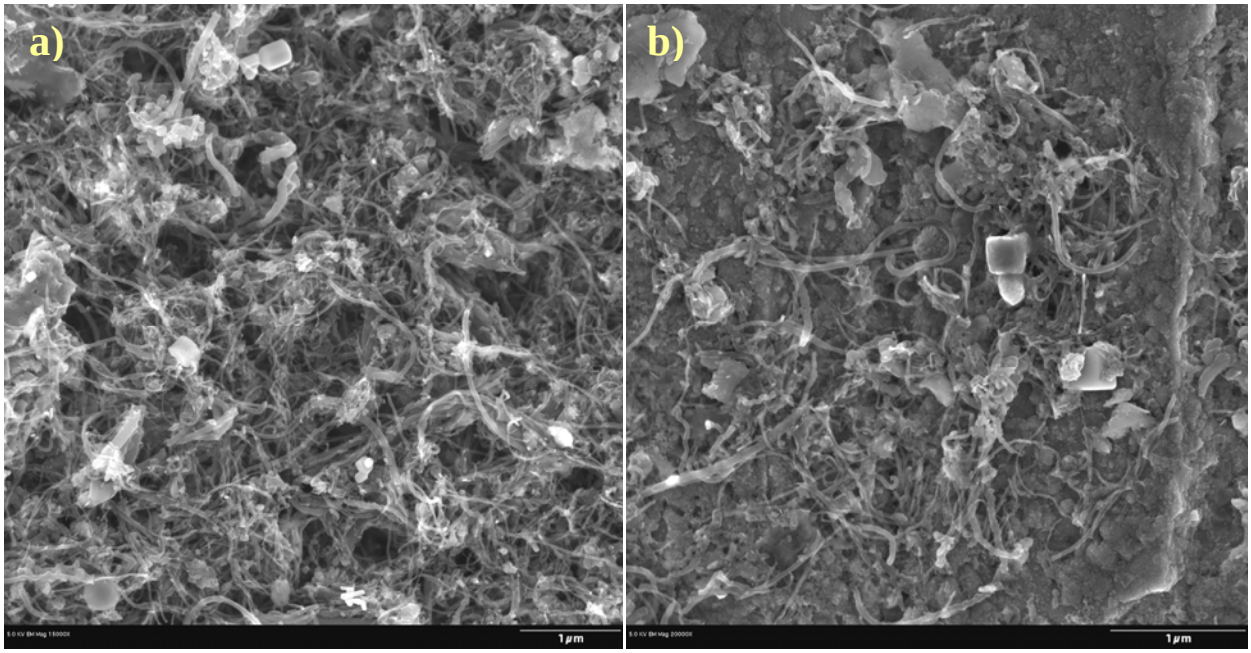

Figure 15. SEM Micrographs of a) High-Density and b) Low Density Collections of CNT on Fin Surface

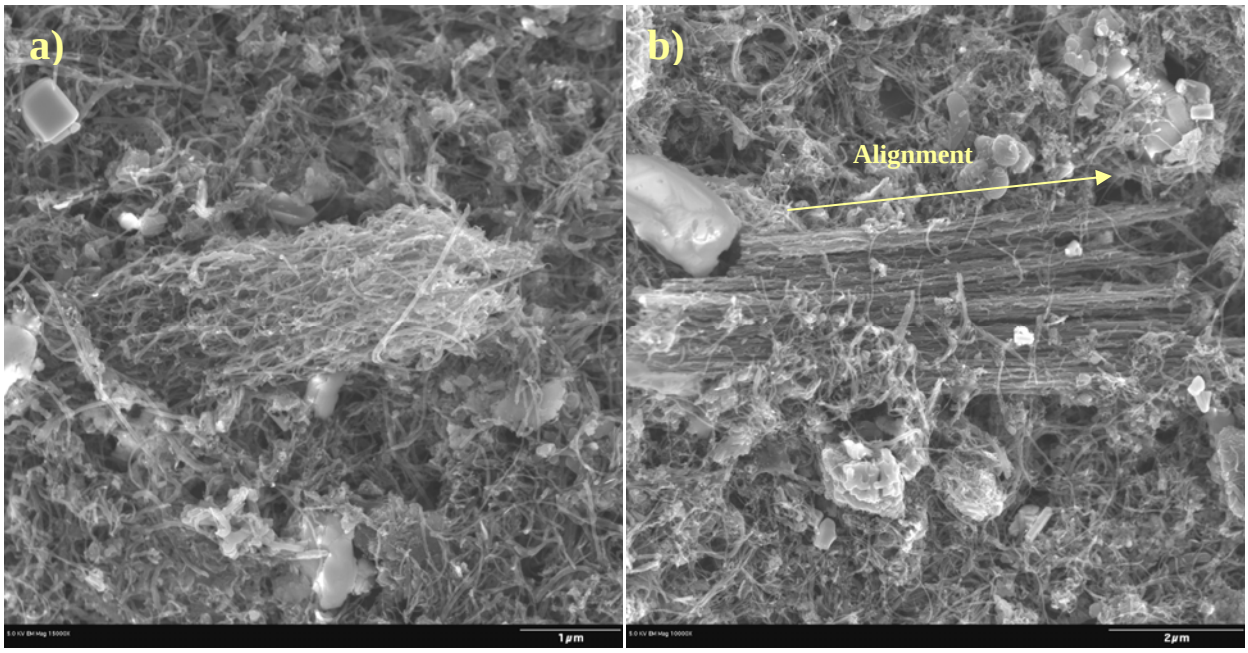

Figure 16. SEM Micrographs of a) Bundled CNT Column and b) Aligned CNTs on Fin Surface

while in others they aligned themselves, perhaps due to flow (as seen in Figure 16 a and b, respectively). Other particles are also observed in these images and are presumably remnants of amorphous carbon produced with the tubes. The smooth appearing shapes are thought to be residual hydrocarbons left behind when the PAO oil was baked off of the surface of the fins (for the sake of maintaining the SEM vacuum pump and components). These particles are in relatively low concentration, and can be assumed to have negligible effects in the experiment. In any case, it is clear that the

tubes deposit on the surface when the nanofluid passed over the surface, from which it is reasonably assumed it results in enhanced surface properties for convection into the fluid on a nano-scale.

As shown by the study of Ding *et al* (Ding, 2006), lower aspect ratio particles such as graphite nano-particles limit the heat transfer enhancement of nanofluids while the higher aspect ratio of carbon nanotubes result in higher enhancement of thermal conductivity as well as forced convective heat transfer. Some of these effects may be explained by the CNT's superiority as a fin element, where could justifiably be reckoned as fins of infinite length because of their aspect ratio and high conductivity. As such, they would hold exhibit the maximum efficiency at dissipating heat at the nano-scale. As a means of comparison, it would be desirable to additionally test single-walled CNTs in a PAO based nanofluid as well as retest the same concentration of MWNT nanofluid but functionalized with the originally intended silane ester compound for enhanced dispersion.

Conclusion

Experiments were conducted using PAO and CNT nanofluids. The nanofluids were found to enhance heat transfer in a flow loop containing a cooler with offset fins as well as in a compact heat exchanger. The nanofluids were also found to have enhanced thermo-physical properties. SEM measurements show that the flow of nanofluids through a system results in the deposition of CNTs on the surface which act as enhanced heat transfer surfaces ("*nano-fins*").

Additional experiments are planned for single-walled CNTs for comparison as well as variations on the nanoparticles including different functionalizing agents in combination with CNT and exfoliated graphite dispersed in PAO.

Acknowledgments

D.B. Author thanks the Air Force Office of Scientific Research (AFOSR) and the American Society for Engineering Education (ASEE) for providing AFRL Summer Faculty Fellowship (2006) which enabled this study. I.C.N. Author thanks the AFOSR and UES for the summer financial support that enables the participation in this research work. The authors would like to express their sincere gratitude to Dr. L. Lin (UDRI), Mr. Dick Harris (UDRI), Mr. Roger Carr (UDRI), Mr. Jacob Lawson (UDRI) and Mr. John Tennant (UES) for their help with performing the experiments. The authors also thank Dr. Sabyasachi (Raj) Ganguli (contractor/AFRL) and Dr. Ajit Roy (ML/ AFRL) for their help with the thermo-physical measurements (specific heat). Last but not the least; the authors thank Dr. K. Lafdi (UDRI) for his help with preparing the nanofluids and for the thermo-physical measurement data for the nanofluids.

Nomenclature

A = Area
Cp = Specific Heat Capacity
D = Hydraulic diameter
l = Length of fin
L = Length of pipe or tube
n = Number of fins
nf = Properties of nanofluid
Nu = Nusselt number
P = Perimeter
Pe = Peclet number
Pr = Prandtl number
q, Q = Heat flux, Total heat transfer rate
Re = Reynolds number
s = Fin parameter
T = Temperature
Ω = Forced convective heat transfer parameter
μ = Viscosity

ρ = Density
κ = Thermal conductivity
α = Thermal diffusivity
φ = Volume fraction

References

Choi, S.U.S., Zhang, Z.G., Yu, W., Lockwood, F.E., and Grulke, E.A., "Anomalous thermal conductivity enhancement in nanotube suspensions", *Applied Physics Letters*, 2001, Vol. 79, No. 14, pp. 2252, 2254.

Das, S.K., Putra, N., Roetzel, W., "Pool boiling characteristics of nanofluids", International Journal of Heat and Mass Transfer, 2003, Vol. 46, No. 5, pp. 851, 862.

Das, S.K., Putra, N., Roetzel, W., "Pool boiling of nanofluids on horizontal narrow tubes", International Journal of Multiphase Flow, 2003, Vol. 29, No. 8, pp. 1237, 1247.

Ding, Y., Alias, H., Wen, D., and Williams, R.A., "Heat Transfer of aqueous suspensions of carbon nanotubes (CNT nanofluids)", International Journal of Heat and Mass Transfer, 2006, Vol. 49, pp. 240, 250.

Eastman, J.A., Choi, S.U.S., Li, S., Yu, W., Thompson, L.J., "Anomalously Increased Effective Thermal Conductivities of Ethylene Glycol-based Nanofluids Containing Copper Nanoparticles," Applied Physics Letters, Vol. 78, Number 6, 2001, pp. 718-720.

Eastman, J.A., et al., Material Science Forum, 1999, Vol. 629, pp. 312,314.

Ghajar, A.J., Tang, W.C., and Beam, J.E., 1994, "Comparison of Hydraulic and Thermal Performance of PAO and Coolant 25R Liquid Coolants", Proceedings of the 6th AIAA/ASME Joint Thermo-physics and Heat Transfer Conference, Colorado Springs, CO (AIAA-94-1965).

Hamilton, R.L., and Crosser, O.K., "Thermal conductivity of heterogeneous two-component systems", *I&EC Fundamentals*, Vol. 1, 1962, pp. 182, 191.

Heris, S.Z., Etemad, S.Gh., Esfahany, M.N., "Experimental investigation of oxide nanofluids laminar flow convective heattransfer", International Communications in Heat and Mass Transfer, 2006, Vol. 33, pp. 529,535.

ITRS, International Technology Roadmap for Semiconductors, 2002.

Joshi, H.M., and Webb, R.L., 1987, "Heat Transfer and Friction in the Offset Strip-Fin Heat Exchanger", International Journal of Heat and Mass Transfer, Vol. 30, pp. 69, 83.

Keblinski, P., Eastman, J.A., and Cahill, D.G., "Nanofluids for Thermal Transport," Materials Today, June 2005, pp. 36-44.

Lai, W.Y., Duculescu, B., Phelan, P. and Prasher, R.S., "Convective heat transfer with nanofluids in a single 1.02 mm tube", Proceedings of the 2006 ASME International Mechanical Engineering Congress and Exposition, 2006, Paper No. IMECE2006-14132.

Lee, S., Choi, S.U.-S., Li, S., and Eastman, J.A., "Measuring thermal conductivity of fluids containing oxide nanoparticles", *ASME Journal of Heat Transfer*, Vol. 121, No. 2, May 1999, pp. 280,289.

Li, C.H., Wang, B.X., Peng, X.F., "Experimental investigations on boiling of nano-particle suspensions", Proceedings of the Boiling Heat Transfer Conference, 2003, Jamaica, USA.

Lin, L., "Thermal Management Research for Power Generation", AFRL-PR-WP-TR-2003-2051, 2002.

Lin, L., Ponnappan, R., and Leland, J.E., "Heat Transfer Correlations for Plain Fin Array Cooler", Proceedings of the 40th AIAA Aerospace Sciences Meeting & Exhibit, 2002, Reno, NV (AIAA 2002-0207).

Maxwell, J.C., A Treatise on Electricity and Magnetism, 2nd ed., Clarendon Press, Oxford, UK, 1881.

Mills, A.F., Heat and Mass Transfer, 1995, Irwin Publishers, Boston.

Pak, B.C., and Cho, Y.I., "Hydrodynamic and heat transfer study of dispersed fluids with sub-micron metallic oxide particles", Journal of Experimental Heat Transfer, 1998, Vol. 11, No. 2, pp. 151, 170.

Prasher, R., Bhattacharyya, P., and Phelan, P.E., "Brownian-Motion_Based Convective-Conductive Model for Effective Thermal Conductivity of Nanofluids", ASME Journal of Heat Transfer, Vol. 128, June 2006, pp. 588-595.

Putnam, S.A., Cahill, D.G., Braun, P.V., Ge Z., and Shimmin, G., 2006, "Thermal

conductivity of nanofluid suspension", *Journal of Applied Physics*, 2006, Vol. 99, Paper No. 084308.

Sieder, E.N., and Tate, G.E., "Heat transfer and pressure drop of liquids in tubes", Ind. Eng. Chem., 1936, Vol. 28, No.12, pp. 1429, 1435.

Thermacore Inc., "High Power Electronics", www.coolingzone.com/Guest/News/NL_JAN_2003/Thermacore/Thermacore_Jan_2003.html

Vassalo, P., Kumar, R., Amico, S.D., "Pool boiling heat transfer experiments in silica-water nanofluids", International Journal of Heat and Mass Transfer, 2005, Vol. 47, pp. 407, 411.

Velasco-Santos, C., Martinez-Hernandez, A.L., Lozada-Cassou, M., Alvarez-Castillo, A., Castano, V.M., "Chemical Functionalization of Carbon Nanotubes through an Organosilane", Nanotechnology, 2002, Vol. 13, pp. 495,498.

Wang, X-Q., and Mujumdar, A.S., "Heat transfer characteristics of nanofluids: a review", International Journal of Thermal Sciences, Vol. 46, 2007, pp. 1-19.

Wasan, D.T., and Nokolov, A.D., "Spreading of nanofluids on solids", Nature, 2003, Vol. 423, pp. 156, 159.

Wen, D.S., and Ding, Y.L., "Effect on heat transfer of particle migration in suspensions of nanoparticles flowing through minichannels", Microfluidics and Nanofluidics, 2005, Vol. 1, No. 2, pp. 183, 189.

Wen, D., and Ding, Y., "Experimental investigation into convection heat transfer of nanofluids at the entrance region under laminar flow conditions", International Journal of Heat and Mass Transfer, 2004, Vol. 47, pp. 5181, 5188.

Wieting A.R., 1975, "Empirical Correlations for Heat Transfer and Flow Friction Characteristics of Rectangular Offset-Fin Plate-Fin Heat Exchangers", ASME Journal of Heat Transfer, Vol. 97, pp. 488, 490.

Xie, H., Wang, J., Xi, T., and Liu, Y., "Thermal Conductivity of Suspensions Containing Nanosized SiC Particles," International Journal of Thermophysics, Vol. 23, Number 2, 2002, pp. 571-580.

Xuan, Y., and Li, Q., "Investigation of convective heat transfer and flow features of nanofluids", ASME Transactions Journal of Heat transfer, 2003, Vol. 125, February, pp. 151, 155.

Yang, Y., Zhang, Z.G., Grulke, E.A., Anderson, W.B., Wu, G., "Heat transfer properties of nanoparticle-in-fluid dispersions (nanofluid) in laminar flow", International Journal of Heat and Mass Transfer, 2005, Vol. 48, pp. 1107, 1116.

You, S.M. and Kim, J.H., "Effect of nanoparticles on critical heat flux of water in pool boiling heat transfer," Applied Physics Letters, Vol. 83, No. 16, 20 October 2003, pp. 3374, 3376.

Douglas Hutchens, PhD
Universal Technology Corporation
1270 N. Fairfield Road
Dayton, OH 45432-2600

Subject: Final Report for Phase I: Subcontract Agreement# 07-S530-0047-03-C, Prime Contract# F33615-02-D-2299,

Dear Doug,

A. Per PART II – Program Requirements of Subject Subcontract Agreement, the Final Report for Phase I is as follows:

1. Complete list of papers submitted for publication during the period of this award

   Bostanci, H., Rini, D.P., Kizito, J.P., Chow, L.C., 2008. Spray cooling with ammonia on micro-structured surfaces: performance enhancement and hysteresis effect. Journal of Heat Transfer (In press)

2. Complete list of all presentations delivered during the period of this award
   1. *Huseyin Bostanci, Daniel P. Rini, John P. Kizito and Louis C. Chow. "HYSTERESIS IN SPRAY COOLING OF MICRO-STRUCTURED SURFACES." This paper was presented at Proceedings of the ASME 2008 Summer Heat Transfer Conference, HT2008, August 10-14, 2008, Jacksonville, Florida, USA.*
   2. *Huseyin Bostanci, Benjamin A. Saarloos, Daniel P. Rini, John P. Kizito, Louis C. Chow. "SPRAY COOLING WITH AMMONIA ON MICRO-STRUCTURED SURFACES." This paper was presented at ITherm meeting in Orlando in May 28-31, 2008, USA.*
   3. *Attended a conference called "More Electric Aircraft Technologies and Thermal Energy Management Workshop," at Florida A&M University.*
   4. *Presented phase 1 project at Air force sponsored forum held in Dayton Oct. 2007*

3. Budget update including forecasted vs. actual budget for all budgeted categories. As the budget shows we did not spend about $20K because of late start and lack of graduate students at the start of the project here at NCAT. Now we have the necessary graduate students to complete the tasks 1 and 2. We are requesting the unspent funds be added to phase-II funding to complete tasks 1 and 2 as will be shown below. Task 1 is 90% complete and task 2 is 60% done. We have completed tasks 3, 4, and 5 at

100%. We now have the graduate students in place;one is expected to graduate at the end of the spring semester 2009 and the other two are expected to graduate at the end of the fall semester 2009 with MS in mechanical engineering. One of these graduate students will proceed to pursue a PhD in Mechanical Engineering.

Account	Title	Adjusted Budget	YTD Activity	Commitments	Available Balance
61113	Grad Research Assist	8,552.91	2,890.91	0.00	5,662.00
61118	EPA Faculty Summer Emplc	14,648.31	12,580.24	0.00	2,068.07
61410	Non-Student Reg Wage	7,905.50	7,665.00	0.00	240.50
61450	Undergraduate Hourly Wag	709.00	708.75	0.00	0.25
61610	Social Security	2,188.45	1,602.94	0.00	585.51
61670	TIAA Opt Retirement	1,441.43	1,441.69	0.00	-0.26
71995	Sub-Agreements: amt over	69,041.47	54,815.12	3,483.40	10,742.95
71996	Sub-Agreements: amt up ti	10,481.62	18,956.92	2,267.65	-10,742.95
72300	Educational Supplies	24,180.00	19,998.30	1,301.66	2,880.04
73100	Travel & Registration Fees	0.19	0.00	0.00	0.19
74600	Indirect Cost	28,042.96	25,870.73	0.00	2,172.23
76593	Tuition Remits -- C&G	7,990.80	0.00	0.00	7,990.80
	Total:	175,182.64	146,530.60	7,052.71	21,599.33

4. List of students partially or fully supported during phase I

Student name: Alvin Greg Davis
Academic standing (graduate)

Student name: Rodward Hewlin
Academic standing (graduate)

Student name: Zireva Madzivanyika
Academic standing (graduate)

Student name: Anissa Cunningham
Academic standing (graduate or undergraduate) Just Graduated from undergraduate in our COE

Student name Shuana Adams
Academic standing (graduate or undergraduate) Undergraduate

Student name Imani Adams
Academic standing (graduate or undergraduate) Undergraduate

Plan to hire these students to partially or fully work on the project:

Student name Alexis Manley
Academic standing (graduate or undergraduate) undergraduate

Student name Charles Henley
Academic standing (graduate or undergraduate) undergraduate

5. Solid Works Professor, Daniel Acree was supported for ¾ month to assist with the design and machining of the test loop.

B. Projected activities for Phase II are as follows:
   1. We will begin phase II activity.
   2. We request to complete phase I activity with the unspent funds.

C. This final report and projected activities is respectfully submitted. Please feel free to let me know if you need additional information or have any questions at 336 334 7620 ext 318.

Sincerely yours,

John Patrick Kizito

Dr. John Patrick Kizito

Task 1: Scaling analysis to identify characteristic time and length scales (90% complete)

In summary, this we have used direct numerical analysis to determine the characteristic length scale and time scale for the present problem.

1. Elicit system requirements. We have determined the division of working fluids to be tested: Ammonia for UCF and R134a or Water for NCAT. (We will consider also the following working fluids (R404A, R507, R290 and/or R1270). We are in the process of assembling the test rig capable of cooling 1000 W/cm2 or more. Fluent has been our working commercial code. We have also used Matlab software to develop our in house models.
2. Identify the thermal physical processes and the partial differential equations which describe the physics. The thermo-physical properties required are in place and we have developed methods of measuring these properties.
3. Identify the control physics to obtain the characteristics parameters (timescales, length scales, velocity and temperature scales). We have the numerical models which can be used to estimate the characteristics parameters. For example: flow rates, velocities, etc.
4. Normalize the partial differential equations to extract the non-dimensional numbers which describe the process. The non-dimensional numbers which describe the processes are Reynolds, Jacobs, Nusselt, ratios of thermo-physical properties (density, viscosities and surface tensions), length scales normalized by nozzle diameters and /or standoff distances.

•

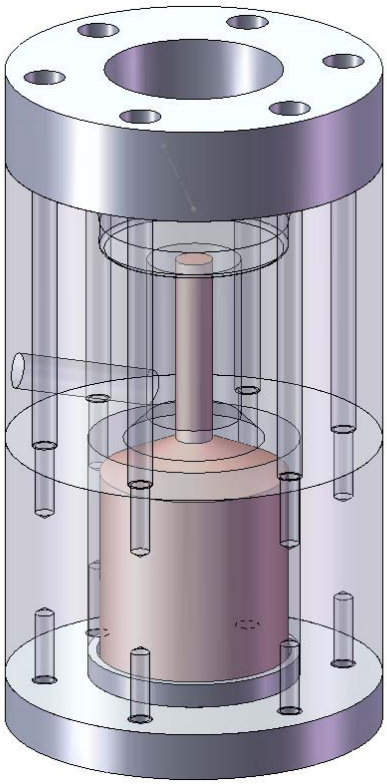

Figure 1: The design of the heat and heater housing including a heater flux gauge for the flow loop

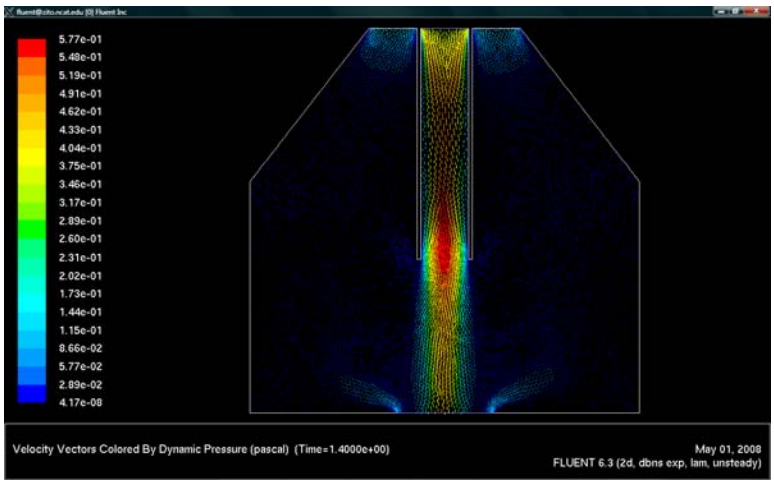

(a)

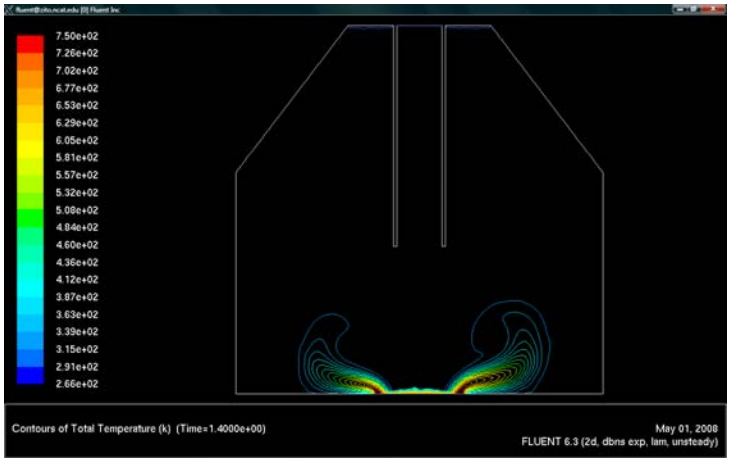
7.50e+02
7.26e+02
7.02e+02
6.77e+02
6.53e+02
6.29e+02
6.05e+02
5.81e+02
5.57e+02
5.32e+02
5.08e+02
4.84e+02
4.60e+02
4.36e+02
4.12e+02
3.87e+02
3.63e+02
3.39e+02
3.15e+02
2.91e+02
2.66e+02
Contours of Total Temperature (k) (Time=1.4000e+00)
May 01, 2008
FLUENT 6.3 (2d, dbns exp, lam, unsteady)

(b)

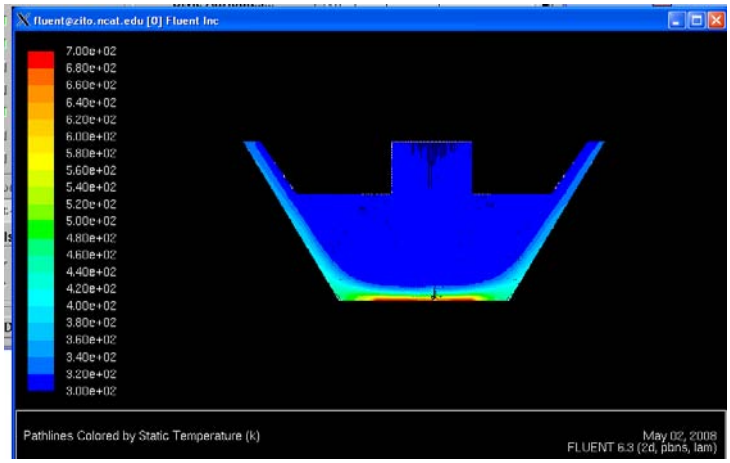
fluent@zito.ncat.edu [0] Fluent Inc
7.00e+02
6.80e+02
6.60e+02
6.40e+02
6.20e+02
6.00e+02
5.80e+02
5.60e+02
5.40e+02
5.20e+02
5.00e+02
4.80e+02
4.60e+02
4.40e+02
4.20e+02
4.00e+02
3.80e+02
3.60e+02
3.40e+02
3.20e+02
3.00e+02
Pathlines Colored by Static Temperature (k)
May 02, 2008
FLUENT 6.3 (2d, pbns, lam)

(c)

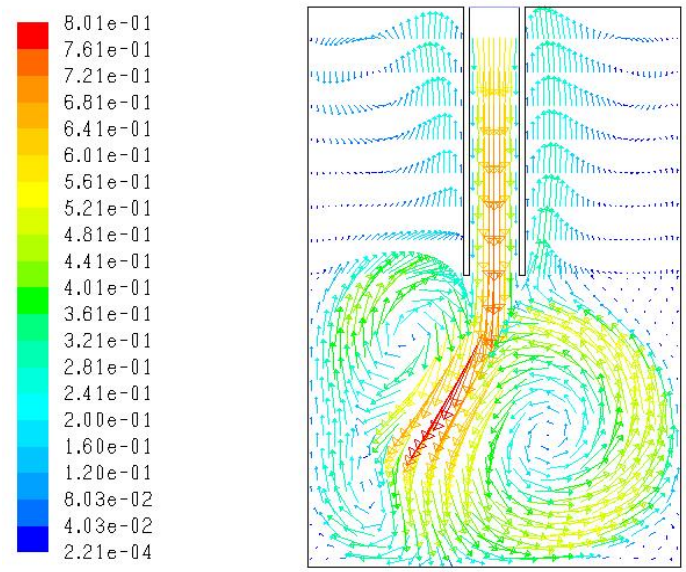
8.01e-01
7.61e-01
7.21e-01
6.81e-01
6.41e-01
6.01e-01
5.61e-01
5.21e-01
4.81e-01
4.41e-01
4.01e-01
3.61e-01
3.21e-01
2.81e-01
2.41e-01
2.00e-01
1.60e-01
1.20e-01
8.03e-02
4.03e-02
2.21e-04
Velocity Vectors Colored By Velocity Magnitude (m/s) (Time=1.0000e+00)
FLUENT 6.3 (2d, dbns exp, lam, unsteady)

(d)

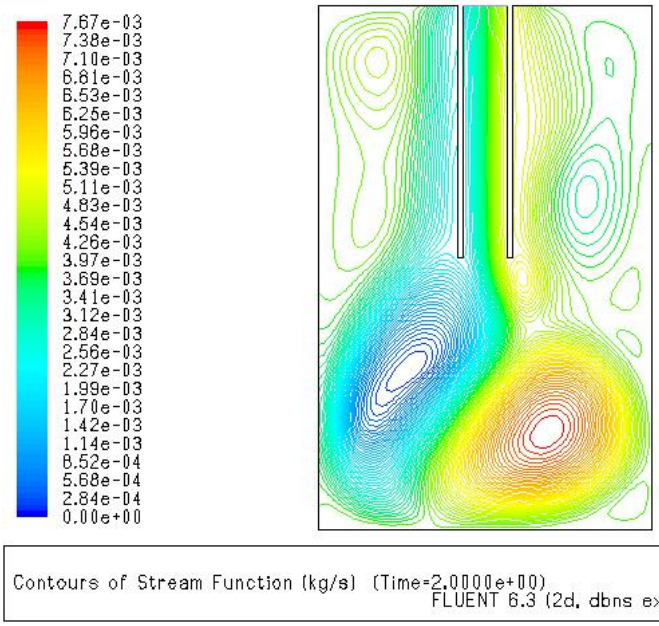
7.67e-03
7.38e-03
7.10e-03
6.81e-03
6.53e-03
6.25e-03
5.96e-03
5.68e-03
5.39e-03
5.11e-03
4.83e-03
4.54e-03
4.26e-03
3.97e-03
3.69e-03
3.41e-03
3.12e-03
2.84e-03
2.56e-03
2.27e-03
1.99e-03
1.70e-03
1.42e-03
1.14e-03
8.52e-04
5.68e-04
2.84e-04
0.00e+00
Contours of Stream Function (kg/s) (Time=2.0000e+00)
May 01, 2008
FLUENT 6.3 (2d, dbns exp, lam, unsteady)

(e)

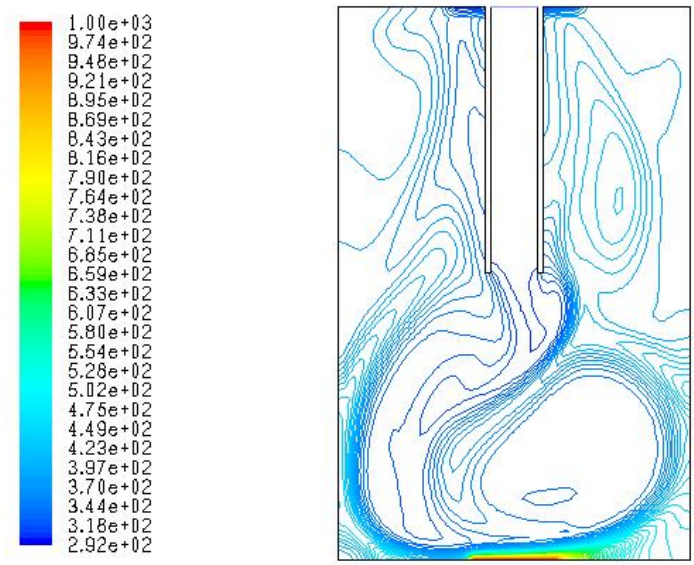

(f)

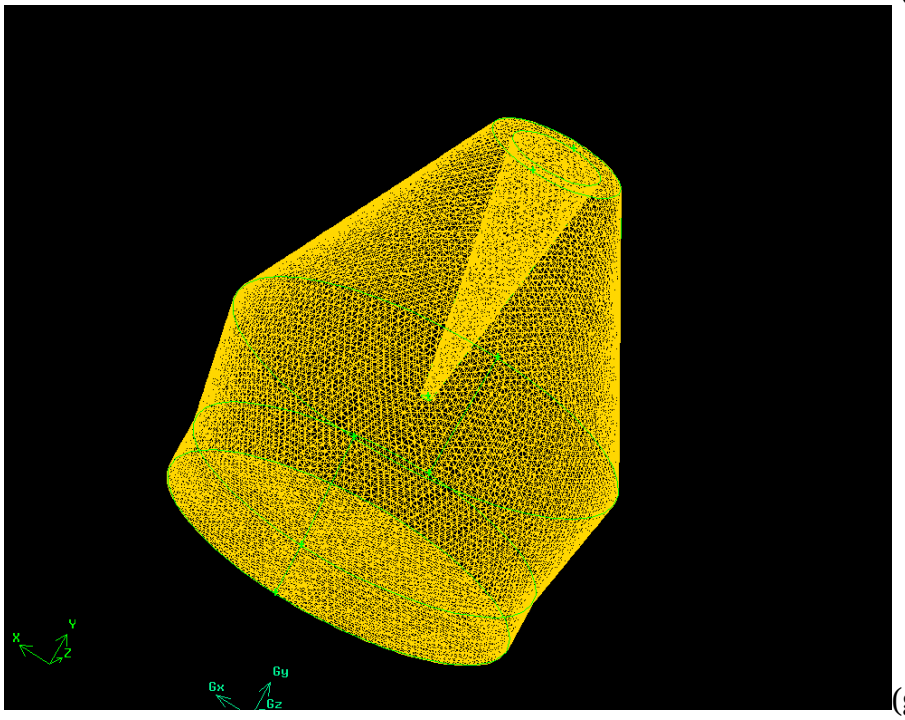

(g)

Figure 2: CFD study designed to obtain optimal chamber design based on shape, operating fluids and to determine characteristic parameters.

Task 2: Development of numerical models for flow in the manifold (60% Complete)

In summary, here are the steps taken to perform this task:

- Acquire the solid CAD model of the manifold and clean CAD prior to volume meshing (RTI model is still being processed)
- Identify surfaces in contact with the fluid or vapor (done)
- Choose mesh type (tetrahedral, polyhedral or hexahedral) after identifying boundary layers surfaces which need special attention (done)
- Identify symmetry and inlet and outlet conditions (done)
- Write advanced scripting for parametric studies (in process)
- Define the multi domain interfaces and the interpolation schemes (done)
- Determine the maximum conditions and if exceeds laminar hydrodynamic range then choose the best-fit turbulence model (done)
- Determine the optimal grid size for resolved and convergent data (done)
- Write scripts to process the data and compare with experimental observations. (in process)
- Below are examples of numerical result obtained to determine the fluid management issues.

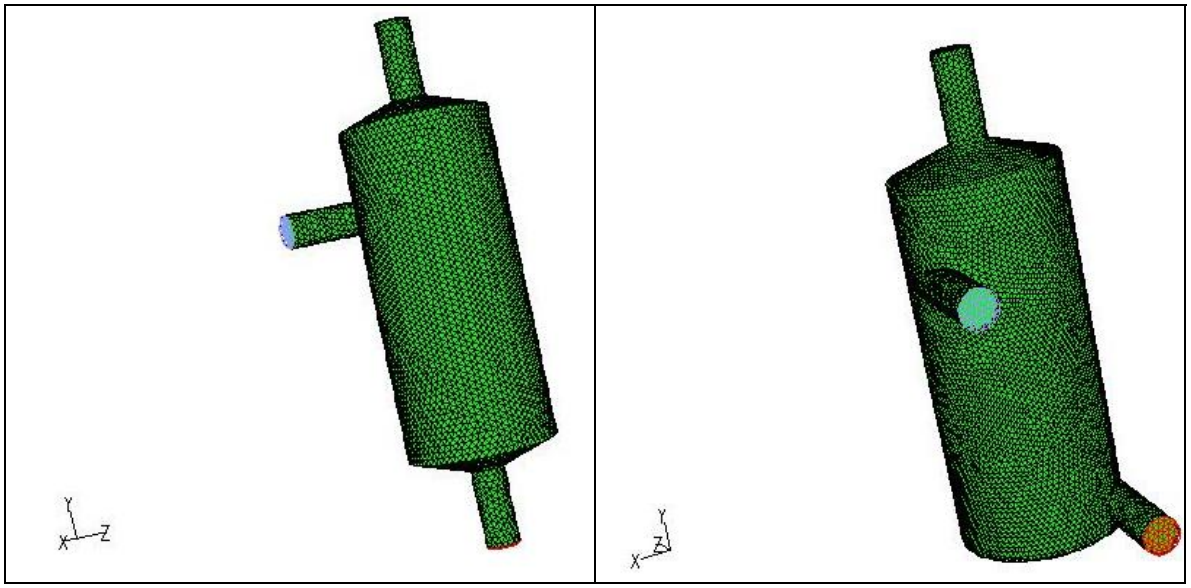

- Figure 3 Design iteration for gas-fluid separator to be used in the NCAT rig.

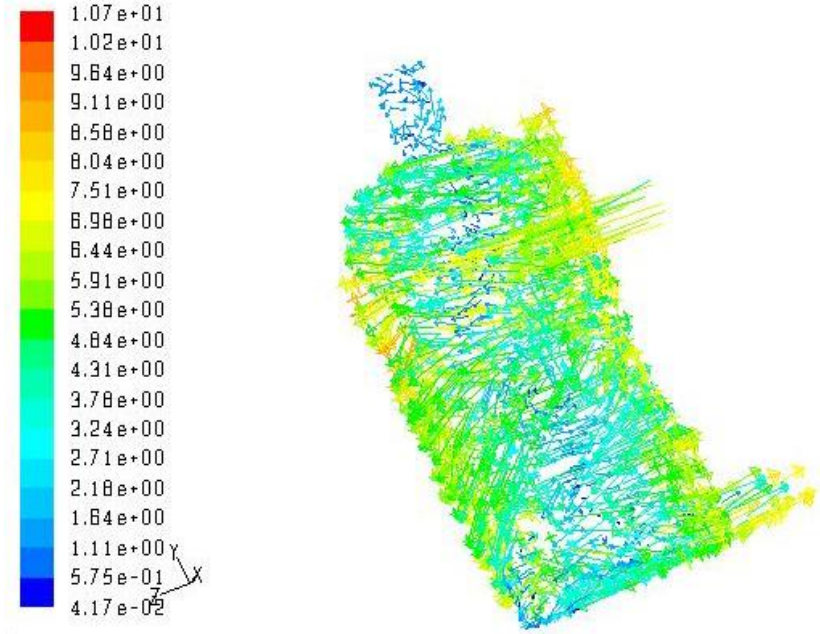

- Figure 4 Three dimensional velocity vector plot of the fluid flow in gas-fluid separator

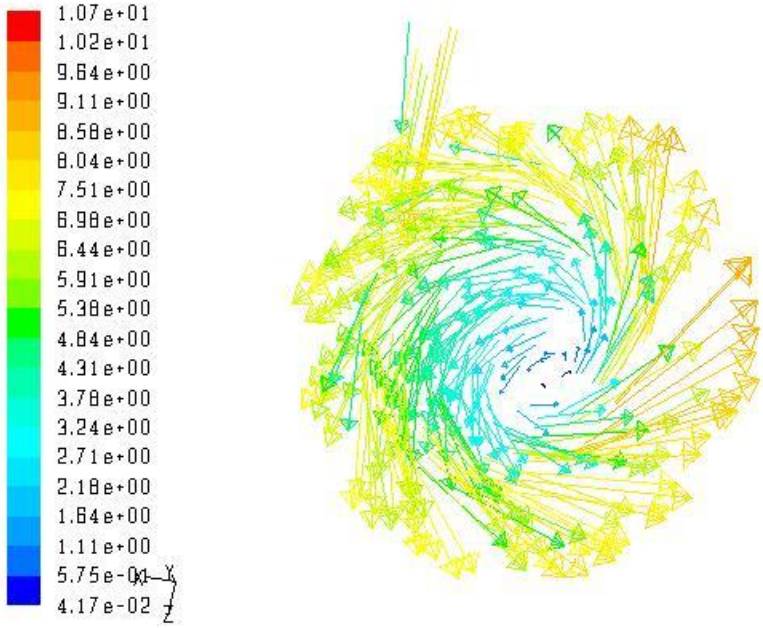

- Figure 5 Plane velocity vector plot of the fluid flow in gas-fluid separator

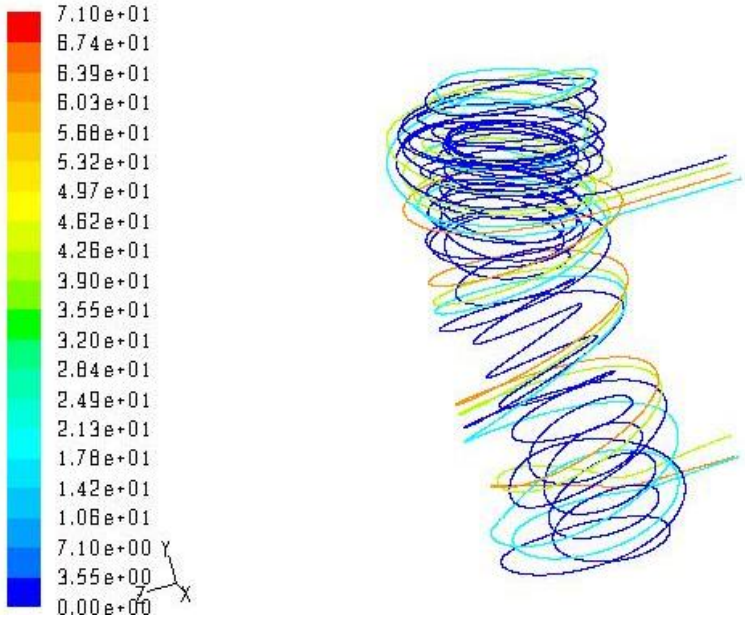

- Figure 6 Three dimensional pathline plot of the fluid flow in gas-fluid separator

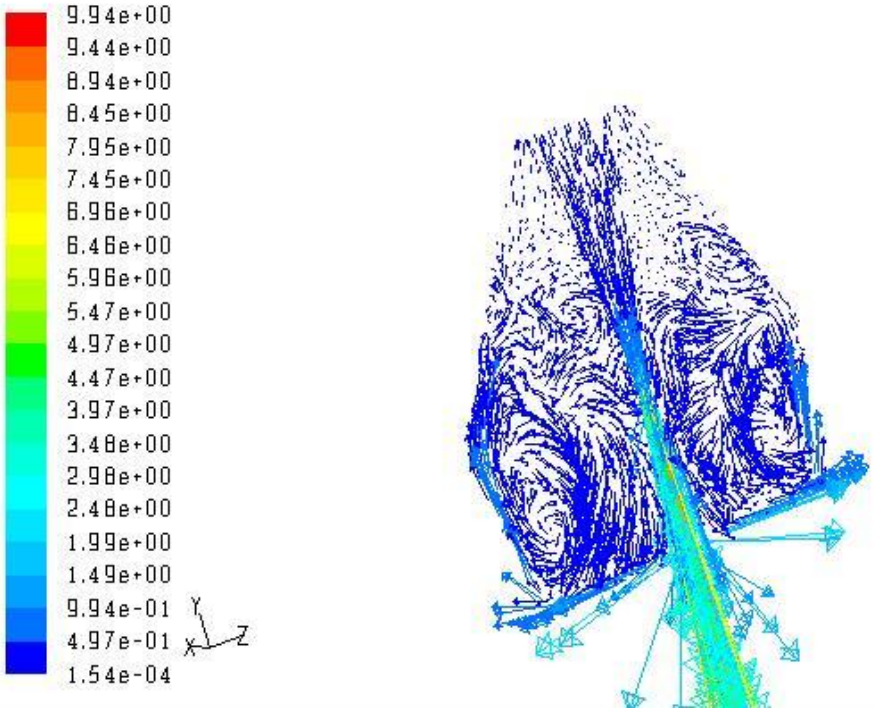

Figure 7 Velocity vectors showing the flow structures in the proposed heater

Task 3: Building Subscale Ammonia Spray Cooling System (100% complete)

In task 3 of the project, a subscale ammonia spray cooling system was built for testing and demonstration purposes. System employs a 1cm x 2cm RTI nozzle array that sprays into an attached heater of same size with two-1 cm^2 unit cells as shown in Figure 3. RTI has developed vapor-assisted atomizer nozzles in which the fine liquid stream is injected into a high velocity vapor stream. The shear force created by the vapor stream atomizes the liquid into fine droplets that are ejected from the nozzle orifice. It was shown that the heat transfer performance of these vapor-assisted atomizer nozzles, in terms of the heat transfer coefficient and percentage of the evaporated liquid, is much better than the commonly used pressure atomizers. Another advantage is that the vapor stream serves as

an excellent mechanism to remove any excess liquid that would otherwise accumulate near the heated surface, especially in a variable–g or low-g environment. It was found that vapor assisted spray cooling performs well even when the heat transfer surface is not flat because the vapor can keep the liquid film on the surface very thin.

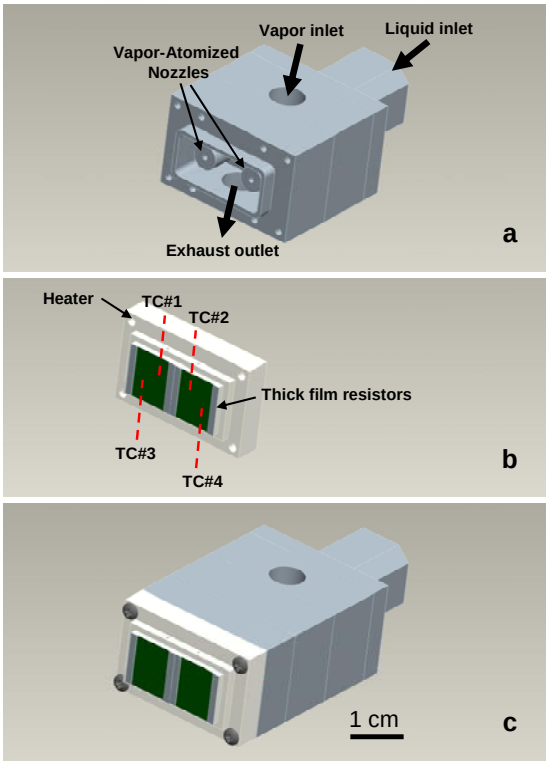

Figure 3. RTI's 1x2 vapor atomized nozzle array (a), 1x2 heater (b) and entire nozzle array-heater assembly (c)

The subscale closed loop cycle allows controlling spray parameters (flow rates, pressures) and is equipped with computer controlled data acquisition system for accurate data recording. All components of the spray cooling system are ammonia compatible and strong enough to withstand high pressures. Figure 4 below includes the schematic diagram of the system.

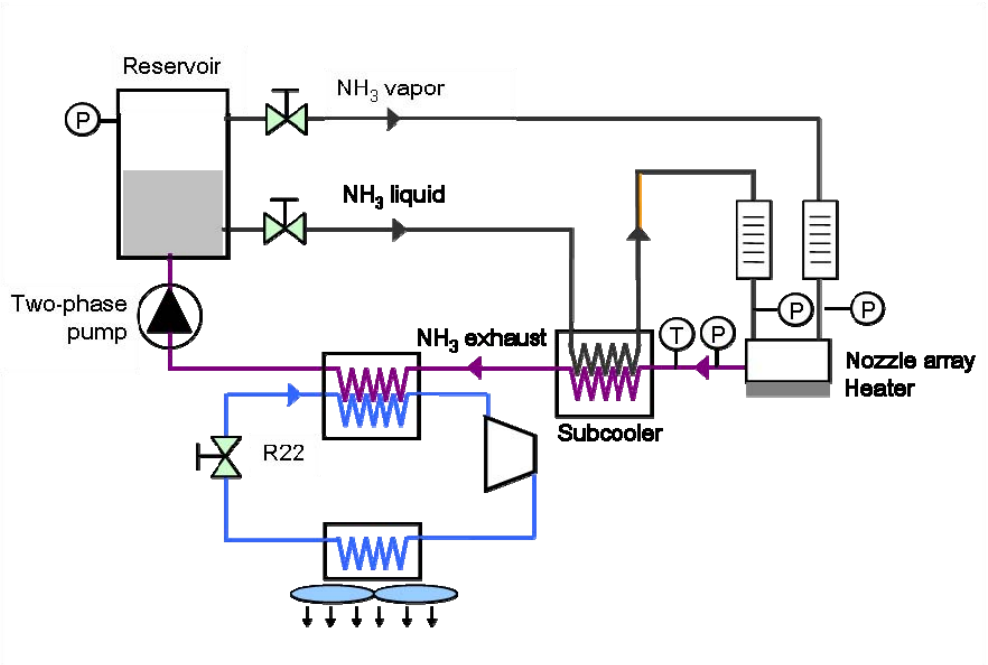

Figure 4. Schematic of spray cooling experimental setup with 1x2 nozzle array

In this setup, the reservoir supplies ammonia liquid and vapor to the nozzle array. Liquid and vapor mixes in the atomizer nozzles and the resulting spray cools the 1cm x 2cm cell plate where heat source thick film resistors are mounted. Exhaust from nozzle array slightly subcools the incoming liquid supply in a small heat exchanger before flowing into the large heat exchanger to condense. Finally, pump takes the two-phase (liquid and vapor) ammonia and transfers it back to the reservoir providing the pressure difference that is needed to drive ammonia in the cycle and generate the spray. A separate air cooled R-22 cycle is employed to reject heat from the ammonia cycle to the ambient. Photographs of the spray cooling system are presented in Figure 5.

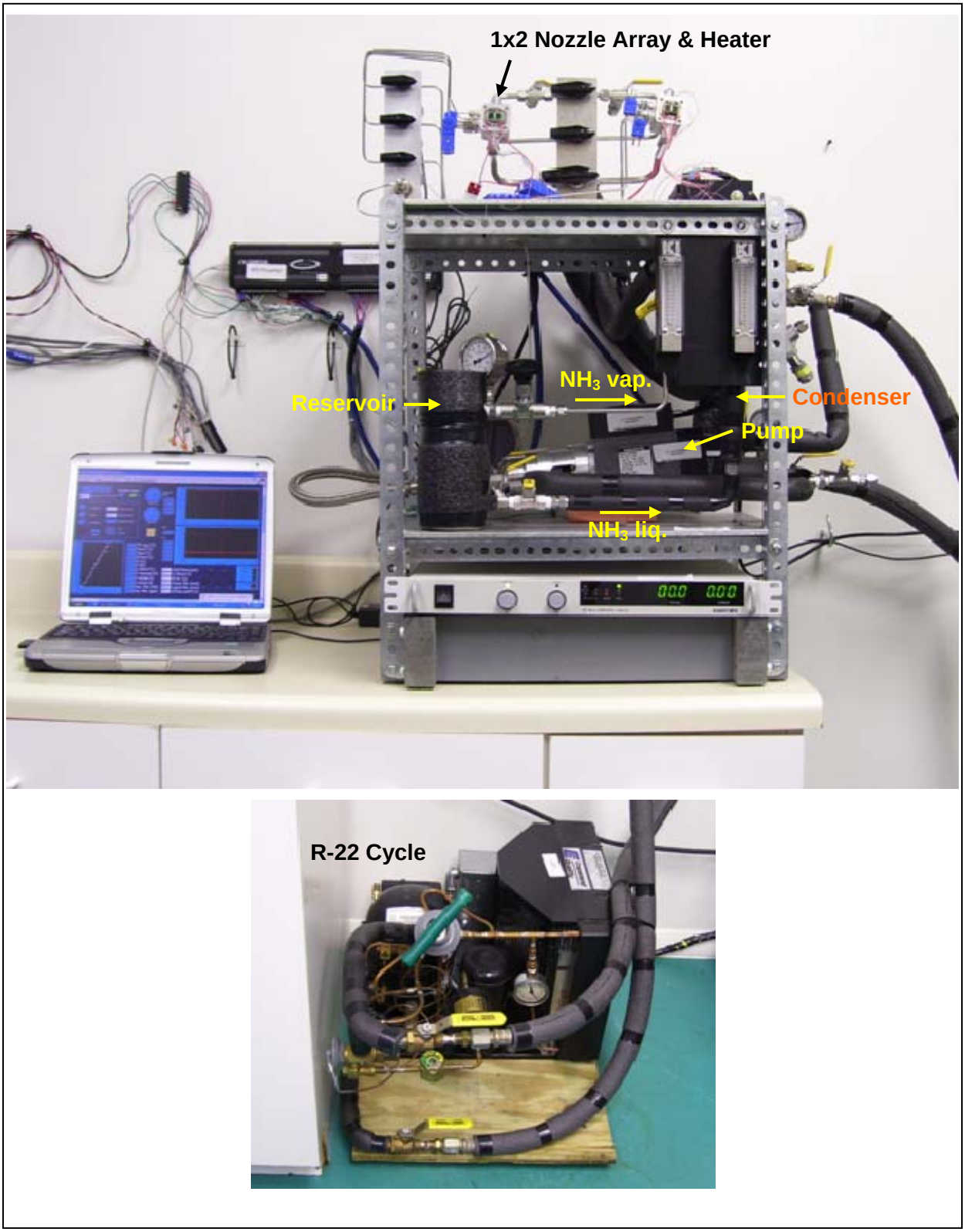

Figure 5. Photographs of spray cooling experimental setup

Task 4: Acquisition of Baseline Data (100% complete)

Prior to starting detailed testing which includes evaluation of many heaters with various micro, macro and multi-scale structured surfaces and optimization of heat transfer performance, some initial tests were conducted to obtain baseline data. These initial tests employed three heaters with one smooth surface, and two kinds of micro-structured surfaces sampling the intended surface modifications. Results of this initial effort are currently in the process of being published by the ASME's Journal of Heat Transfer [1].

One of the test heaters had indentations with average surface roughness, $R_{a,}$ of 2-2.5 μm and referred to as "micro-i" (micro-structured with indentations) while the other heater had protrusions with R_a of 15.0-16.0 μm and referred to as "micro-p" (micro-structured with protrusions). In comparison, heater with smooth surface had R_a of 0.3-0.5 μm. Figure 6 illustrates typical micro-structured surfaces of both types and presents scanning electron microscope (SEM) images at different magnifications. In addition to its characteristic micro size protrusions, micro-p surface also offers many randomly sized re-entrant cavities with some of the large ones marked in Figure 6.

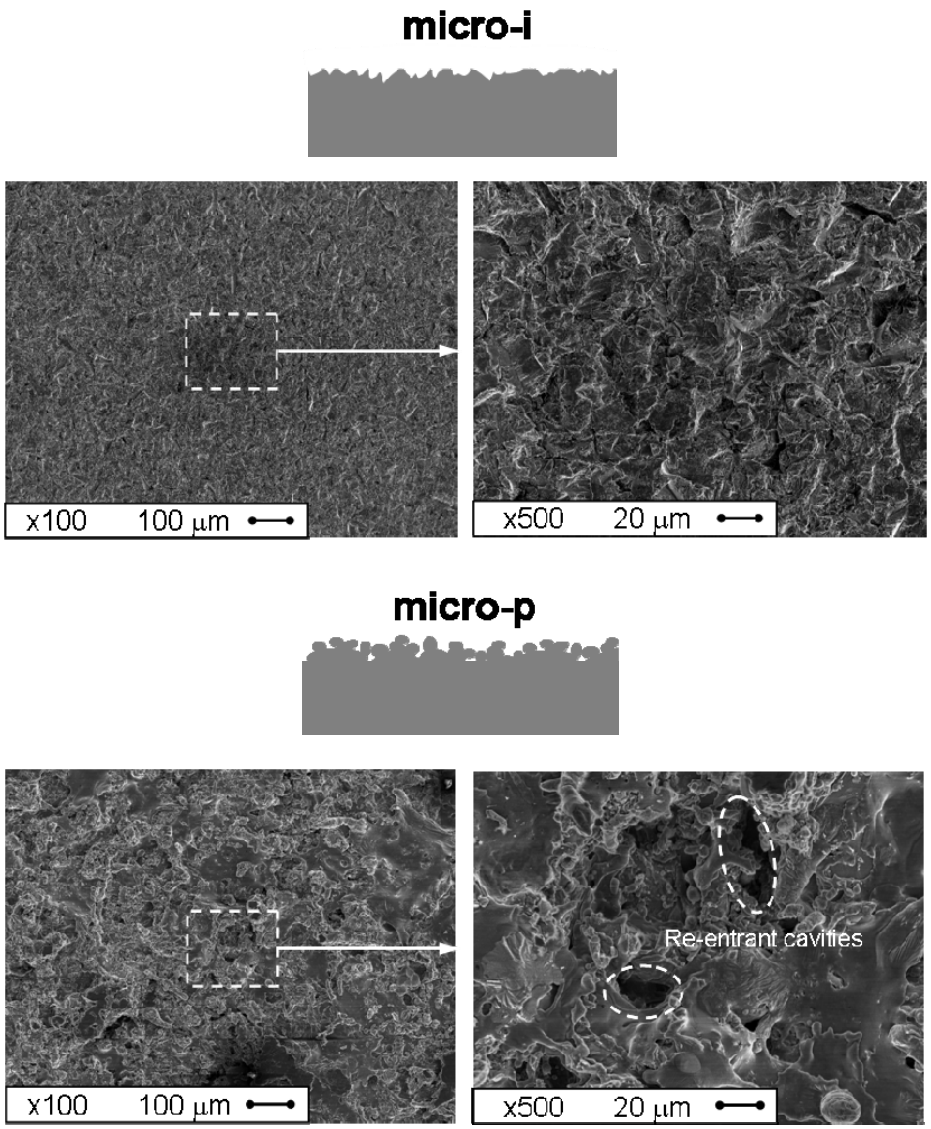

Figure 6. Schematics and SEM images of micro-i (top) and micro-p (bottom) surfaces

All tests were conducted using saturated ammonia at 550-570 kPa [65-68 psig] and 7-8 ^{o}C. Liquid and vapor flow rates for each nozzle were 96 ml/cm^2-min and 13.8 ml/cm^2-s respectively, with only 48 kPa (7 psi) pressure drop across nozzle.

Since the main goal was to investigate spray cooling enhancement on micro-structured surfaces, cooling curves (surface superheat versus heat flux) were generated in the heating-up and cooling-down modes for all test heaters to compare their performance. In all tests, heat flux is gradually increased in steps of 25-100 W/cm^2 up to 500 W/cm^2 and corresponding heater temperatures are recorded every 3 seconds over 3-5 minutes

long steps. Steady-state conditions are usually reached in approximately three minutes. When cooling curves are generated, data is time-averaged over the last 30 seconds of each heat flux step to closely represent the steady conditions.

Spray cooling data obtained from smooth, micro-i and micro-p surfaces are presented in Figure 7. In these tests, heat flux was first gradually increased in steps of 100 W/cm^2 every five minutes from 0 to 500 W/cm^2 (heating-up mode) and then decreased in a similar manner back to 0 W/cm^2 (cooling-down mode). Cooling curves from these three surfaces with time-averaged temperatures are plotted in Figure 8 for an easier performance comparison. As shown, both micro-structured surfaces provided significant performance enhancement over smooth surface while micro-p surface was superior to micro-i surface. Steep changes in the cooling curves of both micro-structured surfaces indicate contribution of phase-change mechanism into overall heat transfer.

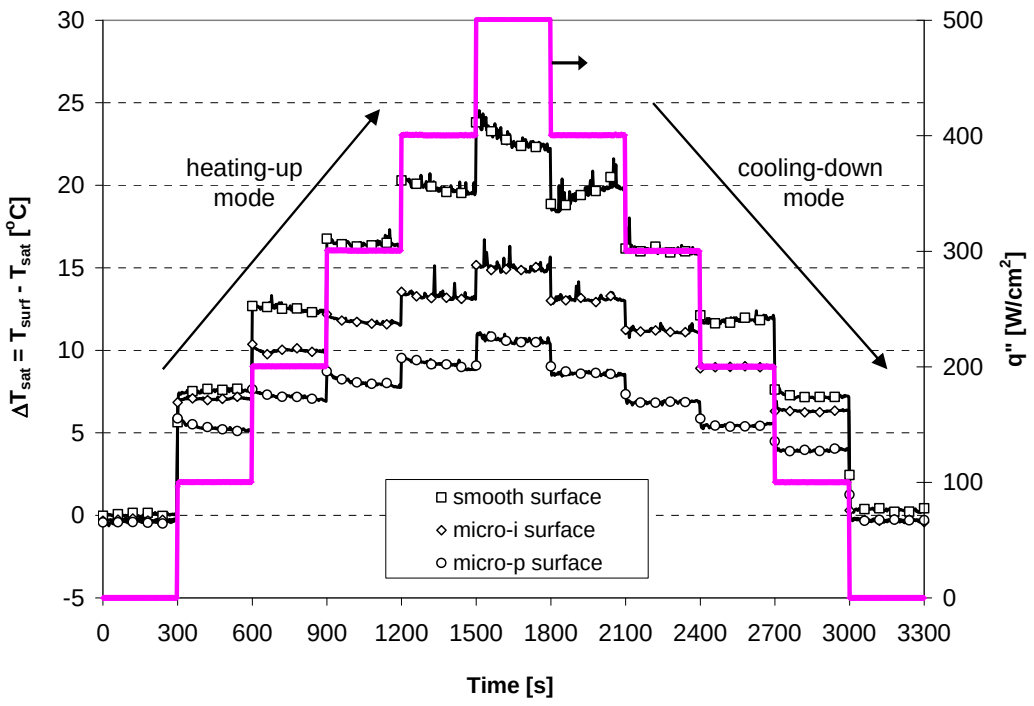

Figure 7. Surface superheat as a function of time as heat flux changes in steps of 100 W/cm^2 every five minutes from 0 to 500 then back to 0 W/cm^2 for smooth and micro-structured surfaces in heating-up and cooling-down mode

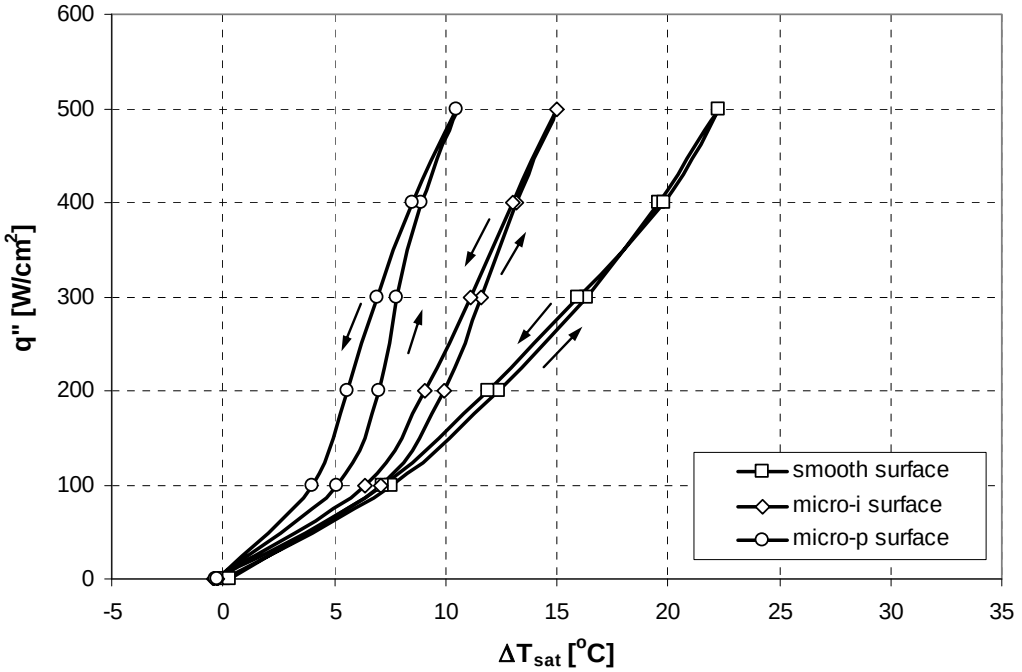

Figure 8. Surface superheat as a function of heat flux for smooth and micro-structured surfaces in heating-up and cooling-down modes

Several heat transfer mechanisms were proposed earlier for the phase-change regime of spray cooling namely, free surface evaporation, boiling through surface and secondary nucleation, and contact line heat transfer. Pais et al. [2] suggested that free surface evaporation provides high heat transfer rates since liquid molecules from a thin liquid film can efficiently escape into vapor/ambient at the surface. As liquid film thickness decreases, heat is conducted from the hot heater surface to the liquid/vapor interface with less resistance, resulting in higher cooling performance. Yang et al. [3] and Rini et al. [4] investigated boiling through surface and secondary nucleation, and observed that in addition to nucleation sites on the surface cavities, many more secondary nucleation sites are generated within the liquid layer as liquid droplets from spray strike on the liquid surface and entrain vapor. Additional bubbles that grow from secondary nucleation sites can greatly enhance boiling heat transfer and increase turbulent mixing within the film, promoting convection and free surface evaporation. Horacek et al. [5] obtained visualization and measurement of three-phase contact line, the region where solid, liquid and vapor phases meet, during spray cooling experiments on a smooth surface. They

found a strong correlation between contact line length and heat flux and concluded that phase-change contribution to heat transfer is directly proportional to contact line length. Horacek et al. considered two possible mechanisms that might be responsible for heat transfer at the contact line, being either thin film heat transfer mechanism or an alternate mechanism such as transient conduction into the liquid when it moves over hot surface as observed in pool boiling.

Based on the outlined phase-change heat transfer mechanisms, current results can now be examined. It is obvious that all three surfaces are subjected to similar free surface evaporation and secondary nucleation mechanisms since the spray conditions are same throughout the tests. In addition to these mechanisms, substantial heat transfer enhancement provided by micro-structured surfaces can be attributed to increase in surface area and stronger contribution of other phase-change mechanisms. Both micro-structured surfaces provide a spectrum of cavity sizes and thus have the potential to generate additional surface nucleation sites and increase three-phase contact line length density. Better performance of micro-p surface, compared to micro-i surface, can be explained with its complex structure that offers more surface area and re-entrant cavities as pointed out in Figure 6.

The heat transfer coefficients obtained from test surfaces are plotted in Figure 9 as a function of heat flux. As seen, heat transfer coefficient continuously increased as heat flux increased and reached to 224,000 $W/m^{2o}C$ for smooth, 334,000 $W/m^{2o}C$ for micro-i and 476,000 $W/m^{2o}C$ for micro-p surface at 500 W/cm^2. An enhancement factor, $h / h_{_smooth}$, is defined to normalize heat transfer coefficients of micro-structured surfaces over smooth surface. Data in Figure 10 shows 1.49X (49%) and 2.12X (112%) improvement for micro-i and micro-p surfaces respectively, over smooth surface at 500 W/cm^2.

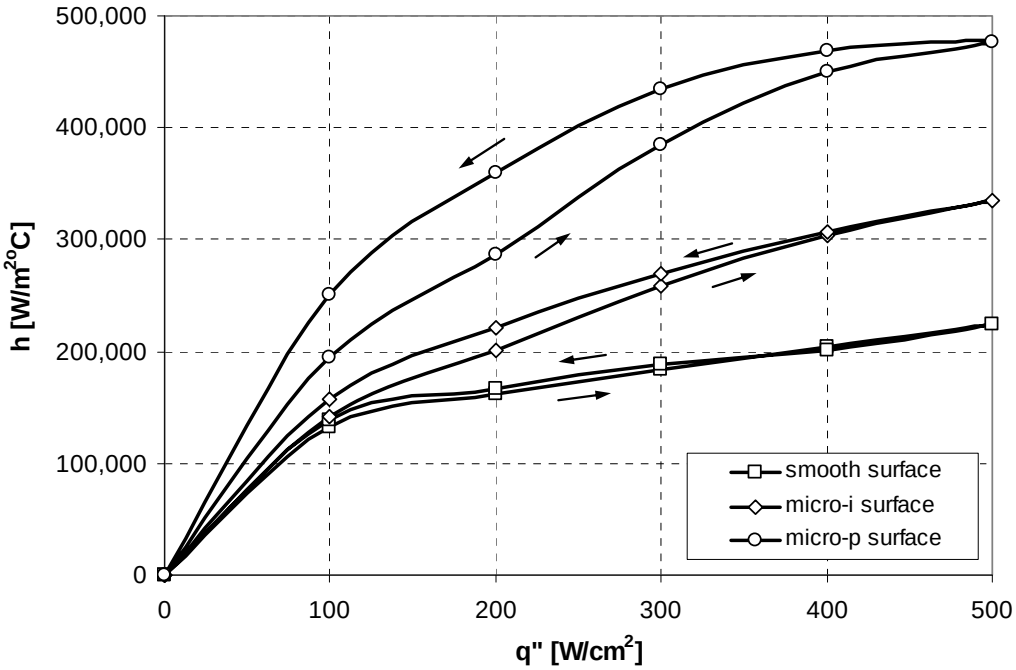

Figure 9. Heat transfer coefficients as a function of heat flux for smooth and micro-structured surfaces in heating-up and cooling-down modes

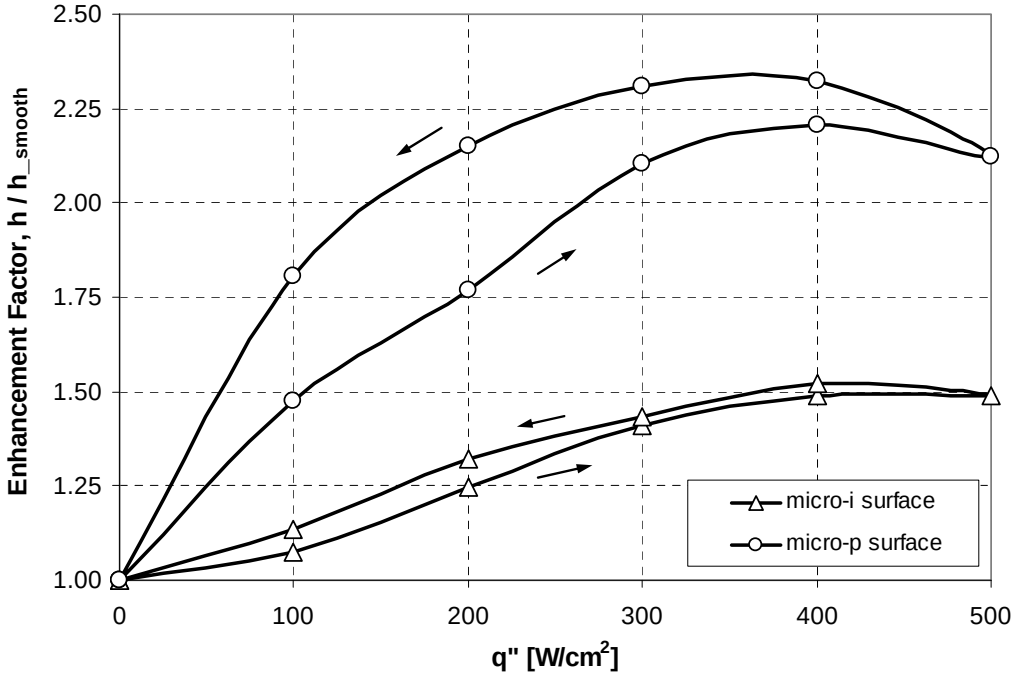

Figure 10. Enhancement Factor as a function of heat flux for smooth and micro-structured surfaces in heating-up and cooling-down modes

Besides the significant heat transfer enhancement, micro-structured surfaces also reveal a hysteresis phenomenon when cooling curves in the heating-up and cooling-down modes are compared in Figure 8. Although smooth surface gives nearly identical cooling curves, micro-structured surfaces experience lower surface superheats in the cooling-down mode at a given heat flux. This deviation in superheats is more pronounced for micro-p surface indicating hysteresis dependence on the surface roughness level. In order to gain better understating on hysteresis effect, additional experiments were conducted with micro-p surface.

First set of experiments considered whether the initially observed hysteresis effect (e.g., temperature deviation between heating up and cooling down curves) changes with varying heat flux conditions. In these tests, heat flux was first ramped up from 0 to 500 W/cm^2. In the following test segments, heat flux was ramped down to gradually decreasing values and then ramped up again through several cycles to observe how hysteresis effect changes. As plotted in Figure 11 along with corresponding surface superheat, heat flux was changed from 0 to 500, then back to 150, then to 300, back to 100, then to 200, back to 50 W/cm^2, and so on. All changes in heat fluxes, up or down, were in steps of 50 W/cm^2 (25 W/cm^2 for q"<100 W/cm^2) every three minutes. Change in hysteresis through the initial heating-up mode and the following test segments can easily be seen when this data is plotted in the form of cooling curves in Figure 12. Results show that once the heater is brought to a high heat flux (and high superheat), superheat will track the same cooling curve on the left with decreasing (as low as 25 W/cm^2 for the present study) or increasing heat fluxes. However, if heat flux is reduced all the way down to zero, then superheat will follow the cooling curve on the right for heating-up mode as can be closely seen in Figure 13. Data therefore suggests that once the three-phase contact line is established on the surface at a certain heat flux, micro-structures are able to retain vapor effectively in the cavities, and the heater can provide a consistent cooling curve and hysteresis effect at lower heat fluxes. At zero heat flux condition, micro-structures can no longer support the retained vapor thus loses the contact line . A

consecutive heat flux increase at this state is no different than initial heating up mode where contact line is established gradually.

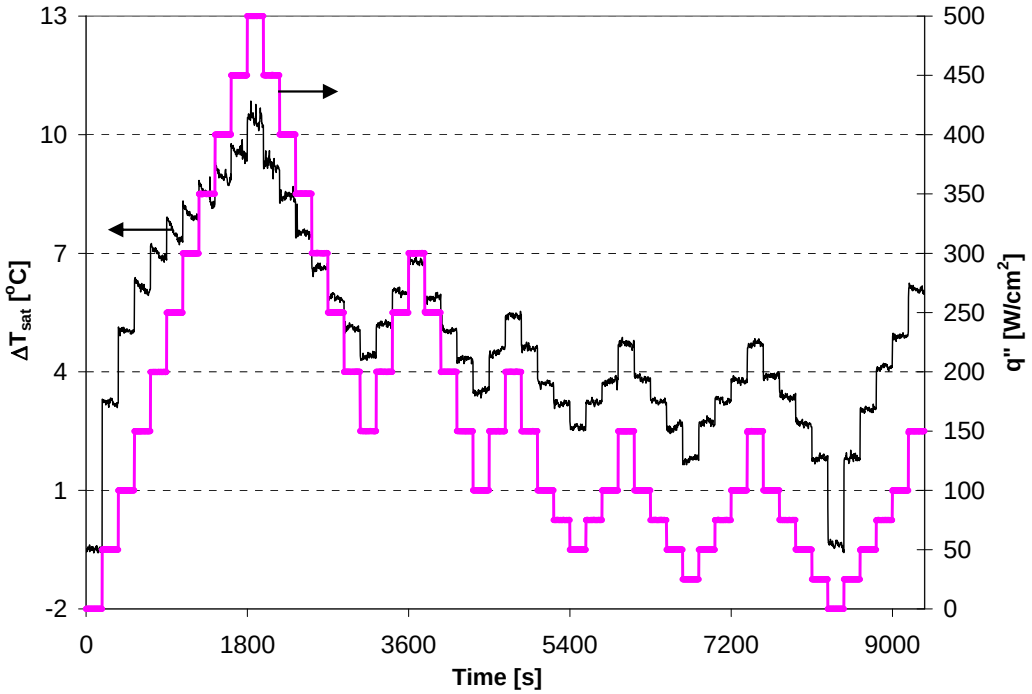

Figure 11. Surface superheat as a function of time as heat flux changes in steps of 25-50 W/cm^2 every three minutes for micro-p surface in heating-up and cooling-down modes

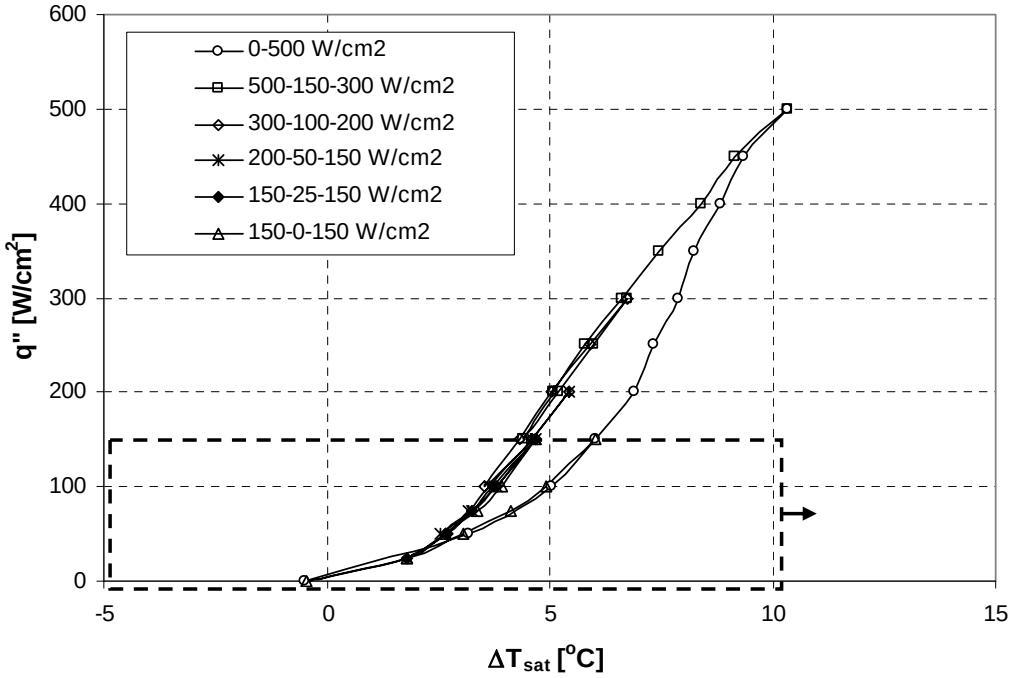

Figure 12. Surface superheat as a function of heat flux for micro-p surface in heating-up and cooling-down modes

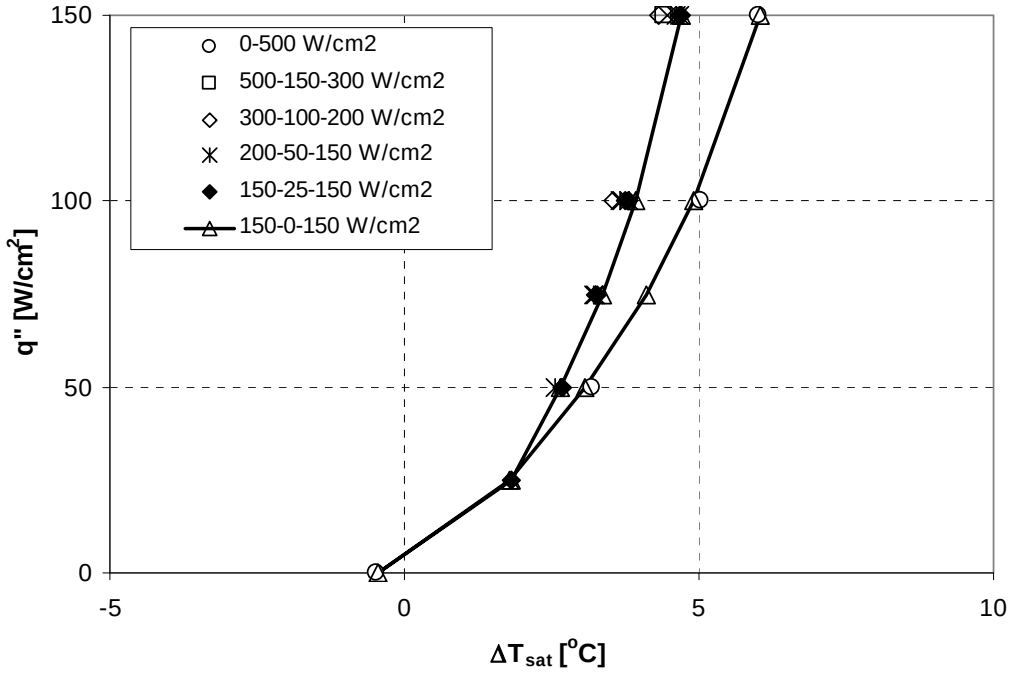

Figure 13. Surface superheat as a function of heat flux for micro-p surface in heating-up and cooling-down modes (a close-up view of Fig.10)

Second set of experiments addressed how hysteresis effect relates to thermal history of the heater. In each segment of these tests, heat flux was increased up to a maximum value and then decreased down to 0 W/cm^2 each time to observe the amount of hysteresis. As seen in Figure 14 along with corresponding surface superheat, heat flux was changed from 0 to 100, then back to 0, then to 200, back to 0, then to 300, back to 0 W/cm^2, and so on. All changes in heat fluxes, up or down, were in steps of 100 W/cm^2 every three minutes. Amount of hysteresis that occurred in each test segment can be better examined when cooling curves are compared in Figure 15. Data here, and further in the close-up view in Figure 16, clearly indicates the trend where amount of hysteresis increases as maximum heat flux increases from 100 to 500 W/cm^2. This observation suggests that as heat flux and surface temperature of the heater increase, contact line length on the micro-structured surface increases. If the surface can maintain some of the established contact line, as in the case of micro-structured surfaces in the present study,

this results in a larger hysteresis or lower superheat later at lower heat fluxes. Figure 17 reflects the change in heat transfer due to hysteresis effect quantitatively. Utilizing data from second set of experiments, heat transfer coefficients in cooling-down mode can be normalized based on those in heating-up mode. For instance, when change in heat transfer at 300 W/cm^2 is considered using normalized heat transfer coefficients of h_c/h_a, h_b/h_a and h_a/h_a in Figure 17, corresponding to points c, b and a in Figure 16, we see that heat transfer coefficient improves 1.08X (8%) and 1.16X (16%) if surface is first exposed to 400 and 500 W/cm^2, respectively, and then brought back to 300 W/cm^2. Similarly, at 100 W/cm^2, heat transfer coefficient can be increased by up to 1.36X (36%) if surface is previously exposed to 500 W/cm^2.

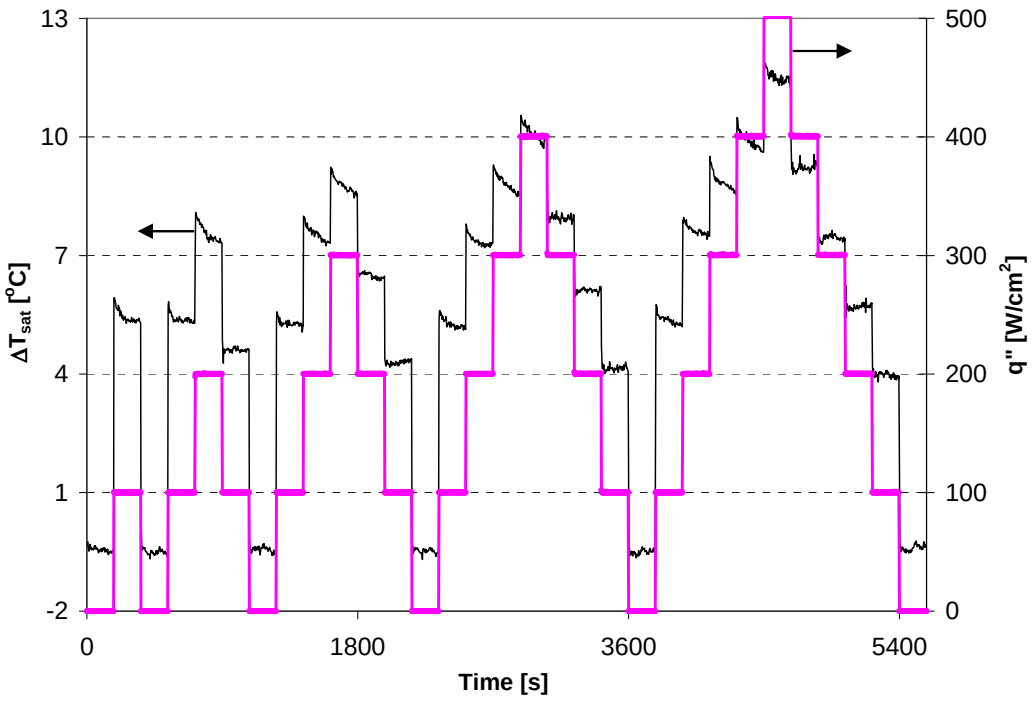

Figure 14. Surface superheat as a function of time as heat flux changes in steps of 100 W/cm^2 every three minutes for micro-p surface in heating-up and cooling-down modes

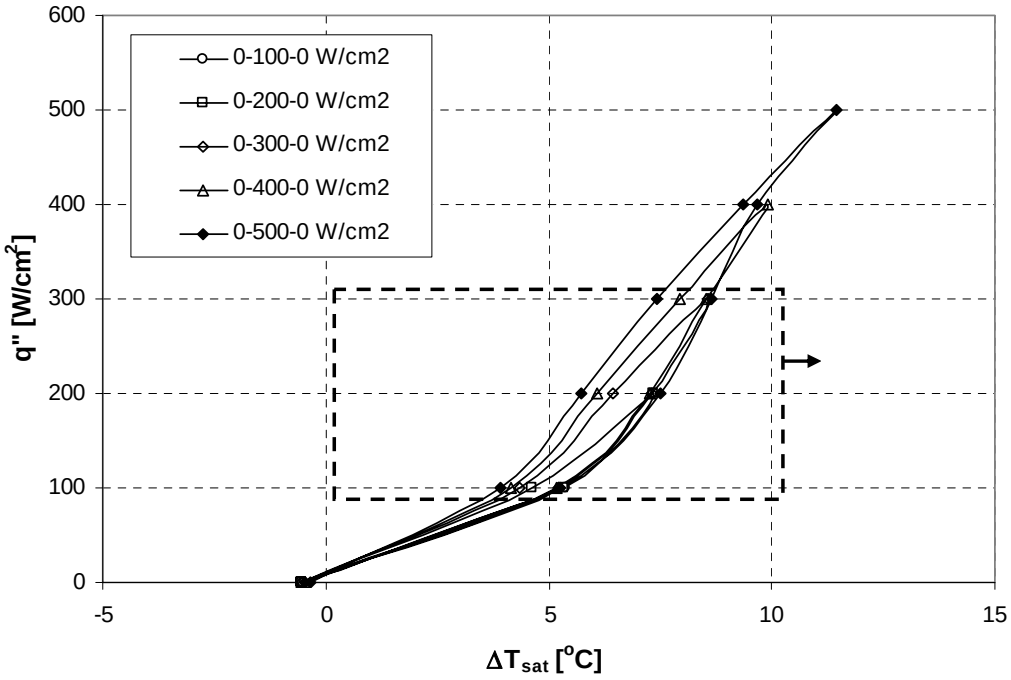

Figure 15. Surface superheat as a function of heat flux for micro-p surface in heating-up and cooling-down modes

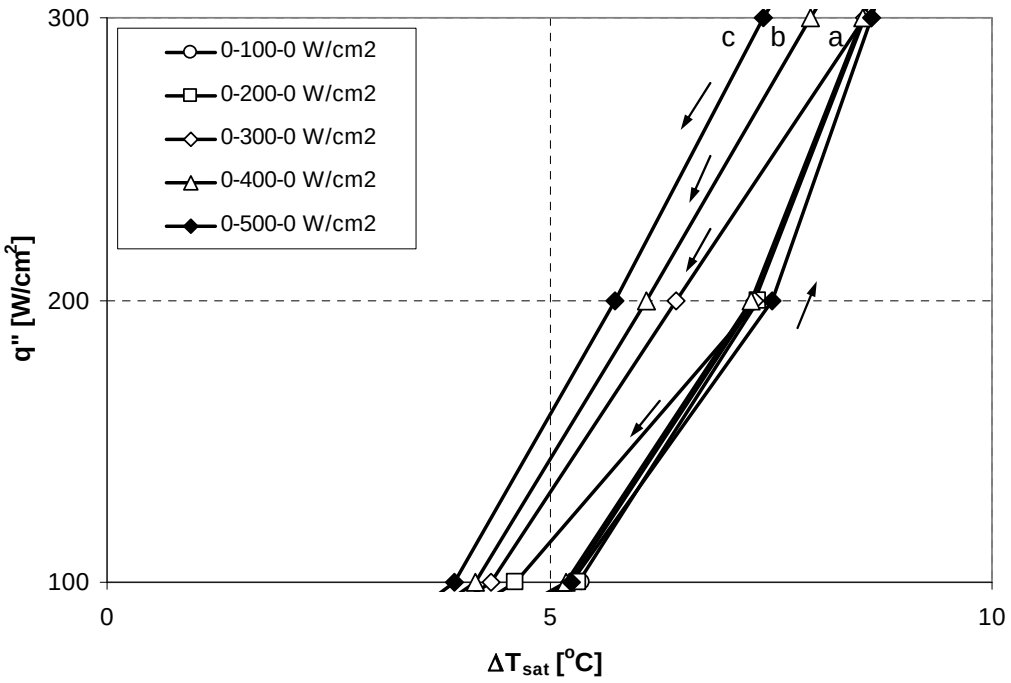

Figure 16. Surface superheat as a function of heat flux for micro-p surface in heating-up and cooling-down modes (a close-up view of Fig.13)

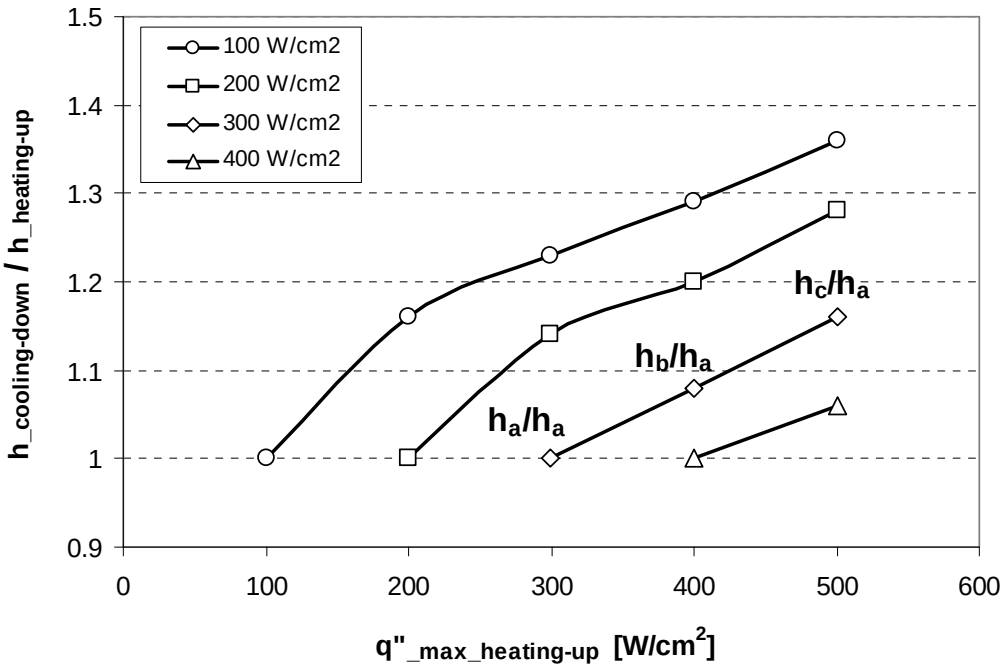

Figure 17. Normalized heat transfer coefficients at constant heat fluxes as a function of maximum heat flux in heating-up mode indicating quantitative change in heat transfer due to hysteresis effect

Based on the findings from tests with micro-p surface, we can also explain the larger hysteresis observed with this surface in Figure 8. Having more surface area and re-entrant cavities, micro-p surface has the potential to capture and retain more vapor, and establish higher three-phase contact line density compared to micro-i surface. Therefore for micro-p surface, the difference between contact line lengths in the heating-up and cooling-down modes is greater, resulting in larger hysteresis.

Task 5: Improving Spray Cooling Performance by Surface Enhancements Using Micro/Macro Structures (100% complete)

Upon acquisition of baseline data, Task 5 aimed to improve the spray cooling performance further through surface modification to address the AFRL needs such as even higher heat fluxes, larger isothermal surfaces, and larger pulses of waste heat. These morphological changes span the range of scales from macro (~1mm) to micro (~1μm). Early dryout is likely to be the cause of why the current record on critical heat flux (CHF) is less than 10% of the kinetic limit.

In addition to improving liquid spray delivery to the surface, we planned to use macro structured surface to create additional surface area (compared to flat base) for heat removal, and micro structured surface to promote both nucleate boiling (through extra nucleation sites) and local liquid spreading (through capillary pumping). Combination of micro- and macro scale surface features leads to the multi-scale structured surface, which could provide ample evaporation surface as bubbles grow and help to replenish boiling surface with liquid, preventing dry spots under the growing bubbles. Successful development of this technology could push the CHF beyond the current limits for all the fluids mentioned.

Task 5 was the initial part of a parametric study that explores different techniques that provide practical and effective surface enhancement in micro- and macro scales. Optimum micro- and macro surface structures to be determined based on experimental results. These optimum surfaces will be combined in the Phase II of this project to develop multi-scale structured surface and investigate the possibility of further enhancement in spray cooling performance. Figure 18 illustrates the summary of the two step approach in this test plan. The first step of the plan includes determining optimum micro, macro and multi-scale structured surfaces for the highest heat transfer coefficient, h, using constant liquid and vapor flow rates at heat fluxes up to 500 W/cm^2. The second

step further evaluates the previously selected optimum surfaces for their CHF limits at increased liquid and vapor flow rates.

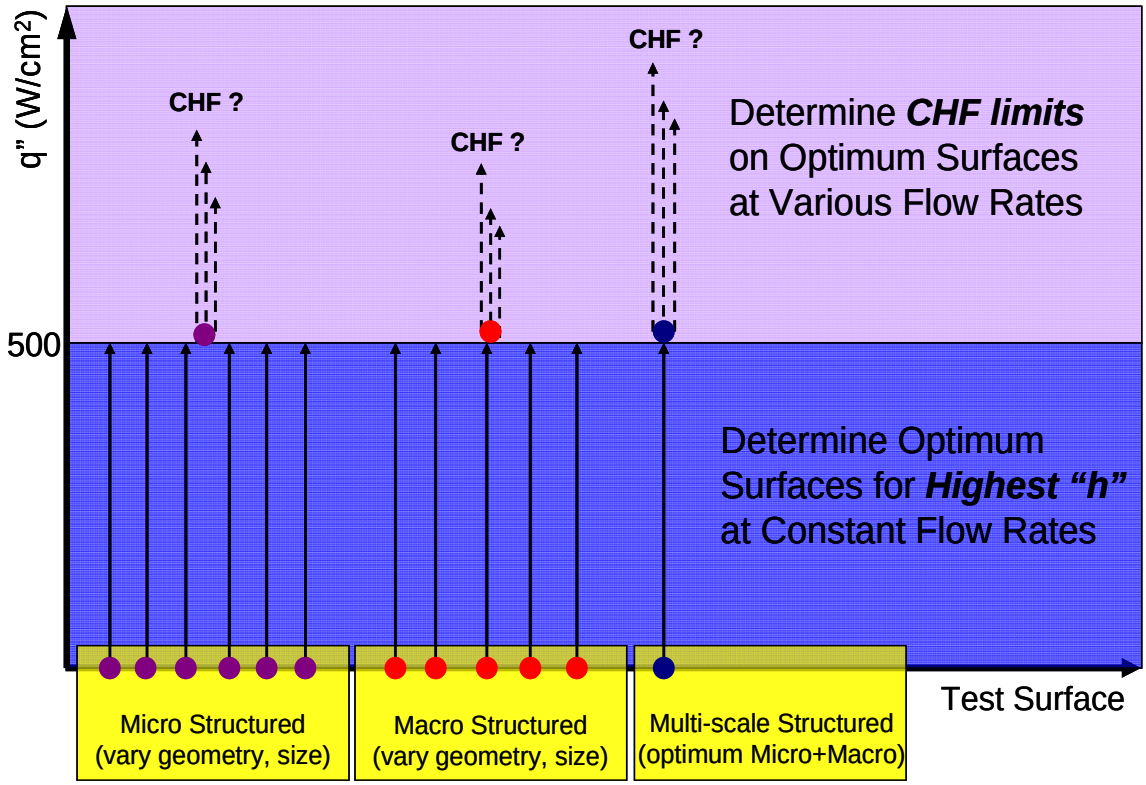

Figure 18. Summary of the anticipated parametric study on surface enhancement

Three copper test heaters used in Task 4 had an aluminum protection layer on their spray surfaces to resist corrosive NH_3 environment. In Task 5, a large batch of new test heaters was fabricated out of aluminum to eliminate the extra protection layer and to facilitate easier surface modifications. Therefore, first test was devoted to generate baseline data using one of the new heaters with a machine finished-smooth surface. Figure 19 shows this baseline data, where smooth surface removed 500 W/cm^2 with 16.7^{o}C surface superheat and gave a heat transfer coefficient of 300,000 W/m^{2o}C.

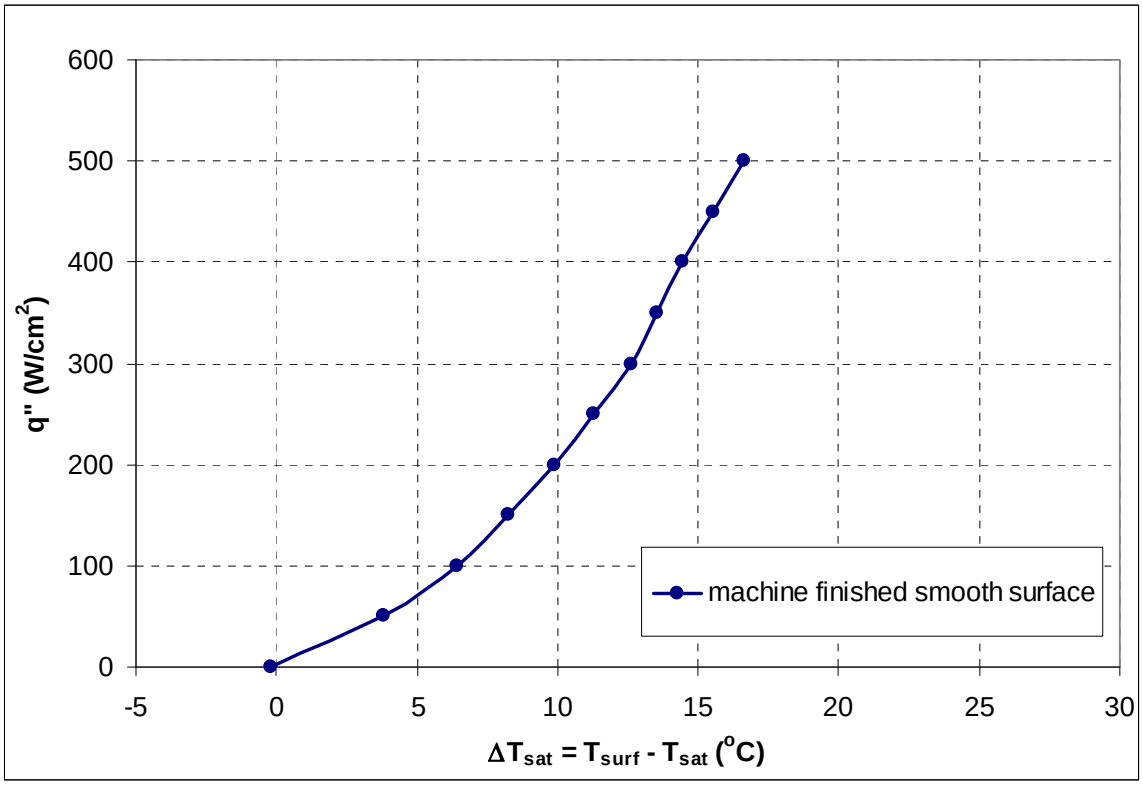

Figure 19. Baseline data for 1 cm x 2 cm heater with machine finished surface

Testing of micro-scale structured surfaces started with a group of heaters having indentations on the spray surface and referred to as "micro-i" (micro-structured with indentations) heaters. Indentations featured three different size ranges, fine, medium, and coarse to evaluate the effect of structure size on cooling performance. All data obtained from micro-i surfaces along with the baseline data from smooth surface are included in Figure 20 below. As can be seen, although the surface with fine size indentations performed the best, the difference in performance of three surfaces diminishes as heat flux approaches to 500 W/cm^2 with a heat transfer coefficient of 522,000 W/m^{2o}C that corresponds to 74% improvement over the smooth surface.

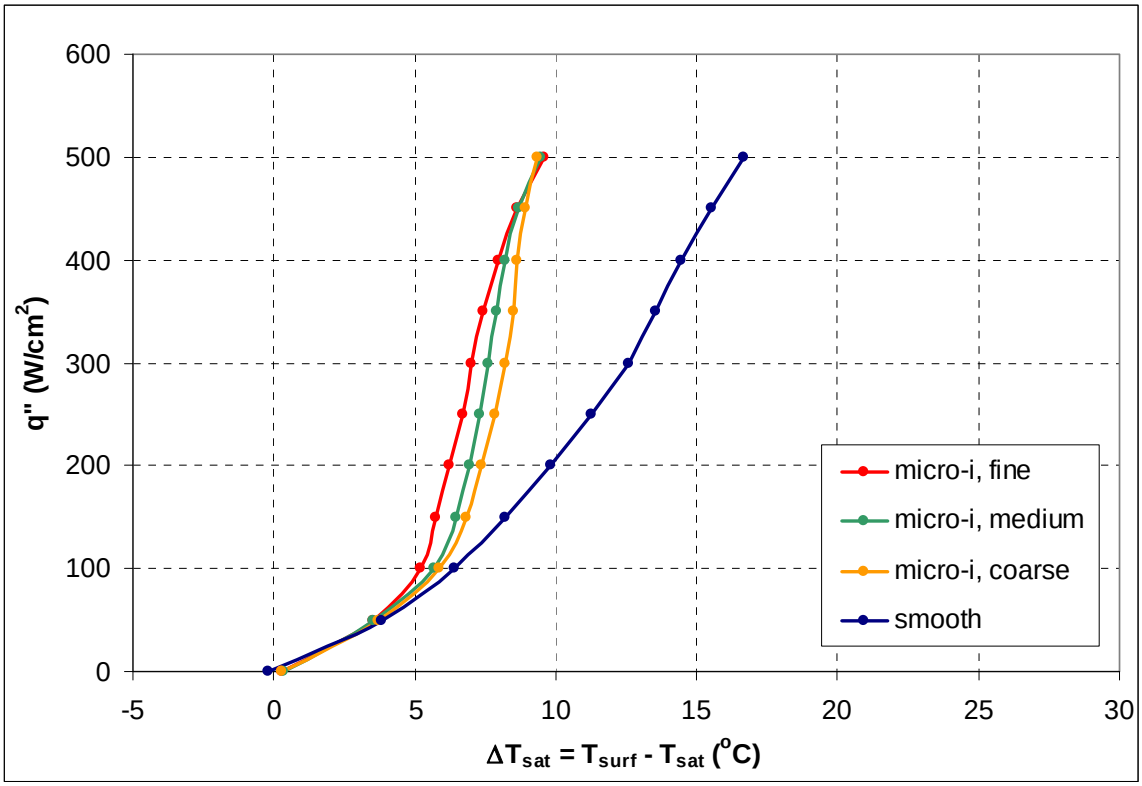

Figure 20. Performance comparison of heaters with micro-structured surfaces (micro-i)

Second group of micro-scale structured surfaces presented protrusions on the spray surface and referred to as "micro-p" (micro-structured with protrusions) heaters. Micro-p structures were fabricated using aluminum particles of three different size ranges- fine, medium, and coarse- to investigate the effect of structure size on cooling performance. Test results from micro-p surfaces along with the baseline data from smooth surface are plotted in Figure 21. Among micro-p heaters, the surface with medium size protrusions clearly outperformed the other two and achieved 500 W/cm^2 with a heat transfer coefficient of 514,000 W/m^{2o}C that corresponds to 71% improvement over the smooth surface.

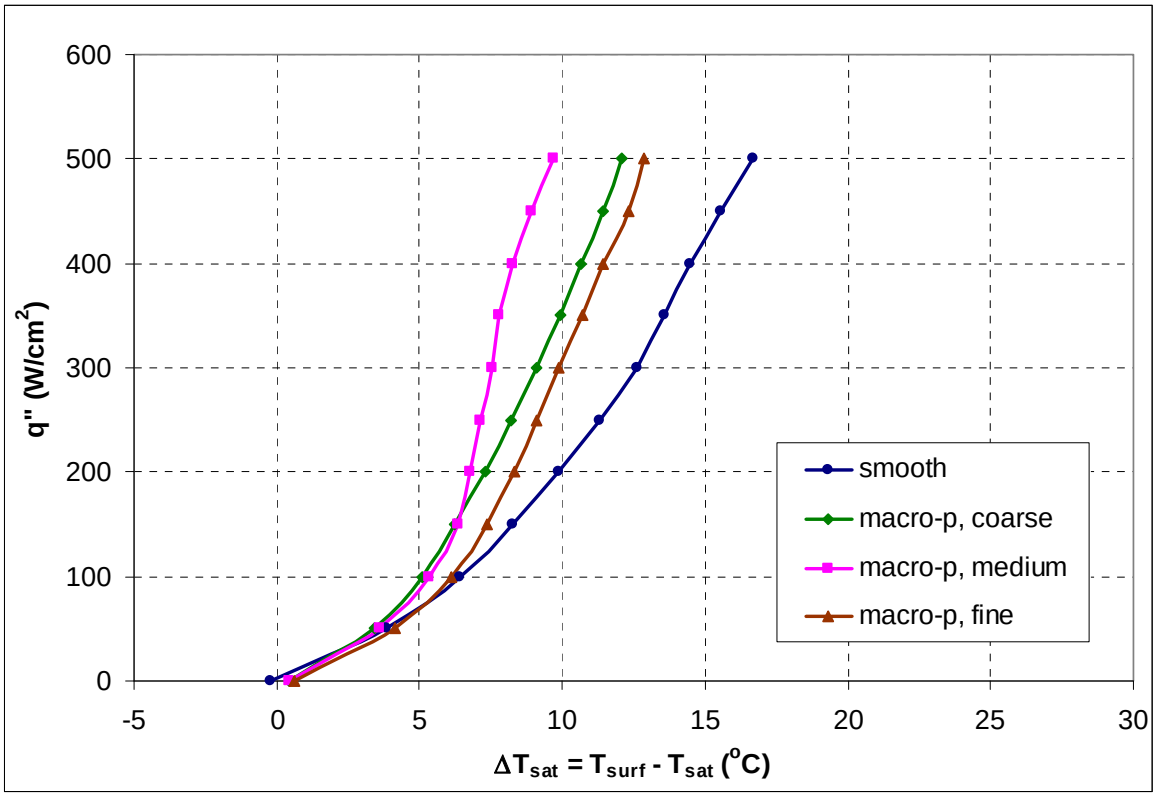

Figure 21. Performance comparison of heaters with micro-structured surfaces (micro-p)

After testing of two groups of micro-scale structured surfaces, four heaters were fabricated with different macro-scale structures. Figure 20 below includes solid models of these heaters that have straight fins, cubic pin fins, triangular grooves and pyramids, all with 0.75mm high fins.

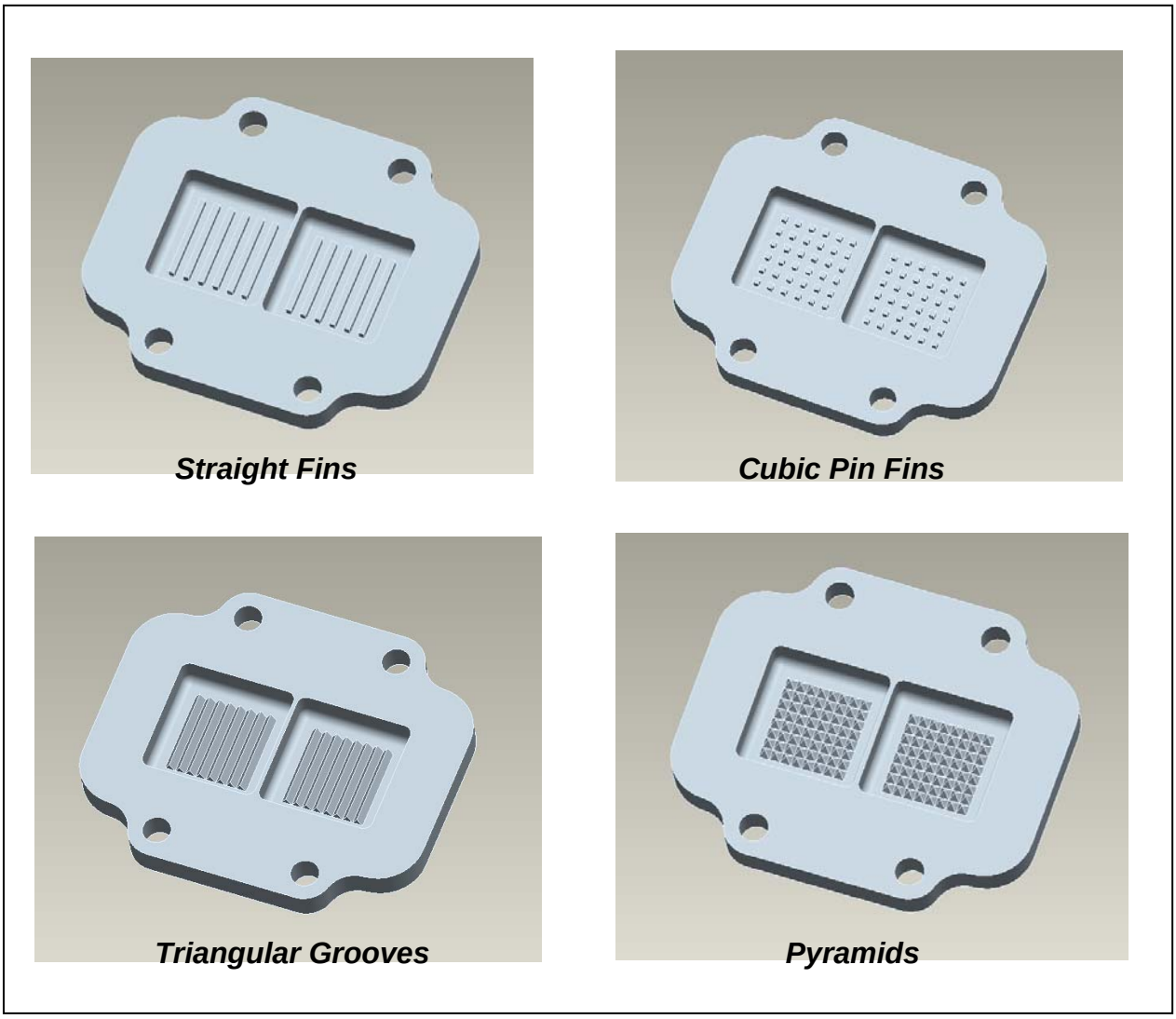

Figure 22. Solid models of heaters with macro-structured surfaces

Data obtained from four macro-structured surfaces are included in Figure 23. As seen, all macro-structured surfaces provide enhancement over smooth surface. Pyramids, among the four structure geometries, gave the highest heat transfer coefficient over the entire heat flux range reaching to 405,000 $W/m^{2o}C$ at 500 W/cm^2 that corresponds to 35% improvement over smooth surface.

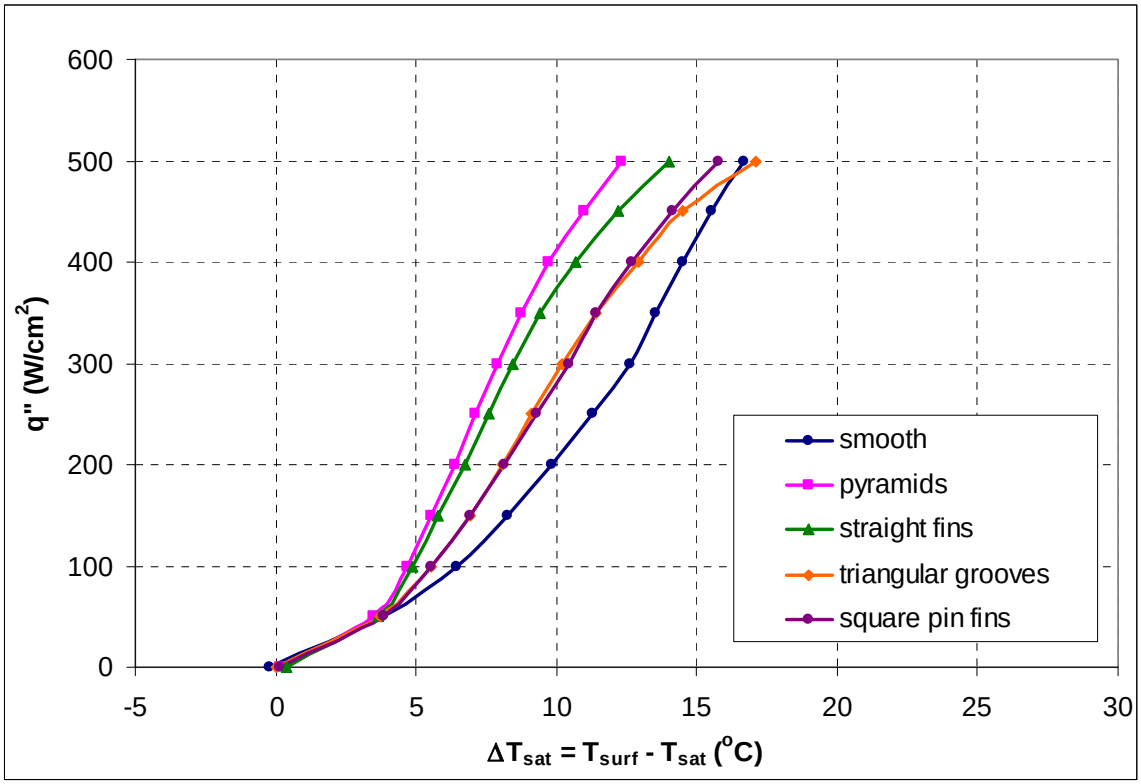

Figure 23. Performance comparison of heaters with macro-structured surfaces

Task 5 completes Phase I of this effort. In Phase II, optimum micro- and macro surface structures will be combined to develop multi-scale structured surface and its potential for further performance enhancement will be evaluated. CHF limits of these optimum surfaces will also be determined afterwards.

References

[1] Bostanci, H., Rini, D.P., Kizito, J.P., Chow, L.C., 2008. Spray cooling with ammonia on micro-structured surfaces: performance enhancement and hysteresis effect. Journal of Heat Transfer, ***In Press***

[2] Pais, M.R., Tilton, D., Chow, L.C., Mahefkey, E.T., 1989. High heat flux, low superheat evaporative spray cooling. In: Proceedings of the 27th AIAA Aerospace Sciences Meeting, Reno, NV.

[3] Yang, J., Chow, L.C., Pais, M.R., 1996. Nucleate boiling heat transfer in spray cooling. Journal of Heat Transfer 118, 668–671.

[4] Rini, D.P., Chen, R.H., Chow, L.C., 2002. Bubble behavior and nucleate boiling heat transfer in saturated FC-72 spray cooling. Journal of Heat Transfer 124, 63–72.

[5] Horacek, B., Kiger, K., Kim, J., 2005. Single nozzle spray cooling heat transfer mechanisms. International Journal of Heat and Mass Transfer 48 (8), 1425-1438.

NEURAL-FUZZY MODELING IN MODEL-BASED FAULT DETECTION, ISOLATION AND CONTROL ADAPTATION AND RECONFIGURATION IN TURBINE ENGINES

Research Final Report

First Year
September 2007 – November 30, 2008

Submitted to

The Propulsion Directorate
Air force Research Laboratory (AFRL)
Wright Patterson Air Force Base
Cleveland, OH 45433-7251

BY

Saleh Zein-Sabatto (PI)

Department of Electrical and Computer Engineering
Tennessee State University

Contact Information:
Saleh Zein-Sabatto, Ph.D.
Department of Electrical and Computer Engineering,
College of Engineering, Technology and Computer Science
Tennessee State University, Nashville, TN 37209
Tele: (615) 963-5369
Fax: (615) 963-2165
Email: mzein@tnstate.edu

TABLE OF CONTENTS

1.0 Proposed Research Activities For Year-1..... 3
1.1 Research Expected Results for Year-1..... 3

2.0 Summary of Research Activities During Year-1.....4

3.0 Research Accomplishments in Year-1, 2008 4
3.1 Literature Review 4
3.1.1 Diagnostics 4
3.1.2 Prognostics 6
3.1.3. Control of Gas Turbine Engines 7

3.2 Development and Testing of Adaptive Controllers for the Turbine Engine..... 9
3.2.1 Existing Controller of the AFRL Engine Model..... 9
3.2.2 Development of Fuzzy-logic Controller 11
3.2.3. Controller Performance under Faulty Conditions 18
3.2.4 Controller Performance under Varying PLA 30
3.2.5 Implementation of other Control Inputs 30

3.3 Development and Testing of the Diagnostic System 35
3.3.1 Data Collection and Pre-processing 35
3.3.2 Fault Classification using Self Organization Map (SOM) Network 36
3.3.3 Fault Identification by the Supervised Neural Network (BPNN) 36
3.3.4 Decision-Making System 36
3.3.5 Testing Results 37

3.4 Integration of the Diagnostics and Control Algorithms 38

4.0 Objectives for the Next Research Period (Year-2)..... 40

5.0 Student Training and Publications 40

REFERENCES 42

1.0 Proposed Research Activities For Year-1

The goal of the proposed multiphase research was to conduct basic and applied research related to fault detection, isolation, accommodation and reconfiguration of turbine engine adaptive control and health management leading to intelligent turbine engines with damage-tolerant control, health and life management system. In pursuit of the above stated goal, several research objectives were been identified and are listed below.

1. Conduct research, and develop algorithms for, sensor data processing and feature extraction suitable for turbine engine fault and operation abnormality detection.
2. Investigate and develop sensor fusion algorithms of multimodality sensors used in turbine engine control and health management system.
3. Develop software and tools for fault detection and isolation in turbine engine based on features extracted by processing and fusion of sensor data (diagnosis).
4. Develop software and algorithms for predicting remaining useful life (URL) of faulty components detected in turbine engine (prognosis).
5. Develop software for reasoning and intelligent decision-making system for reconfiguration and adaptation of control loops in turbine engine.
6. Develop software for system adaptation and performance optimization of turbine engine health-management system.

Advanced signal processing and fusion algorithms using intelligent techniques will be used in development of the engine diagnostics and life management software. Fuzzy logic and neural networks are some of the key technologies will be used to accomplish the above stated objectives. Following is review of current technical approaches and the proposed technical approach that will be pursued in the proposed research. A fault-tolerant system for control adaptation and health management of turbine engine, as it is proposed in this research, consists of four main components. A preprocessing stage or feature extractor followed by, feature clustering (classifier), feature identification (identifier) and finally, a decision-making or information fusion step for reconfiguration and control adaptation.

1.1 Research Expected Results for Year-1

The first year of the research will be a preparatory year during which the specific problem at hand and the scope of the research will be established clearly. The major work of the research will be concentrated on obtaining engine model, identifying type and nature of engine abnormalities to be addressed, running simulation tests and preparing data for supporting practical research work. Specifically, the following topics will be the main activities of the research in the first year.

1. Obtain turbine engine model from the Propulsion Directorate at AFRL, run simulation tests under normal operating conditions, and develop solid understanding of different aspects of the engine health-management challenges to be addressed in the research.
2. Identify specific section of the engine most appropriate to work on and software requirements based on recommendations from the technical monitor of the research.
3. Compile a list of anomalies, classes of faults including potential sensor failures and redundancy, and generate simulation measurements and data associate with each identified fault and receive approval of its validity from AFRL.
4. Perform advanced data preprocess on the simulation measurements and data collected above including noise filtering and fault feature extractions.

2.0 Summary of Research Activities During Year-1

During the first year 2008, research activities were conducted on two tracks; 1) Development of intelligent diagnostics algorithms and, 2) Development of control and reasoning algorithms for the turbine engine model provided by AFRL. These two developments were preceded by a comprehensive literature review reported in the first and second quarterly reports of the research. At the end of the first year, integration of the above two research tracks was initiated. This set the direction for development of the research activities in year-2. In addition to the enhancement and further testing of the already developed control and diagnostics algorithms, in year-1, integration of the two sets of algorithms and software will be the main focus of the research in year-2.

The research team during the first year consisted of two undergraduate students, two graduate students and the PI. In addition to the above mentioned students who are funded by the research fund, one more undergraduate student completed her capstone design project under this research but without direct funding from the research. They all worked on the research according to the time schedule and the goal and objective of the research which shall lead to completion of their degrees. Detailed contributions of each student are included at the end of this report.

3.0 Research Accomplishments in Year-1, 2008

The research accomplishments during the first year are consistent with and exceeded the objectives outlined in the proposal. The research objectives reported in the original proposal are listed in section-1 above. The deliverables completed in the first year of the research are; 1) a comprehensive literature survey on subjects related to turbine engines control, diagnostics, and health management, 2) development of new intelligent control architectures and algorithms and, 3) development of intelligent diagnostics architectures and algorithms and, 4) initial integration of the diagnostics and control architectures leading to a complete turbine engine health management system.

Effort toward accomplishing the above stated objectives resulted in two specific technical deliverables; 1) an adaptive controller based on fuzzy-logic technique implemented and tested on the engine model and, 2) a diagnostics architecture and software implemented and tested on the turbine engine using neural predictive networks. The followings are details of the research accomplishments.

3.1 Literature Review

The diagnostic of a turbine engine involves assessing information regarding the present and past state of the engine. Also, recent research work focused on the prognostics of turbine engines which involve assessing information about the future state of the engine. This section provides an overview of diagnostic methods as well as methods being developed in the area of prognostics for turbine engines. Review of different control strategies for turbine engines is also included in this section. Following is a summary of the findings of the literature review conducted under this research.

3.1.1 Diagnostics

Diagnostics can be defined as an assessment about the current (and past) health of a system based on observed symptoms and prognostics is the assessment of the future of the system [1]. Generally, diagnostics of gas turbine engines consist of two decision-making steps; fault detection and diagnosis (FDD). The first step, detection, involves early detection of incipient, as well as, sudden faults. Detection is then followed by diagnosis of a sensor, actuator, or system component fault. In terms of controls, diagnostics is conducted in three computation steps; fault detection, isolation and accommodation. The

two main approaches to FDD are; data-driven and model-based. Data-driven methods use historical data collected from the system to construct quantitative (neural networks, statistical models) or qualitative (trends-based, rule-based) FDD methods [2]. Model-based FDD methods use a physical or an empirical model of the system to generate residuals (difference between the model outputs and actual system measurements). These residuals are passed through a decision-making system to determine a diagnosis. Some of the methods under these two approaches will be discussed next.

Data-Driven Methods:- Mo et al. [3], propose a fuzzy inference logic system for gas turbine engine fault isolation. They state their reasoning for selecting a fuzzy inference logic system as; 1) the fuzzy logic system is a knowledge based system that has ability to handle uncertainty, 2) the fuzzy logic system does not require estimation of the system parameter and, 3) the fuzzy logic rule base contains control strategies that are applicable to a wide range of qualitatively-similar scenarios. In the work, the gas path measurements used for fault isolation are; exhaust gas temperature, low and high rotor speed, and fuel flow. The fuzzy inference logic uses rules developed from a model for performance influence coefficients to isolate engine faults while accounting for uncertainty in gas path measurements. Inputs to the fuzzy inference logic system are measurement deviations of the gas path parameters which are transferred directly from the ECM (Engine Control Monitoring) program and the outputs are the engine module faults. The proposed fuzzy inference logic system is tested using simulated data developed from the ECM trend plot reports and the results showed that the proposed system isolates module faults with high accuracy rate in the environment of high level of uncertainty.

The previous works is similar to earlier work [2], where an empirical model of the turbine engine is used to generate residuals of key engine parameters such as engine speed, exhaust gas temperature, and fuel flow. These residuals are then subjected to data smoothing techniques, and the smoothened outputs are combined with a fuzzy logic based implementation of the system expert heuristics. The data smoothing techniques are applied to address issues associated with the data variability. Then automated performance trending and fault isolation is accomplished by applying expert based fuzzy logic rules to the engine trends and parameter levels. The method was tested on actual flight data that was collected on legacy data acquisition systems. The method was shown to detect problems in the engine even in the presence of data gaps and system noise. The results generated using this method is very promising as they show that it is possible to reliably diagnosis faults with very few parameters and with many gaps in the data.
Gayme et al. [4] also described a fuzzy logic-based method for fault detection and diagnosis in gas turbines engines and their case study also showed that it is possible to obtain reliable prediction horizon for fault diagnosis with very few parameters and many gaps in the data.
Depold and Gass [5] present strategies in engine condition monitoring including; 1) application of statistical analysis and artificial neural network filters to improve data quality, 2) neural networks for trend change detection and classification to diagnose performance change, and 3) expert systems to diagnose, provide alerts and to rank maintenance action recommendations. Significant improvements in accuracy, quality of analysis, timeliness and usefulness of reporting are shown in this work.

Model-Based Methods:- Kulikov et al. [6] considered an application of Markov model based fault detection method for condition monitoring of a gas turbine engine. The engine Markov model is built using real data obtained from an engine test-bed. In their practical example the simulation of engine work using Markov model was approximately 20 times faster than the same simulation using a radial basis function (RFB) neural network.

Brotherton et al. [7] proposed a technique that couples neural net with automated rule extractors to form systems that have:

- Good statistical performance
- Easy system explanation and validation
- Potential new data insights and rule discovery
- Novelty detection

- Real-time performance

Their approach uses a Dynamically Linked Ellipsoidal Basis Function (DL-EBF) neural network to classify engine sensor data and thereby statistically model the state of the engine with respect to known faults. As is true of all basis-function neural networks, the DL-EBF provides novelty detection capability. The dynamic-link feature allows assessment of trending from the nominal class to each of the identified fault classes. This means that quantitative prognostics are built into the network functionality. To add comprehensibility to the system, the TREPAN [8] approach is used to develop a tree-structured rule set that closely approximates the classification of the neural network. The results were available but not presented in the paper.

In Simon et al. [9], signal processing techniques together with physics-based and empirical-based modeling are applied in the development of an information fusion system for engine diagnostics and prognostics for the C117-T1 aircraft with a P&W F117 engine. The general Propulsion Health Management (PHM) information fusion architecture is complex and the architecture is provided in the publication. In the model, sensory information is obtained from a wide range of engine sensors covering from low to high bandwidth signals. This included aircraft, gas path, lubrication, structural indicators and the FADEC codes. The level of information fusion that is used in [9] is feature level fusion. Feature extraction is conducted through the use of physics-base and empirical model analysis. The fusion process is two tiers, where engine health features are combined from information provided by the sensors together with fault codes, maintenance records and observations to form a comprehensive engine health assessment. The model consists of two levels sensors and information fusions.
The data analysis tools used in the work included both physics-based and empirical information that include:

- *Synchronization of raw data*: Up and down sampling.
- *Gas path anomaly detection*: An empirical model of nominal gas path behavior with a metric for inferring the level of deviation from nominal in the form of an Artificial Neural Network.
- *Gas path analysis*: Isolation, estimation and tracking of engine module performance fault by measuring the change in performance relative to some reference using Kalman Filter approach.
- *Lubrication system modeling*: Empirical derived models for estimating oil quantity and bearing pressure.

The diagnostic feature information from the model and algorithms, along with aircraft operational information are used to assess the health of the engine. In the model, two levels of information fusion are applied to extract information features.
First tier: Delivers engine health information from the sensors and the FADEC codes.
Second tier: Utilizes the information from the first tier together with the engine maintenance history and pilot observations. The second tier is driven by a Bayesian Belief Network (BBN) that consists of graphs with conditional probabilities linking the nodes of the graphs and a process updating the conditional probabilities using the Bayes Law. As an alternative to BBN, Fuzzy Belief Network (FBN) can also be used to ease the computation.
The diagnostics and prognostics architecture proposed by Simon et al. is very complex and comprehensive architecture. Some of the aspect of the architecture will be very useful and relevant to our work in the area of diagnostics.

3.1.2 Prognostics

The field of prognostics is relatively new and since Behbahani et al. [1] has conducted a recent, extensive and knowledgeable literature review in the field. We would like to refer to Section-II of Behbahani and et al.'s review for insight and details about the subject.

3.1.3. Control of Gas Turbine Engines

It is well known that the first jet propelled aircraft provided thrust modulation using rudimentary hydro-mechanical governor regulation. The late 1960's saw the introduction of a digital processor into a turbofan (the F100) which performed a supervisory function to the hydro-mechanical controller [10]. In the 1970's De Hoff and Hall Jr. presented a practical control design methodology for turbine engine control synthesis [10]. Their procedure utilized optimal control syntheses to produce practical, implementable digital controllers for aircraft turbine engines of the time.

In the early 1990s, digital controllers for gas turbine engines became common. With the increasing use of active control technology (ACT) in military aircraft to allow reductions in wing and tail areas giving greater maneuverability, it became the case where many aircraft were unflyable without automatic stabilization functions. Any failure of a controller in an aircraft can have serious consequences. Thompson and Fleming [11] investigated the use of transputer arrays for fault tolerant gas turbine engine control, where transputers are concurrent computing microprocessors.

Also during the 1990s, the controllers for aircraft gas turbine engines were termed full authority digital engine controllers (FADEC) [12]. The FADECs were conventional propulsion controllers which use closed-loop control of selected parameters such as low-pressure spool speed or engine pressure-ratio to set engine fuel flow [13]. Different control strategies were investigated during this time period in the design of the FADEC and these strategies often involved a model since the gas turbine engine is a nonlinear system as well as the fact that testing of a proposed FADEC with real engines was expensive. Some works found in the literature are as follows.

Kulikov et al. [12] discussed techniques for testing and perfecting FADEC systems with the use of Markov models in the testbed. Perez and Nwokah [14] used model reference control strategy for the development of a controller and tested on a FORTRAN source code simulation of a gas turbine engine. Model reference control was developed by Whitaker et al. [15] and the FORTRAN source code package titled HYTESS I was developed by Merrill et al [16]. Qi et al. [17] researched a model-based observer approach using a nonlinear model of the gas turbine engine. Qi et al. [18] also investigated translating the performance requirements and constraints, of fast thrust while ensuring engine safety, into compressor characteristics for the controller to achieve. The controller was designed and evaluated using gain scheduling. Samar and Postlethwaite [19] investigated a different control system to control the engine thrust and regulate compressor surge margins for a gas turbine engine. Perez and Lou [20] decentralized the MIMO gas turbine engine control system structure to a SISO system by adding static compensators within the loops of the system.

The aforementioned gas turbine engine control strategies were considered for the fixed cycle gas turbine engines and the characteristics of its operation such as specific thrust and specific fuel consumption were fundamental to the engine design. The design of these engines were a compromise between conflicting requirements for performance at different points in the flight envelope and the achievement of low life-cycle costs, while maintaining structural integrity [21]. The demand of flight propulsion systems to improve fuel economy, wide flight envelopes and mission capabilities was met by new engine design which incorporated more active internal variable geometry devices. This engine is known as the variable cycle engine (VCE) [13]. Variable geometry components, such as the inlet guide vanes and nozzle area may be used to optimize the engine cycle over a range of flight conditions with regard to thrust, specific fuel consumption and engine life, assisting in the reduction of life-cycle costs [22]. Use of these variable geometry components within the gas turbine lead to more complexity in the design of the FADEC. Approaches in the design of the FADEC for the variable cycle engine found in the literature from the mid 1990s to the present will now are presented next.

Schutler [13] discussed a control configuration design for aircraft turbine engines. The control configuration design method is based on a necessity for the development of a formal methodology to solve the engine parameter and control mode selection for the more complex variable cycle engine. Control configuration design is viewed as the process of identifying a control structure which allows a

satisfactory trade-off between the conflicting requirements of system performance (favoring more complex system with multiple inputs, outputs and closed loops) and system reliability and maintainability (favoring a system with a minimal number of measurements and closed loops). Control configuration design covers two stages in the total design process. The first stage allows for the selection of the most appropriate set of measurements and manipulations and the choice of particular open-loop or closed loop control modes. The second stage covers the partitioning of the total number of closed-loop controls into subsections of single and multiple closed loops. Schutler [13] presented two methods of control configuration designs. The first method is based on a steady-state sensitivity matrix relating all the engine performance and safety parameters of interest to all engine input variables. The method allows parameter choice and open-loop versus closed-loop options to be compared. The second method is based on dynamic relationships between engine inputs and outputs and allows selected closed-loop options to be compared in terms of achievable bandwidth and robustness criteria.

Chipperfield and Fleming [23] described the use of multi-objective genetic algorithms (MOGA) in the design of a multi-variable control system for a gas turbine engine. They showed how the MOGA confers an immediate advantage over conventional multi-objective optimization methods by evolving a family of Pareto-optimal solutions allowing the control engineer to examine the trade-offs between the different design methods. They concluded that implementation of their design may prove infeasible due to the numerically intensive nature of evaluating objective functions. The authors also presented research work on the application of evolutionary algorithms for the control of gas turbine engines [21]. Subbu et al. [24] stated that although the FADEC allows designers to implement the high level of complexity necessary to achieve the many and varied operating objectives, the combination of a complex engine, varied performance objectives and constraints, and a computer sufficiently powerful for real-time operation of extensive amounts of code results in a formidable design challenge. The authors presented methods to automatically identify and optimize controllers for an aircraft gas turbine engine. They showed how the optimization of different elements, including local actuators, control modifiers and control schedules, within the overall controller can be addressed in an efficient manner using evolutionary algorithms and multi-objective optimization. The authors also stated that minimal attention has been given to the application of optimization techniques to aircraft control systems design.

Van Essen and de Lange [25] presented the feasibility and benefits of model based predictive control (MPC) applied to a gas turbine engine. They apply a nonlinear MPC configuration to gas turbine control and succeeded in a real-time implementation on a laboratory gas turbine built from an industrial turbocharger and custom made combustion chamber. They concluded that the performance of the implemented MPC configuration is good. Similarly, Brunell et al. [26] applied nonlinear MPC to a simplified real time model (SRTM) that captures all of the relevant dynamics of a gas turbine engine. They tested their controller on a high-fidelity model of a military aircraft engine and showed that the controller developed for the SRTM has the potential to achieve better performance than the production controller. Also, Diwanji et al. [27] investigated the application of nonlinear MPC. Their controller was realized on a developed nonlinear black-box model of a gas turbine engine based on Weiner modeling approach. The model consisted of linear dynamic block parameterized by Laguerre, orthonormal basis functions, followed by a static nonlinear block captured by artificial neural network. Mu and Rees [28] use Nonlinear Auto-Regressive Moving Average with eXogenous inputs (NARMAX) and neural network models to represent the global dynamics of a gas turbine engine [29, 30]. The authors developed a control strategy incorporating the Generalized Predictive Control (GPC) called Approximate Model Predictive Control (AMPC) to control shaft speed of a gas turbine engine.

Diao and Passino [31] applied stable indirect and direct adaptive controller to achieve fault-tolerant engine control by using Taki-Sugeno fuzzy systems to “learn” the unknown dynamics caused by faults and to accommodate faults by updating the controller. By developing the analytical model and studying system zero dynamics, they proved that both adaptive schemes achieve asymptotic tracking results. The performance of the controller was also demonstrated through the component level model simulation of the XTE46 engine provided by General Electric Aircraft Engines.

Kreiner and Lietzau [32] stated that newer control theories being applied to jet engines include the application of LQG, (Linear Quadratic Gaussian Regulator) theory combined with LTR (Loop Transfer Recovery) [32], the application of robust control (H-Infinity) theory [34, 35, 36], fuzzy logic [37], and adaptive one-step-ahead control [38].

3.2 Development and Testing of Adaptive Controllers for the Turbine Engine

The objective of this part of the research is to develop a fuzzy-logic based adaptive controller for control of the turbine engine model provided by the Air Force Research Lab (AFRL). The AFRL turbine engine model provides a comprehensive and complex model of a turbine engine. As with most modeling of turbine engines, it is assumed that the fundamental dynamic characteristics of the engine can be represented by a single-input single-output (SIS0) system. First, detailed development of a fuzzy-logic controller for the turbine engine is reported. Then, testing results of the engine performance using this fuzzy-logic controller are compared with the engine performance using the original PI-controller under normal and faulty operating conditions.

This report is organized as follows. In Section-3.2.1 the proportional-integral (PI) controller for the SIS0 subsystem used in the AFRL turbine engine model is presented. Section-3.2.2 included discussion of the development of the fuzzy-logic controller for the SIS0 subsystem. Simulation results produced by the fuzzy-logic controller under normal operating conditions are compared to the PI-controller results. Also, comparison between simulation results of the fuzzy-logic controller and the PI-controller under faulty condition is presented in Section-3.2.3. Section-3.2.4 included result comparison obtained from implementing the fuzzy-logic controller and the PI-controller as the power lever angle (PLA) input is varied under normal operating conditions. Section-V included the result of investigating the affects of Variable Stator Vane (VSV) control and the Inlet Guide Vane (IGV) control on the engine model as input variables.

3.2.1 Existing Controller of the AFRL Engine Model

A high-level representation of the controller block derived from the AFRL gas turbine engine Simulink model is shown in Figure 1. The controller consists of two sections: 1) a single-input single-output (SISO) control section and, 2) a multiple-input multiple-output (MIMO) regulator section. Each of the above sections consists of a PI-controller with gain adaptation mechanism. The SISO control section operates on the low pressure spool speed error signal (NLerr). The regulator section operates on the NLerr, the inlet stator vanes (SM2err) and the booster stator vanes (SM27err) error signals respectively. As stated in previous reports at this time the fuel flow actuator (WF36) is the only actuator being controlled by the control subsystem.

The gain adaptation blocks and the error loops for both the SISO controller and the regulator are also show in Figure 1. Each adaptation block consists of two sections; one for computing the proportional gain (GP) and the other for updating the integral gain (GI). Each of the above two sections contains four constants and acts on three feedback signals provided by the Sensor and Condition block within the engine model. These are; the inlet temperature T2, the inlet pressure P2 and the percent corrected fan speed PCN2R. Figure 2 shows the structure of the gain adaptation block for the SISO controller. The MIMO regulator has similar architecture as the SISO controller and is show in Figure 3.

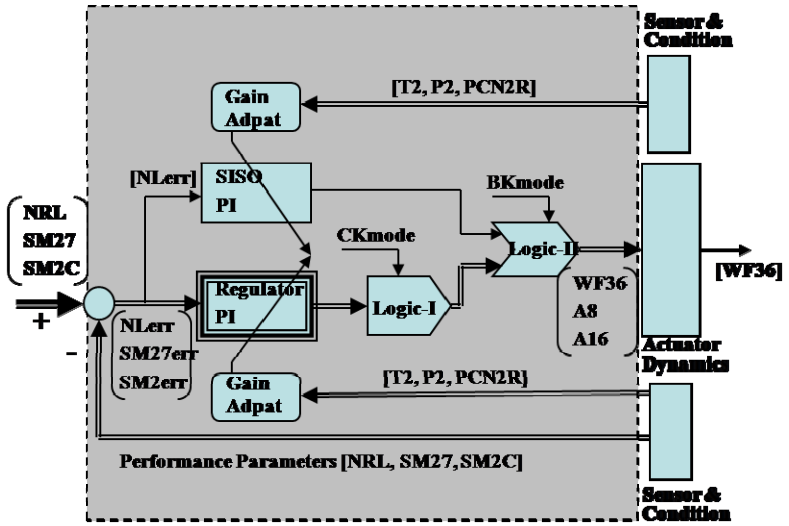

Figure 1. Internal Details of the Engine Model Controller Block

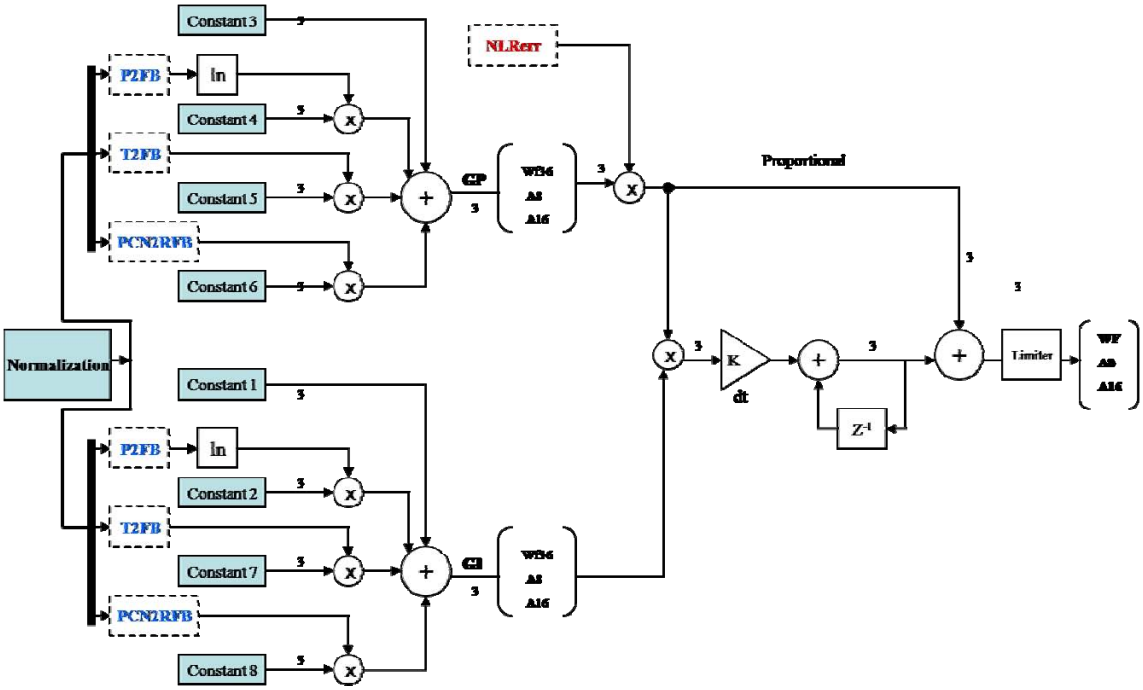

Figure 2. SISO Gain Adaptation Block and its Error Loops

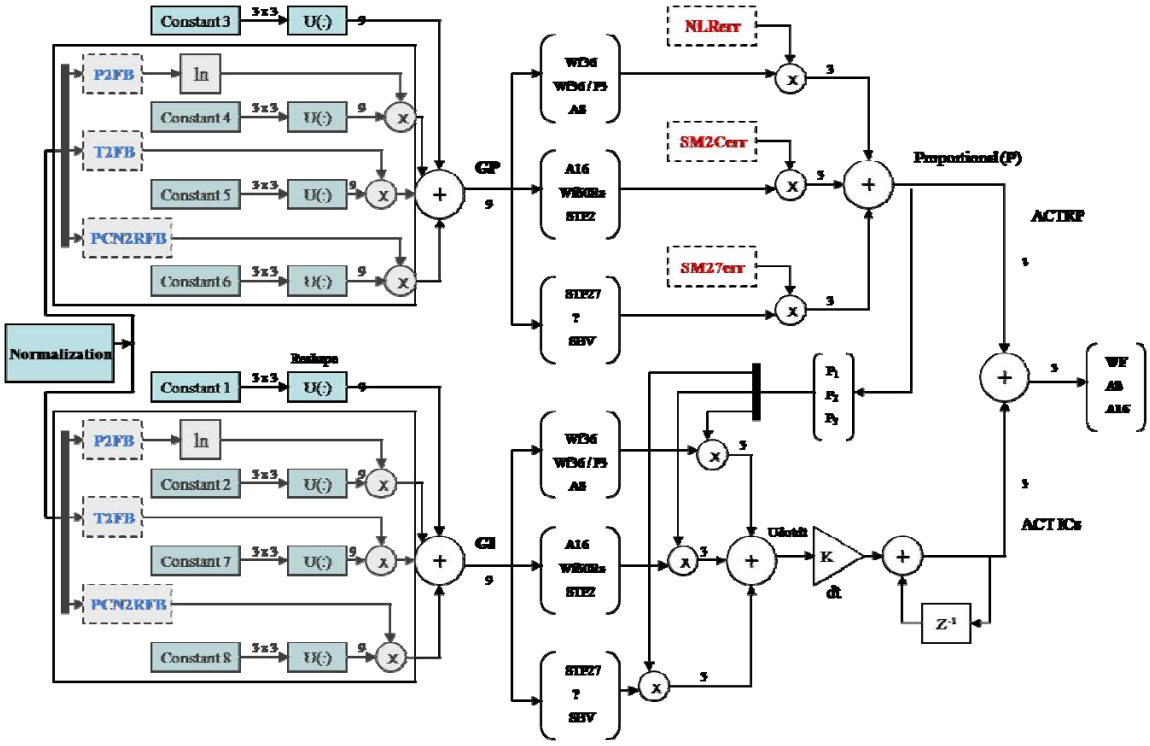

Figure 3. Regulator Gain Adaptation Block and its Error Loops

3.2.2 Development of Fuzzy-logic Controller

Since the MIMO regulator controller and the SISO controller have similar architectures, a fuzzy-logic controller was developed only for the SISO controller at this phase of the research. A high-level representation block diagram of the fuzzy-logic control architecture developed to replace the SISO controller is shown in Figure 4.

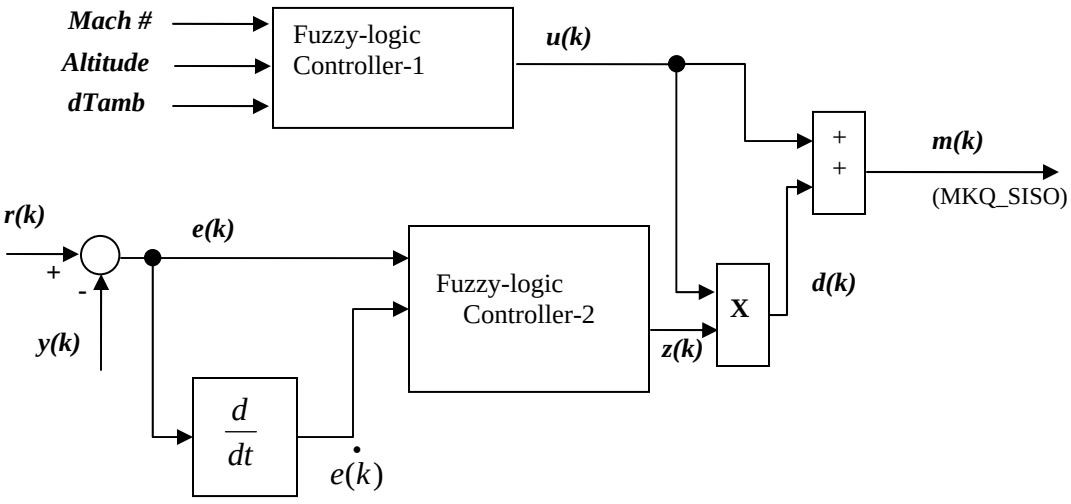

Figure 4. Block Diagram of the Fuzzy Control Architecture

From Section-I, it was stated that the SISO controller operates on the feedback error signal NLerr only. Thus the variables shown in Figure 4 are defined as follow.

- *y(k)* is low pressure spool speed performance NL

- *r(k*) is the low pressure spool speed demand NL
- *e(k*) is the error signal NLerr
- *u(k)* is steady-sate values of the control signal *m(k)* generated by the PI-controller based on Mach #, Altitude and dTamb inputs of the model
- *d(k*) is the same as *u(k)* multiplied by a scaling factor *z(k)*
- *m(k)* is the control signal (MKQ_SISO) sent to the Control Action block of the model
- *Mach #* is the mach number input
- *Altitude* is the altitude input
- *dTamb* is the ambient temperature input

For development of the fuzzy-logic controller-1, steady state values of the MKQ_SISO control signal were generated using the engine model for different inputs of altitude, dTamb, and Mach # using the existing PI-controller as shown in Table 1. The PLA input in the model was set to a constant value at position 100. Fuzzy-logic controller-1 was then designed to generate the same MKQ_SISO control signal steady state values based on the input of altitude, dTamb, and Mach #.
Next, Fuzzy-logic controller-2 was developed. Based on the demand input *r(k)* and its responses *y(k)*, the steady state value of the MKQ_SISO control signal *u(k)* and *d(k)* are added to produce *m(k)* and send it to the Control Actions block of the model. The scaled control signal *d(k)* is a value ranging from zero to the steady state value of the MKQ_SISO control signal. The input variables to the fuzzy-logic controller-2 are *e(k)* and $\dot{e}(k)$ can be defined as follows

$$e(k) = r(k) - y(k)$$

and

$$\dot{e}(k) = e(k) - e(k-1)$$

When $y(k) > r(k)$ then *e(k)* and $\dot{e}(k)$ both will be negative. When $y(k) < r(k)$ then *e(k)* and $\dot{e}(k)$ both will be positive. For purpose of fuzzification *e(k)* and $\dot{e}(k)$ are represented using the following linguistic fuzzy variables.

1) Very High (VH) - positive
2) Medium High (MH) - positive
3) High (H) - positive
4) Zero (Z)
5) Low (L) - negative
6) Medium Low (ML) - negative
7) Very Low (VL) – negative

Looking at the error signals generated by the PI- controller, the range for *e(k)* and $\dot{e}(k)$ are determined. Next, fuzzification of the linguistic variables and selection of the membership functions used for the linguistic variables of e*(k)* and $\dot{e}(k)$ are developed. The output variable of the fuzzy-logic controller-2, *z(k)*, is constrained to values between 0 and 1. The variable *z(k)* is represented using the following linguistic variables.

1) Zero Increase (Z)
2) Small Increase (S)
3) Moderately Small Increase (MS)
4) Medium Increase (M)
5) Moderately Medium Increase (MM)
6) Large Increase (L)
7) Moderately Large Increase (ML)

Table 1

MKQ_SISO Control Signal Steady State Values

Altitude (ft)	Mach#	dTamb	MKQ_SISO Control Signal
1,000	0	-60	19.7891
1,000	0.325	-60	19.9993
1,000	0.65	-60	23.5212
1,000	0	18	14.2622
1,000	0.325	18	20.9614
1,000	0.65	18	23.4909
1,000	0	96	14.5922
1,000	0.325	96	14.7051
1,000	0.65	96	23.6487
35,000	0	-60	11.6302
35,000	0.325	-60	11.7793
35,000	0.65	-60	12.2967
35,000	0	18	13.4842
35,000	0.325	18	13.6714
35,000	0.65	18	14.2451
35,000	0	96	14.3704
35,000	0.325	96	14.2773
35,000	0.65	96	14.1307
70,000	0	-60	12.0561
70,000	0.325	-60	12.1633
70,000	0.65	-60	12.6239
70,000	0	18	14.1293
70,000	0.325	18	14.2464
70,000	0.65	18	14.3440
70,000	0	96	14.2971
70,000	0.325	96	14.2077?
70,000	0.65	96	14.2193?

The rules used by the inference engine of the fuzzy-logic controller-2 are shown in Table 2.

Table 2

Fuzzy-logic Controller-2 Rule Base

	$\dot{e}(t)$							
		VH	MH	H	Z	L	ML	VL
	VH	ML	L	MM	M	MS	S	Z
	MH	L	MMI	M	MS	S	Z	Z
	H	MM	M	MS	S	Z	Z	Z
e(t)	Z	M	MS	S	Z	Z	Z	Z
	L	MS	S	Z	Z	Z	Z	Z
	ML	S	Z	Z	Z	Z	Z	Z
	VL	Z	Z	Z	Z	Z	Z	Z

Figures 5, 6 and 7 show comparisons of the control signal *MKQ_SISO* and the error signal *NLerr* values generated by the PI-controller and the fuzzy-logic controller for different inputs. In Figure 5, both controllers show oscillation in the *NLerr* and *MKQ_SISO* values however the *NLerr* for the fuzzy-logic controller oscillates around zero from the start. In Figures 6 and 7 the fuzzy-logic controller performs well with the *NLerr* error parameter settling at zero faster than with the PI- controller.

The performance parameters, therefore thrust, fuel consumption, thermal efficiency and propulsive efficiency generated by the PI-controller and the fuzzy-logic controller for different inputs are included in Appendix-B. One can see from these plots that the fuzzy-logic controller yields similar results to the PI-controller.

Three dimensional plots of these performance parameters generated by the PI-controller and the fuzzy-logic controller at 1,000 feet with the dTamb and Mach # varied as ramp functions from 0 to 60 seconds are also recorded. They are shown in Appendix-B, Figure B1 and appear to be very similar.

The same performance parameters were generated in three dimensions generated by the PI- controller and the fuzzy-logic controller at 35,000 feet with the dTamb and Mach # varied as ramp functions from 0 to 60 seconds and are shown in Figure B2 of Appendix-B. There is a small difference in the thrust generated by the two controllers. The propulsive efficiencies appear to be very similar. There are also differences in the fuel consumptions where at some periods it seems that the parameter generated by the fuzzy-logic controller is higher than that generated by the PI-controller and vice versa. The thermal efficiency of the fuzzy-logic controller appears to be lower than that of the PI-controller.

The same performance parameters were also generated in three dimensions for the PI controller and the fuzzy-logic controller at 70,000 feet with the dTamb and Mach # varied as ramp functions from 0 to 60 seconds and are shown in Figure B3 of Appendix-B. There are more defined differences in the thrust generated by the two controllers. The propulsive efficiencies appear to be very similar. There are also clear differences in the fuel consumptions where at some periods it seems that those generated by the fuzzy-logic controller are higher than that generated by the PI controller and vice versa. The thermal efficiency of the fuzzy-logic controller appears to be lower than that of the PI controller.

These observations prove that a fuzzy-logic controller can be designed to perform very similar or better than the PI controller under normal operating conditions. We feel that the differences in engine performance at the 35,000 and 70,000 feet altitudes are due in part to the design of the fuzzy-logic controller. At this stage of the research, the fuzzy-logic controllers are designed with a minimum number of membership functions as well as with the basic triangular shaped functions. An increase in the number of membership functions as well as the use of other shaped membership functions should provide better results. For example, considering Table 1, *MKQ_SISO* was only computed for three flights' range, i.e., low, mid and high altitudes. Reduction of the ranges for instance would produce better results.

Recall the PI controller consists of two sections: 1) a single-input single-output (SISO) control section and, 2) a MIMO regulator section. The SISO control section operates on the NLerr error signal. The MIMO regulator section operates on the NLerr, SM2err and SM27err error signals. In this section a fuzzy-logic controller was designed for the SISO control section only and the regulator section was not enabled within the model. Based on this approach, a fuzzy-logic controller should be designed for the regulator section. This would encompass using three variables and thus leading to a multi-variable fuzzy-logic controller.

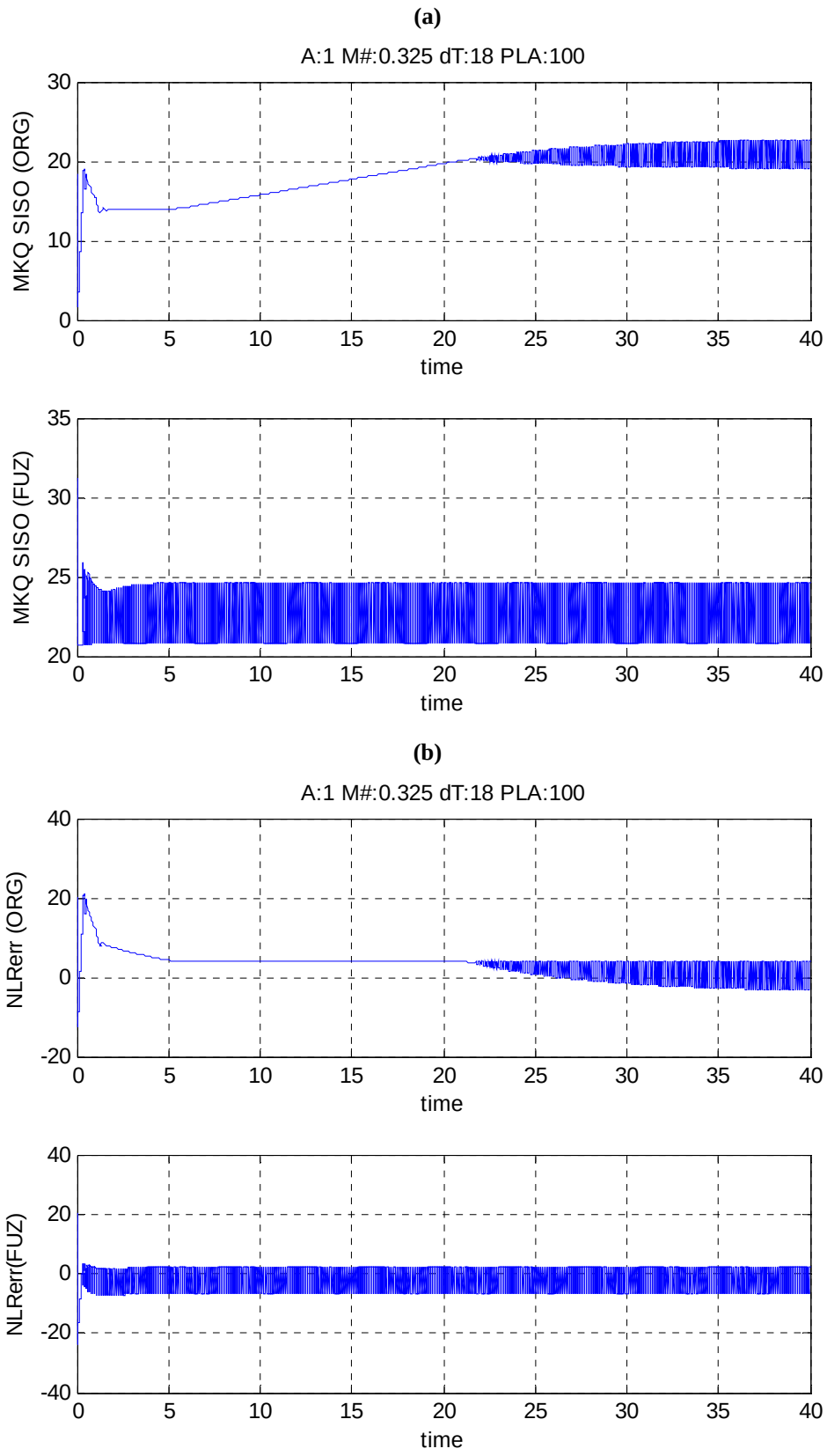

Figure 5. Performance of PI vs. Fuzzy-logic Controller at 1,000 Feet

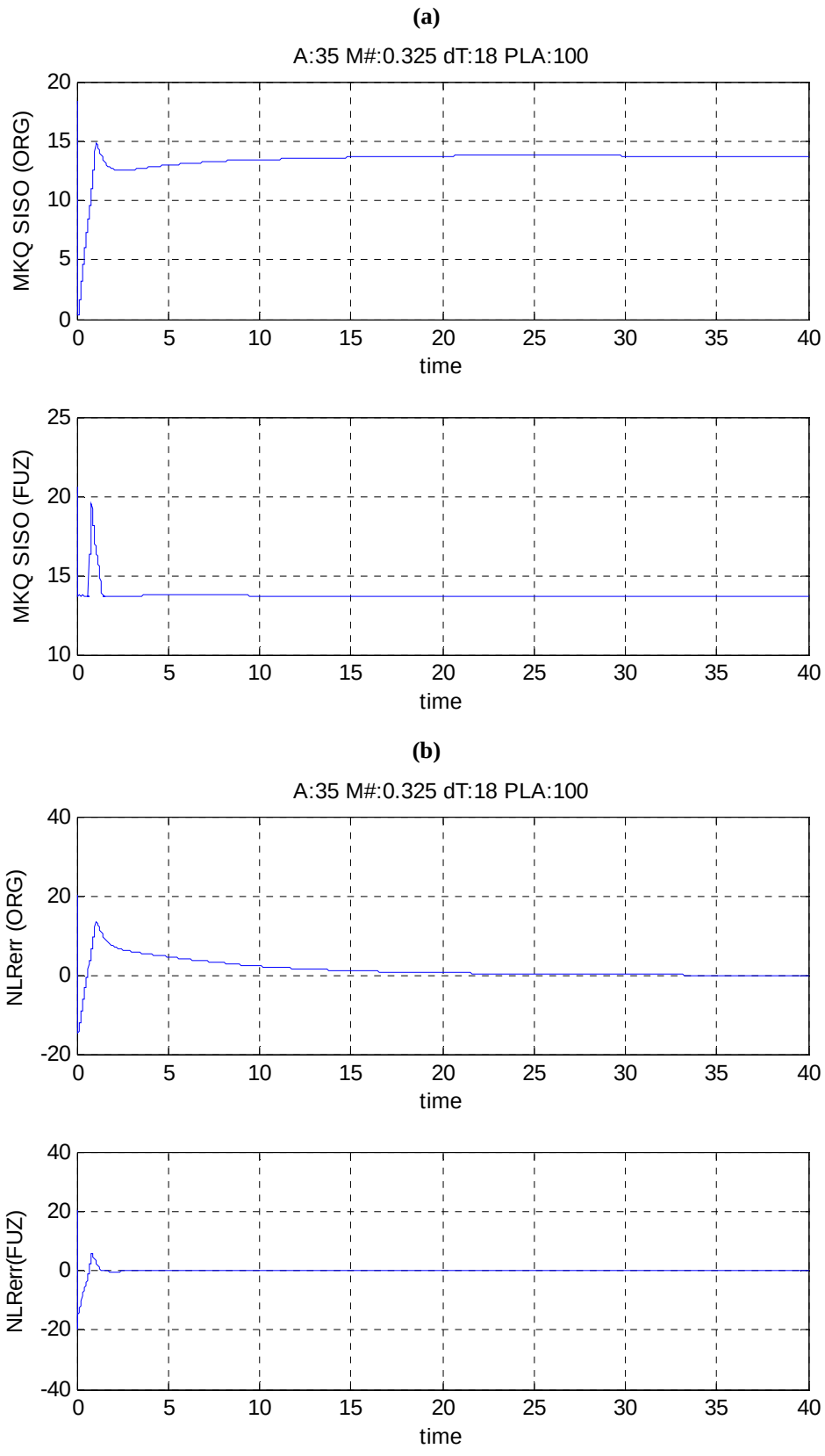

Figure 6. Performance of PI vs. Fuzzy-logic Controller at 35,000 Feet

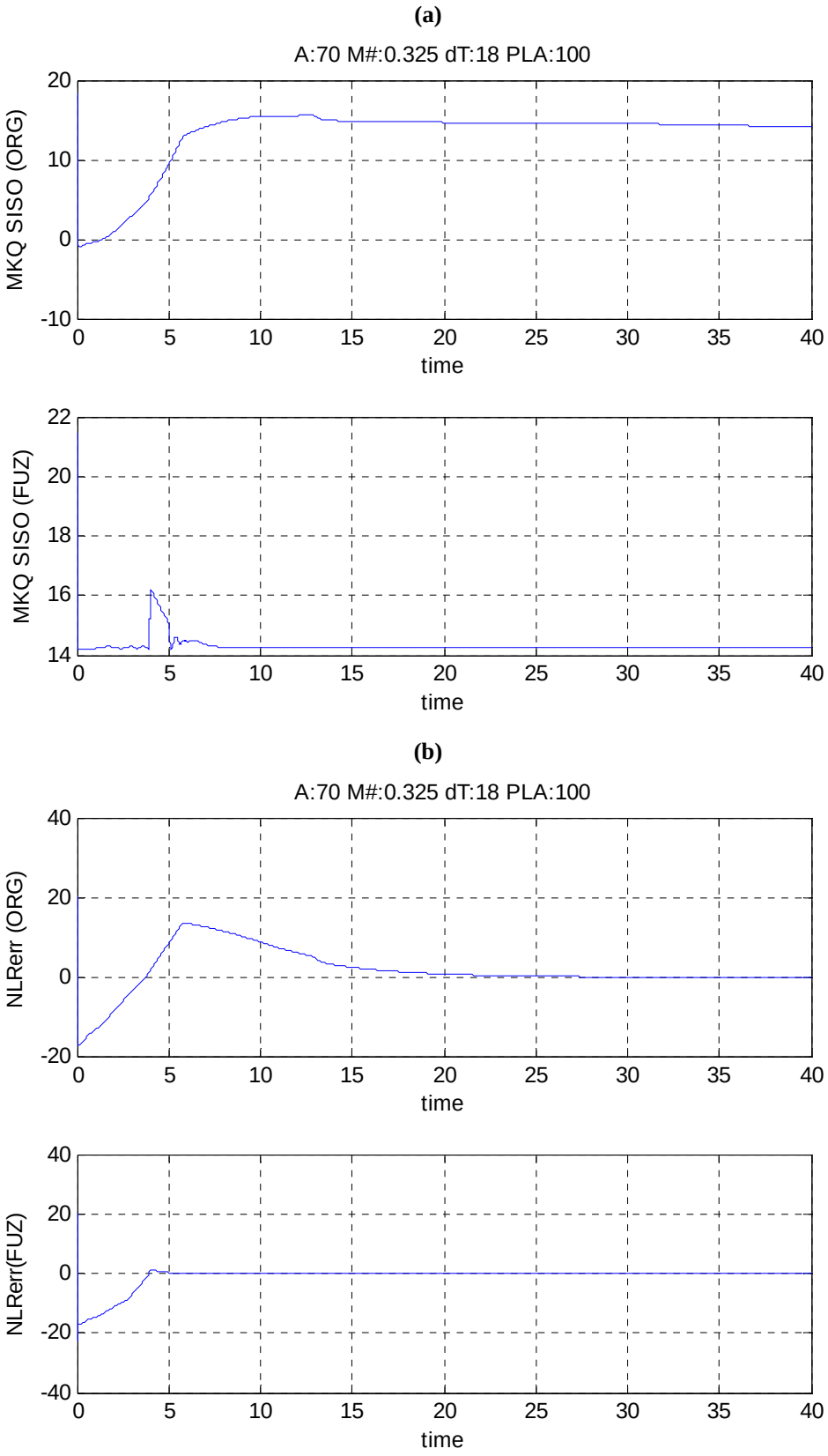

Figure 7. Performance of PI vs. Fuzzy-logic Controller at 70,000 feet

3.2.3. Controller Performance under Faulty Conditions

Several testing scenarios were conducted under this part of the research. First, the engine model performance was simulated under the following sensor fault conditions using the original PI-controller and then using the developed the fuzzy-logic controller.

The fault scenario-1 is "*A signal fault at the inlet total temperature (T2FB) sensor inflected at t = 13 seconds*." T2FB were selected based on its influence on the control signal of the fuel flow (WF36) actuator. As it was stated in the previous report, fuel flow actuator is the only actuator connected to the turbine block part of the engine model at hand. In the scenario, a noise signals equivalent to ±10% of the sensor signal was added to the sensor signal during the transient response period of the fuel flow (WF36) actuator during the engine different runs. Figure 8 shows the Sensor and Condition subsystem part of the engine model with the logical switch that controls the noise level added at the inlet sensor's output.

Figures 9 through 11 show a comparison of the MKQ_SISO and NLerr values generated by the PI-controller and fuzzy-logic controller with the T2 fault for different inputs shown in the figures. Figures C1 through C3 included in Appendix-C show comparison among the performance parameters of the engine generated using the PI-controller and the fuzzy-logic controller for different inputs.

In Figure 9 both controllers show oscillation in the *NLerr* and *MKQ_SISO* values. However the *NLerr* for the fuzzy-logic controller oscillates around zero from the start. The performance parameters are not affected as shown in Figure C1.

In Figure 10 the fuzzy-logic controller performs wells with the *NLerr* error parameter settling to zero faster than with the PI-controller. Important is the fact that the fuzzy-logic controller does propagate minimum noise through the MKQ_SISO signal as the PI- controller does. This in turns allows minimum noise propagation through the performance parameters referring to Figure C2.

In Figure 11 the fuzzy-logic controller performs wells with the *NLerr* error parameter settling to zero faster than with the PI-controller. At this higher altitude, more of the noise does propagate through the MKQ_SISO signal. This in turns allows more propagation of the noise through the performance parameters referring to Figure C3.

The fuzzy-logic controller was designed such that a ±10% fault in T2 would have a minimum effect on the *MKQ_SISO* response and likewise the performance parameters. Further revision of the fuzzy-logic controller design yielded better results at higher altitudes and further design is required for the implementation of higher level of noise.

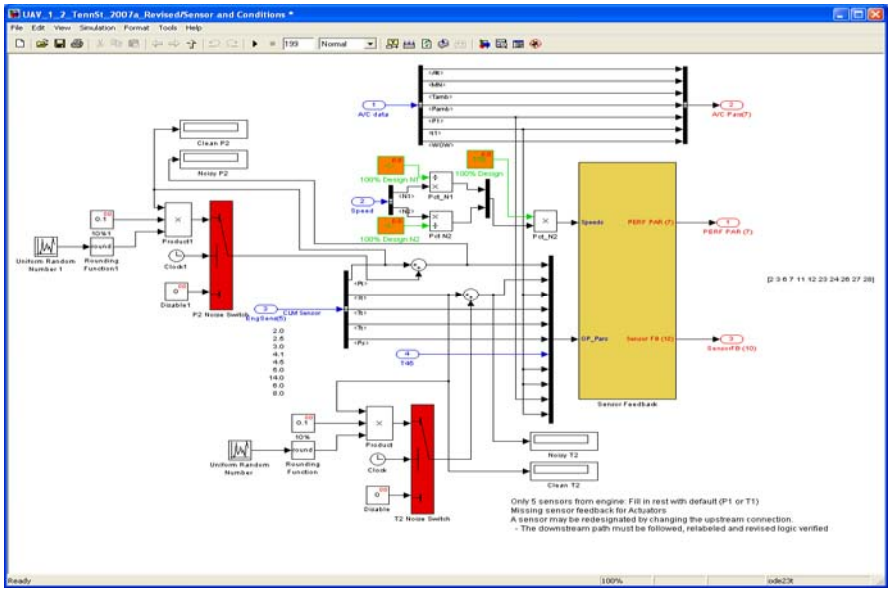

Figure 8. Sensor and Conditions Subsystem Block with Added Noise Switches

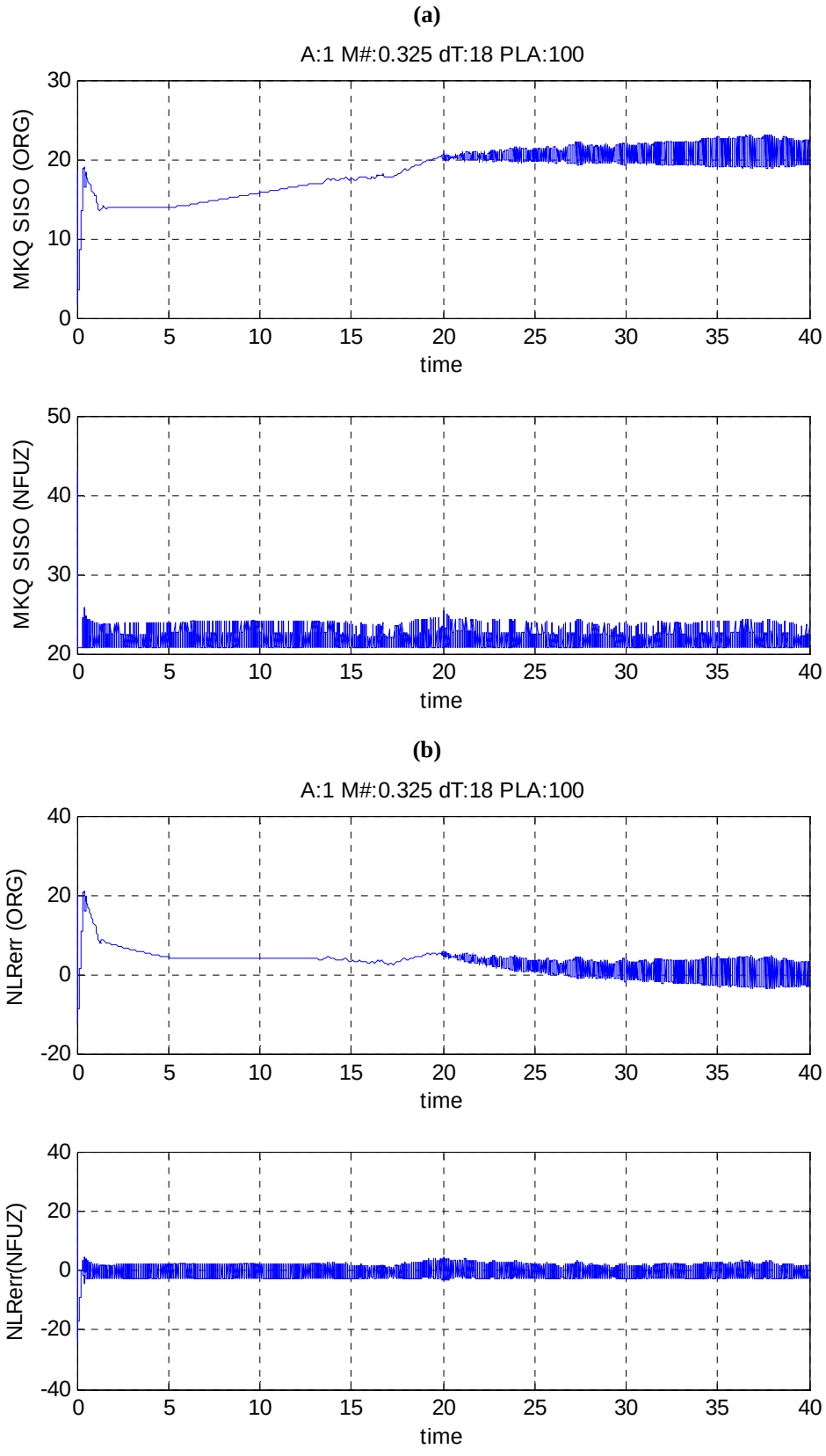

Figure 9. Engine Performance with PI vs. Fuzzy Controller at 1,000 ft & T2 ±10%

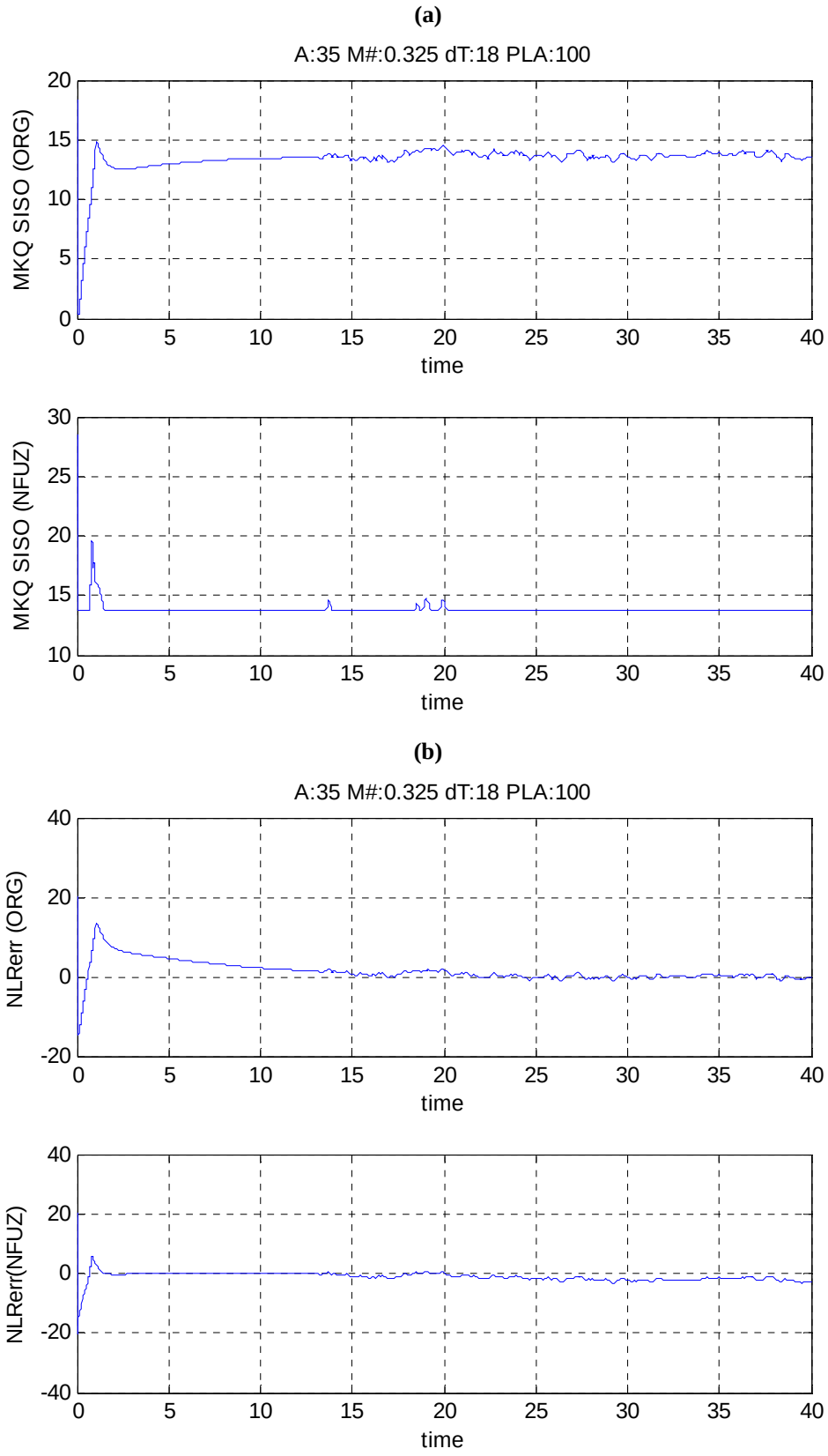

Figure 10. Engine Performance with PI vs. Fuzzy Controller at 35,000 ft & T2 ±10%

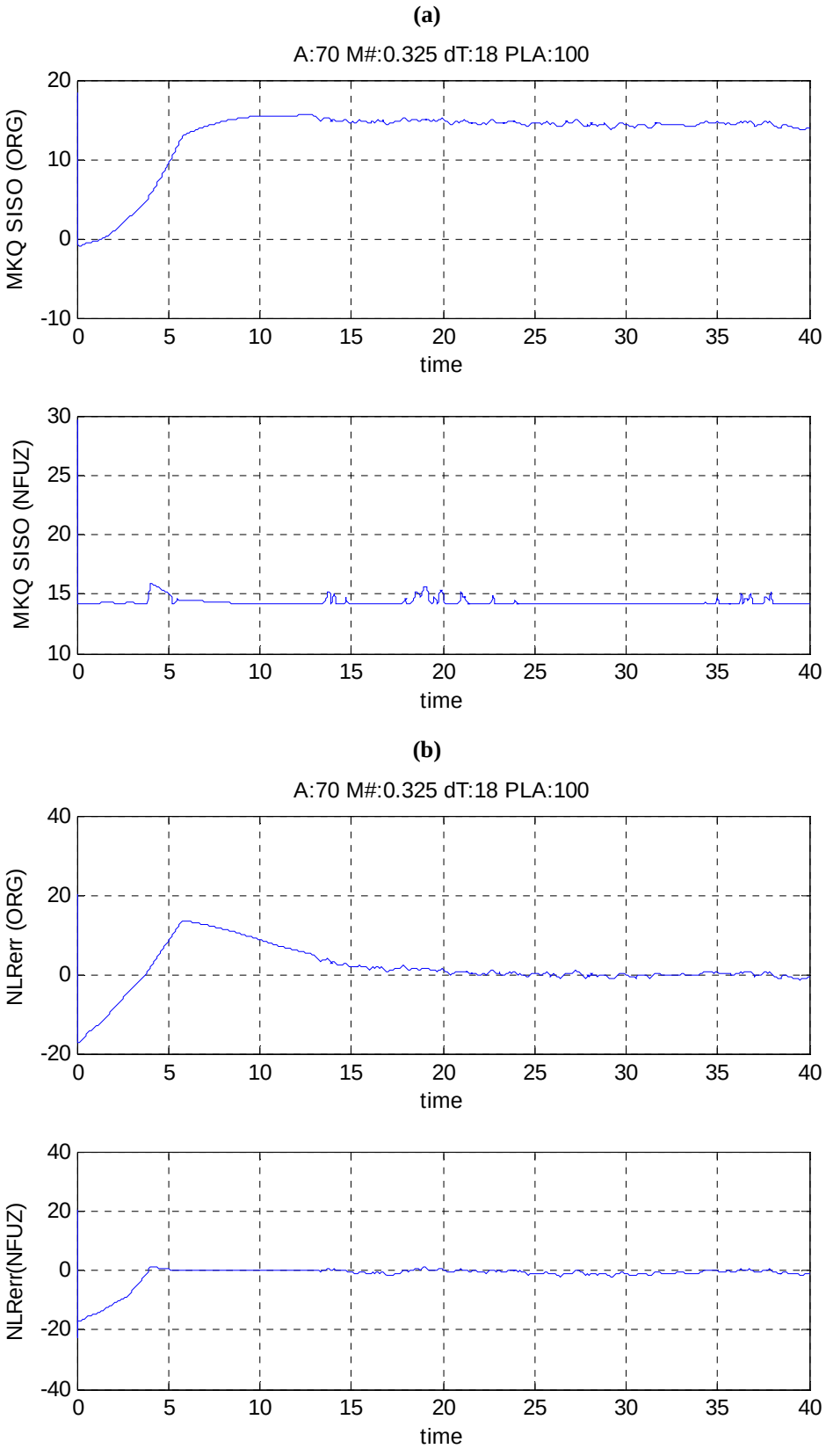

Figure 11. Engine Performance with PI vs. Fuzzy Controller at 70,000 ft & T2 ±10%

Next, the engine was tested using the fuzzy-logic controller under two additional fault conditions inflected on the fuel flow actuator (WF36) itself. These conditions are:

Scenarios-2 "*A fault was introduced at the fuel flow actuator's input signal (WF36DM) where 10% of noise was added to the actuator input control signal during the transient response period at t = 6 seconds.*"

Scenarios-3 "*A fault was introduced at the fuel flow actuator's output position (WF36P) depicting a mechanical failure of the fuel flow actuator at t = 6 seconds. The actuator output position was limited to a predetermined fixed position.*"

Figure 12 shows the fuel flow (WF36) actuator subsystem part of the engine model. In this part of the model two switches were added; one at the actuator input and the other at the actuator output. The input switch functions as a noise switch where the control signal to the actuator is corrupted with ±10% noise. The second switch was added at the actuator output as a mechanical stop (limiter) that restricts the output of the actuator to a fixed position. Again, in the above two scenarios, the fuel flow actuator (WF36) was selected because it is the only actuator connected to the turbine subsystem block of the provided engine model.

Figures 13 through 15 show comparison of the MKQ_SISO and NLerr values generated by the PI-controller and the fuzzy-logic controller with the WF36DM noise fault for different inputs shown in the figures. Figure D1 through D3 included in Appendix-D show comparison of the performance parameters generated with the PI-controller and the fuzzy-logic controller for different inputs as shown in the figures.

Figures 16 through 18 show comparison of the MKQ_SISO and NLerr values generated by the PI-controller and the fuzzy-logic controller with the WF36DM mechanical failure fault for different inputs. Figure D4 through D6 included in Appendix-D show comparison of the engine performance parameters generated with the PI-controller and the fuzzy-logic controller for different inputs as shown in the figures.

In Figure 13 both controllers show oscillation in the *NLerr* and *MKQ_SISO* values however the *NLerr* for the fuzzy controller oscillates around zero from the start. The performance parameters are not affected as shown in Figure D1.

In Figures 14 and 15, the fuzzy-logic controllers perform wells with the *NLerr* where error parameter settling to zero faster than with the PI-controller. The fuzzy-logic controller in both cases does propagate minimum noise through the MKQ_SISO signal. Figures D2 and D3 show more of the noise does propagate through the performance parameters for both the altitudes shown in the figures. However, the fuzzy-logic controller has less noise in the parameters compared to the PI-controller response.

In Figure 16, both controllers show oscillation in the *NLerr* and *MKQ_SISO* values. However, the *NLerr* for the fuzzy-logic controller oscillates around zero from the start. The performance parameters are not affected as shown in Figure D4.

In Figures 17 and 18 the fuzzy-logic controller gives a steady state value for MKQ_SISO even though the actuator is stuck while the PI-controller does not. This allows the performance parameters for the fuzzy-logic controller to reach a steady state faster as shown in Figures D5 and D6.

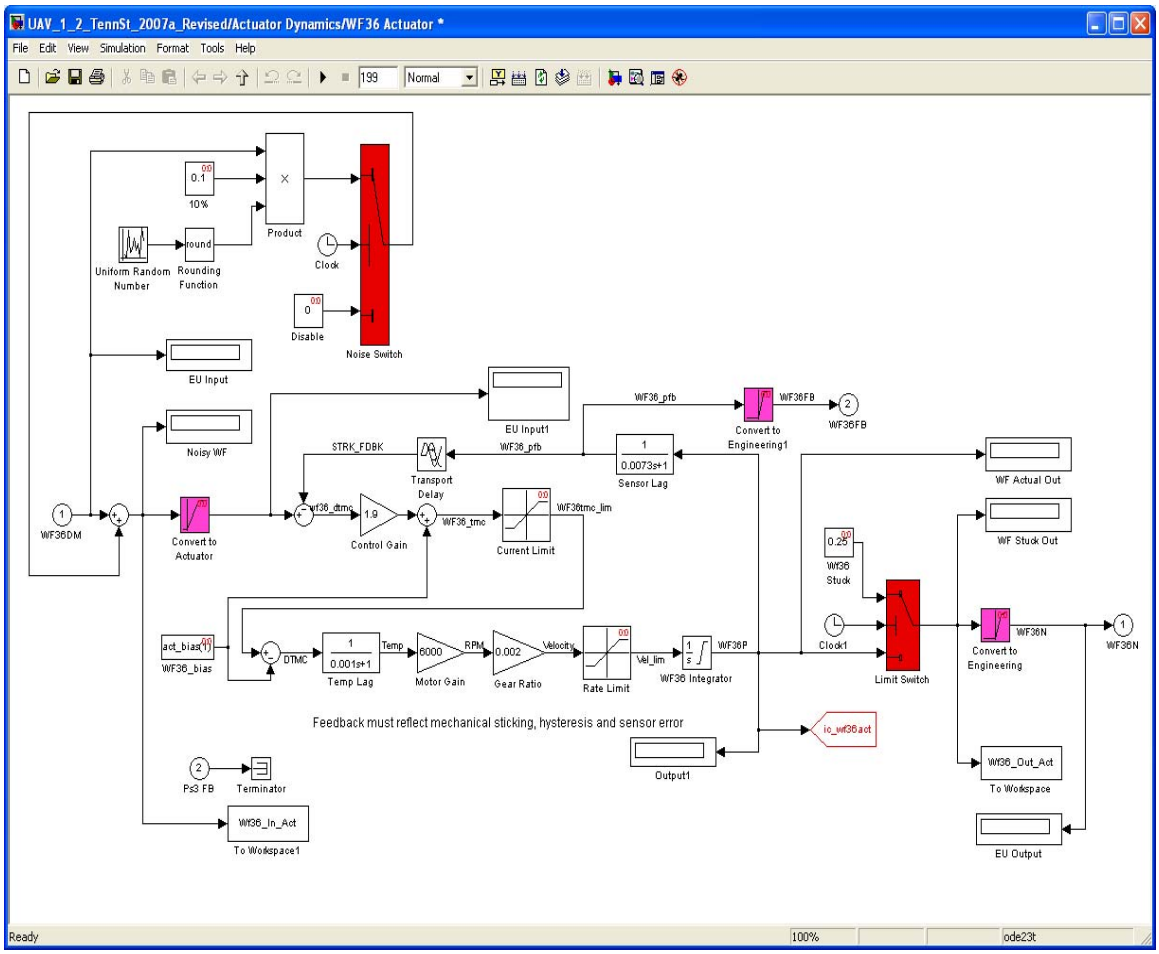

Figure 12. Fuel Flow (WF36) Dynamics Subsystem with Added Faults

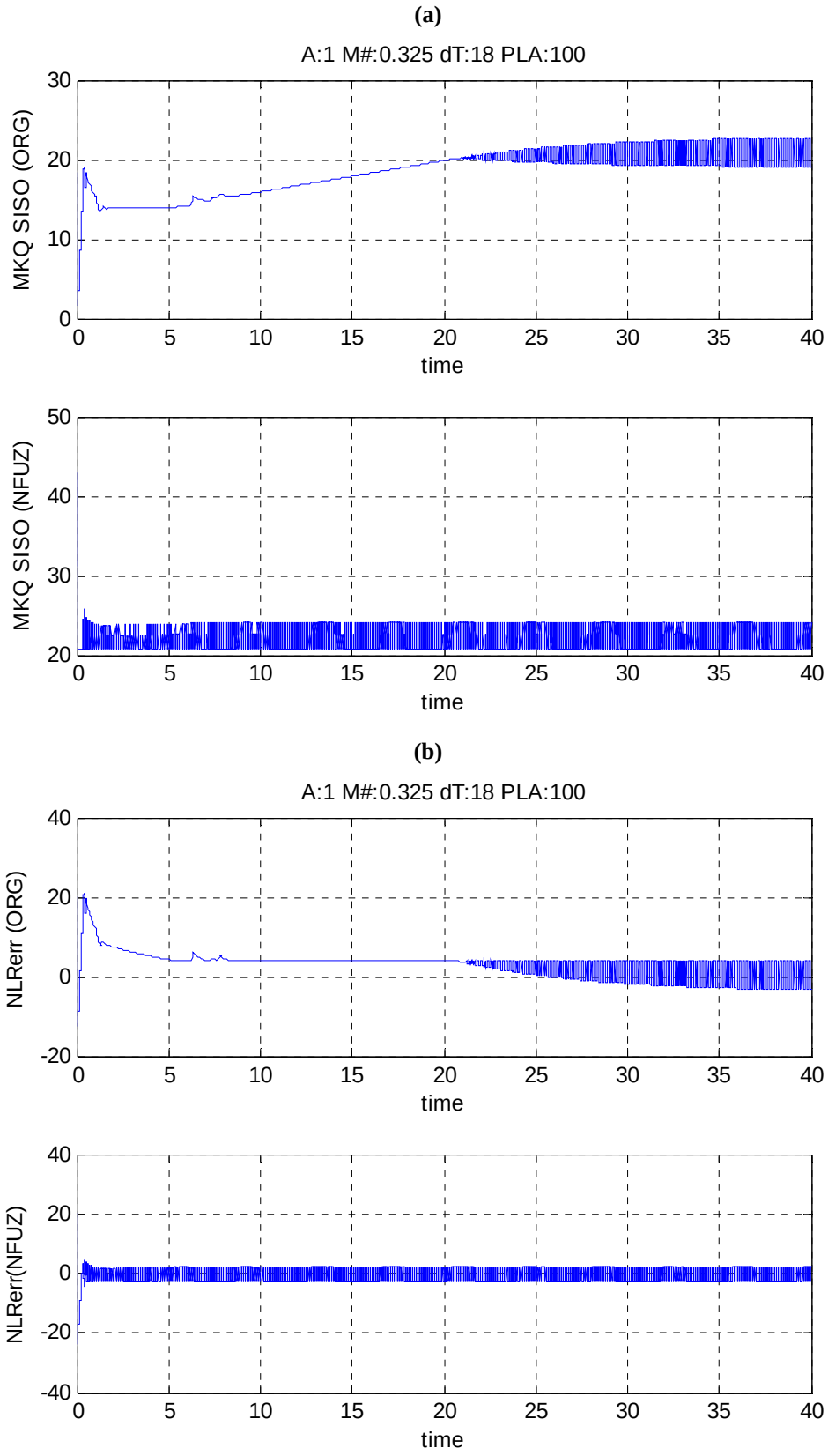

Figure 13. Engine Performance PI vs. Fuzzy Controller at 1,000 ft & WF36 ±10%

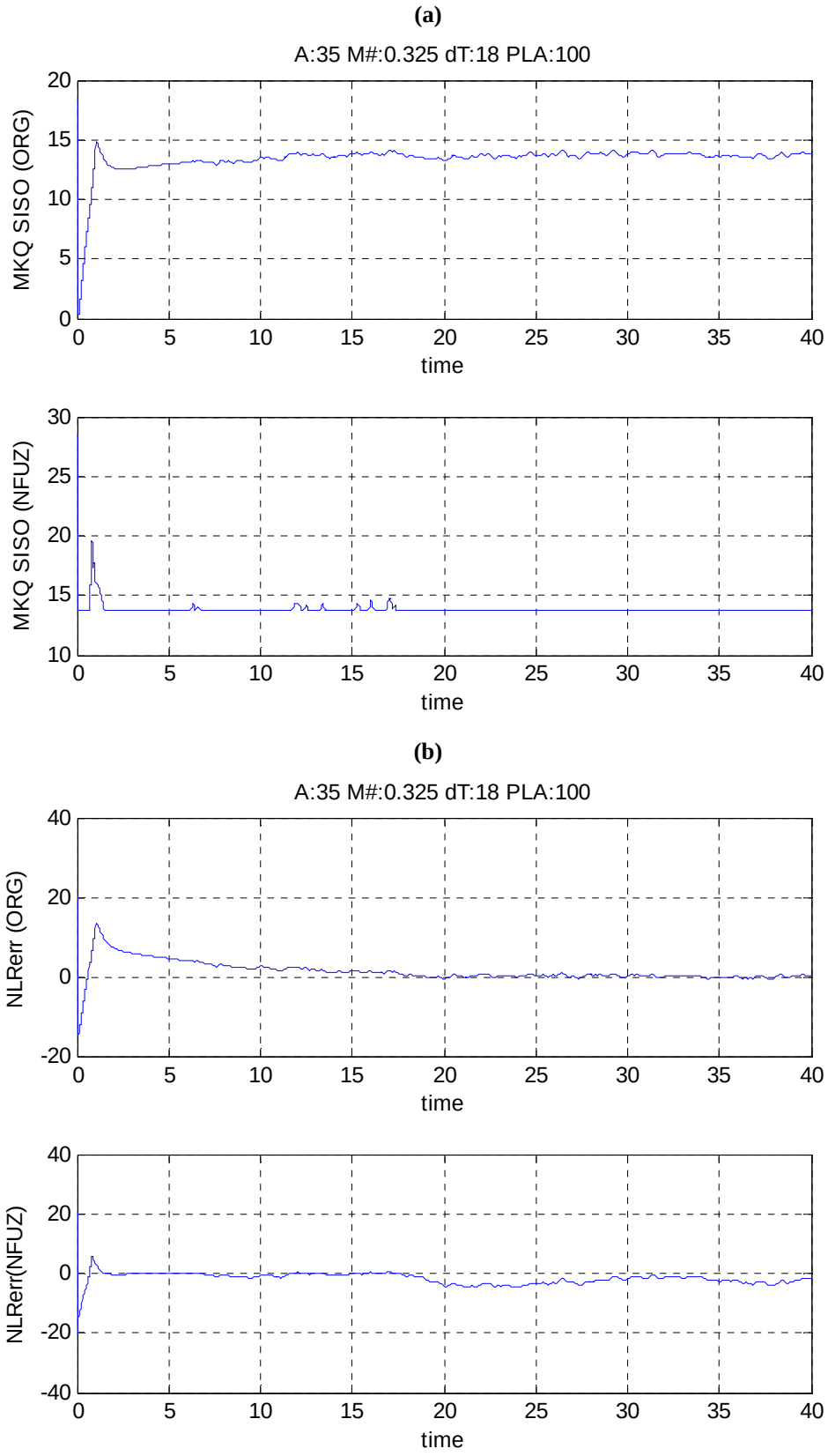

Figure 14. Engine Performance PI vs. Fuzzy Controller at 35,000 ft & WF36 ±10%

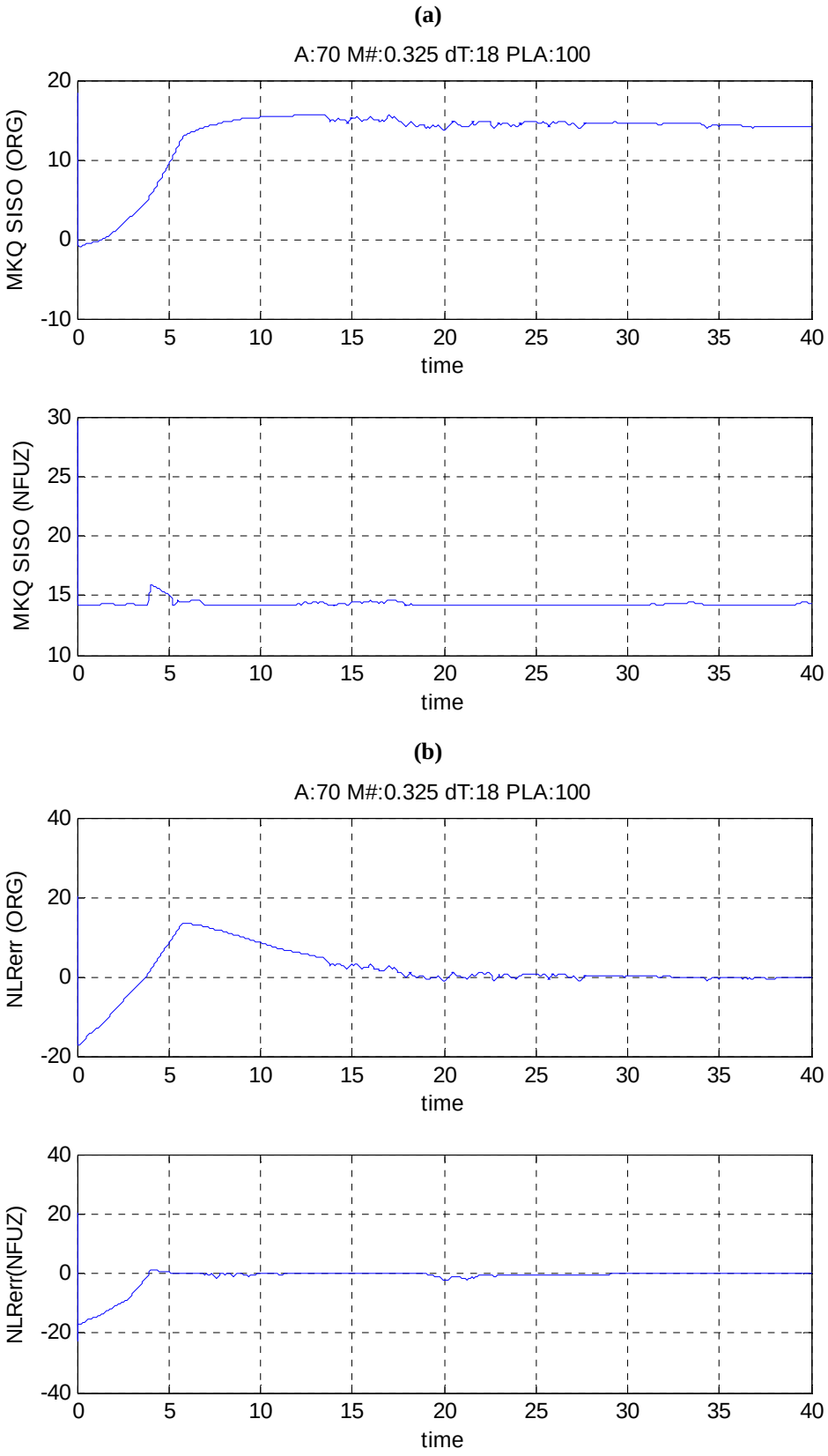

Figure 15. Engine Performance PI vs. Fuzzy Controller at 70,000 ft & WF36 ±10%

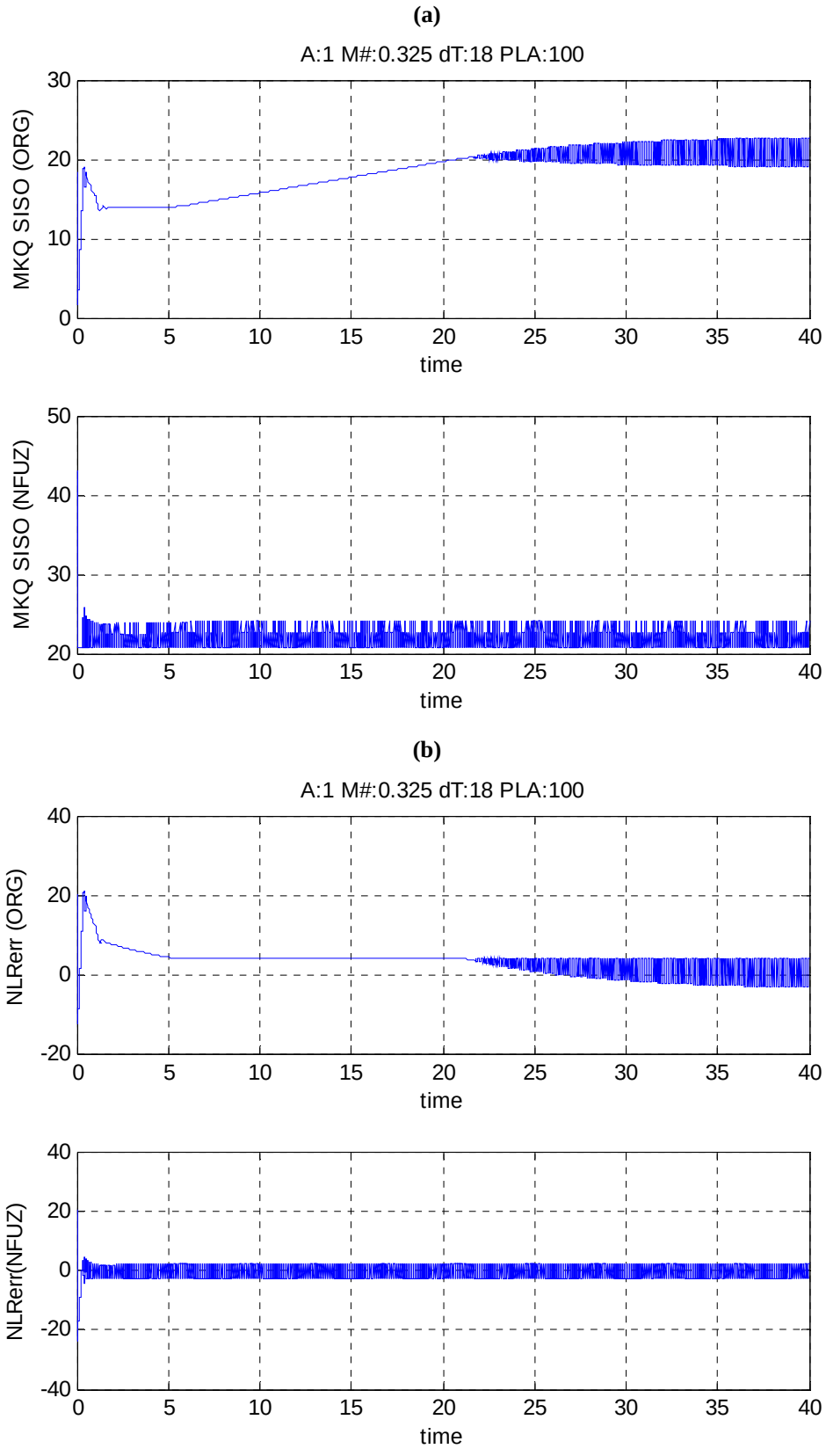

Figure 16. Engine Performance PI vs. Fuzzy Controller at 1,000 ft & WF36 Limit

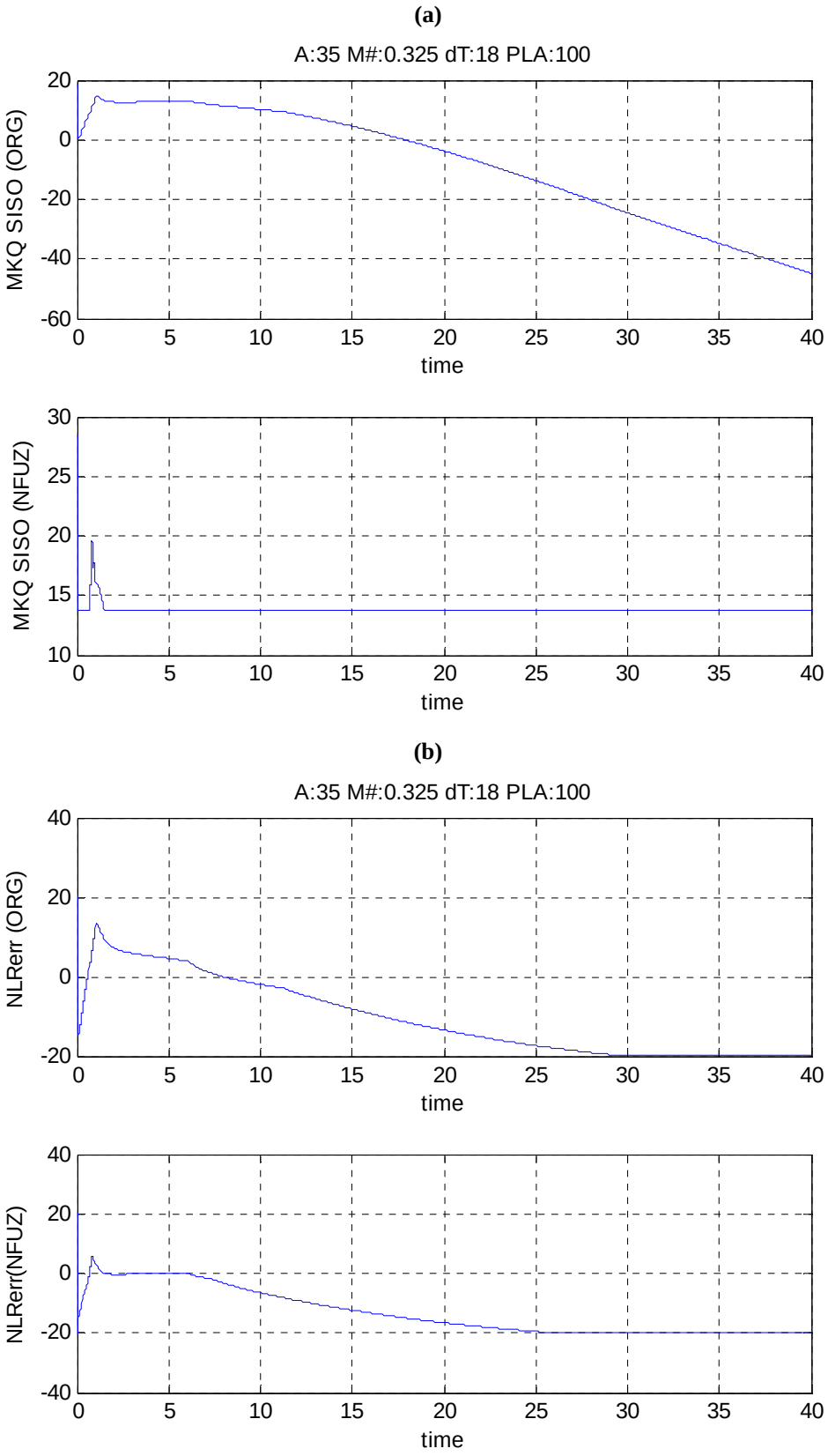

Figure 17. Engine Performance PI vs. Fuzzy Controller at 35,000 ft & WF36 Limit

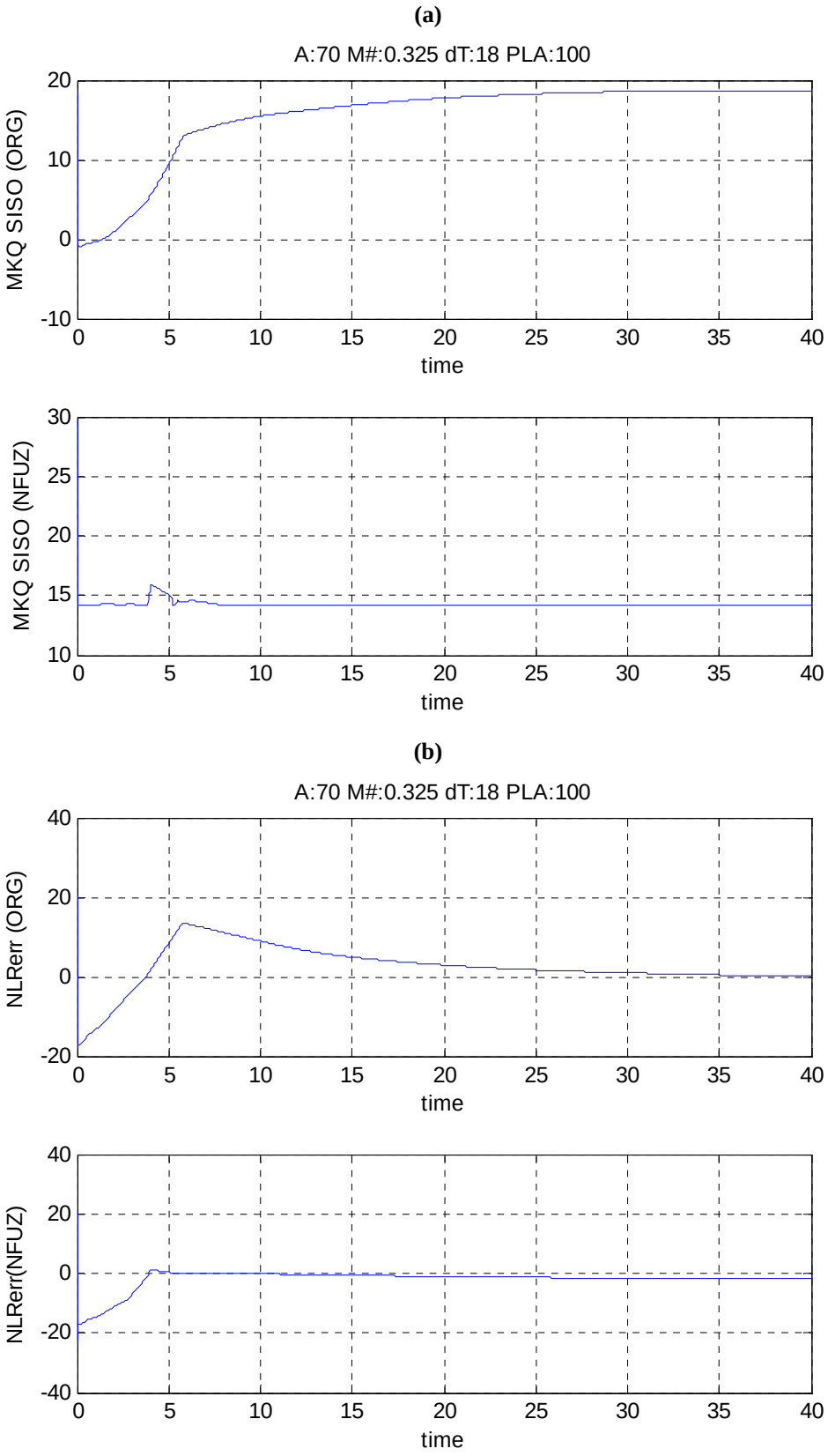

Figure 18. Engine Performance PI vs. Fuzzy Controller at 70,000 ft & WF36 Limit

3.2.4 Controller Performance under Varying PLA

In this section, the case of varying the PLA as a ramp input with a slope of one and comparing the two controllers was investigated. It should be noted that for the simulation to run with PLA values lower that 45 the regulator section of the PI-controller had to be enabled. Thus in one simulation, the scenario consisted of the fuzzy-logic controller for the SISO section and the PI-controller for the regulator section. While in the other simulation, the scenario consisted of PI-controllers for both sections.

The performance parameters for three different altitudes are shown in Figures 19 through 21. It can be seen that after a PLA value of 45 is reached the fuzzy/PI scenario maintains a constant thrust value. As mentioned earlier a fuzzy-logic controller will also be implemented for the regulator section in future work. Based upon these results we believe that a fuzzy-logic control system can be designed for the model that is able to achieve constant thrust based on varied PLA values.

3.2.5 Implementation of other Control Inputs

The Variable Stator Vane (HPC VSV) control, Inlet Guide Vane (Fan IGV) and augmented fuel ratio (AugWFRa) control scheduling is located within the Calculate Demands and Schedules block of the model as shown in Figures 22 and 23. However, these inputs are not used in this engine model. The control of these variables is based on the model inputs specifically the PLA and performance parameters from the Sensor and Conditions block. Control of the HPC VSV will be investigated in the future research since there is a hook to implement the HPC VSV found within the Compressor block of the Engine block model with a similar fuzzy-logic approach.

In conclusion, this effort has shown that a fuzzy-logic controller can be designed to produce similar and in some cases better results compared to the PI-controller provided in the original engine model. These preliminary research results prove that investigation of fuzzy-logic control architecture for the control of turbine engines should further be pursued in accordance with the research as being defined in the previous sections II through V.

(a)

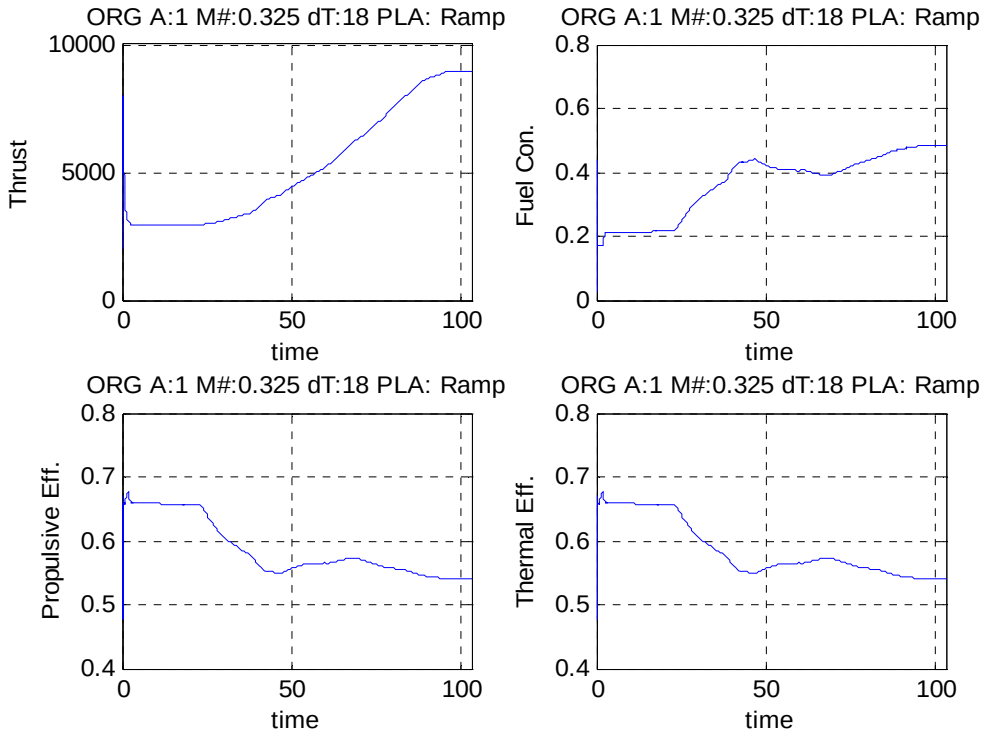

(b)

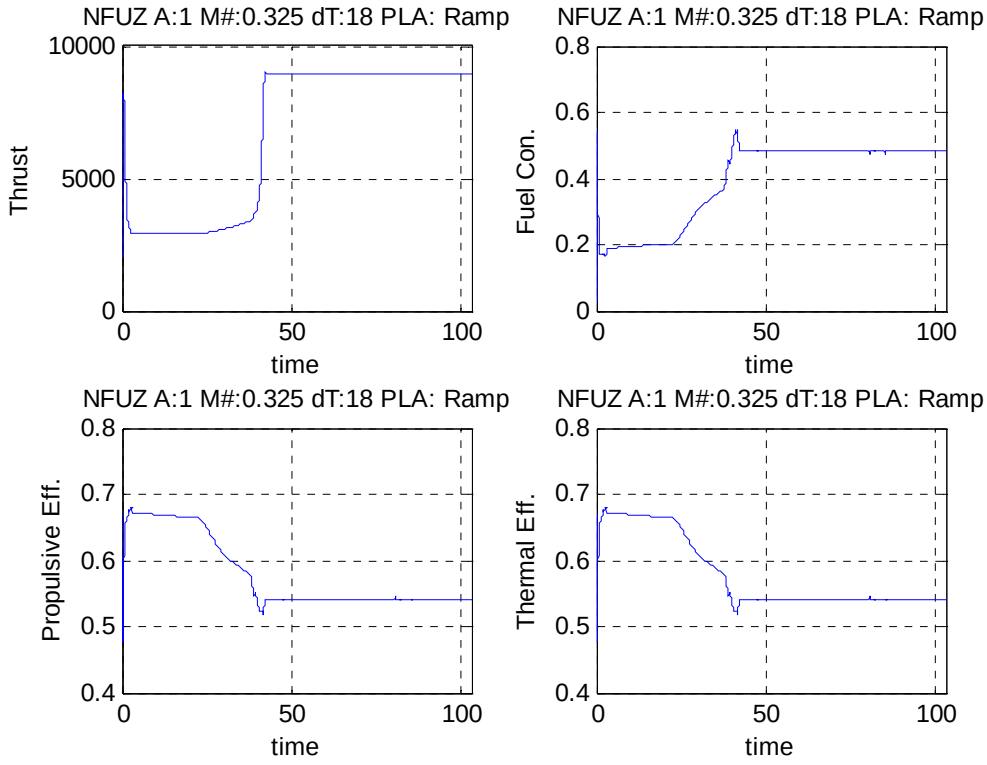

Figure 19. Engine Performance PI (a) vs. Fuzzy (b) Controller at 1,000 ft & PLA=Ramp

(a)

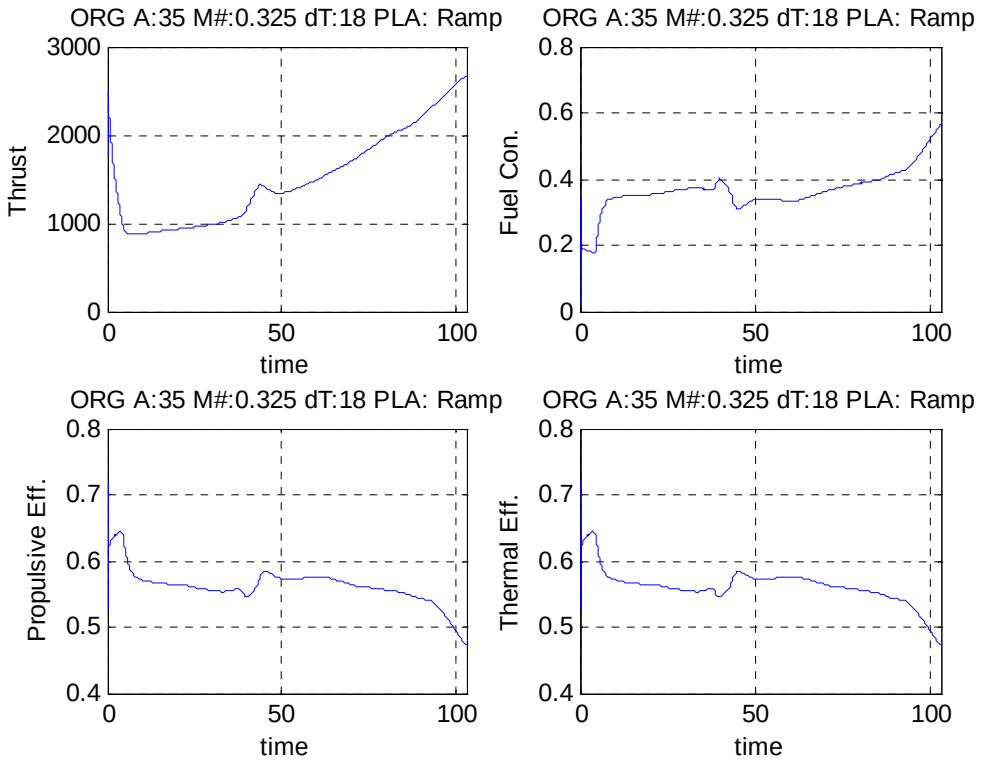

(b)

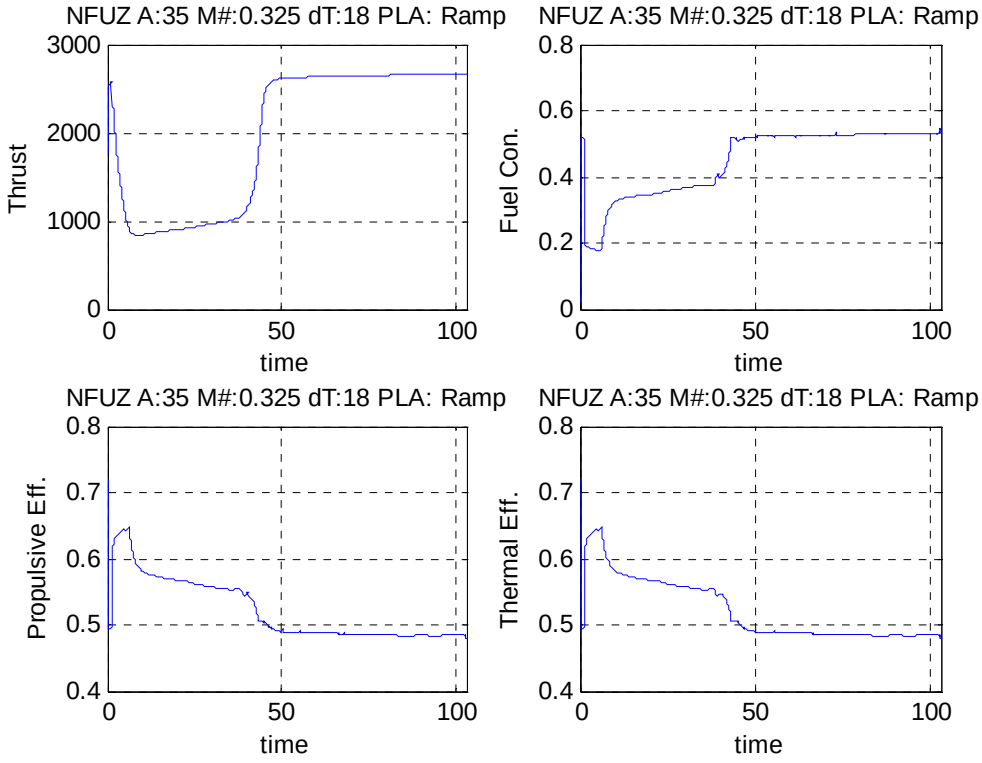

Figure 20. Engine Performance PI (a) vs. Fuzzy (b) Controller at 35,000 ft & PLA=Ramp

(a)

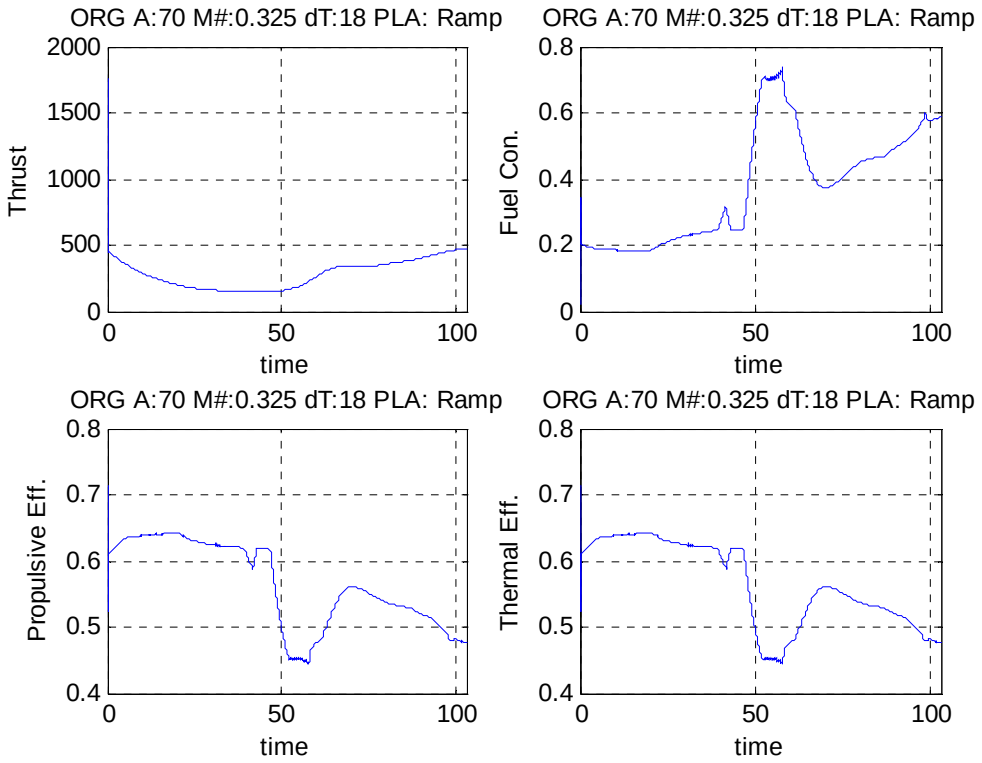

(b)

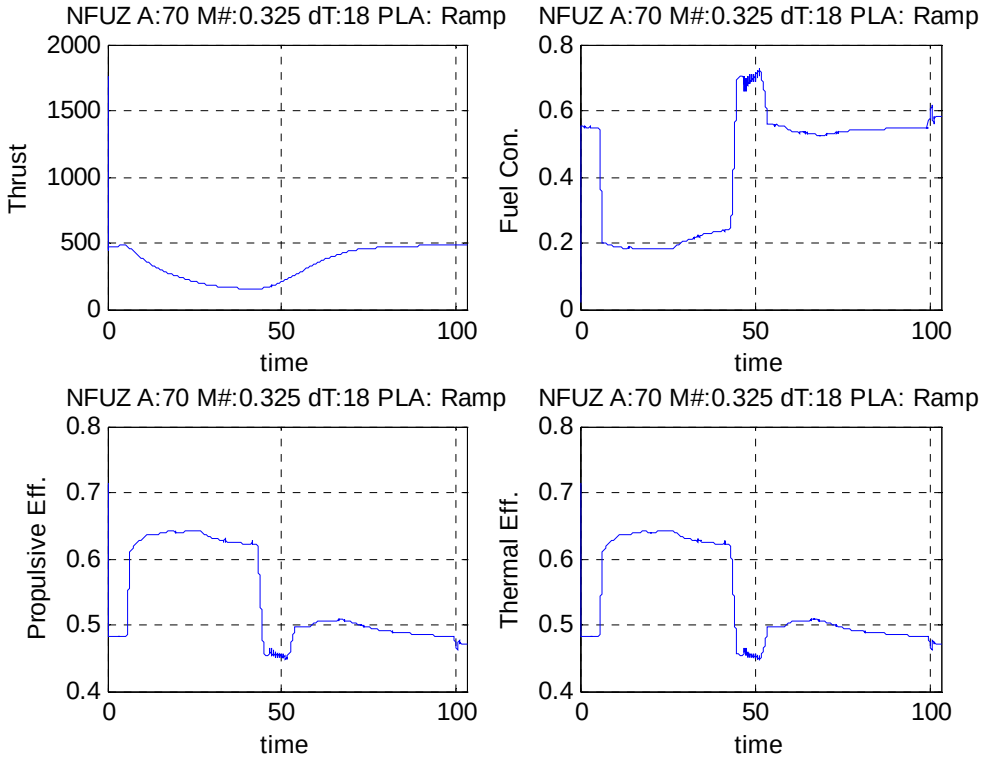

Figure 21. Engine Performance PI (a) vs. Fuzzy (b) Controller at 70,000 ft & PLA=Ramp

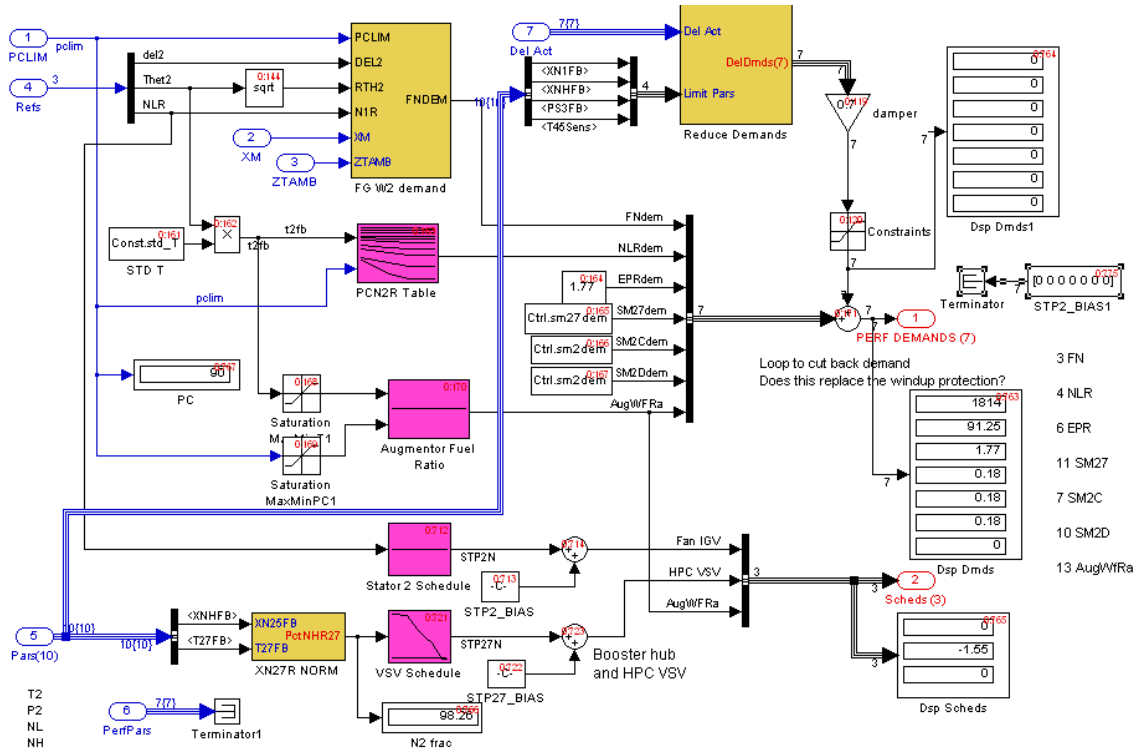

Figure 22. Calculate Demands and Schedules Block

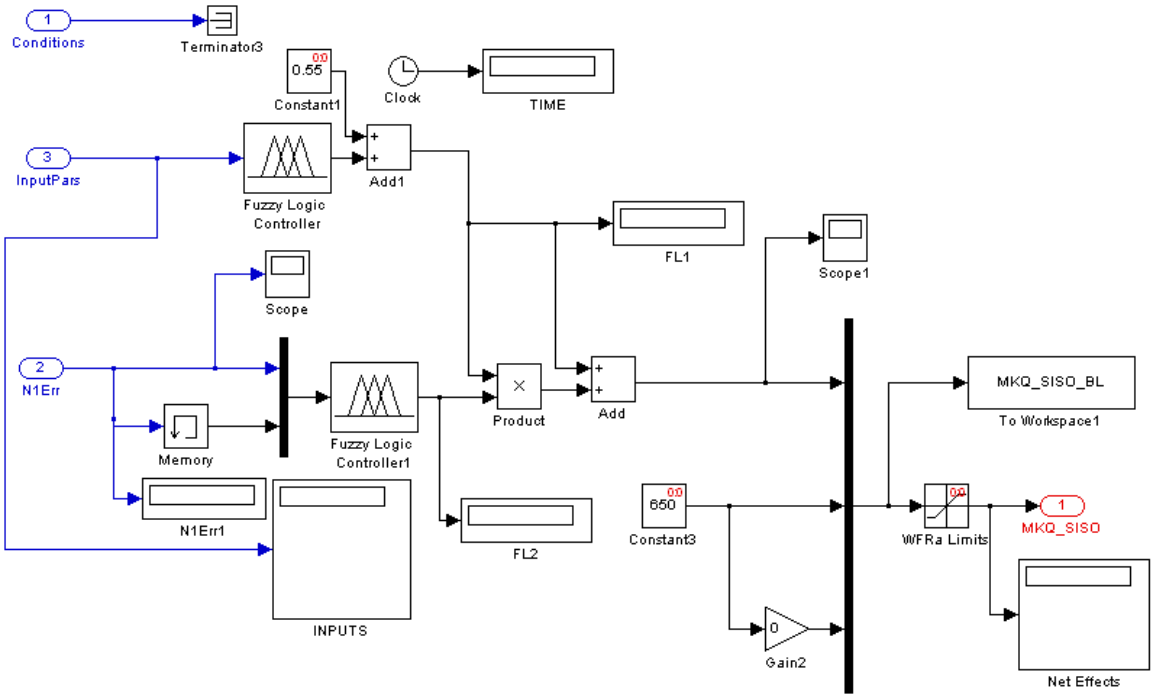

Figure 23. Fuzzy Controller Simulink Model

3.3 Development and Testing of the Diagnostic System

Fault diagnosis and prognosis for gas turbine engines rely heavily on effective data processing since the data can be unpredictable and imprecise. Some of the approaches that have been established in the literature are based on modeling of the engine in question together with rule-based expert system [2]. The challenge in this approach is the knowledge required in order to produce the rules, documentation from an experienced expert and extensive analysis of the process and data monitoring.

Artificial Neural Network (ANN) can be used as an alternative means for capturing the needed knowledge about the engine. ANN is based on binary logic which can store knowledge by learning from recorded data. With ANN information about faults can be learned by training the network on a set of data that represent a normal condition and that of faulty conditions. ANN can also be used as a backup for critical parameters, detection of sensor failures and estimation of parameters [2]. Turbine engines have unique behaviors as a result of age, manufacturing tolerance, and operating conditions. The sensors also are unique in their response and calibration. A diagnostic system with ANN can adapt to individual variables for each turbine engine [3].

In this research, fault diagnosis architecture using ANN was developed and investigated. The neural network-based fault diagnostic system consisted of supervised and unsupervised neural networks. An unsupervised network was trained using Self Organization Map (SOM) network. The supervised neural network used the back propagation learning algorithm therefore named (BPNN). The following sections summarize the development steps.

3.3.1 Data Collection and Pre-processing

Three sets of data were collected from the turbine engine model under three different operating conditions as shown in Table 3. Each data set contained transient and steady state data points. The first set contained data points for normal conditions. The second and third sets contained fault condition data for the fuel flow actuator and the low speed spool sensor respectively. The sensed parameters/signals used are:

- Fan rotor speed (XNLFB)
- Core rotor speed (XNHFB)
- HPC total temperature (T27FB)
- HPC exit pressure (Ps3FB).
- HPC exit temperature(T3FB)
- Turbine inlet temperature(T45)

Table 3

Operating Conditions

Mach #	**Altitude (ft)**	**dTamb**	**PLA**
0.15	1,000	35	100
0.35	35,000	25	100
0.60	70,000	25	100

The total number of data collected after the three runs were 47,000 data points. However, in these data sets it was noted that the sampling rate is different based on the operating conditions. It was later concluded that the change in the sampling rate was caused by the solver used by the Matlab engine model for simulation purposes. On the actual turbine engines different sensors can have different acquisition rate but the sampling rate should never be changed. In such cases the sensed signals have to go through level-

1 fusion for data alignment and synchronization. However, in order to test the developed detection scheme a sampling rate of 100 data points per second (100 Hz) is selected.

The data collected was divided into segments of 100 data points with each segment representing one second. For the pre-processing of the raw data, each sample was normalized before it was used by the neural network. The idea behind normalization was to preserve and analyze the behavior of the sensed signals at the same scale and also for consistent training the neural networks.

3.3.2 Fault Classification using Self Organization Map (SOM) Network

The Self Organization Map (SOM) neural network used for classification/ clustering of different faults is the Manhattan distance neighborhood with 10x10 neurons architecture shown in Figure 24. The normalized samples of the six (6) sensed parameters were used to train the SOM for 1000 presentation cycles. Figure 24 shows the map of the firing neurons for each class of the operating conditions.

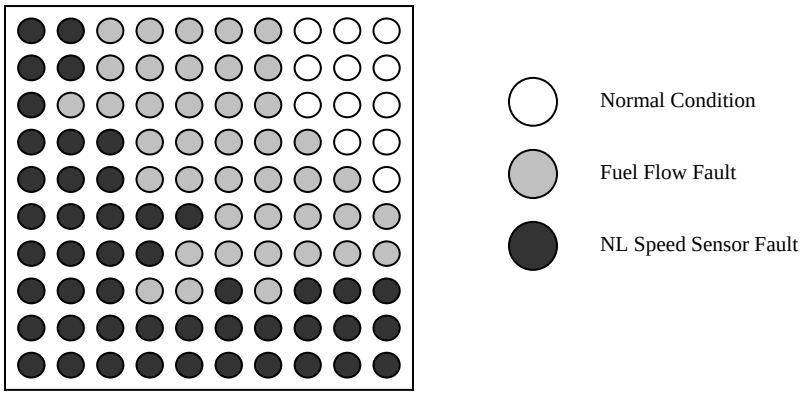

Figure 24. Self Organizing Map Neural Network Classes

3.3.3 Fault Identification by the Supervised Neural Network (BPNN)

The patterns from the SOM representing normal and fault conditions were used to train a multi-layer supervised neural network. The network architecture used is of the feed forward with back propagation training algorithm. The structure of the network is 100-200-3 neurons. The structure represents the number of neurons in the input, hidden and the output layers respectively. Number of patterns used together with the mean square error (MSE) for each training session is shown in the Table 4.

Table 4

Training Information and Accuracy

NN	Number of Pattern	Structure	MSE
BPNN	117	100-200-3	0.01

3.3.4 Decision-Making System

For fault-type final decision making, the Mamdani fuzzy inference system was implemented using set of fuzzy rules. This module so that the desired input/output mapping of detected faults by neural network and true faults is achieved.

Figures 25 and 26 below show the overall diagnostics architecture and the Simulink model for the developed diagnostics system. This diagnostics model will be integrated with the turbine engine model.

3.3.5 Testing Results

The preliminary results from implementing this developed architecture are summarized in Table 5. The test results included the engine operating under two different fault conditions, i.e., faulty fuel flow actuator and corrupted senor data collected from the low pressure speed spool. The obtained results are promising and show more than 90% fault detection rate.

Table 5

Testing Results

Fault Type	**Percentage Correct Identification**
Fuel Actuator	95 %
Low Speed Spool Sensor	92.5 %

In conclusion, this part of the research effort described the initial research work for sensors and components failure detections. The classification and identification was done using two artificial neural networks with the aid of fuzzy inference system for decision making. The six inputs diagnostics system was constructed using normal and faulty samples generated from the turbine engine model. The objective of this preliminary investigation was to investigate the effectiveness of using artificial neural networks in diagnosing the engine under selected faults with a minimum success rate of 90%. The results reported in Table 5 showed that neural network was able to produce such results. However, further examination of the developed architecture with more and other fault scenarios is necessary.

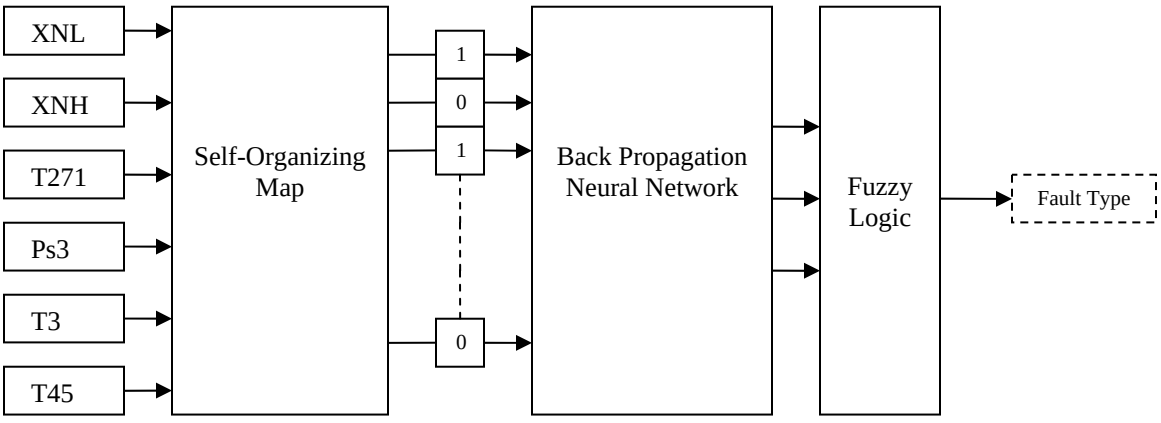

Figure 25. Engine Diagnostics Architecture Using Neural Networks

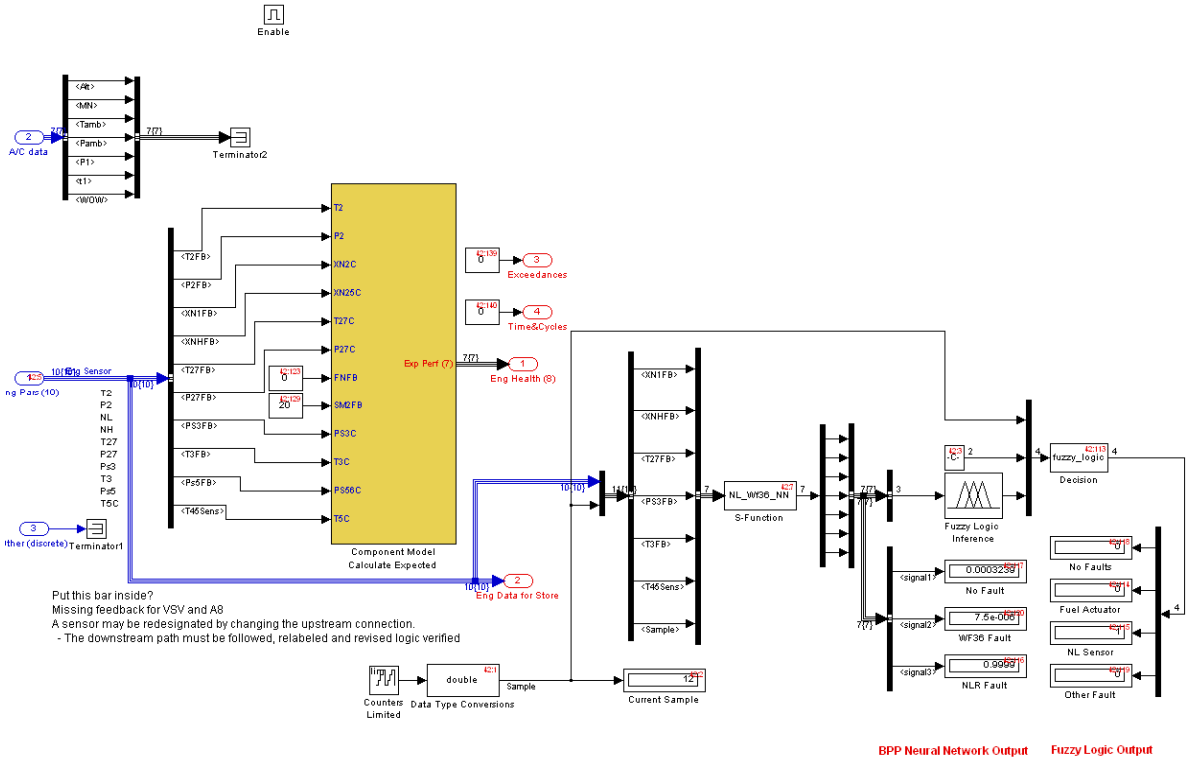

Figure 26. Simulink Model of the Diagnostics System

3.4 Integration of the Diagnostics and Control Algorithms

As it was presented above, the focus of the research has been on the diagnostic and control aspects of the health management of turbine engines. So far, diagnostics and controls algorithms have been developed independently to some extent. In the diagnostics, intelligent approaches such as neural networks and fuzzy-logic inference were used. For the engine control, intelligent controllers were developed and implemented using the fuzzy-logic concepts. These intelligent controllers were used to replace the original classical controllers came with the engine model. The next step in advancing these controllers is to include adaptation features to the controllers. Such features will provide reconfiguration and adaptability function and make it easier to integrate with the diagnostics algorithms. This step of the development will provide complete system for the health management of turbine engines.

So, the focus of the research will be shifted towards designing and implement intelligent control algorithms that can be integrated with the diagnostics aspects of the gas turbine engine. The goal for the integration is for the diagnostics algorithm to detect, identify and isolate faults and failures and for the controls algorithms to deliver the best performance possible in the presence of these faults and failures. In the next phase of the research the focus will be on sudden faults and failures that are exerted on the turbine engines. It is intended to design and implement intelligent strategy that adapts the controllers in the presence of faults or failures. As first step towards this objective, a Graphical User Interface (GUI) has been design to assist in the integration and testing of different diagnostics and control algorithms. The GUI has been developed in the Matlab Graphic User Interface Developing Environment (GUIDE). From the GUI the operator can simulate different types of faults or failures at different operating conditions and also monitor the responses of the engine and the controllers in adapting their variables to accommodate the faults. Figure 27shows a snapshot of the GUI designed for the demonstration purposes.

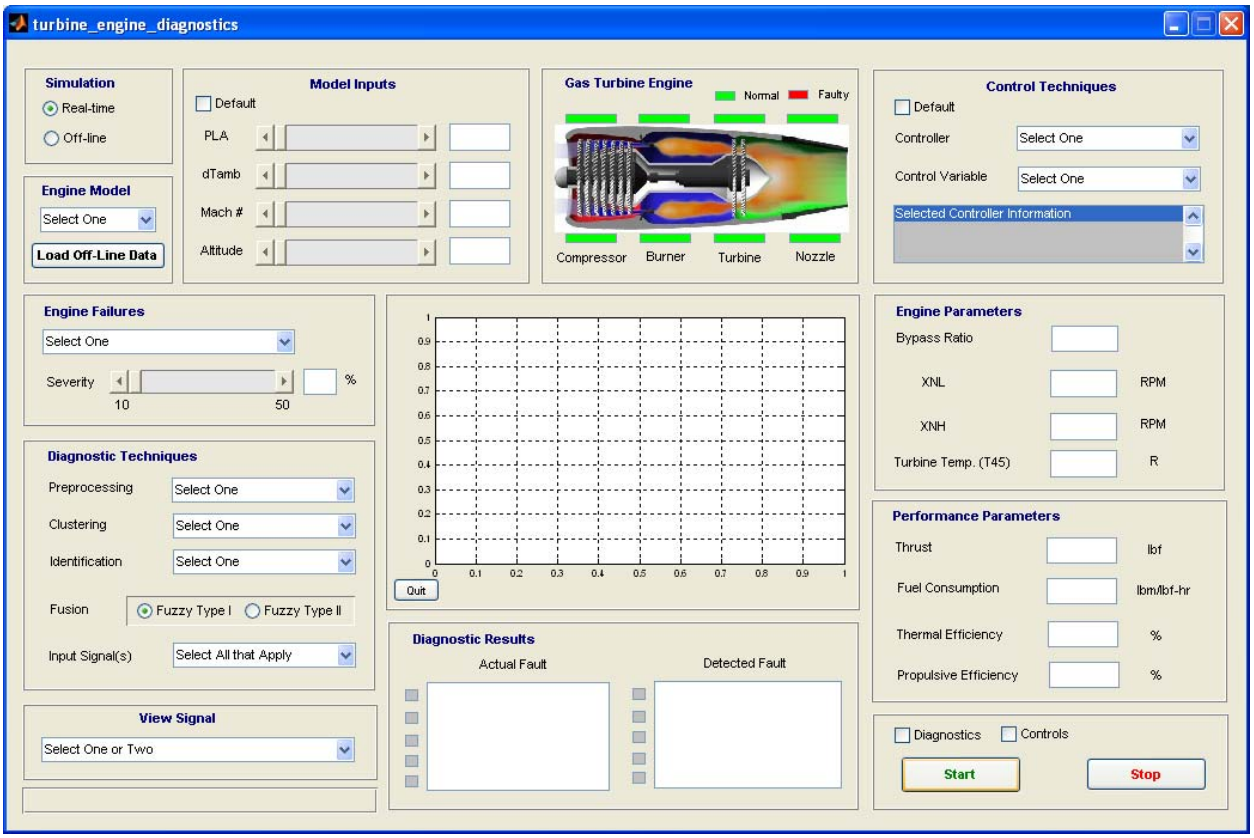

Figure 27. Graphic User Interface for Gas Turbine Engine Diagnostics and Control Integration

Through the GUI the operator has an option to run the simulation test in real-time or off-line mode. In the real-time mode the operator has the option to select the type of the turbine engine model, such as the AFRL model or the CMAPSS model. Where in the off-line mode the recorded data from these models can be uploaded and used for simulation tests. The operating parameters such as the PLA, dTamb, Mach number and Altitude can also be adjusted to simulate real operating conditions.

From the diagnostics side, different types of faults and failures can be simulated together with their severity level. The data processing part of the diagnostics provides options for selecting preprocessing techniques such as FFT, Wavelets, statistical feature or raw data segments. For the clustering of the feature vectors, techniques such as LVQ, RBF and SOM are some of the options included in the GUI. The fault identification portion of the diagnostics has techniques selection option such as BPNN and for the decision fusion techniques option such as fuzzy-logic I or II can be selected. The GUI provides option to view single or multiple signals and also to displays the diagnostic results such as the type of fault and the faulty section and the specific component of the engine model.

In the GUI, engine control techniques can be simulated independent of the diagnostics results or integrated with the diagnostics algorithms. It provides options such the specific controller to be used and the variables and engine operating conditions. Also, the GUI provides display for the tested engine key parameters such as the fuel flow, low and high spool speed, and the exhaust temperature. The performance parameters such as the thrust, fuel consumption, thermal efficiency and propulsive efficiency can also be view and recorded for each run for comparison purposes.

4.0 Objectives for the Next Research Period (Year-2)

The following is a list of the short term objectives which are either in progress or planned to be addressed in the next a few months of the research activities.

1. Apply, test and verify the developed diagnostics and control algorithms on the turbine engine model CMAPSS obtained from NASA.

2. Extend the fault detection and identification algorithms to include multiple faults scenarios on the new engine model. The fault identification fusion and the final decision-making will be the main challenge to be addressed in the next phase of the research.

3. Expand the fuzzy-logic controller design architecture to include both the SISO as well as MIMO portion of the new engine model and replace the current engine controllers.

4. Update the fuzzy-logic controller with different membership functions and additional fuzzy rules and tested on the new engine model.

5. An ongoing objective of the research activities is to engage and train students on research topics related to the turbine engine's diagnostics, health management and controls.

Some of the long term objectives planned to be addressed during the second half of year-2 and future month of the research activities are listed below.

1. Complete integration of the fault diagnostics and intelligent controller into one system suitable for health management of the turbine engine model.

2. Expand the fault detection and identification module to predict the remaining useful life of the faulty components. This step will initiate the prognostics task of the turbine engine health management.

3. Replace the intelligent fuzzy-logic controller with a reconfigurable adaptive controller to accommodate expected faults in the engine.

4. Develop a new approach for design and implementation of distributed control strategy for the turbine engine.

Table 6 shows the time schedule for conducting the above stated short term and long term research activities. It is our expectation that the short and long term research objective will be completed in three years.

5.0 Student Training and Publications

The research work reported during the first year 2008, involved several undergaraduate and graduate students. Two graduate students, Richard Mgaya and Charles McCurry both worked full time on the project during summer 2008. Two undergraduate students, Verles Westbrook and Reginald Cartmell, have joined the research team and they are conducting their capstone design projects in the area of diagnostics and control of turbine engines. They are expected to graduate at the end of the spring semester of 2009. Also, the research PI spent 10% of his time on the project.
Two technical papers were submitted and have been accepted for publication in the IEEE SoutheastCon 2009 to be held in Atlanta GA, from March 5-8, 2009. These two papers were generated and written with contribution of the students involved in the research and are listed in the reference list as [39, 40].

Table 6

Time-Schedule for Year-2 Research Activities

Proposed Research Activities	Research Period December 2008 to November 2009
Short Term Activities	**D08 | J09 F M A M J J A S O N**
Apply, test and verify the developed diagnostics and control algorithms on the turbine engine model CMAPSS obtained from NASA.	● ● ● ●
Extend the fault detection and identification algorithms to include multiple faults scenarios on the new engine model.	● ● ● ●
Expand the fuzzy-logic controller design architecture to include both the SISO as well as MIMO portion of the new engine model and replace the current engine controllers.	● ● ● ●
Update the fuzzy-logic controller with different membership functions and additional fuzzy rules and tested on the new engine model.	● ● ● ● ●
An ongoing objective of the research activities is to engage and train students on research topics related to the turbine engine's diagnostics, health management and controls	● ● ● ● ● ● ● ● ● ● ● ● ● ● ● ● ● ● ●
Long Term Activities	
Complete integration of the fault diagnostics and intelligent controller into one system suitable for health management of the turbine engine model.	● ● ● ●
Expand the fault detection and identification module to predict the remaining useful life of the faulty components.	● ● ● ● ● ● ● ●
Replace the current engine controller with a reconfigurable and adaptive controller	● ● ● ● ●
Develop a new approach for design and implementation of distributed control strategy	● ● ● ●
Quarterly Reporting	● ● ●
Annual Reporting and Review	●

REFERENCES

[1] A. Behbahani, R. Yedavalli, P. Shankar and M. Siddiqi, "Modeling, Diagnostics and Prognostics of a Two-Spool Turbofan Engine," *American Institute of Aeronautics and Astronautics*, 2005.

[2] D. Gayme, S. Menon, C. Ball, D. Mukavetz and E. Nwadiogbu, "Fault detection and diagnosis in turbine engines using fuzzy logic," *Fuzzy Information Processing Society, 2003. NAFIPS 2003. 22nd International Conference of the North American*, pp. 341-346, July 2003.

[3] E. Mo, M. Jie, C. Kim and K. Lee, "Gas Turbine Fault Isolation Based Fuzzy Inference Logic with ECM Trend Plot Report," *Int. Conf. on Control, Automation and System*, pp. 454-458, October, 2007.

[4] D. Gayme, S. Menon, C. Ball, D. Mukavetz and E. Nwadiogbu, "Fault Diagnosis in Gas Turbine Engines using Fuzzy Logic," *IEEE Int. Conf. Systems, Man and Cybernetics*, pp. 3756-2762, 2003.

[5] H. Depold and F. D. Gass, "The Application of Expert Systems and Neural Networks to Gas Turbine Prognostics and Diagnostics," *ASME Journal of Gas Turbine and Power*, October 1999, vol. 121, no. 4, pp. 98-101.

[6] G. Kulikov, T. Breikin, V. Arkov and P. Fleming, "Gas Turbine Fault Detection Using Markov Simulation Technique," *Int. Conf. on Simulation*, pp. 69-72, September 1998.

[7] T. Brotherton, G. Jahns, J. Jacobs, and D. Wroblewski, "Prognosis of Faults in Gas Turbine Engines," *IEEE Aerospace Conference*, pp. 163-171, 2000.

[8] M. Craven and J. Shavlik, "Extracting tree-structured representations of trained networks," *Advances in Neural Information Processing Systems*, vol. 8, MIT Press.

[9] Donald Simon et al., "Development of an Information Fusion System for Engine Diagnostics and Health Management," NASA/TM-2004-212924, Prepared for 39th Combustion/ 27th Air breathing Propulsion/ 21th Propulsion Systems Hazards/3rd Modeling and Simulation Joint Subcommittee Meeting, Dec 1-5, 2003, Colorado Springs, Co.

[10] R. De Hoff and W. Hall Jr., "Design of a Multivariable Controller for an Advanced Turbofan," U. S. A. F., Aero Propulsion Laboratory, Wright-Patterson A. F. Base, Dayton, Ohio, Contract No. F33615-75-C-2053.

[11] H. Thompson and O. Fleming, "Fault-tolerant transputer arrays for gas turbine engine control," *Computing and Control Engr. Journal*, September 1991.

[12] G. Kulikov, V. Arkov, and T. Breikin, "On Markov Model Applications in Aircraft Gas Turbine Engine Full Authority Digital Controller Test-Beds," *UKACC int. Conf. on Control*, vol. 1, pp. 120-124, September 1996.

[13] A. Shutler, "Control configuration design for the aircraft gas turbine engine," *Computing and Control Engineering Journal*, vol. 6, issue 1, pp.22-28, February 1995.

[14] R. Perez and O. Nwokah, "Model Reference Control of a Linear Plant with Feedthrough Element," *IEEE Int. Conf. on Systems Engr.*, pp. 81-84, August 1991.

[15] H. Whitaker, J. Yamron and A. Kezer, "Design of Model Reference Adaptive Control Systems for Aircraft," Rep. R-164, Instrumentation Laboratory, MIT, Cambridge, MA, 1958.

[16] W. Merrill, E. Beattie, R. LaPrad, S. Rock, and M. Akther, "HYTESS – A Hypothetical Turbofan Engine Simplified Simulation," NASA-TM-83561, 1984.

[17] O. Qi, P. Gawthrop and N. Maccallum, "Model-based observer: a gas turbine engine case study," *1st IEEE Conf. on Control Applications*, vol. 2, pp. 877-882, September 1992.

[18] O. Qi, P. Gawthrop and N. Maccallum, "Meeting the Performance Requirements of a Single-Spool Gas Turbine Engine Using a Gain Scheduled Controller," *Proc. IEEE Int. Sym. On Intelligent Control*, pp. 385-391, August 1992.

[19] R. Samar and I. Postlethwaite, "Multivariable Controller Design for a High Performance Aero-engine," *Int. Conf. on Control*, vol. 2, pp. 1312-1317, March 1994.

[20] R. Perez and K. Lou, "Decentralised Multivariable Control and Stability of a gas Turbine Engine," *IEE Proc. on Control Theory and Applications*, vol. 141, issue 6, pp. 357-366, November 1994.

[21] A. Chipperfield and P. Fleming, "More Integrated Gas Turbine Engine Controller Design," *Int. Conf. on Genetic Algorithms in Engr. Systems: Innovations and Application,* pp. 357-363, September 1997.

[22] K. Garwood and D. Baldwin, "The Emerging Requirements for Dual and Variable Cycle Engines," *10th Int. Sym. On Air Breathing Engines*, RAE-TMP-1220, 1992.

[23] A. Chipperfield and P. Fleming, "Gas Turbine Engine Controller Design Using Multiobjective Genetic Algorithm," *Int. Conf. on Genetic Algorithms in Engr. Systems: Innovations and Application,* pp. 214-219, September 1995.

[24] R. Subbu, K. Goebel, and D. Frederick, "Evolutionary Design and Optimization of Aircraft Engine Controllers," *IEEE Trans. Systems, Man, and Cybernetics*, vol. 35, issue 4, pp.554-565, November 2005.

[25] H. van Essen and H. de Lange, "Nonlinear Model Predictive Control Experiments on a Laboratory Gas Turbine Installation," *ASME Jour. of Engr. For Gas Turbines and Power*, 2001.

[26] B. Brunell, R. Bitmead and A. Connolly, "Nonlinear model predictive control of an Aircraft Gas Turbine Engine," *IEEE Proc of Conf. on Decision and Control,* vol. 4, pp. 4649-4651, December 2002.

[27] V. Diwanji, A. Godbole and N. Waghode, "Nonlinear Model Predictive Control for Thrust Tracking of a Gas Turbine," *IEEE Int. Conf. on Industrial Technology,* pp. 3044-3048, December 2006.

[28] J. Mu and D. Rees, "Approximate Model Predictive Control for Gas Turbine Engines," *American Control Conf.,* vol. 6, pp. 5704-5709, June 2004.

[29] N. Chiras, C. Evans, and D. Rees, "Global Nonlinear Modeling of Gas Turbine Dynamics using NARMAX structures," *ASME Jour. Of Engr. And Power*, vol. 124, no. 4, pp. 817-826, 2002.

[30] N. Chiras, C. Evans, and D. Rees, "Nonlinear Gas Turbine Modeling Using Feedforward Neural Networks,' *ASME Turbo Expo congress,* Amsterdam, Netherlands, GT-2002-30035, 2002.

[31] Y. Diao and K. Passino, "Fault-Tolerant Apaptive Fuzzy/Neural Control for a Turbine Engine," *IEEE Trans. on Control Systems Technology*, vol 9, no. 3, pp. 494-509, May 2001.

[32] A. Kreiner and K. Lietza, "The Use of Onboard Real-time models for Jet Engine Control," MTU Aero Engines, Germany.

[33] Z. Feng, J. Sun, and Q. Li, "ZP/LTR Control for Turbofan Engines," *ASME Turbo Expo 2000,* 2000-GT-0043, Munich, 2000.

[34] I. Postlethwaite, R. Samar, B. CHoi, and D. Gu, "A Digital H Infinity Multi-Mode Controller for the Spey Turbofan Engine," *European Control Conf.,* Rome, 1995.

[35] M. Harefos, "Application of H Infinity Robust Control to the RM12 Jet Engine,"Control Engineering Practice, vol. 5, no. 9, Pregamon Press, 1997.

[36] S. Adibhatla, G. Collier, and X. Zhao, "H Infinity Contol Design for a Jet Engine,' *34th Joint Propulsion Conf.*, Cleveland, USA, 1998.

[37] A. Garassino and P. Bois, "An Advanced Control System for Turbofan Engine: Multivariable Control and Fuzzy Logic (Application to the M88-2 Engine)," *AGARD PEP Symposium, "Advanced Aero-Engine Concepts and Controls"*, Seattle, USA, 1995.

[38] L. Dambrosio, S. Camporeale, and B. Fortunato, "Performance of Gas Turbine Power Plants Controlled by One Step Ahead Adaptive Technique," *ASME Turbo Expo 2000,* 2000-GT-0037, Munchen, 2000.

[39] Saleh Zein-Sabatto,

[40] Saleh Zein-Sabatto,

Optimization of Supersonic Inlet Based on Multi-Objective Optimization Approach Using Genetic Algorithm

(Subcontract Agreement No. 08-S530-0047-03-C3)

Final Report
December 31, 2008

By

Ziaul Huque

Department of Mechanical Engineering
Prairie View A&M University
Prairie View, Texas 77446
(936)-261-9957
zihuque@pvamu.edu

ABSTRACT

A computational fluid dynamics (CFD) and response surface based multi-objective design optimization was performed for a two dimensional mixed compression supersonic inlet and the Pareto optimal front is presented. A study of the performance trends of the inlet is also presented. Mass flow rate through the inlet and entropy gain were used as the objective functions. Three variables were used for CFD simulations. These variables are the angle of attack, the axial length from the ramp tip to the cowl tip, and the inlet Mach number. The inlet dynamic pressure was kept constant at 1500 psf. The CFD simulations of the inlet were carried out with CHEM, a general purpose, multidimensional, multi-species, viscous chemistry solver built upon a rule-based specification system. The standard least square method is used to generate response surface by the statistical code JMP. Elitist Non-Dominated Sorting Genetic Algorithm (NSGA-II) was used to determine the Pareto optimal solution. Each Pareto optimal solution represents a different compromise between design objectives. This gives the designer a choice to select a design compromise that best suits the requirements from a set of optimal solutions. The Pareto solution set is presented in the form of a Pareto optimal front.

Optimization of Supersonic Inlet Based on Multi-Objective Optimization Approach Using Genetic Algorithm

1. Introduction

A major challenge to successful full-scale development of an improved space propulsion system is to address the competing needs of various design parameters. It is important to establish a framework enabling the designer to assess these competing needs, to rank priorities, and to reach a good compromise. Design of supersonic inlets and other propulsion components is often complex, expensive, and may involve harsh environments. Coupling of computational Fluid Dynamics (CFD) and surrogate modeling to optimize performance of propulsion components is becoming popular due to reduction in computational expense. For the past several decades, much energy is focused on improving the design and efficiency of the different air-breathing propulsion engines in order to expand their Mach number range of operability. The inlet is the first component of an air-breathing propulsion system. The function of the inlet is to provide appropriate mass flow and velocity to the engine with high total pressure recovery, flow uniformity and flow stability, all of which are important to the overall engine efficiency. The leading edge shock system, the terminal shock boundary layer interaction, the decelerating subsonic flow and the associated rapidly growing boundary layers combine to form typical inlet flows [1]. Stability of flow is one of the major considerations in designing supersonic inlets. An inlet configuration generates a very complicated flow field, in which flow separation, inlet unstart, discontinuities, and shock/boundary layer interactions are among the flow characteristics. Thus an optimum inlet design is an important aspect of a ramjet/scramjet engine.

2. Objectives

The major objective of the current work is to demonstrate an optimization of a supersonic inlet through a range of Mach numbers ranging from 4 to 10. A multi-objective optimization approach was taken to determine the Pareto Optimal Front. A response surface based methodology was implemented. CFD simulations of various inlet designs were performed based on a matrix of design variables/parameters to develop the response surface. This optimization effort can be extended in follow up activities to include more design variables and objective functions including nozzle and combustor. The results of individual components can be later integrated to generate a system level global Pareto optimum surface.

3. CFD Simulations

3.1 Mixed Compression Inlet Geometry

The mixed compression inlet configuration chosen for the current study was based on the numerical simulation of a two dimensional mixed compression supersonic inlet carried out by M. K. Jain and S. Mittal [2]. This geometry presented the most comprehensive set of data readily available in the open literature.

The details of the inlet, along with the dimensions, are shown in Figure 1. The geometric throat is located at 58.8 in. from the leading edge of the intake. The first compression ramp is at an angle of 7^0 to the flow and is 28 in. long. It is followed by the second ramp which is at an angle of 14^0 to the free-stream flow. The geometry of the ramp surface between the end of

second linear segment of the ramp and throat, i.e. points *d* and *e* (refer to Figure 1), were graphically extracted. The geometry shown in Figure 1, R52.1, extends to 52.1 in. from the leading edge of the intake to the throat.

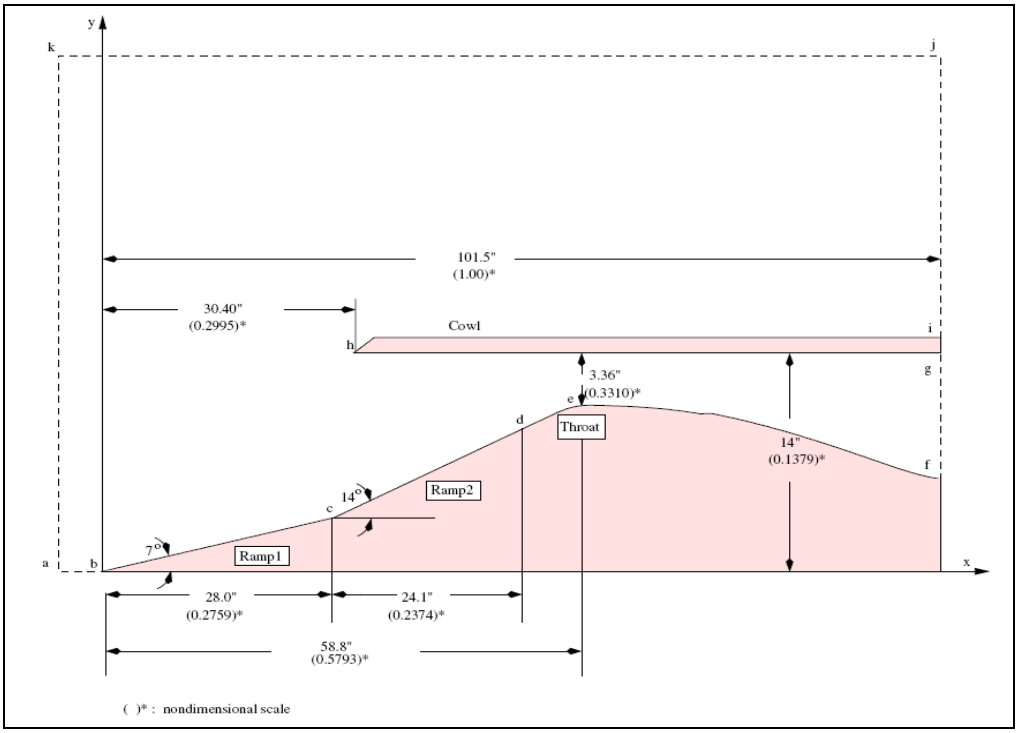

Figure 1: Geometry of the supersonic mixed-compression inlet [2].

3.2 Solution Algorithm

The CFD simulations of mixed compression supersonic inlet internal flow path were performed with the CFD code CHEM, developed by Mississippi State University. CHEM is the first application developed using the Loci framework [3]. CHEM is a full featured Navier-Stokes solver for non-equilibrium flows involving chemical reactions. The solver uses advanced generalized grid algorithms based on finite-volume methods and high resolution Riemann solvers. In the code, a finite-volume procedure is applied to discretize the flow equations. The governing equations are written in vector form for an arbitrary control volume for a three-dimensional flow with non-equilibrium chemistry and equilibrium internal energy.

Input file in CHEM is called **.vars* file which describes the boundary conditions and direct the numerical solver. All input into the solver is assumed to be in the international MKS system. A grid file which is in the portable XDR binary representation, will have a **.xdr* extension. A variety of converter programs are provided to convert to the *xdr* grid format used by CHEM. Boundary conditions are tagged in the *xdr* grid file with a boundary condition specification. In the current work, there is no chemical reaction so ideal gas air model (air_1s0r) is used. For solving linear equations, Gauss Seidel iterations are used. To limit *Muscl* extrapolation scheme *Venkatakrishnan* limiter was used.

3.3 Grid Description

The grids for the CFD simulations were generated using the commercial code GRIDGEN. To obtain a grid independent solution several grid density parametrics were performed with the base line configuration. The computational domain consists of a 2-D representation of the experimental hardware internal flow path and direct surrounding. The grid is created using unstructured Delaunay triangulation mesh. The grid used for the computations is shown in Figure 2.

The number of nodes remained constant throughout the research. . Nodes are clustered in the critical flow path regions. Because of the symmetrical structure of the mixed compression inlet along the center line, only one-half of the symmetrical cross sectional area is taken for CFD modeling.

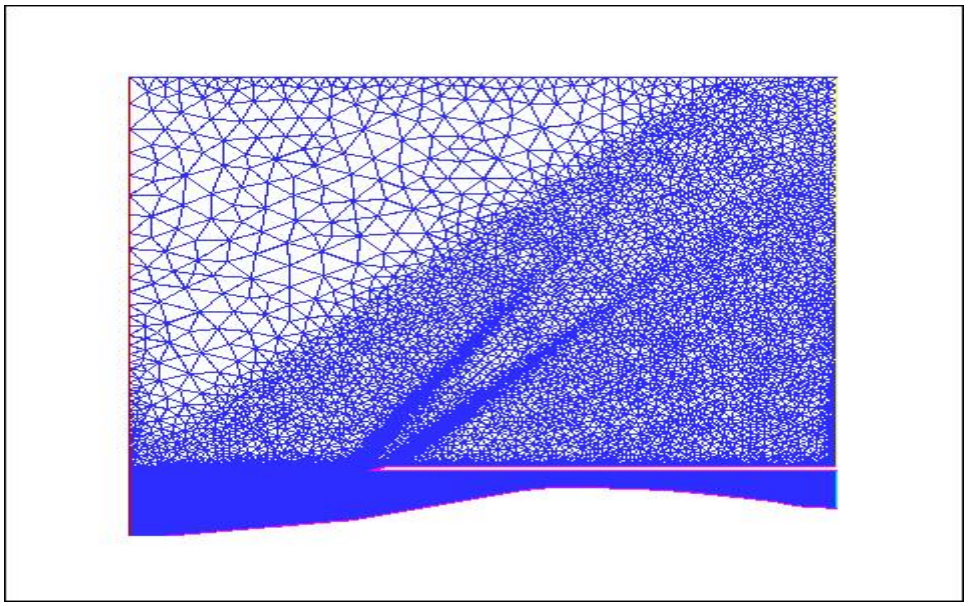

Figure 2: View of the finite element mesh with triangular elements

3.4 Boundary Conditions

Boundary Conditions Used for Validation

The boundary conditions used in this work for benchmarking were extracted from the work of M. K. Jain and S. Mittal [2] case R52.1. The computational line is shown via broken lines in Figure 1. The axial length of the inlet ramps is 52.1 in. thus the name R52.1.
The following boundary conditions and variables were used:

- Inlet flow as Supersonic Inflow:
  - Mach number = 3
  - Temperature = 229 K
  - Static Pressure = 0.2975 atm
- Cowl and inlet surfaces as no-slip adiabatic Viscous Wall

- Upper boundary ***j-k*** as Farfield
  - Mach number = 3
  - Temperature = 229 K
  - Static Pressure = 0.2975 atm
- Outflow boundary ***i-j*** as Supersonic Outflow
- Outflow boundary ***g-f*** as extrapolate (same as supersonic outflow)

Boundary Conditions Used for Generating Response Surface

The flow boundary conditions used in the current work are similar to those used for the validation case, only the variables differ.

- Inlet flow as Supersonic Inflow:
  - Mach number variable (M = 4, 6, 8, 10)
  - Temperature = 229 K
  - Dynamic Pressure = 1500 psf
  - Static Pressure = 6412.6 Pa, 2850 Pa, 1603 Pa, and 1026 Pa corresponding to M = 4, 6, 8, 10 respectively
- Cowl and inlet surfaces as reflecting (recommended for inviscid flow)
- Upper boundary ***j-k*** as Farfield
  - Mach number variable (M = 4, 6, 8, 10)
  - Temperature = 229 K
  - Dynamic Pressure = 1500 psf
  - Static Pressure = 6412.6 Pa, 2850 Pa, 1603 Pa, and 1026 Pa corresponding to M = 4, 6, 8, 10 respectively
- Outflow boundary ***i-j*** as Supersonic Outflow
- Outflow boundary ***g-f*** as Supersonic Outflow:

3.5 Design Variables and Objective Functions

In order to perform optimization three design variables and two objective functions are used. The design variables used are the axial length of the ramp tip to the cowl tip (L), inlet Mach number (M) and angle of attack (α). Three lengths are used: L = 0.9246 m, 0.7722 m, and 0.5944 m. Four Mach number values are used. They are M = 4, 6, 8, and 10. Five angles of attacks are used. They are α = 0, 2, 4, 6, and 8. The two objective functions used are mass flow rate and entropy gain. With the above mentioned design variables a total of 60 CFD cases were simulated.

3.6 CFD Results

Validation Simulation

Before starting CFD simulations to generate the response surfaces an initial simulation was performed to validate the results with those of Jain et. al. [2]. The boundary conditions and the grids used are described in the previous section and used Euler flow to be consistent. Figures 3 and 4 show the color contour plots of pressure and Mach number respectively. Figure 5 shows the plot of Mach number distribution along the ramp of the inlet. The figures show excellent agreement with Jain et. al. [2]. The Mach numbers along the ramp are almost identical with a slight over prediction near the exit.

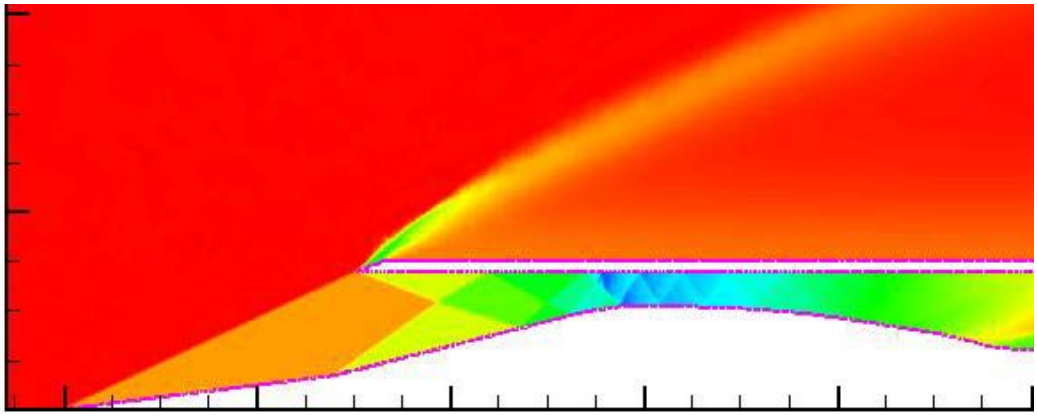

Figure 3. Contour plot for pressure for validation case

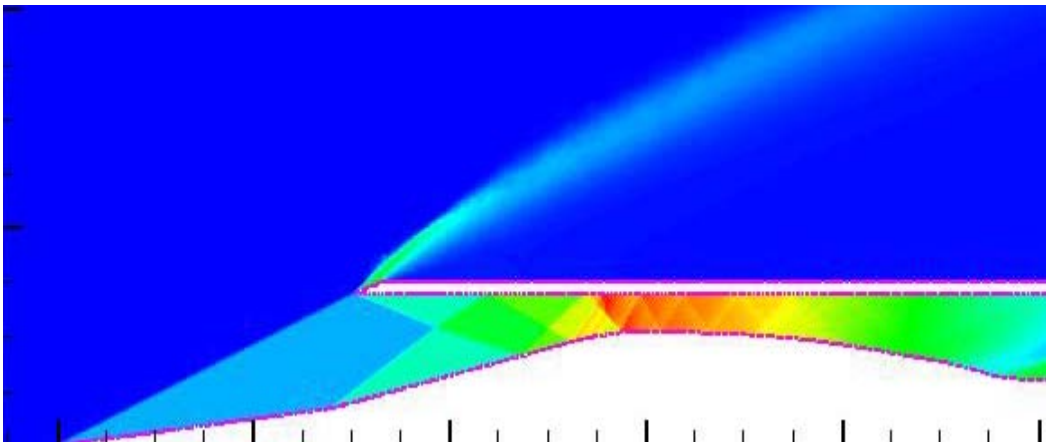

Figure 4. Contour plot for Mach number for validation case.

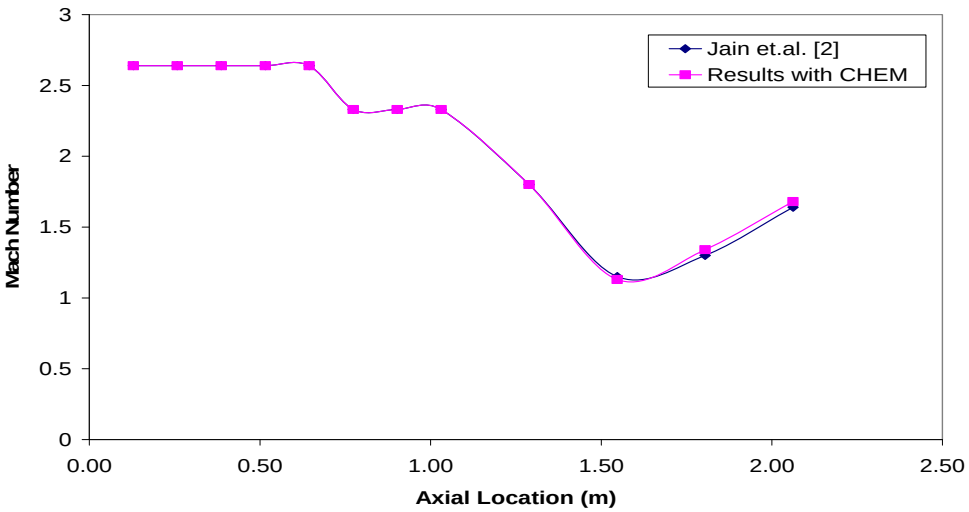

Figure 5. Comparison of Mach Number Along the Ramp of the Inlet.

CFD simulations for Response Surface

In order to perform optimization a total of 60 simulations were performed with various combinations of the design variables. As mentioned in previous section, three design variables were used. They are the axial length of the ramp tip to the cowl tip, inlet Mach number and angle of attack. Three lengths were used. They are 0.5944 m, 0.7722 m, and 0.9246 m. These lengths are the axial distance from the inlet tip to the cowl tip. Four Mach number values were used. They are M = 4, 6, 8, and 10. Five angles of attacks were used. They are α = 0, 2, 4, 6, and 8. For each case two objective functions, mass flow rate and entropy gain, were calculated.

Table 1 shows the spread sheet with the results of the 60 simulated cases. The entropy values at the inlet and exit were calculated by obtaining the integrated value of the inlet and exit temperatures and pressures. Instead of the vertical plane at the cowl tip as the inlet plane an oblique plane from the cowl tip to the inlet tip was used as the inlet plane.

For zero angle of attack and the ramp length of 0.7722 m, the angles of the external shock were calculated for each of the inlet Mach numbers and are shown in Figure 6. For an inlet Mach No. of 4, the first external oblique shock occurs at an angle of 14^o from the inlet ramp. It reflects on the upper inside wall of the inlet, just past the cowl. As the inlet Mach No. increases to 10, the oblique shock angle decreases to 4^o from the inlet ramp and merges with the second shock. Figure 7 shows the static pressure variation along the ramp surface as a function of inlet Mach No. for the cases of zero angle of attack and the ramp length of 0.7722 m. The sharp edges represent the locations where oblique shocks intercept the ramp surface. With increasing inlet Mach No. the external oblique shock angle decreases, which pushes the axial location of the shock intercept location to the right. One interesting observation is that for inlet Mach Numbers of 6 and above, the pressure variation from the throat to the exit becomes identical.

Table 1. CFD Simulation Results

Case #	Length (m)	Angle of Attack	Mach #	Mass Flow Rate (kg/s)	Entropy Gain kJ/(kg.K)	
1	0.9246	0	4	2.1356	0.02188	
2	0.9246	0	6	1.4169	0.16642	
3	0.9246	0	8	1.0627	0.32129	
4	0.9246	0	10	0.85186	0.52395	
13	0.9246	2	4	2.3335	0.02942	
14	0.9246	2	6	1.5541	0.20883	
15	0.9246	2	8	1.1636	0.41750	
16	0.9246	2	10	0.93206	0.57965	
25	0.9246	4	4	2.52885	0.03352	
26	0.9246	4	6	1.6858	0.24132	
27	0.9246	4	8	1.2627	0.48083	
28	0.9246	4	10	1.008	0.68480	
37	0.9246	6	4	2.7202	0.03963	
38	0.9246	6	6	1.8123	0.25722	
39	0.9246	6	8	1.3647	0.54511	
40	0.9246	6	10	1.0887	0.78634	
49	0.9246	8	4	2.9105	0.05663	
50	0.9246	8	6	1.9442	0.29894	
51	0.9246	8	8	1.455	0.60335	
52	0.9246	8	10	1.1593	0.91217	
5	0.7722	0	4	2.14	0.02911	
6	0.7722	0	6	1.43	0.18466	
7	0.7722	0	8	1.06	0.35538	
8	0.7722	0	10	0.85	0.53874	
17	0.7722	2	4	2.4583	0.05063	
18	0.7722	2	6	1.5332	0.24134	
19	0.7722	2	8	1.1452	0.43988	
20	0.7722	2	10	0.91847	0.63149	
29	0.7722	4	4	2.2984	0.06232	
30	0.7722	4	6	1.6403	0.24071	
31	0.7722	4	8	1.2299	0.49898	
32	0.7722	4	10	0.9788	0.77909	
41	0.7722	6	4	2.6116	0.07034	
42	0.7722	6	6	1.7415	0.31199	
43	0.7722	6	8	1.3042	0.60245	
44	0.7722	6	10	1.0418	0.82215	
53	0.7722	8	4	2.7632	0.08372	
54	0.7722	8	6	1.8382	0.35950	
55	0.7722	8	8	1.3809	0.65415	
56	0.7722	8	10	1.1031	0.90044	
9	0.5944	0	4	2.14	0.03702	
10	0.5944	0	6	1.42	0.18756	
11	0.5944	0	8	1.07	0.33785	
12	0.5944	0	10	0.85	0.52022	
21	0.5944	2	4	2.26	0.05988	
22	0.5944	2	6	1.5	0.23129	
23	0.5944	2	8	1.12	0.42571	
24	0.5944	2	10	0.9	0.61385	
33	0.5944	4	4	2.38	0.09120	
34	0.5944	4	6	1.59	0.25536	
35	0.5944	4	8	1.19	0.51062	
36	0.5944	4	10	0.95	0.72262	
45	0.5944	6	4	2.49	0.12124	
46	0.5944	6	6	1.67	0.34447	
47	0.5944	6	8	1.25	0.60404	
48	0.5944	6	10	0.99	0.85491	
57	0.5944	8	4	2.61	0.1553	
58	0.5944	8	6	1.74	0.4038	
59	0.5944	8	8	1.31	0.6900	
60	0.5944	8	10	1.05	0.9753	

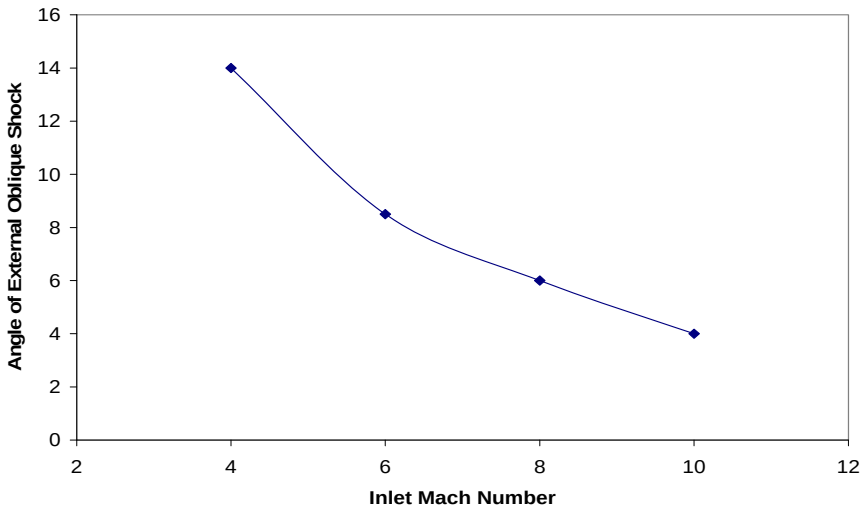

Figure 6. Angle of External Oblique Shock With the Ramp as a Function of Inlet Mach Number.

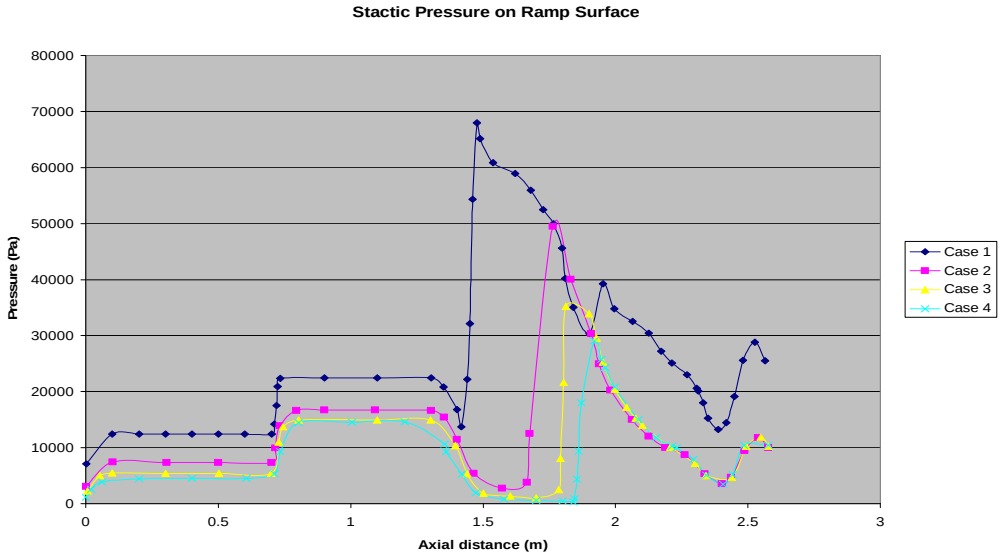

Figure 7. Pressure Trend Along the Inlet Ramp Surface

Figures 8, 10, and 12 show the mass flow rates vs. Mach number and Figures 9, 11, and 13 shows the plot of entropy gain vs. Mach number at various angles of attack for the three length values. The effect of changes in length on both mass flow rates and entropy gain were not very significant. For each of the lengths the mass flow rate continuously decreases as the inlet Mach No. increases. This is because of keeping the inlet dynamic pressure constant which reduces the inlet static pressure. On the other hand as expected the mass flow rate increases with increasing angle of attack. The variation of the mass flow rate with angle of attack also decreases as the Mach number increases. The entropy gain for all angle of attack increases with Mach number and at all Mach Numbers increases with angle of attack. But at higher Mach numbers the variation of entropy gain with angle of attacks become quite large.

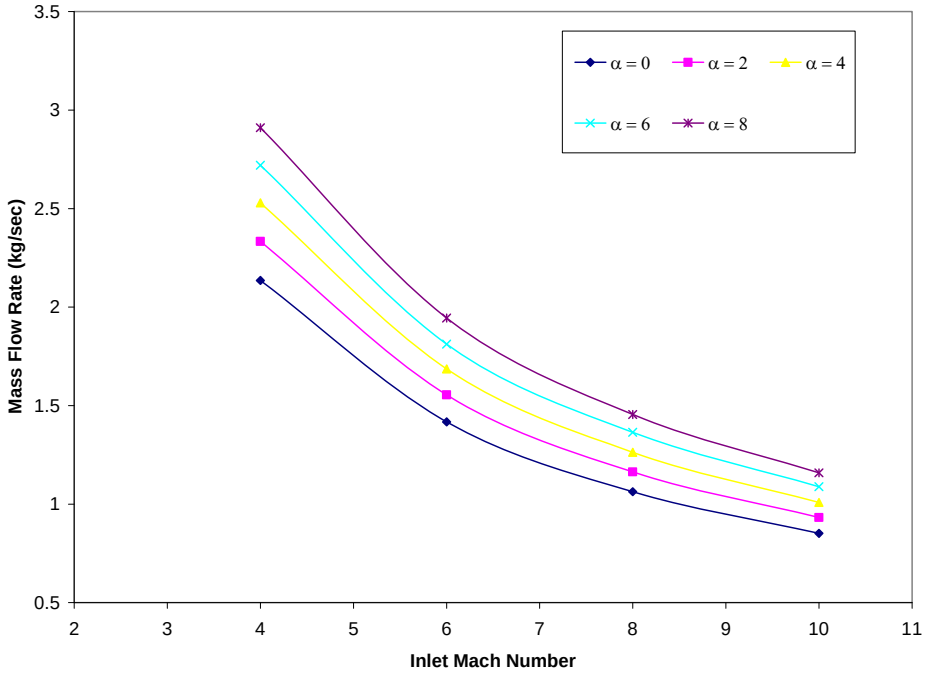

Figure 8. Variation of Mass Flow Rate with Initial Mach Number
for various Angle of Attack (Length Between Ramp and Cowl Tips = 0.9246 m)

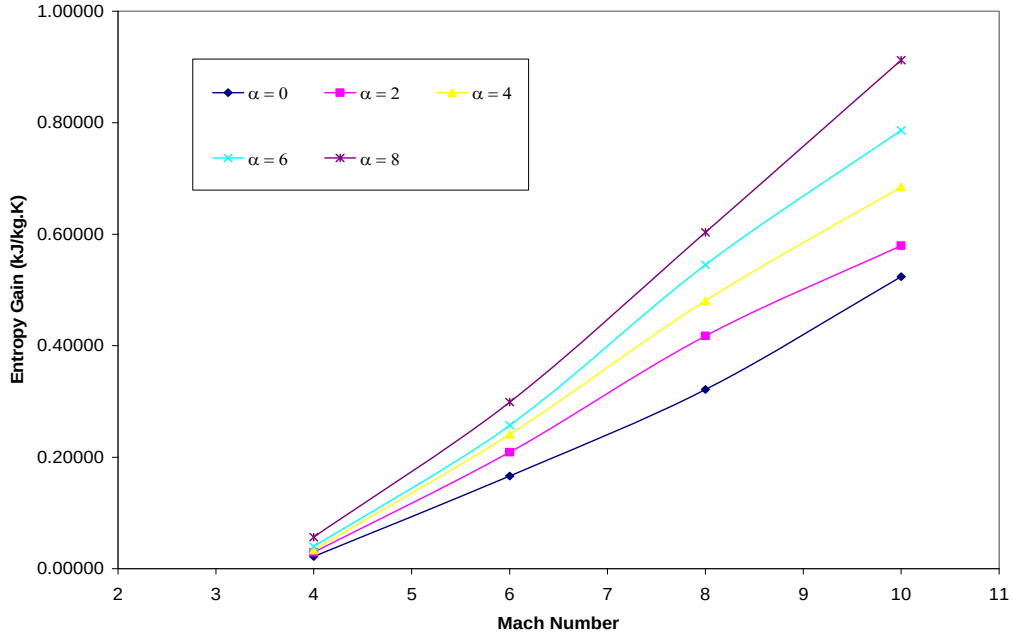

Figure 9. Variation of Entropy Gain with Initial Mach Number

for various Angle of Attack (Length Between Ramp and Cowl Tips = 0.9246 m)

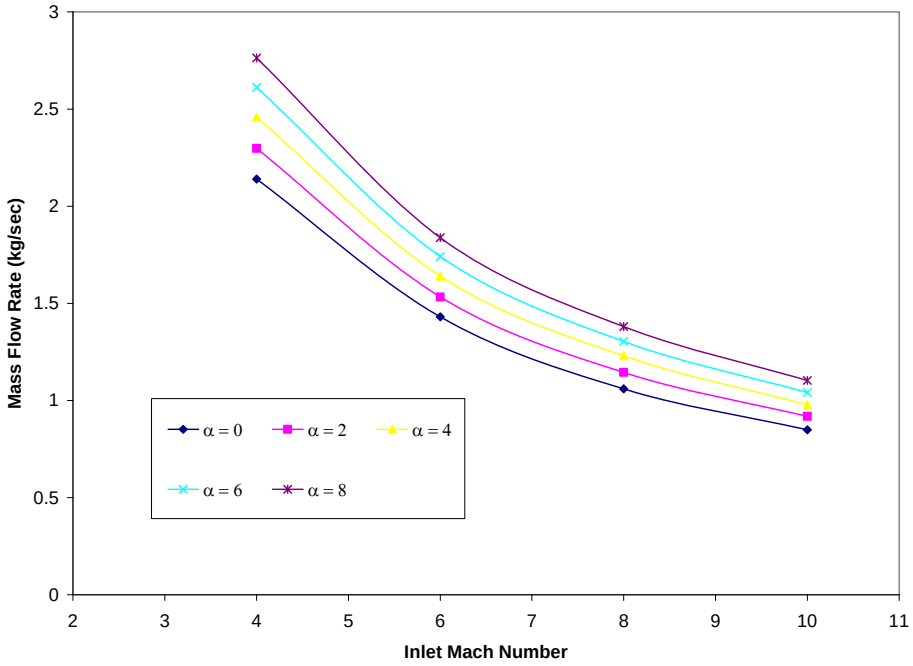

Figure 10. Variation of Mass Flow Rate with Initial Mach Number
for various Angle of Attack (Length Between Ramp and Cowl Tips = 0.7722 m)

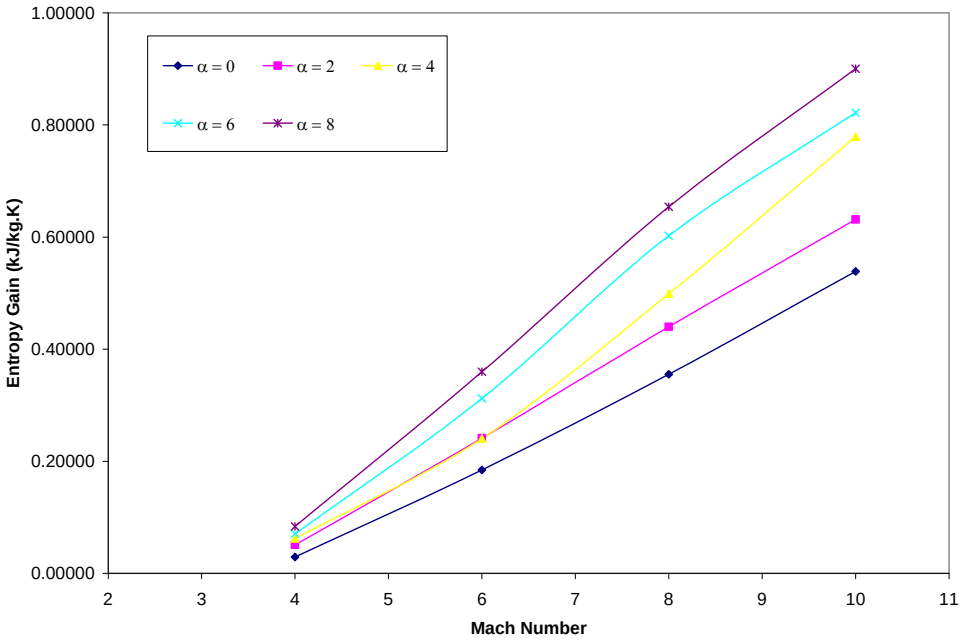

Figure 11. Variation of Entropy Gain with Initial Mach Number
for various Angle of Attack (Length Between Ramp and Cowl Tips = 0.7722 m)

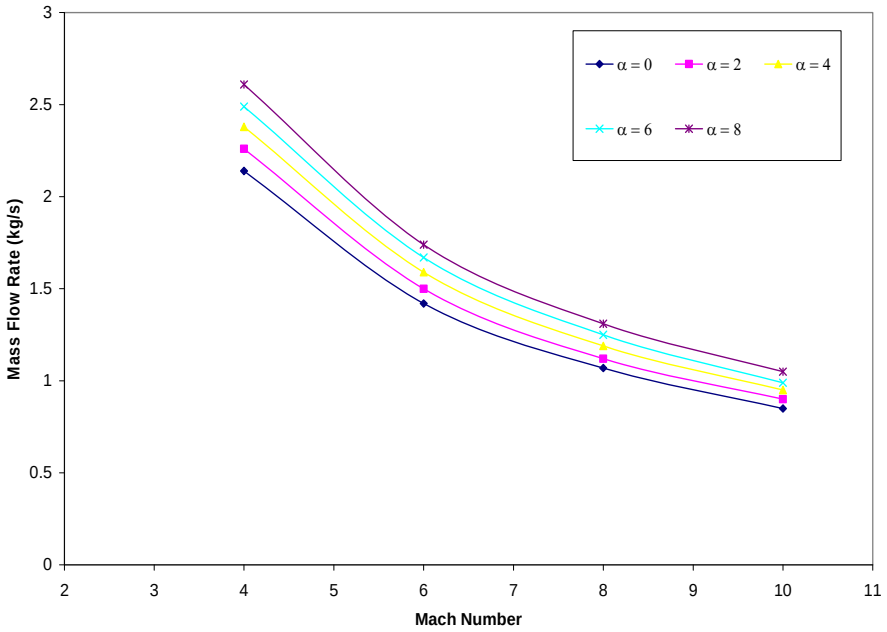

Figure 12. Variation of Mass Flow Rate with Initial Mach Number for various Angle of Attack (Length Between Ramp and Cowl Tips = 0.5944 m)

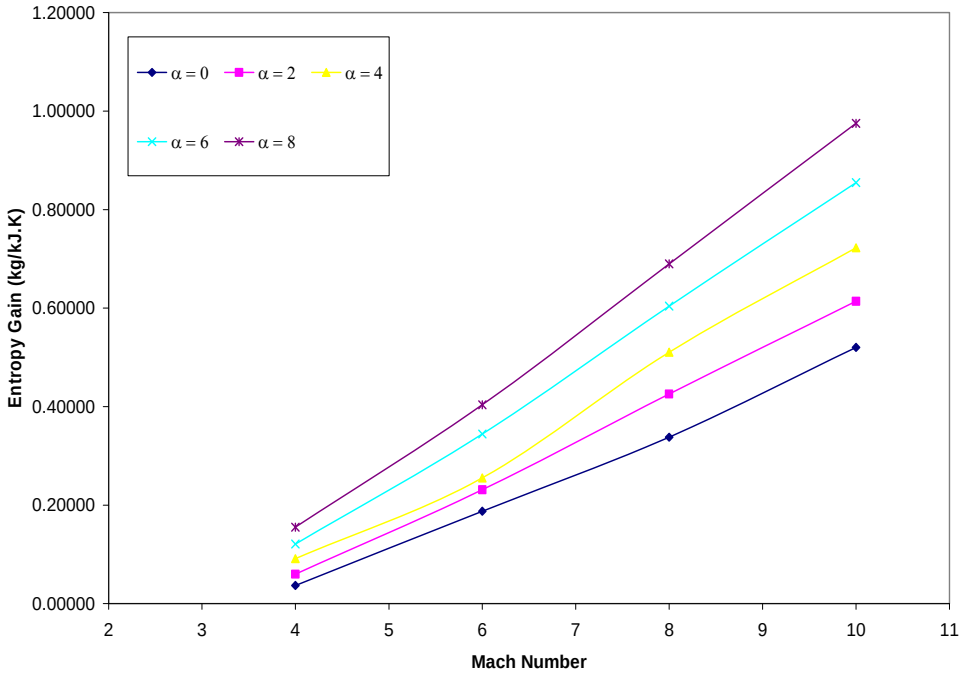

Figure 13. Variation of Entropy Gain with Initial Mach Number for various Angle of Attack (Length Between Ramp and Cowl Tips = 0.5944 m)

4. Response Surface Approximation of Objective Functions

Response surface methodology (RSM) is a collection of statistical and mathematical techniques useful for developing, improving, and optimizing processes. It also has important applications in the design, development, and formulation of new products, as well as in the improvement of existing product designs. The most extensive applications of RSM are in the industrial world, particularly in situations where several input variables potentially influence some performance measure or quality characteristic of the product or process. This performance measure or quality characteristic is called the response [4]. It is typically measured on a continuous scale. Most real-world applications of RSM will involve more than one response. The input variables are sometimes called independent variables, and they are subject to the control of the engineer or scientist, at least for purposes of a test or an experiment. The field of response surface methodology consists of the experimental strategy for exploring the space of the process or independent variables, empirical statistical modeling to develop an appropriate approximating relationship between the yield and the process variables, and optimization methods for finding the levels or values of the process variables that produce desirable values of the responses.

The response surface methodology is adapted in the present study. The RSM is effective in presenting the global characteristics of the design space and filtering the noise associated with design data. However, depending on the order of polynomial employed and the shape of the actual response surface, the RSM can introduce substantial errors due to its generally low order representation. Additionally, the number of design points needed to construct a response surface increase rapidly with the number of design variables. For example, for a second order response surface, the number of coefficients associated with the polynomial scales with the number of design variables, N as (N+1)(N+2) / 2! , while a third order polynomial scales as (N+1)(N+2)(N+3) / 3! .

In this study, the response surfaces are fit with 2^{nd} order polynomials using standard least-squares regression. Statistical analysis software, JMP [5], is used for the generation of the polynomials. When the standard least-squares regression method [6] is used to generate response surface, an appropriate order polynomial is fitted to a set of data points, such that the adjusted RMS error σ_a is minimized and quality parameter, R^2_{adj} is made as close as possible to one. The σ_a and R^2_{adj} are defined as following:

Let N be the number of data points and N_p be the number of coefficients and error e_i at any point i being define as:

$$e_i = f_i^a - f_i^p$$

Where, f_i^a is the actual value of the function at the design point and f_i^p is the predicted value. Hence:

$$\sigma_a = \sqrt{\frac{\sum_{i=1}^{N} e_i^2}{(N - N_p)}}$$

$$R_{adj}^2 = 1 - \frac{\sigma_a{}^2 \left(N_p - 1\right)}{\sum_{i=1}^{N} \left(y_i - \bar{y}\right)}$$

Where,

$$\bar{y} = \frac{\sum_{i=1}^{N} y_i}{N_p}$$

The CFD data of 60 cases were used to generate response surfaces. The results were first normalized (design variables and objective functions) with respect to the maximum value of each of the parameter. The normalized variables and objective functions are given in Table 2. The following response surfaces were obtained between design variable and objective functions:

Mass Flow Rate = $1.45609 + 0.12381*\alpha + 0.06151*L - 2.33075*M - 0.00029*\alpha*\alpha + 0.18332*\alpha*L + 0.02349*L*L - 0.19740*\alpha*M - 0.14229*L*M + 1.22625*M*M$

Entropy Gain = $0.04252 + 0.04628*\alpha - 0.59528*L + 0.52264*M + 0.03898*\alpha*\alpha - 0.30526*\alpha*L + 0.35336*L*L + 0.56207*\alpha*M - 0.07646*L*M + 0.23809*M*M$

The quality of the response surface is given in Table 3. The response surface for the entire objective had very high adjusted coefficient of multiple determination which indicate good capabilities. The RMS error for response surface fitted to both objective functions mass flow rate and entropy gain are quite low.

Table 2. Normalized CFD Data

Case #	Angle of Attack	Ramp Length	Mach Number	Mass Flow Rate (kg/s)	Entropy Gain (kJ/kg.K)
1	0	1	0.4	0.734	0.00829
2	0	1	0.6	0.487	0.14642
3	0	1	0.8	0.365	0.29832
4	0	1	1	0.293	0.48401
5	0	0.835	0.4	0.735	0.01093
6	0	0.835	0.6	0.491	0.15608
7	0	0.835	0.8	0.364	0.31274
8	0	0.835	1	0.292	0.48912
9	0	0.643	0.4	0.735	0.03702
10	0	0.643	0.6	0.488	0.18756
11	0	0.643	0.8	0.368	0.33785
12	0	0.643	1	0.292	0.52022
13	0.25	1	0.4	0.802	0.00925
14	0.25	1	0.6	0.534	0.18083
15	0.25	1	0.8	0.4	0.36537
16	0.25	1	1	0.32	0.5599
17	0.25	0.835	0.4	0.845	0.03021
18	0.25	0.835	0.6	0.527	0.19775
19	0.25	0.835	0.8	0.393	0.37881
20	0.25	0.835	1	0.316	0.56856
21	0.25	0.643	0.4	0.776	0.06048
22	0.25	0.643	0.6	0.515	0.23158
23	0.25	0.643	0.8	0.385	0.42571
24	0.25	0.643	1	0.309	0.61371
25	0.5	1	0.4	0.869	0.01216
26	0.5	1	0.6	0.579	0.20545
27	0.5	1	0.8	0.434	0.43169
28	0.5	1	1	0.346	0.64115
29	0.5	0.835	0.4	0.79	0.03327
30	0.5	0.835	0.6	0.564	0.22356
31	0.5	0.835	0.8	0.423	0.44864
32	0.5	0.835	1	0.336	0.70028
33	0.5	0.643	0.4	0.818	0.0912
34	0.5	0.643	0.6	0.546	0.15634
35	0.5	0.643	0.8	0.409	0.51062
36	0.5	0.643	1	0.326	0.72262
37	0.75	1	0.4	0.935	0.0153
38	0.75	1	0.6	0.623	0.2261
39	0.75	1	0.8	0.469	0.48639
40	0.75	1	1	0.374	0.73568
41	0.75	0.835	0.4	0.897	0.04854
42	0.75	0.835	0.6	0.598	0.2643
43	0.75	0.835	0.8	0.448	0.53359
44	0.75	0.835	1	0.358	0.75954
45	0.75	0.643	0.4	0.856	0.12124
46	0.75	0.643	0.6	0.574	0.34447
47	0.75	0.643	0.8	0.429	0.60404
48	0.75	0.643	1	0.34	0.85491
49	1	1	0.4	1	0.02833
50	1	1	0.6	0.668	0.25448
51	1	1	0.8	0.5	0.55169
52	1	1	1	0.398	0.82622
53	1	0.835	0.4	0.949	0.06377
54	1	0.835	0.6	0.632	0.30632
55	1	0.835	0.8	0.474	0.59528
56	1	0.835	1	0.379	0.85069
57	1	0.643	0.4	0.897	0.1553
58	1	0.643	0.6	0.598	0.4038
59	1	0.643	0.8	0.45	0.69
60	1	0.643	1	0.361	0.9753

Table 3. Quality Parameter of Response Surfaces

Observations	Mass Flow Rate	Entropy Gain
RSquare	0.925564	0.959971
RSquare Adj	0.921576	0.957626
Root Mean Square Error	0.056451	0.053942
Mean of Response	0.540217	0.35805

5. Optimization Approach

The methodology that will be used for generating Pareto optimal front is a multi-objective evolutionary algorithm (MOEA). The specific algorithm to be used is the Elitist non-dominated Sorting Genetic Algorithm (NSGA-II) [4]. All genetic algorithm codes use some form of sorting scheme to get non-dominated solutions. Non-dominated solutions are the best solutions. Among the non-dominated solutions one cannot be said to be better then the other. NSGA-II uses an explicit diversity-preserving mechanism. The starting point is the identification of constraints, performance criteria, design variables and allowable range of design variables. The response surfaces generated from the results of the CFD simulations are incorporated into the NSGA-II code.

In NSGA-II algorithm the code first creates a parent population of P_t of size N. From the parent set it then creates an offspring population Q_t of size N. The NSGA-II algorithm instead of finding the non-dominated front of Q_t only, uses the combined population of P_t and Q_t to form R_t of size $2N$. Then, a non-dominated sorting is used to classify the entire population R_t. Although this requires more effort compared to performing a non-dominated sorting on Q_t alone, it allows a global non-domination check among the offspring and parent solutions. Once the non-dominated sorting is over, the new population is filled by solutions of different non-dominated fronts, F_i, one at a time. The filling starts with the best non-dominated front and continues with solutions of the second non-dominated front and so on. Since the overall population size of R_t is $2N$, not all fronts may be accommodated in N slots available in the new population. All fronts which could not be accommodated are simply deleted. When the last allowed front is being considered, there may exist more solutions in the last front than the remaining slots in the new population. Instead of arbitrarily discarding some members from the last front, a niching strategy[1] is used to choose the members of the last front based on crowding distance. The solutions kept in the population are those which have the largest crowding distance thus keeping the diversity of the solution. This new set of solutions is now the parent set for the next generation. The procedure is then repeated till the best non-dominated set is obtained.

Pareto Optimal Solutions

In order to obtain the Pareto optimal solutions of the two objective functions, namely, the Mass Flow Rate and Entropy Gain, NSGA-II was simulated using the response surface equations. The two response surface equations were incorporated in the code through a subroutine. The parameters needed to run the code were provided in an input file. The relevant parameters were set [7] as follows for our simulations:

Population size : 100
Generations : 250
Crossover probability (P cross) : 1.00
Distribution parameter (for crossover) : 20
Mutation probability (P_{mut}) : 0.250
Distribution parameter (for mutation) : 200

After the simulation, the code generates several output files of which one file contains all the optimal solutions called the global population archive (for our case containing 3,931 solutions) and the second one is a file containing 100 non dominated solutions created during the final iteration. Domination and non-domination criteria are described in the previous section. Non-dominated values are the best values according to desired maximization/minimization of the objective functions among all values in the global output. The range of the values of the design variables used are angle of attack (0 – 1), Length (0.643 – 1), and Mach number (0.4 – 1). A 2-D plot of entropy gain with respect to the mass flow rate using only the 100 non dominated solutions is shown in Figure 14. During non-domination check, it is found that the best non-dominated solution has a normalized mass flow rate of 0.3534 and a normalized entropy gain of 0.9685. The normalized design variables corresponding to this optimum condition are angle of attack = 1, length = 0.643, and Mach number = 1.

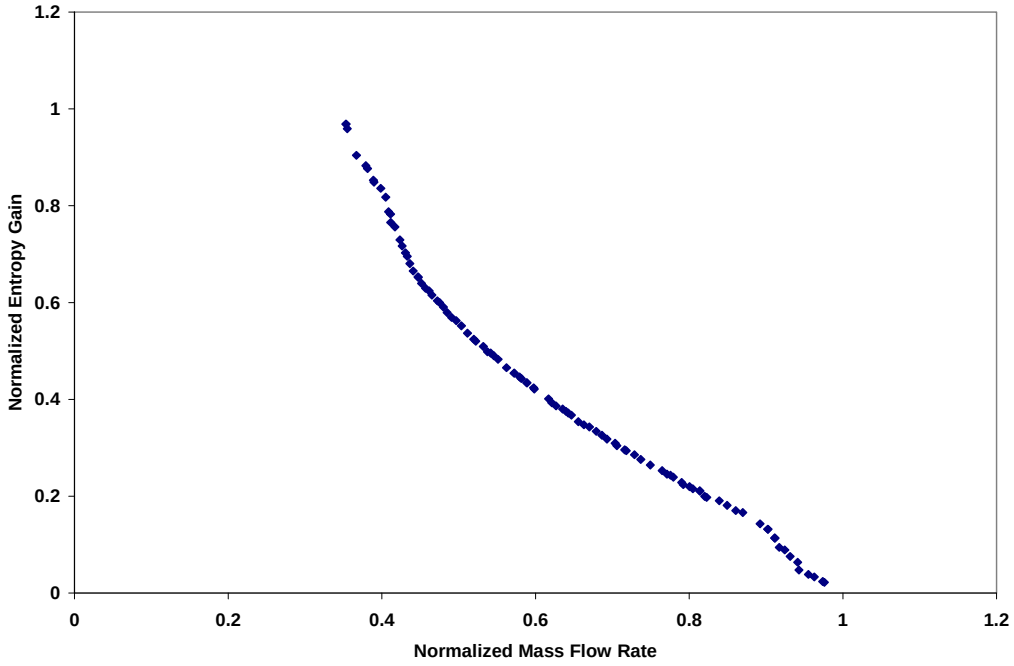

Figure 14. Non-dominated solution of entropy gain vs. mass flow rate

6. Conclusions

A response surface based Pareto optimization scheme using genetic algorithm is presented on a supersonic 2-D mixed-compression engine. The scheme can be expanded in a practical and meaningful way by including more objective functions and design variables. The current work tried to demonstrate the application of the scheme with two objective functions and three design variables.

References

[1] D. Rozario and Z. Zouaoui, "Computational Fluid Dynamic Analysis of Scramjet Inlet", University of Wales, UK

[2] M.K. Jain and S Mittal "Euler Flow in a Supersonic Mixed-Compression Inlet", International Journal for Numerical Methods in Fluids, 2006; 50: 1405 – 1423.

[3] E.A. Luke "CHEM: Computational Combustion Modeling", Mississippi State University, 2004.

[4] Kalyanmoy Deb: Multi-objective Optimization using Evolutionary Algorithms, John Wiley and Sons, New York, 2004.

[5] JMP, The Statistical Discovery SoftwareTM, Version 5, Copyright @ 1989-2002, SAS Institute Inc., Cary, NC, USA

[6] Rajkumar Vaidyanathan, P.Kevin Tucker "CFD-Based Design Optimization for A single Element Rocket Injector ", AIAA paper 2003-0296, 6-9 January 2003

[7] Tushar Goel, Rajkumar Vaidyanathan, "Response Surface Approximation of Pareto optimal front in multi-objective optimization", 10th AIAA/ISSMO Multidisciplinary Analysis and Optimization Conference, Albany, New York, Aug. 30-1, 2004